Mathematical modelling of the embolization process in the treatment of arteriovenous malformations

Alexander H. White

Centre for Mathematics and Physics in the Life Sciences
and Experimental Biology
University College London
University of London

A thesis submitted for the degree of
Doctor of Philosophy

Supervisors

Prof. F. T. Smith and Mr. N. D. Kitchen

December 2007

ProQuest LLC
789 East Eisenhower Parkway
P.O. Box 1346
Ann Arbor, MI 48106-1346

I, Alexander White, confirm that the work presented in this thesis is my own. Where information has been derived from other sources, I confirm that this has been indicated in the thesis.

Abstract

Arteriovenous malformations (AVMs) are neurological defects where the arterial and venous systems are connected directly with no intervening capillaries. The absence of capillaries means that blood at high pressure is entering the venous system directly and so a venous haemorrhage is possible. AVMs can be treated by embolization in which a glue is injected into a local artery with the aim of diverting the blood flow away from the AVM and so reducing the risk of haemorrhage.

The thesis introduces a mathematical model for the embolization process by considering a two phase fluid dynamical model. Both numerical and asymptotic techniques are used to analyse the flow of the two fluids in different configurations. At the start of the thesis both the fluids are treated as inviscid and their interaction modelled using analytical techniques such as conformal mapping theory. Next, viscous effects are included in the model by assuming that both fluids are present in a thin wall layer as would be the case just before the glue has set. Finally the problem of both fluids being present in the core of the artery is treated numerically using the Volume of Fluid method. A detailed account of this method is given. The method essentially tracks the interface between the glue and the blood over time and thus can model how the glue spreads, for instance just after injection.

Acknowledgements

First I would like to thank Rob Seymour and Anne Warner for giving me the chance to undertake this work. Thanks to my supervisor Frank Smith, with whom it has been a pleasure to work. I would also like to thank Neil Kitchen and Fergus Robertson, for interesting discussion on the medical application of this work and my colleagues in the mathematics department in particular Linzhong Li, Mehmet Sahin, Renzo Ricca and Isidoros Strouthos.

Contents

List of Figures

List of Tables

Chapter 1

Arteriovenous malformations and their treatment

1.1 Stroke

Stroke is one of the major causes of death and disability in the western world, and in the United States it is the third leading cause of death after cancer and heart disease. A stroke may occur when normal blood supply to the brain is interrupted, which is usually caused by a burst artery in the brain or a blockage caused by debris in the arterial network in the brain. An interruption to the blood flow can deprive cells of oxygen which is supplied by the blood, resulting in death of these cells; the latter, unlike other cells in the body, cannot regrow.

There are two main types of stroke: these are ischemic and haemorrhagic. An ischemic stroke is more common, with figures in the literature estimating that 83% of all strokes are ischemic. An ischemic stroke occurs when there is an obstruction to the blood flow in arteries supplying the brain. A blood clot may form somewhere in a vessel, blocking the path of the blood. This is known as cerebral thrombosis. Cerebral embolism, on the other hand, is the other major type of obstruction associated with ischemic stroke. Here the

blood clot forms at another location in the circulatory system, commonly in the heart or lungs. This blood clot then passes through the arterial network until it encounters vessels that are too small for it to continue its journey and at this point a blockage to the flow occurs. The third and least common type of ischemic stroke is called lacunar stroke. Here, very small blood vessels in the brain may become blocked leading to the death of cells in the immediate neighbourhood. This type of stroke though is usually much less severe than the other two described.

Haemorrhagic stroke generally results from a weakened vessel wall. The vessel ruptures, resulting in bleeding or a haemorrhage. This type of stroke makes up 17% of all strokes. There are two main forms of hemorrhagic stroke. These are intracerebral haemorrhage and subarachnoid haemorrhage. Subarachnoid haemorrhage is a bleed into the subarachnoid space just outside the brain. This is most often caused by a break in a blood vessel at the base of the brain. Intracerebral haemorrhage on the other hand occurs when arteries within the brain burst, and blood leaks inside the brain. The sudden pressure change can lead to unconsciousness or death straight away. Intracerebral haemorrhage usually occurs in specific areas of the brain, including the basal ganglia, cerebellum, brainstem, or cortex [104].

In general haemorrhagic stroke is caused by two main underlying factors, aneurysms and arteriovenous malformations (AVMs). An aneurysm is a weakened arterial wall, which may be balloon shaped. This weakness can cause the balloon-like structure to burst, leading to haemorrhage. An arteriovenous malformation on the other hand is an abnormally formed network of arteries, capillaries and veins, which again lead to weakness in the vessel walls and may be prone to rupture. A detailed review of AVMs is given in the next section.

1.2 Arteriovenous malformations

In a healthy and properly functioning human body, arteries carry oxygen-rich blood from the heart to the body's organs and cells. These vessels get progressively smaller to the point where they become very thin-walled capillaries which allow nutrients in the blood to enter the tissues. The nutrient-deficient blood then returns to the heart via a system of moderately thin-walled vessels called veins. When there are no intervening capillaries an abnormal flow pattern results, and a complex tangle of arteries and veins develops, resembling a knotted rope, see figures 1.1 and 1.2. This is called an arteriovenous malformation(AVM).

Arteriovenous malformations (AVMs) can be categorized as defects of the circulatory system, which are assumed to be congenital (present at birth or early in life and slowly developing over time), and usually no specific cause for the AVM can be identified. They can occur in many different areas of the human body, not just the brain; however we shall concentrate on cerebral AVMs because of the health consequences and their ability to lead to a mortality. In an AVM, blood at high pressure in the arterial system empties directly into the venous system (low pressure) due to the absence of intermediate capillaries. Veins however only have very thin walls and are only capable of containing blood at relatively low pressure. The abnormally high flow rate causes the blood pressure to rise to dangerously high levels, and there is a possibility that the wall of the vein may break due to this high pressure and hence a venous haemorrhage may result. Another important consequence of blood flow directly from arteries to veins is that oxygen and glucose, both essential for survival, cannot be extracted correctly by the tissues in the walls of either arteries or veins. This causes an abnormal response by the immune system and may cause the onset of a stroke. Cerebral AVMs occur in approximately 3 out of 10,000 people [103], and are slightly more common in males. Although

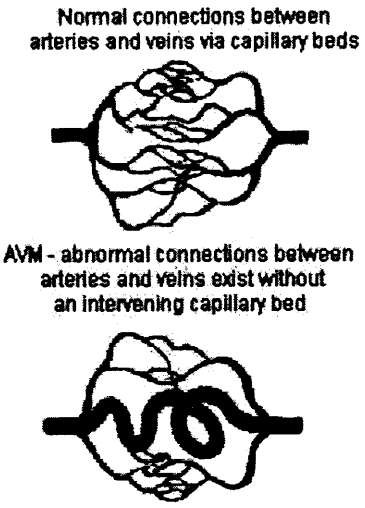

Figure 1.1: Comparison between a healthy system (top) and an AVM (bottom). Taken from [105]

the lesion is present at the time of birth, symptoms may occur at any time and often present themselves when the patient is aged between twenty and forty. In an AVM there is a reduced vascular resistance and hence an increased flow rate occurs from the arterial to the venous system. The two main surgical procedures used to try to reduce the flow rate are clipping and glue-casting, to reduce the mass flux through the AVM. Due to the limited understanding of these procedures and their outcomes, these procedures tend to err on the side of caution.

1.2.1 Structure of AVMs

Cerebral AVMs are typically large and wedge shaped, and consist of three distinct components: arterial feeders (AFs), a conglomerate of enlarged abnormal vessels (the nidus) and draining veins (DVs). The veins of the brain drain into venous sinuses, blood-filled areas located in the dura mater, before leaving the

skull and travelling to the heart. An AVM without a nidus is known as an aretiovenous fistula (AVF). In an AVF there is a direct connection between one or more arteries and veins or sinuses. Dural AVFs and carotid-cavernous fistulas (CCF) are the most common AVFs.

The structure of an AVM may be seen by using angiography. An angiogram gives detailed pictures of the structure of the blood vessels in the region of the AVM. An angiogram of a cerebral AVM is shown in Figure 1.3. Here the nidus and draining veins can be seen quite clearly.

1.2.2 Different types of AVM

There are four main types of AVMs, which are categorized below

1. True AVM. The most common form of AVM consisting of the tangle of arteries and veins as described above. There is a further division into convex and deep AVMs, which is known as Yasargilis classification. Convex malformations are further categorised into sulcal and gyral types, which are so named according to their location. Deep AVMs are also subdivided into two types, Subarachnoid AVMs and Paraenchymal AVMs, again dependent on location [79].

2. Venous malformation (VM). One or more dilated veins in the brain. The walls of these channels are unusually thin because of a relative lack of smooth muscle cells [101]. They may occur in many different parts of the body and brain.

3. Dural fistula (also known as dural AVFs). Occurs when there is an abnormal connection of vessels in the dura mater, a protective layer surrounding the brain, and fast shunting of blood occurs between the arteries and veins. There are three main kinds: Dural carotid cavernous sinus fistula,

Transverse-sigmoid sinus dural fistula and Sagittal-sinus dural fistula. These types of malformation are often treated using embolization.

4. Cavernous malformation. This is another vascular malformation in the brain. It effects the capillaries and smallest veins, vessels which have abnormally thin walls that are prone to leak. With these malformations no supportive tissues are present, so when blood enters they stretch and may not return to their initial state when the blood vessels have emptied.

1.3 Symptoms of AVMs

People with neurological AVMs (those affecting either the brain or spinal cord) may experience few if any major symptoms; in many cases the patient does not know they have an AVM and it is sometimes only discovered when treating an unrelated condition or even at autopsy. However about 12 % of these lesions do become symptomatic and indeed 1% of those affected will die due to the AVM [103].

A common complaint is a headache. These headaches vary greatly in severity and can be as serious as migraines. Sometimes headaches may be accounted for by the location of the AVM, but usually the pain encompasses the whole head. Perhaps the most distinctive symptom of an AVM is an audible bruit. This term, from the French word for noise is used to describe a sound which is caused by a large amount of blood travelling through the veins at a given time. This sound is likened to the sound heard when water is gushing out of a pipe or waterfall. However the phenomenon is usually heard only by the clinician and rarely by the patient.

Among problems caused by AVMs are weakness and paralysis. Other problems can be a loss of coordination, loss of memory and swelling of part of the optic nerve called the optic disk. Also patients may suffer from numbness, tin-

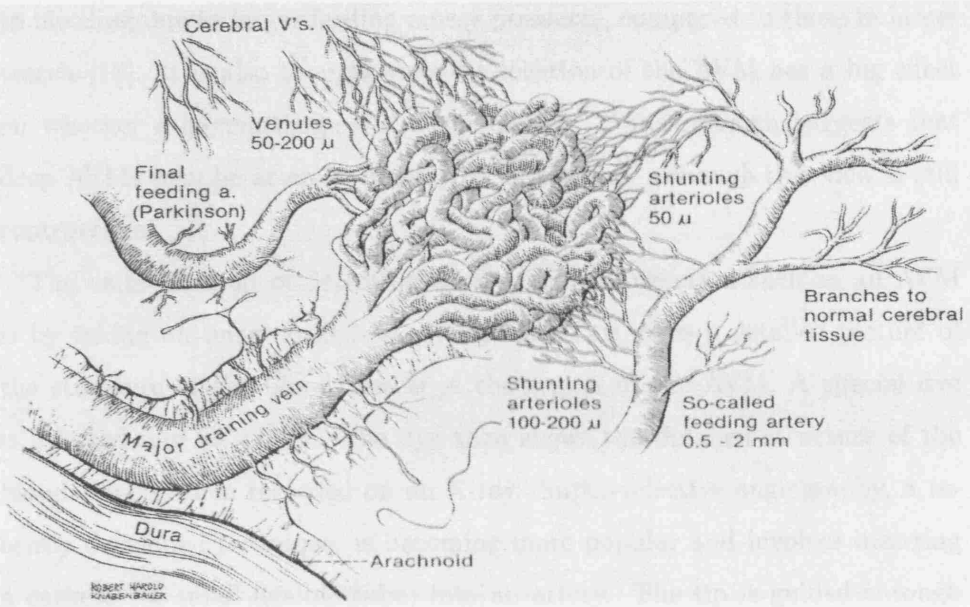

Figure 1.2: The complex geometries of a typical AVM with en-passant feeders. Taken from [106].

gling in the hands and feet and even hallucinations and dementia. It has been found recently that the presence of an AVM may be responsible for learning and behavioural disorders, usually in teenage years, long before the AVM is usually identified.

1.3.1 Detection and treatment

Approximately 50% of patients with AVMs come to medical attention after haemorrhage [18]. The next most common symptom is a seizure. The rate of haemorrhage for AVMs varies in the literature but the common consensus is that the rate is between 2 and 4%. It is still unknown whether factors such as alcohol and tobacco use, pregnancy and hypertension could increase the risk of a bleed, however. It may be the case that smaller AVMs are more susceptible

to bleeding due to larger feeding artery pressures, compared to those in larger vessels [18]. It is also thought that the location of the AVM has a big effect on whether a haemorrhage will occur or not. Some research suggests that deep AVMs may be at an increased risk of rupture, although this view is still controversial.

The usual method of detecting a vascular malformation such as an AVM is by taking an image called an *angiogram*. This gives a detailed picture of the structure of the blood vessels in the region of the AVM. A special dye is injected into an artery. The dye then shows the detailed structure of the blood vessels when recorded on an X-ray. Super-selective angiography, a recently developed technique, is becoming more popular and involves inserting a catheter (a small flexible tube) into an artery. The tip is guided through the arterial network until the tip reaches the site of the AVM and then a small amount of contrast agent is released directly into the lesion. Two other techniques used for the detection of AVMs are Magnetic Resonance Imaging (MRI) scans and computed axial tomography(CT). MRI uses magnetic fields to detect change in neurological tissue: this has recently been developed to a new more powerful technique called magnetic resonance angiography(MRA), which may record both the pattern and the velocity of the blood flow through an AVM, and indeed give a three-dimensional representation of it by taking images at many different angles.

An AVM poses a complicated clinical problem. The clinician must determine the best strategy for removing the malformation without causing a haemorrhage, which can be difficult due to abnormally weak blood vessels. Administration of drugs may help to overcome the symptoms (described earlier) associated with AVMs but the main aim is either to remove or to alter the lesion. There are currently three main techniques used to do this: conventional neurosurgery, endovascular embolization and radiosurgery. The choice

of technique is dependent both on the size and position of the AVM. Only complete obliteration of the AVM is a definitive cure and this is only possible in a small amount of cases.

Neurosurgery acts by directly removing the core part of the AVM from the brain, while of course trying to cause as little damage as possible to surrounding tissues. This method is best when the AVM is small in size; however it cannot be performed if the AVM is located deep inside the brain. Radiosurgery involves directing a beam of radiation at the AVM. The aim of this is to damage vessel walls of the AVM so that they will eventually close. There are four main methods of radiosurgery used today, two of which use photons (high energy x-rays, gamma knife) while the other two use charged particles (helium ions, proton beams). These methods are not usually used to treat inter-cranial AVMs. Embolization aims to plug the fistula in order to correct the abnormal flow of blood. It utilizes glue or other objects which travel through blood vessels to obstruct the blood flow through the AVM, and in effect it aims to close off abnormal vessels.

The embolization procedure is often combined with micro-neurosurgery or indeed radiosurgery. For instance characteristics of an AVM such as a large nidus and deep feeding veins could be treated first with embolization and next with micro-surgery. It is often found that the preceding embolization treatment reduces both operation times and blood loss during the following operation. For AVMs which are situated in the eloquent cortex, radiosurgery is often the primary choice for treatment. Again embolization may be performed prior to this to reduce the overall size of the AVM.

The choice of which of the three main methods to use depends on many factors. For instance a patient with an AVM which is in an accessible area may be treated directly by micro-surgery which, if the surgery goes according to plan, can provide a cure. An AVM with multiple secondary feeders may also not

be suitable for treatment by embolization due to these vessels being too small for the catheter. Indeed such AVMs must in general be treated either with micro-neurosurgery or radiotherapy. If an AVM has already haemorrhaged and caused a fixed deficit it is likely to haemorrhage and so should be removed surgically if this is possible.

1.4 The embolization process

Embolization is one of the most common procedures in the treatment of AVMs and is popular as it is less invasive than forms of conventional neurosurgery. The technique was pioneered in the early 1960s by Lussenhop and Spencer [53] as well as Doppman and De Chiro. With improved technology and understanding, it is now possible to reach and successfully embolize quite complex AVMs in functional-dependent areas of the brain. Embolization may be performed as the only treatment for an AVM or may be combined with radiosurgery or conventional neurosurgery, and indeed patients having these treatments usually require embolization first if the lesion is larger than 3 cm across.

Embolization is almost always given to a patient under general anaesthetic. A small catheter is inserted into a blood vessel, typically the femoral artery in the thigh and then passed along the network of blood vessels to the feeding artery of the AVM, using X-ray guidance. Sometimes a very fine micro guide wire is used to achieve optimum positioning of the catheter. A glue is then passed through the catheter into the AVM and the tip of the catheter is positioned as close as possible to the branching site of the AVM. The aim of this procedure is to make the glue occlude the abnormal blood vessels so blood is no longer able to pass through the malformation. When there is no longer any blood passing through an AVM, there should be no further risk of bleeding. For larger AVMs, embolization is often done in stages such that at each stage

a certain section of the AVM is blocked off. The glue that is used is initially in a liquid state to penetrate small vessels and then hardens on contact with ions such as those present in blood.

The catheter can be flushed with dextrose to prevent solidification inside the catheter. The glue is pushed through the arterial network, until in reaches the correct position. Care must be taken to inject the glue neither too fast nor too slowly. If the glue is injected too slowly there is a risk that the feeding vessel may become occluded, whereas if the glue travels too fast it may continue through to the veins and back into the circulatory system, with perhaps disastrous consequences. When the glue has been injected the catheter must be withdrawn straight away to stop the catheter becoming glued in place, which can also cause a stroke.

When the AVM has been obliterated there is little chance that a haemorrhage can occur in future. However with embolization treatment obliteration of the AVM is not the goal and such treatment is unlikely to prevent complete occlusion. Perhaps the main reason for this is that it is extremely difficult to embolize all of the arterial feeders associated with the AVM which may be very small and difficult to reach.

Following the treatment the patient is kept lying on their back for the next five to ten hours and is usually kept in hospital for a few days. Sometimes more than one embolization is needed, particularly when the AVM is large, and also to avoid altering blood flow patterns in the brain too rapidly or drastically. It should be noted that even though the embolization procedure may have been carried out successfully the blood vessels may open again over time as the body tries to remove a foreign material such as the glue. If this happens the procedure can be repeated, or another type of treatment may be more beneficial.

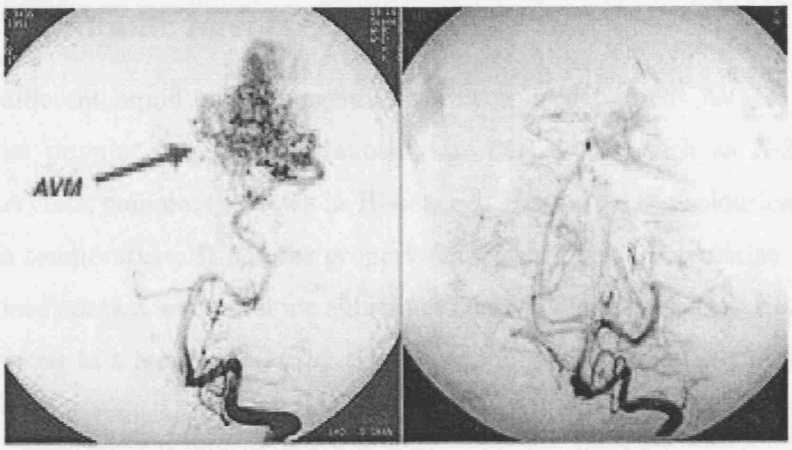

Figure 1.3: Two angiograms showing the blood flow when the AVM is present (left) and after treatment with embolization (right). Now blood has returned to other vessels. Taken from [102].

1.4.1 Complications of endovascular surgery

Due to the relatively short time frame in which embolization has been used, approximately forty years, there are still many ways in which such treatments can be improved. Indeed research into embolization of AVMs is ongoing worldwide. In general, complications due to endovascular surgery are divided into two distinct categories: those that occur during the surgery and those that occur within a seventy-two hour period following the operation. It is possible for the catheter to damage the arterial wall when the embolization is performed, resulting in a bleed. This however can usually be treated with another immediate embolization. After the operation neurological deterioration can be identified by means of a computerized tomography scan. Conditions such as oedema or haemathoma can either be treated with mannitol which reduces intracranial blood pressure or they can be removed with microsurgery.

1.4.2 Embolic agents

Many different liquid embolic agents have been used to treat AVMs. Today the most popular choices are cyanoacrylate derivatives, such as N-2-butyl-cyanoacrylate, commonly known as Histoacryl. Histoacryl is a colourless liquid at room temperature. It has the property that it begins to polymerise when it comes into contact with an ionic substance such as blood or saline. Histoacryl is converted to a long polymer by the nucleophiles present in the blood [36].

The polymerization happens very rapidly, and in fact if the operation were to be performed with Histoacryl only, the glue would solidify at the catheter tip. To stop this from happening and to delay the overall time for solidification the Histoacryl is mixed with a fat-based substance such as lipidol, which slows down the overall time for the polymerization by reducing the contact of the blood and the monomer. In general the mixture will contain 20-40 % Histoacryl, which extends the time for polymerization sufficiently for the glue to penetrate the nidus and solidify in the desired position. The viscosity of lipidol is 26cP at 25 degrees C, whereas the viscosity of the N-butyl cyanoacrylate is taken to be 3.2cP in the literature. Therefore the viscosity of the resulting glue is linearly dependent on the amount of lipidol. Also glacial acetic acid may further be added to the mixture to increase still further the overall time for polymerization [26]. In this study different embolic agents composed of ethiodized oil (formed by iodinating the ethyl ester groups in the fatty acids in poppyseed oil), NBCA and glacial acetic acid were used in the embolization process in the femoral and subclavian arteries in rabbits. The blood flow through the arteries was analyzed carefully and the time taken for the blood flow to stop was found. The research found that the time elapsed for flow arrest (TEFA) was independent of the concentration of ethiodized oil present in the scenario; however the addition of the glacial acetic acid affected the TEFA factor quite significantly and indeed a linear relationship between the amount

of glacial acetic acid and the TEFA factor was found.

Mixing the Histoacryl with the lipidol, however, changes not only the polymerization time but also the properties of the glue. The resulting mixture comes out of the catheter in droplets rather than a continuous stream [36]. In general, lesions that can be cured with Histoacryl are those with a single parent vessel and those which are small in size.

Another commonly used substance for embolization is Onyx, a mixture of ethylene-vinyl alcohol (EVOH) and dimethyl sulfoxide (DMSO) that was first used by Taki [92]. This embolic mixture does not stick to the sides of the vessel wall but it is thick enough to become lodged in the vessel without damaging the arterial walls.

Various different concentrations of EVOH are given in the literature to make Onyx, which range from 6% to 8%. In fact the lower the concentration of the EVOH the less viscous is the Onyx and hence the further the Onyx will travel. Because Onyx is non-adhesive it has several advantages over Histoacryl as a candidate for intravascular embolization. Gluing the catheter in place and the occurrence of reflux are no longer a problem. Also Onyx can be injected more slowly than Histoacryl due to no polymerization occurring when Onyx comes into contact with the blood. Some practitioners favour Onyx for this reason and suggest a greater control over the travel of the glue with Onyx compared with Histoacryl. It has also been reported in the literature that the cure rate for AVMs treated with Onyx is greater than for those treated with Histoacryl.

1.4.3 Advantages and Disadvantages

Perhaps the main advantage of this treatment is that it is less invasive than forms of conventional neurosurgery and it can be used to treat deep or inoperable AVMs. Embolization is very useful in making the AVM smaller in size in order to be suitable for radiation treatment and is also useful for reducing

the blood flow through an AVM prior to surgery. This procedure can also be repeated when needed and there is generally only a short stay in hospital for the patient.

Disadvantages include the risk of embolic stroke from the catheter, and haemorrhage since the AVM is not completely obliterated: in such cases multiple treatments may be necessary. This treatment is however only possible if the AVM is composed of vessels that can be reached with a catheter. The risk of a stroke occurring while the treatment is being performed is approximately 2%. Occasionally the patient may suffer some side effects immediately after the treatment is performed. Headaches are common, which may be due to the blood vessels of the AVM clotting, and other symptoms such as lack of feeling in the arms and legs as well as loss of vision are also often observed.

1.4.4 The Spetzler-Martin scheme

Certain grading scales for the risk of treatment of AVMs have been put forward, of which the most commonly used is that proposed by Spetzler and Martin [47]. This system is a tool for assessing the risk associated with microsurgical resection [24]. It uses three characteristics of the AVM to arrive at a number between one and five, five being the most serious case. The characteristics are given in table 1.4.4 below. The Spetzler-Martin grade is determined as the sum of the three components of the table. Experience has shown that patients with a grade 1 or 2 AVM have a low morbidity rate associated with resection and indeed patients with a low grade AVM are often treated by surgery. In fact it is thought that AVMs which are of grade 4 or 5 should not be treated by embolization as the risks tend to outweigh the benefits [18]. Grade 4 and 5 AVMS are categorized as high risk and here the morbidity levels rise to 12-38%. There are differing opinions as to whether grade 3 AVMs should be treated or not, and indeed it is suggested that there should be a further subdivision for

Characteristic	Point value
Size	
< 30mm	1
30-60mm	2
>60mm	3
Location	
Eloquent brain	1
Non-eloquent brain	0
Pattern of venous drainage	
Superficial	0
Deep	1

Table 1.1: Spetzler-Martin system for grading arteriovenous malformations, taken from [47].

AVMs in this category [47].

Although the Spetzler-Martin grading system is useful, no two AVMs are the same. Each AVM needs to be examined individually, and the consequences of any surgery made known to the patient. In general the patients which are most suitable for any of the three main surgeries are those who are otherwise in a good medical condition and with small to medium sized AVMs which are in accessible parts of the brain. In fact the younger the patient the lower the risk when undergoing treatment and the greater the likelihood of benefit for the patient [58].

1.5 Physiological fluid dynamics

Fluid flows are commonplace in the human body, for example the transport of blood around the circulatory system, the flow of air in the lungs and the transport of urine in the bladder, to name just three. There is obvious potential benefit in trying to be able to model such flows; this is done to work out for example why a certain function of the body is not performing well and usually what action can be taken to eliminate or reduce the problem. Obviously work in this area requires expertise from specialists in the physiological sciences as well as those in fluid dynamics. The flows in the human body are generally quite different from those encountered in engineering applications [52] due mainly to the geometric structure, for example branching, to unusual fluid properties and to effects of pulsatility and wall flexibility.

1.5.1 Arterial blood flow

Modelling of arterial blood flow is widespread and has been the subject of much interest since the seventeenth century when Poiseuille found that the velocity distribution in a cylindrical pipe is parabolic and that the ratio of the pressure gradient and the flow rate is inversely proportional to the fourth power of the diameter of the tube. In general, two main areas have come to prominence when modelling arterial blood flow [63], namely propagation of pressure pulse and flow patterns, and wall shear distributions in complicated arterial geometries. Concerning the former, the pressure exerted by the blood on the artery wall can result in deformations to the wall, which in turn affect the blood flow [38]. Concerning the second, there is a link between high wall shear stress and cardiovascular disease such as atherosclerosis.

The cardiovascular system has an extremely complicated geometric configuration: blood vessels are typically short and curved and branching is present

throughout the body. It is of fundamental importance to understand the dynamics of the blood flow at a bifurcation: as most atherosclerotic lesions are found in such regions. They tend to form on the outer wall of a daughter at major bifurcations (most notably the carotid bifurcation). It is thought that this is caused by the shear stress imposed by the moving blood on the vessel wall. When the shear stress is high, structural damage may occur to the wall of the artery, whereas when the shear stress is too low there is a chance that this may result in the deposition of particles (plaque) on the artery wall.

Even for simple models, for example a one-dimensional model for a Newtonian fluid, the complex geometric structure makes the boundary conditions extremely complicated and makes solving the equations of motion a difficult task. Usually additional simplifications are made or advanced computational methods are implemented to gain a greater depth of understanding. Numerical techniques such as the well known finite-element method have been used to good effect, for instance [108]. Here a three dimensional Navier-Stokes solver in a moving domain aims to simulate blood vessels undergoing large deformations. Finite-volume simulations [43], [91] are also commonplace in blood flow modelling.

Previous studies have also considered the aortic or carotid bifurcation [15], where a single mother undergoes a symmetric bifurcation into two daughters, and the flow of air in the lung where a similar bifurcation is present. There are numerous accounts addressing the flow in such configurations but much less work has concentrated on the case of a single mother to multiple daughters and even grand-daughters, as is the case in AVMs.

The literature on the mathematical modelling of blood flow is vast, reviews can be found by [52], [63] and [98].

1.5.2 Mathematical Modelling of AVMs

As discussed in the previous section, there has been a considerable amount of research dedicated to the modelling of blood flow in arteries ([8], [23], [52], [98] and [107],) but much less on the haemodynamics associated with AVMs. Some models have aimed to simulate the flow in a simplified geometric configuration where the model is made up of a multiple array of parallel compartmentalized vessels. Another type of model for AVMs uses electrical circuit analysis [30], which aims to relate flow pressures to volume fluxes in networks, primarily with the desire to explain steal phenomena. Here 'steal' refers to strong throughput in the AVM which weakens cerebral throughput elsewhere.

Typically an AVM has many feeding arteries, each one of which may branch into as many as fifty daughters. Attempts have been made to analyse the flow structure in both the mother and the daughters [12], [85], [86] and [87]. The first of these studies a linear problem of a flow at high Reynolds number through a branching geometry both in two- and three-dimensional settings. The role of the geometric structure as well as the mass flux in the daughters is analysed for multiple small daughters. Work in [86] on the other hand gives a non-linear analysis of the flow assuming that the flow is inviscid; this is justified in some contexts by the fact that the boundary layer thickness is small compared to the thickness of the vessel downstream. The model analyses flow over short length scales, finds recurrence relations between the flow profiles in each of the daughters and then aims to solve them numerically. The model is useful because it is able to deal with branchings that produce considerably less solid area downstream, and hence more realistic geometries may be applied to this model. Fully three-dimensional effects of flow from one mother to two daughters have also been studied [10], [91]. Here a purely numerical finite-volume simulation is compared to slender flow analysis where the streamwise length scale is of order of the Reynolds number and strictly larger than the

two cross sectional length scales. Results for wall shear and pressure as well as velocity profiles are found for the flow in the cases of one mother branching to two daughters and close agreement is found between the theory and the numerical computations.

Recently Lattice-Boltzmann methods have been used to model AVMs [20]. These methods use a combination of ideas from statistical mechanics and cellular automata to model the flow in complicated geometries. Lattice-Boltzmann methods aim to simulate macroscopic flow conditions by considering the statistical distribution of particles representing the microscopic fluid flow. This method is becoming ever more popular and appears to be potentially very useful for modelling AVMs. Other methods that potentially could be applied to the glue and blood problem are those of particle tracking [5] and [93]. Preliminary modelling was tried at the start of this work, but was abandoned in favour of a full two-phase flow model.

It is intended that the present work will set up a basic mathematical model for the embolization process. Very little work has been done in this area previously, to the best of our knowledge, so this work is seen as a first step at modelling such a complex procedure, which hopefully can be expanded upon in the future. Although some of the simplifications made in the present work may oversimplify the complex chemical processes at work here, it is hoped this can be incorporated into further studies on the subject.

Chapter 2 below considers the mathematical model, with details given on the assumptions for the model and the governing equations of motion are stated. Chapter 3 considers a relatively simple inviscid model for flow, whereas chapters 4, 5 and 6 extend the analysis to include viscous effects. Chapters 7-10 concentrate on a purely numerical solution of the governing equations. Conclusions and indication of possible further work are given in chapter 11. A more detailed description of the individual chapters of the thesis is given at

the end of the next chapter.

Chapter 2

The mathematical model and governing equations of multiphase flow

2.1 Overview of the model

Throughout this work we will aim to model the embolization process using a two-phase fluid dynamical model. In all the chapters we refer to either the blood or the glue, the two fluids present in the embolization process. Throughout the thesis all glue properties such as viscosity, density and velocity have a subscript 1 and the blood properties are assigned the subscript 2.

Both fluids are taken to be incompressible and Newtonian fluids. This may be quite an accurate assumption for the blood, taking into account the size of the vessels considered here, but is probably a more naive assumption for the glue. Blood is a complex fluid and is made up of a suspension of platelets, red blood cells and lipids, where the red blood cells make up 40 % by volume. The kinematic viscosity of blood is approximately four times that of water.

Because many different types of glues are used, as outlined in chapter 1, and

different amounts of lipidol or other such substances are added, it is clearly not suitable to make exact judgements on the behaviour or properties of the glue. Indeed although the glue polymerizes on contact with the blood, little is known about the actual chemical reaction that takes place, although the reaction is thought to be exothermic [61]. In the present work we treat the density and viscosity of the glue as constant over space and time, which, although clearly not fully realistic, creates a firm starting point and will hopefully help when studying more complicated situations in future work.

Many other simplifications are also made to model the complex process. The walls of all the vessels are assumed fixed, similar to [85] and [86]. Models of flow of a single fluid through a branched network with moving walls can be found in [27]. It is assumed that the flow remains laminar at all times. This approximation is valid as experience shows that blood flow rarely becomes turbulent. The incompressibility assumption in both fluids means that the governing equations of motion are the incompressible Navier-Stokes equations, where the continuity equation dictates that the velocity field must be divergence-free. All the modelling in the thesis is two-dimensional and in most cases the Cartesian coordinates (x, y) are used for the distance parallel and perpendicular to the vessel walls respectively. Some of the problems studied are steady, so the time derivatives in the governing equations and boundary conditions can be ignored.

We define the ratios $\rho = \rho_1/\rho_2$ and $\mu = \mu_2/\mu_1$, for the density and dynamic viscosity respectively. These two formulae and the ratio for kinematic viscosity $\nu = \nu_2/\nu_1$ lead to the relation

$$\nu = \mu\rho, \tag{2.1}$$

in this setting. As stated earlier in this work, the values for the viscosities and densities of the two fluids do not vary in space or time. However when the problem is tackled numerically the density field over the whole domain is

discretized. Further details of this are given in chapter 8.

Later in this work, we usually assume that the Reynolds number Re is large where Re=ul/ν, and u is a representative velocity scale while l is taken to be the width of the vessel. In a typical feeding artery in an AVM, the diameter is approximately 0.001-0.005 m, and a typical local blood velocity of 1m/s. If the kinematic viscosity of blood is taken as $4.78\times10^{-6}\mathrm{m}^2\mathrm{s}^{-1}$, the Reynolds number is found to be in the range of 200 to 1000, similar to values given in [86]. (We note in passing that in chapter 4 it becomes necessary to non-dimensionalize the problem differently and so there the form of the Reynolds number is different to that given above.)

It should be pointed out that perhaps the main complexity involved with the current investigation is the fact that two fluids are present. As the interface conditions are inherently non-linear, little analysis is possible for the full system of governing equations. Analytical techniques are however useful when simplifications such as treating both fluids to be inviscid are used. Direct numerical computation is thus the main technique used to address the problem, although there are still many complexities in setting up the numerical method, which shall be described later on in the thesis.

Now that the model has been described in broad terms, a brief outline of the governing equations for multiphase flow is given. No attempt is made to derive these equations from first principles as these are readily available in the literature [7], [46].

2.2 Governing equations of multiphase flow

Consider two fluids (fluid 1, the glue and fluid 2, the blood) separated by an interface with zero thickness and given by the single-valued function $y = f(x,t)$, where t is time. We define the unit normal vector to the interface as

$\hat{\mathbf{n}}$ and the unit tangent vector $\hat{\mathbf{t}}$. The presence of the interface demands the application of boundary conditions between the two fluids. This is complicated by the fact that the free surface location is unknown and in a sense must be determined before the conditions can be applied. The velocity fields of the respective fluids are given by $\mathbf{u}_i = (u_i, v_i)$ with corresponding density and pressure fields ρ_i and p_i, with $i = 1, 2$. Both fluids satisfy the dimensional Navier-Stokes equations, written in conservative form as

$$\frac{\partial \mathbf{u_i}}{\partial t} + (\mathbf{u}_i \cdot \nabla)\,\mathbf{u}_i = \frac{1}{\rho_i}(-\nabla p_i + \nabla \cdot \mathbf{T}_i) + \mathbf{f}_i, \tag{2.2}$$

$$\nabla \cdot \mathbf{u}_i = 0. \tag{2.3}$$

Here $\mathbf{T}_i = \mu_i(\nabla \mathbf{u}_i + (\nabla \mathbf{u}_i)^T)$ is the viscous stress-tensor with the dynamic viscosity μ_i and kinematic viscosity $\nu_i = \mu_i/\rho_i$. Body forces are contained in the term $\mathbf{f}_i$, gravity being a typical example. These equations hold in both the glue and the blood, i.e. for $i = 1, 2$. The no-slip condition

$$\mathbf{u}_i = 0, \tag{2.4}$$

is applied at solid boundaries for viscous flow.

As noted in the previous section a rigorous derivation of the interfacial conditions for multiphase flow will not be given here, but details can be found in [7] or [46]. These conditions are made up of a kinematic condition and a dynamic condition as well as a condition on the velocity field at the interface. The kinematic condition,

$$\frac{\partial F}{\partial t} + \mathbf{u}_i . \nabla F = 0, \tag{2.5}$$

where $F = y - f(x,t)$, effectively states that a fluid particle on the interface must remain on the interface and is advected with the local velocity field $\mathbf{u}_i$.

The condition that the components of velocity normal to the interface are equal in each fluid is written as

$$\mathbf{u}_1 . \mathbf{n} = \mathbf{u}_2 . \mathbf{n}. \tag{2.6}$$

In the case of viscous flow this is supplemented by the condition

$$\mathbf{u}_1.\mathbf{t} = \mathbf{u}_2.\mathbf{t}, \tag{2.7}$$

although equation (2.7) is abandoned for inviscid flow.

The dynamic condition at the interface is obtained by applying a momentum balance to a volume element at the interface [8]. This balance gives

$$[\mathbf{T}.\mathbf{n}] = \sigma\kappa\mathbf{n}, \tag{2.8}$$

where the [ ] notation denotes the jump condition in the properties between the fluids at the interface $y = f(x,t)$. Here κ is the curvature of the interface and σ is the surface tension coefficient. In this work, surface tension is not considered to be an important effect and so is ignored. Taking the normal component of the dynamic condition it is found

$$[\mathbf{n}.\mathbf{T}.\mathbf{n}] = \sigma\kappa. \tag{2.9}$$

So in the case of inviscid flow with no surface tension we find the simple relation $p_1 = p_2$. See Appendix A for the components of the viscous stress tensor. Taking the tangential stress balance yields

$$[\mathbf{t}.\mathbf{T}.\mathbf{n}] = 0. \tag{2.10}$$

To summarise, the conditions that must be satisfied at the interface between two viscous fluids are: the continuity of velocity vector, the kinematic condition (2.5), and the continuity of normal and tangential stresses given by equations (2.9) and (2.10) respectively. In this work a Cartesian coordinate system is used and so now each of these equations will be transformed to Cartesian coordinates. Extensions to three dimensions follow similarly.

2.3 Interfacial boundary conditions in Cartesian coordinates

This section is devoted to transferring the interfacial conditions stated in the previous section to Cartesian coordinates which will be used in this thesis. Consider an interface in two dimensions as shown in figure 2. The velocity

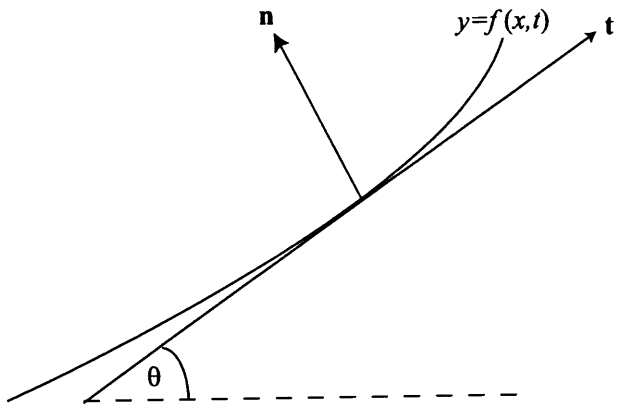

Figure 2.1: The position of the normal **n** and tangent vector **t** to the interface and the definition of the angle θ.

components in Cartesian coordinates are (u, v) and the velocity components tangential and perpendicular to the interface are given respectively by (u_t, u_n). From figure 2.1 we can write these components as

$$u_{\mathbf{n}} = -u\sin(\theta) + v\cos(\theta), \tag{2.11}$$

$$u_{\mathbf{t}} = u\cos(\theta) + v\sin(\theta). \tag{2.12}$$

The corresponding derivatives are given by

$$\partial_{\mathbf{n}} = -\sin(\theta)\partial_x + \cos(\theta)\partial_y, \tag{2.13}$$

$$\partial_{\mathbf{t}} = \cos(\theta)\partial_x + \sin(\theta)\partial_y, \tag{2.14}$$

and $\tan(\theta) = df/dx$. The curve $y = f(x)$ is parameterized as $(x, f(x))$, dropping the time dependence for the time being, and so the tangent and normal to the interface are then given respectively by

$$\mathbf{t} = \frac{(1, f'(x))}{(1 + f'(x)^2)^{1/2}}, \tag{2.15}$$

$$\mathbf{n} = \frac{(-f'(x), 1)}{(1 + f'(x)^2)^{1/2}}. \tag{2.16}$$

The interfacial conditions for normal and tangential stresses written out in component form are

$$\left(-p + 2\mu_1 \frac{\partial u_n}{\partial \mathbf{n}}\right)_1 = \left(-p + 2\mu_2 \frac{\partial u_n}{\partial \mathbf{n}}\right)_2 + \sigma\kappa, \tag{2.17}$$

$$\mu_1 \left(\frac{\partial u_n}{\partial \mathbf{t}} + \frac{\partial u_t}{\partial \mathbf{n}}\right)_1 = \mu_2 \left(\frac{\partial u_n}{\partial \mathbf{t}} + \frac{\partial u_t}{\partial \mathbf{n}}\right)_2. \tag{2.18}$$

Now substituting equations (2.15) and (2.16) into equations (2.17) and (2.18) we find the respective conditions in Cartesian coordinates are [1]

$$\begin{aligned} -p_1 + 2\mu_1 \frac{\left[\frac{\partial v}{\partial y}(1 - f_x^2) - f_x\left(\frac{\partial u}{\partial y} + \frac{\partial v}{\partial x}\right)\right]_1}{1 + f_x^2} \\ = -p_2 + 2\mu_2 \frac{\left[\frac{\partial v}{\partial y}(1 - f_x^2) - f_x\left(\frac{\partial u}{\partial y} + \frac{\partial v}{\partial x}\right)\right]_2}{1 + f_x^2} + \kappa\sigma, \end{aligned} \tag{2.19}$$

and for the tangential components

$$\mu_1 \left[\left(\frac{\partial u}{\partial y} + \frac{\partial v}{\partial x}\right)(1 - f_x^2) - 4f_x \frac{\partial u}{\partial x}\right]_1 = \mu_2 \left[\left(\frac{\partial u}{\partial y} + \frac{\partial v}{\partial x}\right)(1 - f_x^2) - 4f_x \frac{\partial u}{\partial x}\right]_2. \tag{2.20}$$

The kinematic boundary condition remains in the form

$$v_i = f_t + u_i f_x, \tag{2.21}$$

for each of the fluids. The curvature here can be expressed as

$$\kappa = \frac{f_{xx}}{(1 + f_x)^{3/2}}. \tag{2.22}$$

[1] These expressions are valid provided $\theta \neq \pi/2$; in this case $\partial u_n/\partial \mathbf{n} \to \partial u/\partial x$

In this work, however, surface tension effects are not considered hence the curvature does not need to be calculated. Indeed from now on curvature is omitted from all governing equations and boundary conditions.

2.3.1 Inviscid flows

Inviscid flows are governed by the Euler equations, i.e. the Navier-Stokes equations (2.2) without the stress tensor terms and equation (2.3). Hence the equations now reduce to

$$\frac{\partial \mathbf{u}_i}{\partial t} + (\mathbf{u}_i \cdot \nabla)\mathbf{u}_i, = -\frac{1}{\rho_i}\nabla p_i, \tag{2.23}$$

$$\nabla \cdot \mathbf{u}_i = 0, \tag{2.24}$$

in each fluid. At the interface we still have the kinematic relation given by equation (2.5) or (2.21). Because no tangential stresses are exerted in inviscid flow; equation (2.20) is abandoned and as the only normal forces exerted on a fluid element are pressures, the condition on the normal stress balance (2.19) reduces to

$$p_1 = p_2. \tag{2.25}$$

These are the only conditions applied for inviscid flow, equation (2.7) is no longer valid. Also the no-slip condition (2.4) is replaced with the free-slip condition, which insists that only the component of velocity normal to the wall must vanish.

2.3.2 The boundary conditions for free surface flow

The boundary conditions for viscous fluids at a free surface take a similar form to those of multiphase flow, in fact free surface flow can be thought of as a limiting case of the multiphase case. Again we have the kinematic relation

(2.5), and the stress balances (2.19) and (2.20) now become

$$-p_1 + 2\mu_1 \frac{\left[\frac{\partial v}{\partial y}(1 - f_x^2) - f_x\left(\frac{\partial u}{\partial y} + \frac{\partial v}{\partial x}\right)\right]_1}{1 + f_x^2} = -p_2 + \kappa\sigma, \tag{2.26}$$

$$\mu_1 \left[\left(\frac{\partial u}{\partial y} + \frac{\partial v}{\partial x}\right)(1 - f_x^2) - 4f_x\frac{\partial u}{\partial x}\right]_1 = 0. \tag{2.27}$$

In the case of the inviscid fluids with no surface tension, the normal stress reduces to $p_1 = p_a$ where p_a is taken to be atmospheric pressure, taken to be zero in this thesis.

2.4 Outline of the thesis

In chapter 3 both fluids are treated as inviscid and the motion in the core of the parent artery is analysed. Here a complex variable method is used to solve the equations of the flow. The flow is solved in a transformed plane, where the solution can be found using analytic methods. This solution can be mapped to the physical plane to give the solution of the problem. With this method the streamlines of the flow can be found when the glue and blood have different initial velocities. However this method is only applicable when the glue and blood have the same density.

When the two fluids have different densities the situation is more complicated. In the second part of the chapter we consider the linearised problem where a slight perturbation is made to the glue velocity. This results in solving Laplace's equation for the leading order correction for the streamfunction. The plots of the initial solution and the added disturbance can then be analysed to give an idea of how the density difference between the fluids affects the flow.

In chapter 4 viscous effects are incorporated into the model. Here the flow structure is different and there is assumed to be a thin layer next to the wall where viscous effects are deemed to be important. The interface of the two

fluids is assumed to be situated in this viscous layer. The flow in the core of the artery, on the other hand, is assumed to be inviscid and full of glue only. This analysis aims to simulate the process just before the glue has set. Two different cases are studied in this chapter: the flow over a roughness, and the flow to two symmetric daughters. For different viscosity and density ratios, separation is looked for, as is the pressure and, perhaps more crucially in regard to embolization, the interface position between the glue and the blood.

The flow over roughness is studied as this case gives equations and boundary conditions very similar to the case of flow to two daughters. This case is used to verify the computational solution described in this chapter, as this problem has been studied for a single fluid [40]. The problem also has direct relevance to a mother vessel where roughness effects of the vessel wall are significant.

Chapter 5 provides a continuation of the wall layer analysis, however here we study the problem using analytic methods, again assuming that the Reynolds number for the flow is large. First a linearised analysis based on a small roughness height is studied and the solution considered where the viscosity of the glue is much greater than that of the blood. Indeed this assumption is at the heart of most of the analysis in this section. Asymptotic expansions for the flow variables are formulated in this limit in an aim to solve the non-linear equations. Other problems studied in this section are the flow over a roughness where the density of the glue is much larger than that of the blood, and a lubrication approximation seems valid. Analysis of the flow to two daughter vessels far downstream is also considered.

Chapter 6 is an extension to the wall layer analysis of the previous section. Here the problem is made unsteady and an attempt is made to model chemical effects occurring at the interface between the fluids. Although only a rather simplistic model, the equations arising are still relatively complicated and exact solutions cannot be found. However a similarity solution at large

negative times and small negative times can be found and the velocity profiles calculated.

In order to consider effects where the interface is in the core of the artery, a numerical treatment of the governing equations is perhaps the most worthwhile course of action. There is a multitude of numerical methods for free surface and multiphase flows and a brief overview of some of these is given in chapter 7. The method of choice here is the Volume of Fluid method, which allows the interface to be tracked over time. The method is made up of two main parts: solving the equations of motion, and moving the interface according to the computed velocity field. These are described in chapters 7 and 8. The method described in chapter 7 assumes that the velocity field is known, and interface reconstruction and advection algorithms are discussed in this chapter. The method used here to advect the interface is the PLIC method [50], while the governing equations are solved using a finite-difference approach and the well known projection method for incompressible flows. A detailed discussion of the derivation of the difference formulae and method for solving the incompressible Navier-Stokes equations is given in chapter 8. A thorough account of the method of solution for free surface flows is given. This is effectively a simplified form of multiphase flow and proved a useful starting point to begin the multiphase numerical method.

To verify the numerical method, several test cases which have been well reported in the literature were studied. These included the lid-driven cavity flow problem, dam-break, Rayleigh-Taylor instability and the Fractured-Diaphragm problems. Next the code is applied to problems related to the modelling of the embolization process. The cases of glue being injected as a droplet and a continuous column are investigated in chapter 10. Analysis to two or more daughters is also studied, where the glue and blood are treated as inviscid fluids. Next viscous effects are incorporated into the numerical model and the

motion of a viscous glue droplet in the feeding artery is studied.

Finally the results of all the different chapters are outlined in chapter 11 and some indications of possible further work are given.

Chapter 3

Analysis of motion in the core

3.1 The case where the density of glue and blood are identical

Assuming that the Reynolds number is large in both fluids, the core flow can be treated as inviscid to a good approximation. We consider the case where the glue is injected in the middle of the mother artery and analyse the steady motion of the glue and blood in this vessel. We assume that the glue is injected from the catheter at a constant velocity u_1 and the oncoming blood flow has constant velocity u_2 in the streamwise direction. To start with it is assumed that the densities of the two fluids are equal and hence $\rho = 1$. As the flow is inviscid and irrotational, the problem becomes that of solving Laplace's equation

$$\nabla^2 \phi = 0, \tag{3.1}$$

for the velocity potential ϕ in both fluids. Here $u_i = \partial\phi/\partial x$ and $v_i = \partial\phi/\partial y$ where $i = 1, 2$ for the respective fluid and again x and y are the coordinates parallel and perpendicular to the direction of the initial flow respectively. If we define the complex potential of the flow to be $F = \phi + i\psi$, where F is an

analytic function of $z = x + iy$, then the Cauchy-Riemann equations apply and hence the stream function ψ also satisfies Laplace's equation. We aim to solve Laplace's equation to find ψ and then find the streamlines given by $\psi =$ constant, to model how the blood and glue interact when they have different initial velocities.

The geometry of the problem is shown in the upper half of figure 3.1. This is the case where the catheter is positioned symmetrically in the middle of the mother artery. The problem of solving Laplace's equation is transformed from the physical plane, i.e. the z-plane, to the upper half of the ζ-plane, where $\zeta = u + iv$. If the mapping from the z-plane to the ζ-plane is conformal then a function that satisfies Laplace's equation in the ζ-plane will also satisfy the equation in the z-plane since

$$\frac{\partial^2\psi}{\partial x^2} + \frac{\partial^2\psi}{\partial y^2} = |\hat{F}'(z)|^2 \left(\frac{\partial^2\psi}{\partial u^2} + \frac{\partial^2\psi}{\partial v^2} \right), \tag{3.2}$$

where $\hat{F}$ is the associated mapping. So first the main aim is to find the map from the transformed space to the physical space, i.e. the ζ-plane to the z-plane. Then the solution to Laplace's equation which will be found in the transformed plane can be mapped to the physical plane, to give the solution of the relevant problem.

We seek a solution where the velocity is smooth at the edge of the catheter. However as the velocity of the injected fluid (the glue) is different to the velocity of the blood, a vortex sheet would be created in practise. The presence of vortex sheets then breaks the irrotational flow assumption. Due to the limitations of this model, viscous effects are introduced into the model in the next chapter. In this case, if the velocity of the glue being injected is larger than that of the blood, boundary layer separation would be expected.

3.1.1 Determination of the conformal map

The setup for the problem is shown in figure 3.1, which shows the z-plane, (the physical plane) and the ζ-plane. In this setting the catheter takes up the position between the points D and E and the channel width is normalised to π for convenience. The first task is to find the mapping which takes the upper half of the ζ-plane to the interior of the shape shown in the z-plane.

We exploit the fact that a Schwartz-Christoffel transformation may be used to map the upper half-plane to the interior of any closed regular polygon. In general we choose n points, $\omega_1, \omega_2, \cdots, \omega_n$, on the real axis in the ζ-plane. These points are mapped to the vertices of an n-sided polygon in the z-plane, i.e. the physical plane, by the map $z = \hat{f}(\zeta)$ where $\hat{f}$ is the mapping function and should not be confused with the interface position. The internal angles of the polygon are given by $\alpha_1, \alpha_2, \cdots, \alpha_n$ which leads to the expression for the map from the real line to the polygon in the ζ plane, and is given by the indefinite integral

$$z = K \int \prod (\zeta - \omega_k)^{(\alpha_k - \pi)/\pi} d\zeta, \tag{3.3}$$

where K is a constant to be determined. We can see from figure 3.1 that the interior angles of the shape are $0, 0, 3\pi/2, 3\pi/2$ at the points BC, FG, D and E in the z-plane corresponding to the points -1, 1, $-a$ and a in turn on the real line in the ζ-plane. Hence the map is given by

$$\frac{dz}{d\zeta} = K(\zeta + 1)^{-1}(\zeta - 1)^{-1}(\zeta - a)^{1/2}(\zeta + a)^{1/2}, \tag{3.4}$$

$$= K\frac{(\zeta^2 - a^2)^{1/2}}{(\zeta^2 - 1)}. \tag{3.5}$$

Integrating gives an expression for the map as

$$z = K\left[\cosh^{-1}(\zeta/a) - \frac{\sqrt{1-a^2}}{2}\cosh^{-1}\left(\frac{\zeta^2(2-a^2) - a^2}{a^2(\zeta^2 - 1)}\right)\right], \tag{3.6}$$

where the constant of integration vanishes as the point (0,0) in the ζ-plane is mapped to the point $(0, i\pi/2)$ in the z-plane and the constant K is found to

be 1. So the height of the channel is fixed to be π and the point O in the ζ plane is mapped to the point O in the z-plane and similarly for the points D and E. Figure 3.1 shows that the points in the ζ-plane are mapped to the points with the same letter in the z-plane. It should be noted however that the origin is taken to be the point O′ in the z-plane, in order that the constant of integration above still vanishes. The origin lies directly beneath the points D, O and E and on the line $y = 0$, of course.

Now as the function $\cosh^{-1}$ is double-valued the expression (3.6) does not give a precise definition of the map. So now different sections of the z-plane are examined individually and by inspection we find that the map to the different regions of the z-plane is given by

$$z = \begin{cases} \cosh^{-1}(\zeta/a) - \kappa \cosh^{-1}(\chi) & \text{on AB, CD, DO, GH,} \\ \cosh^{-1}(\zeta/a) + \kappa \cosh^{-1}(\chi) & \text{on OE,} \\ \cosh^{-1}(\zeta/a) - \kappa[\mathrm{Re}(\cosh^{-1}(\chi) - \mathrm{Im}(\cosh^{-1}(\chi))] & \text{on EF.} \end{cases} \tag{3.7}$$

Here $\kappa = \sqrt{1-a^2}/2, \chi = (\zeta^2(2-a^2) - a^2)/(a^2(\zeta^2 - 1))$ and $\cosh^{-1}$ represents the positive value or branch of the function. Applying these expressions for the mapping in each region allows calculation of the co-ordinates of the points D and E, which are found to be

$$D = (0, i\pi(1 - \sqrt{1-a^2}/2)), \tag{3.8}$$

$$E = (0, i\pi\sqrt{1-a^2}/2). \tag{3.9}$$

Also we find that as $u = \mathrm{Re}(\zeta) \to \infty$, then $z \to \infty$ and as $u \to -\infty$ then $z \to \infty + i\pi$. Hence equation (3.7) now gives the complete map of the upper half of the ζ-plane ($u > 0$) to the interior of the figure in the z-plane and it is clear that the map preserves symmetry in the line $y = \pi/2$. We also note that the catheter width w is given by

$$w = \pi(1 - \sqrt{1-a^2}), \tag{3.10}$$

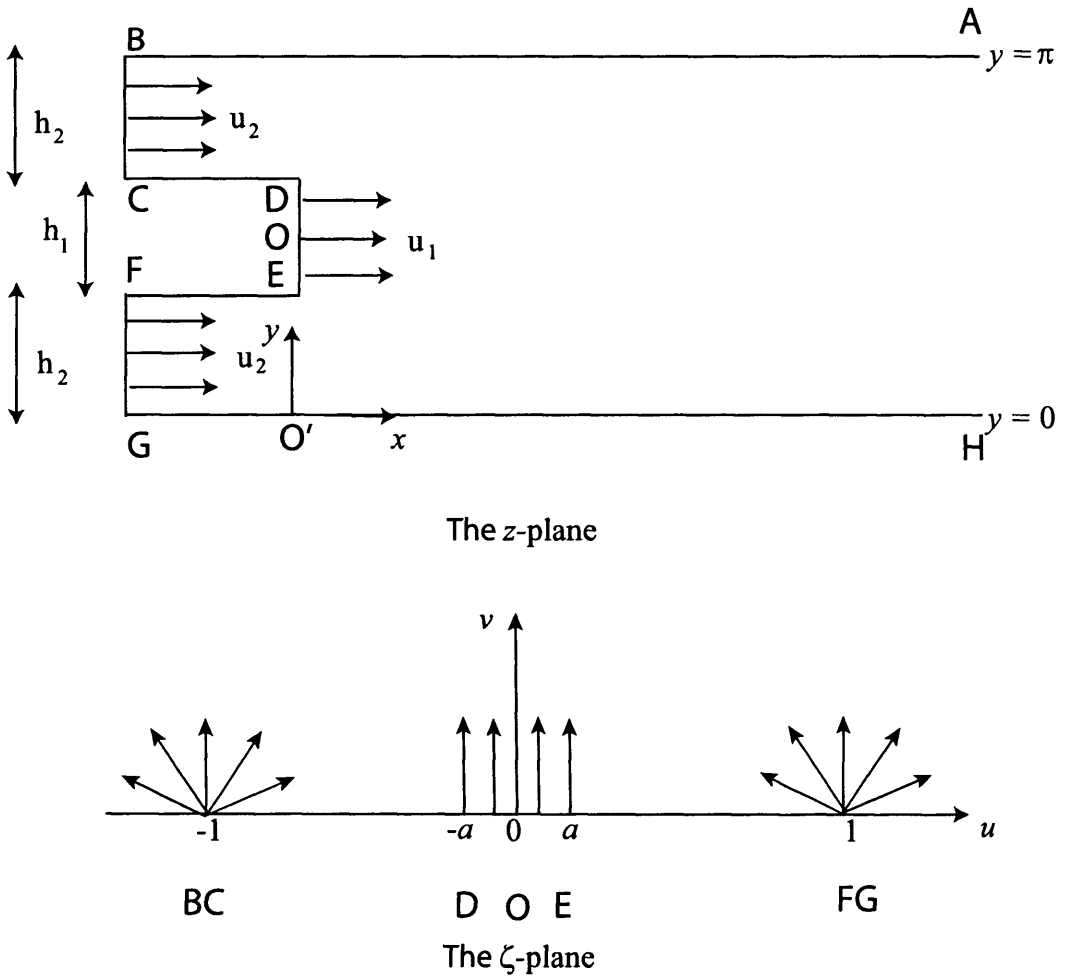

Figure 3.1: The conformal map takes the point $\zeta = u + iv$ to the point $z = x + iy$. Here the points B, C, D, O, E, F and G are mapped to the respective points in the z-plane. The origin in the z-plane is denoted O′. Laplace's equation is solved in the ζ-plane and then mapped onto the physical plane using the pre-determined map $z = \hat{f}(\zeta)$.

and hence the two limiting cases are $w \to 0$ as $a \to 0$ and $w \to \pi$ as $a \to 1$. The first of these cases corresponds to a source in a uniform stream [57], whereas in the second case we have two small sources for the blood at the top and the bottom of the artery as the catheter width approaches that of the mother tube. This is similar to the situation studied in chapter 4, where viscous effects are also thought to be important.

3.1.2 An expression for the stream function in the z-plane

In the setup for figure 3.1 the initial velocity of the glue is taken to be u_1 and the oncoming blood flow between the points B and C and F and G has velocity u_2, preserving symmetry.

Interpretating the stream function as mass flux leads to the following expressions for ψ on the different boundaries:-

$$\psi = \begin{cases} 0 & \text{on GH,} \\ u_2 h_2 & \text{on FE,} \\ u_1 y + c_1 & \text{on DE,} \\ u_2 h_2 + u_1 h_1 & \text{on CD,} \\ 2u_2 h_2 + u_1 h_1 & \text{on AB.} \end{cases} \tag{3.11}$$

Here c_1 is a known constant given by $c_1 = h_2(u_2 - u_1)$ to match ψ at the points D and E. We note that the constant vanishes for the trivial case $u_1 = u_2$. Having determined ψ in the z-plane we obtain an expression for ψ along the corresponding positions on the real line of the ζ-plane. The two components of blood flow in the z-plane between the points BC and FG correspond to a uniform source at the points BC and FG in the ζ-plane. Hence we are able to find a solution to Laplace's equation in the whole of the upper half of the

ζ-plane.

3.1.3 Solution of Laplace's equation in the upper half-plane

The problem reduces to that of solving Laplace's equation in the upper half-plane with known values for the stream function ψ on the axis $v = 0$. Thus the task is to solve

$$\psi_{uu} + \psi_{vv} = 0 \qquad \text{on } -\infty < u < \infty,\ v > 0, \tag{3.12}$$

subject to the condition $\psi(u, 0) = c(u)$, with $c(u)$ being known from equation (3.11). Taking the Fourier transform of (3.12) with respect to the variable u gives

$$-\omega^2\psi^* + \psi^*_{vv} = 0, \tag{3.13}$$

where the Fourier transform is defined by

$$\psi(\omega, v)^* = \int_{-\infty}^{\infty} \psi(u, v)e^{-i\omega u}du. \tag{3.14}$$

Hence using the boundary conditions and assuming the solution is bounded in the far field, we obtain the solution

$$\psi^* = c^*(\omega)e^{-\omega|v|} = c^*(\omega)g^*(\omega). \tag{3.15}$$

With the equation in this form, with all functions suitably transformed, we can use the convolution theorem which states

$$\psi(u, v) = \frac{1}{2\pi}\int_{-\infty}^{\infty} c(\zeta)g(u - \zeta, v)d\zeta. \tag{3.16}$$

So we need to determine $g(u, v)$, which is found by taking the inverse Fourier-transform of $e^{-\omega|v|}$. This is determined by evaluating the integral

$$g(u, v) = \int_{-\infty}^{\infty} e^{-\omega|v|}e^{i\omega u}d\omega, \tag{3.17}$$

$$= 2\int_0^{\infty} e^{-\omega v}\cos(\omega u)\, d\omega = \frac{2v}{u^2 + v^2}. \tag{3.18}$$

Consequently substituting this back into the expression for ψ, (3.16) gives an expression for ψ everywhere in the upper half-plane as

$$\psi(u,v) = \frac{1}{\pi}\int_{-\infty}^{\infty} \frac{c(\zeta)v}{(u-\zeta)^2+v^2}d\zeta, \tag{3.19}$$

which is the well known Poisson integral formula for the half-plane. Now using the expressions for the boundary conditions of the streamfunction we can find an expression for ψ in the different regions and hence an expression for ψ everywhere. There are four contributions to ψ as the value for the stream function vanishes on GH. Hence an expression for the stream function is

$$\begin{aligned}\psi = &\frac{1}{\pi}\int_{-\infty}^{-1} \frac{(2u_2h_2+u_1h_1)v}{(u-s)^2+v^2}ds + \frac{1}{\pi}\int_{-1}^{-a} \frac{(u_2h_2+u_1h_1)v}{(u-s)^2+v^2}ds \\ &+ \frac{1}{\pi}\int_{-a}^{a} \frac{(u_1y+c_1)v}{(u-s)^2+v^2}ds + \frac{1}{\pi}\int_{a}^{1} \frac{(u_2h_2)v}{(u-s)^2+v^2}ds. \end{aligned}\tag{3.20}$$

Here, three of the integrals can be evaluated straight away but the integral on the region $[-a,a]$ needs more attention as ψ is not constant on this region. We make use of the substitution

$$\zeta = at, \ |t| < 1, \tag{3.21}$$

and noting that $\mathrm{Im}(\cosh^{-1}(x)) = \cos^{-1}x$, for $|x| < 1$, equation (3.7) gives an expression for the imaginary part of the map as

$$y = \begin{cases} \cos^{-1}(\zeta/a) - \sqrt{1-a^2}\cos^{-1}(\chi)/2, & \text{for } -a \le \zeta < 0, \\ \cos^{-1}(\zeta/a) + \sqrt{1-a^2}\cos^{-1}(\chi)/2, & \text{for } \ 0 \le \zeta < a, \end{cases} \tag{3.22}$$

with χ as defined earlier and y now denoting a real value everywhere in the range $-1 \le t \le 1$. Therefore an expression for ψ is

$$\begin{aligned}\psi = &\frac{(2u_2h_2+u_1h_1)}{\pi}\tan^{-1}\left(\frac{v}{u+1}\right) \\ &+ \frac{(u_1h_1+u_2h_2)}{\pi}\left[\tan^{-1}\left(\frac{v}{u+1}\right) - \tan^{-1}\left(\frac{v}{u+a}\right)\right] \\ &+ \frac{u_2h_2}{\pi}\left[\tan^{-1}\left(\frac{v}{u-1}\right) - \tan^{-1}\left(\frac{v}{u-a}\right)\right] + \frac{1}{\pi}\int_{-a}^{a}\frac{f(s)v}{(u-s)^2+v^2}ds, \end{aligned}\tag{3.23}$$

[1] where

$$f(s) = \begin{cases} u_1(\cos^{-1}(s/a) - \sqrt{1-a^2}\cos^{-1}(\chi)/2) + c_1, & \text{for } -a \le s < 0, \\ u_1(\cos^{-1}(s/a) + \sqrt{1-a^2}\cos^{-1}(\chi)/2) + c_1, & \text{for } 0 \le s < a, \end{cases} \tag{3.24}$$

with χ evaluated at $\zeta = s$. We also notice that the final integral in (3.23)

$$I = \frac{1}{\pi}\int_{-a}^{a} \frac{f(s)v}{(u-s)^2+v^2} ds, \tag{3.25}$$

applies for all u and $v > 0$ and the substitution $s = u + v\tan q$ shows that $I \sim f(s) = u_1 y + c_1$ as $v \to 0+$ as required to satisfy the boundary conditions.

The integral I is calculated numerically using Simpson's rule and an expression for ψ is found in the ζ-plane. These values are transferred to the physical plane using the map and the streamlines are plotted by setting $\psi =$ constant: see results below. To start with, the constant a is set to be 0.5, so the catheter width is $w = \pi(1 - \sqrt{3}/2)$.

As a check, when the catheter width $w \to 0$ we recover exactly the same pattern for the streamlines as for a source in a uniform stream, as shown in figure 3.7 and given by Milne-Thomson [57] p. 211.

3.1.4 Results

Results are shown for a range of different initial velocities. The blood velocity is kept constant, $u_2 = 1$ in all the computations, while the glue velocity u_1 is varied. In all figures the glue streamlines are shown in blue and those of the blood are red. Figures 3.2–3.6 show the streamlines produced due to the different velocities of the glue where the catheter width is given by $\pi(1-\sqrt{3}/2)$. When the initial velocity of the blood is much greater than that of the glue, the dividing streamlines are less than the catheter width apart. The plots in figures 3.3 and 3.4 show the streamlines for large u_1 values. Here the glue

[1] The relation $\tan^{-1}(x) + \tan^{-1}(1/x) = \pi/2$ has been used here.

dominates and spreads quickly, in a spatial sense, taking up most of the feeding artery by the position $x = 0.5$.

Figures 3.8 to 3.11 show the case where the catheter width is increased so that it takes up most of the channel. In this case we take $a = 0.96$, resulting in a catheter width of $w = 2.26$. Similar results are obtained in this case compared to those described earlier. Again the glue spreads rapidly when the initial velocity is 10 or 100, as shown in figures 3.8 to 3.9. When the blood velocity is large the blood dominates and the dividing streamline far downstream for the case $u_1 = 0.01$ is approximately at $y = 1$ and $y = 2$, as shown by figure 3.11.

It should be noted that the streamlines do not in general extend all the way across the domain, especially near the walls. This is due to the fact that it is difficult to find the value of the streamfunction at these points, as extreme values of u and v must be taken in the ζ-plane.

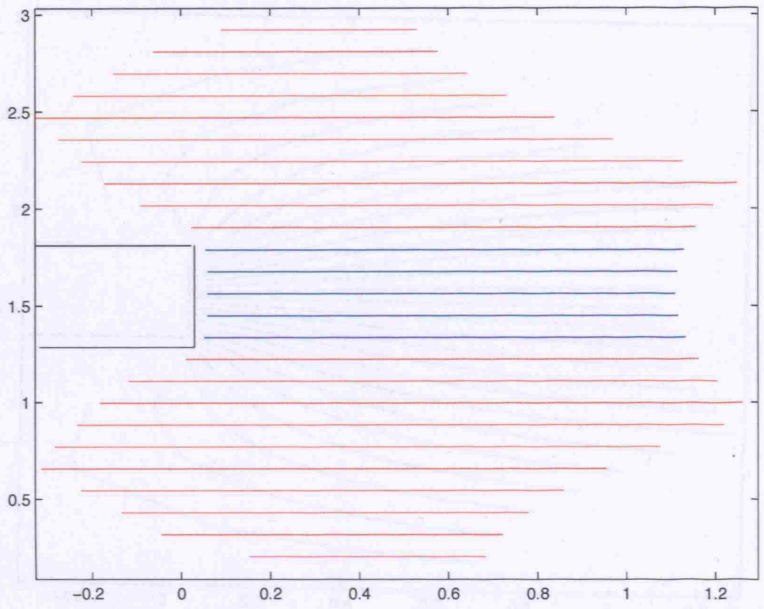

Figure 3.2: Streamlines for the case where $u_1 = u_2 = 1$. As expected there is no deviation from the initial flow solution.

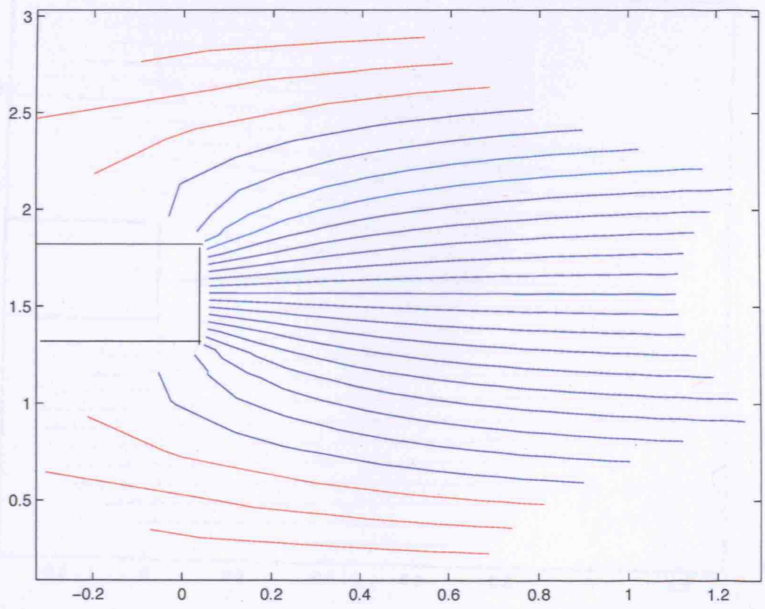

Figure 3.3: Streamlines for the case $u_1 = 10$.

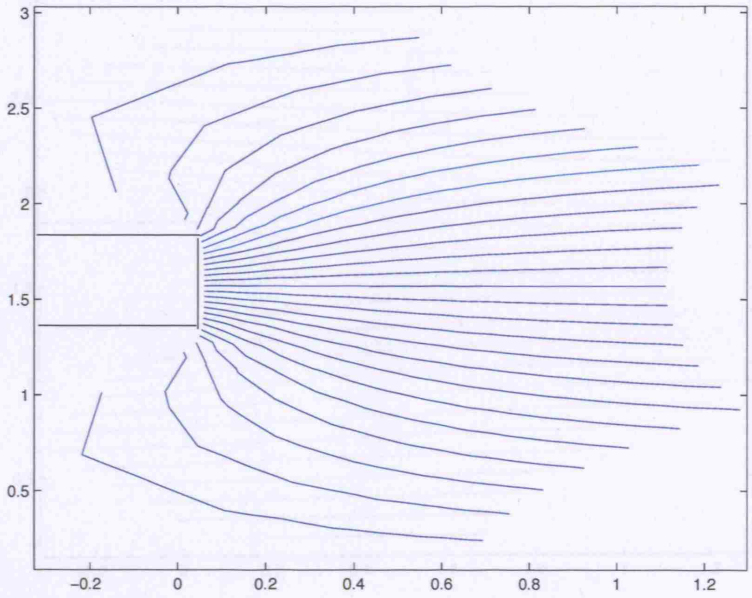

Figure 3.4: Streamlines for the case $u_1 = 100$.

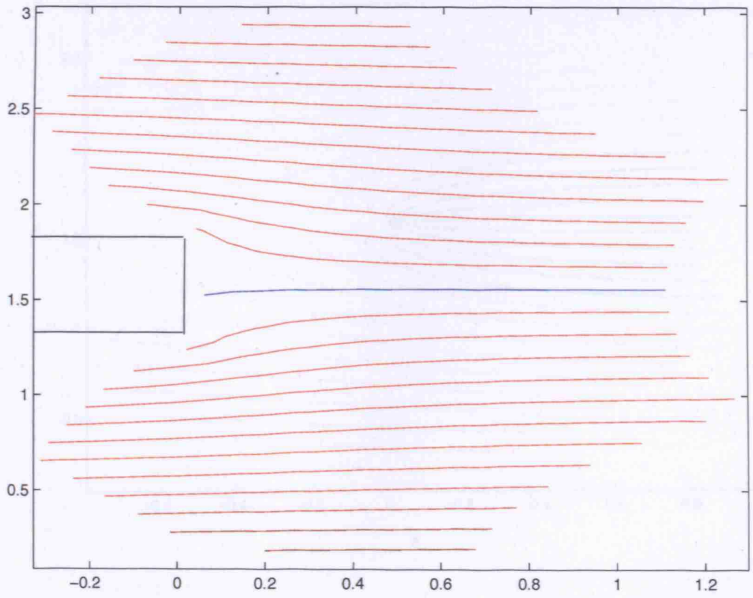

Figure 3.5: Streamlines for the case $u_1 = 0.1$.

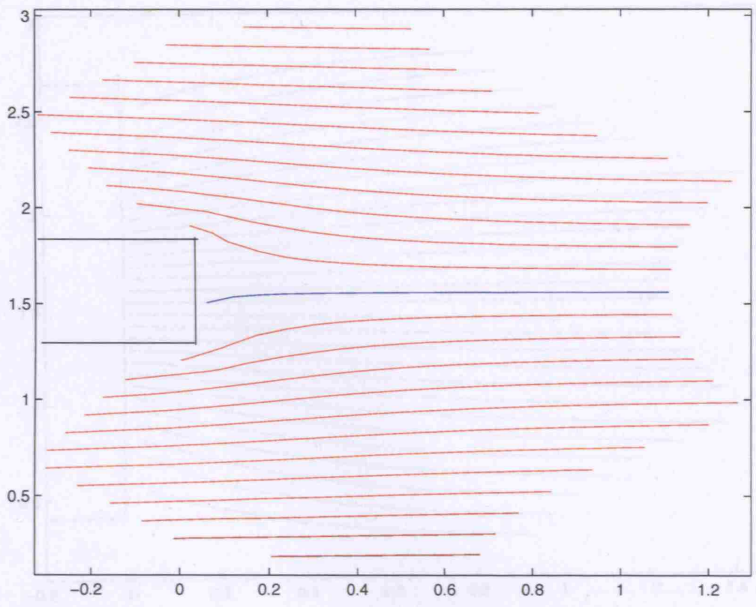

Figure 3.6: Streamlines for the case $u_1 = 0.01$.

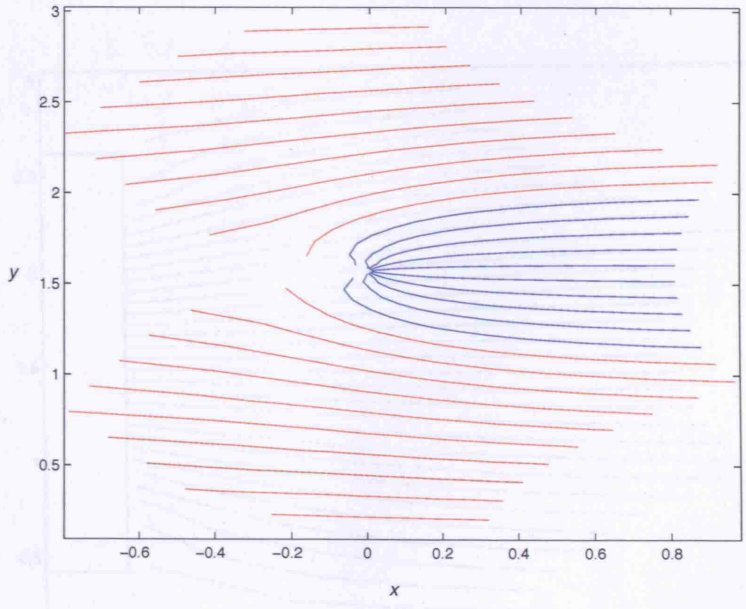

Figure 3.7: Streamlines for a source in a uniform stream. Good agreement is found with the analytic solution as given by [57] p. 211.

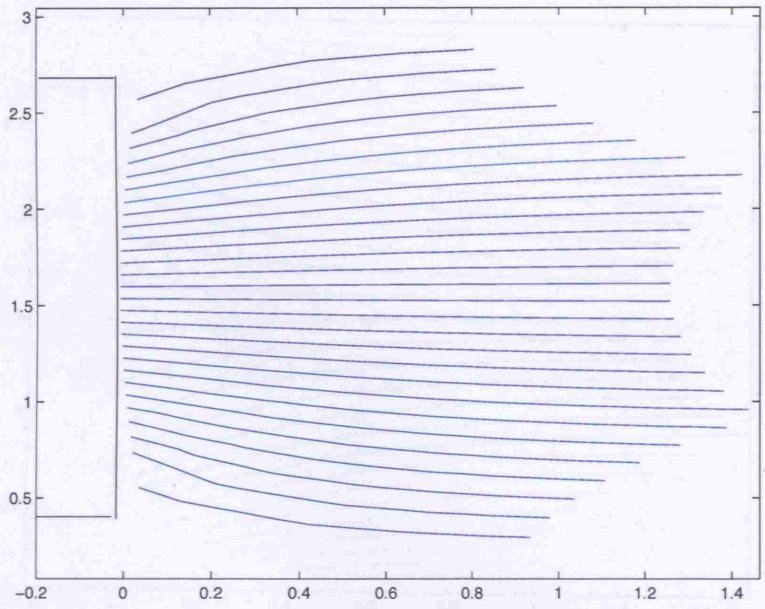

Figure 3.8: The case where the catheter width is increased to w= 2.26. The case $u_1 = 10$.

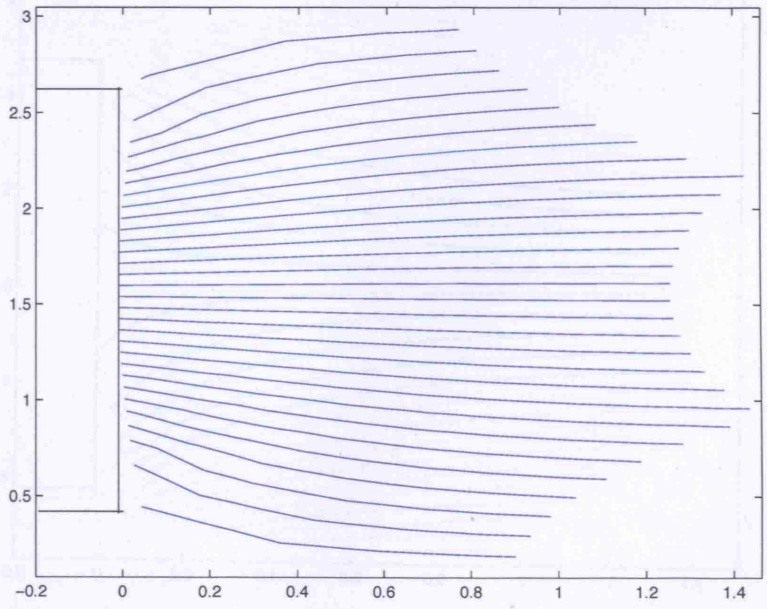

Figure 3.9: $u_1 = 100$.

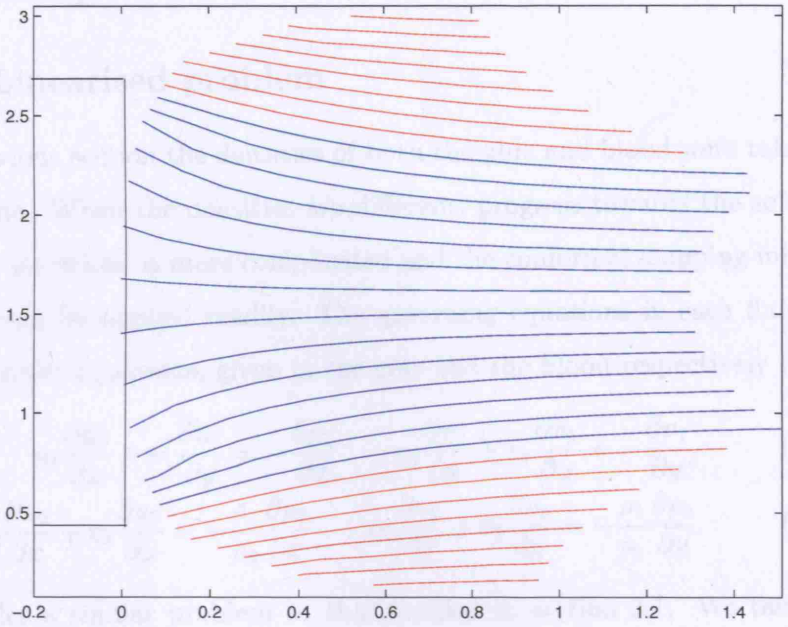

Figure 3.10: $u_1 = 0.1$.

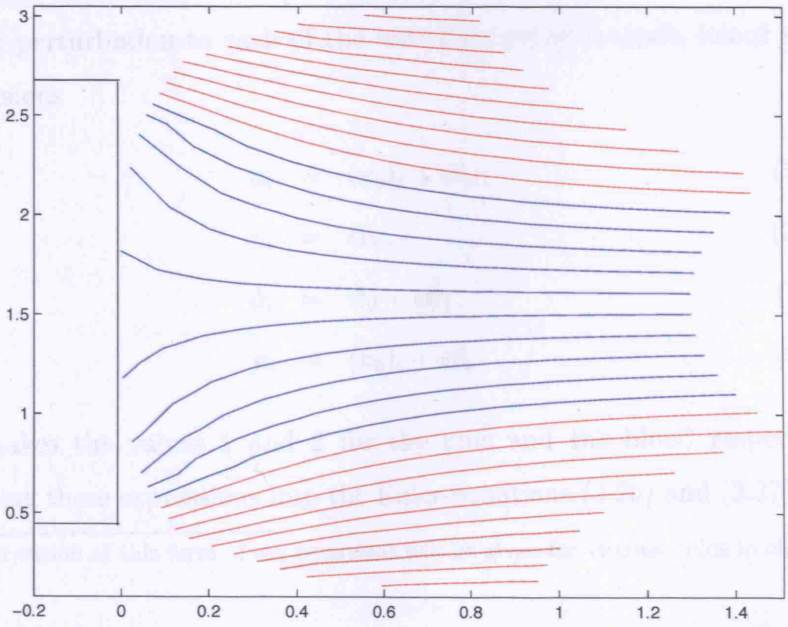

Figure 3.11: $u_1 = 0.01$.

3.2 Unequal densities

3.2.1 Linearised problem

In the previous section the densities of both the glue and blood were taken to be the same. When the densities are different, progress towards the solution of the flow equations is more complicated and the conformal mapping method can no longer be applied readily. The governing equations in each fluid are again the Euler equations, given in the glue and the blood respectively by [2]

$$u_1\frac{\partial u_1}{\partial x}+v_1\frac{\partial u_1}{\partial y}=-\frac{\partial p_1}{\partial x} \qquad u_1\frac{\partial v_1}{\partial x}+v_1\frac{\partial v_1}{\partial y}=-\frac{\partial p_1}{\partial y}, \tag{3.26}$$

$$u_2\frac{\partial u_2}{\partial x}+v_2\frac{\partial u_2}{\partial y}=-\frac{\rho_1}{\rho_2}\frac{\partial p_2}{\partial x} \qquad u_2\frac{\partial v_2}{\partial x}+v_2\frac{\partial v_2}{\partial y}=-\frac{\rho_1}{\rho_2}\frac{\partial p_2}{\partial y}. \tag{3.27}$$

We consider a similar problem to that studied in section 3.1. We take the initial velocities of the glue and the blood to be $(u_0)_1$ and $(u_0)_2$ respectively. We start with a simple case where these velocities are constant and equal, although generalisations to taking these velocity profiles to be unit shear are also possible, but not discussed here.

A slight perturbation to each of the initial velocities is made, hence we set the expansions

$$u_i = (u_0)_i + \epsilon\tilde{u}_i\,, \tag{3.28a}$$

$$v_i = \epsilon\tilde{v}_i\,, \tag{3.28b}$$

$$\psi_i = \psi_0 + \epsilon\tilde{\psi}_i\,, \tag{3.28c}$$

$$p_i = (p_0)_i + \epsilon\tilde{p}_i. \tag{3.28d}$$

Again i takes the values 1 and 2 for the glue and the blood respectively. Substituting these expressions into the Euler-equations (3.26) and (3.27) leads

[2]The derivation of this form of the equations will be given for viscous fluids in chapter 4

to the linearised leading order equations

$$(u_0)_1\frac{\partial \tilde{u}_1}{\partial x} = -\frac{\partial \tilde{p}_1}{\partial x}, \qquad (u_0)_1\frac{\partial \tilde{v}_1}{\partial x} = -\frac{\partial \tilde{p}_1}{\partial y}, \tag{3.29}$$

$$(u_0)_2\frac{\partial \tilde{u}_2}{\partial x} = -\frac{\rho_1}{\rho_2}\frac{\partial \tilde{p}_2}{\partial x}, \qquad (u_0)_2\frac{\partial \tilde{v}_2}{\partial x} = -\frac{\rho_1}{\rho_2}\frac{\partial \tilde{p}_2}{\partial y}. \tag{3.30}$$

Eliminating the pressure leads to Laplace's equation for the stream-function perturbation in each fluid, which is independent of the factor ρ and given in each fluid by

$$\nabla^2\tilde{\psi}_i = 0. \tag{3.31}$$

At the interface, given now by $f_0 + \epsilon\tilde{f}$, the only conditions that need to be satisfied are the steady kinematic condition and the continuity of pressure. As the flow is inviscid the continuity of velocity is redundant here as, of course, is the tangential stress condition. Integration of the x-momentum equation in each fluid gives

$$\tilde{p}_1 = -\tilde{u}_1(u_0)_1, \tag{3.32}$$

$$\tilde{p}_2 = -\frac{\rho_2}{\rho_1}\tilde{u}_2(u_0)_2. \tag{3.33}$$

Hence the pressure condition at the interface $p_1 = p_2$ at this order leaves

$$\rho_1(u_0)_1\frac{\partial\tilde{\psi}_1}{\partial y} = \rho_2(u_0)_2\frac{\partial\tilde{\psi}_2}{\partial y}\,. \tag{3.34}$$

The steady kinematic condition leads to the relations

$$\tilde{v}_1 = (u_0)_1\tilde{f}_x, \qquad \tilde{v}_2 = (u_0)_2\tilde{f}_x. \tag{3.35}$$

Hence on integration with respect to x we find the boundary condition for ψ at the linearised interface position as

$$(u_0)_1\tilde{\psi}_1 = (u_0)_2\tilde{\psi}_2\,. \tag{3.36}$$

So although the density ratio ρ does not appear explicitly in the reduced governing equation of motion (3.31) it does appear in the interface condition (3.34). This condition must be satisfied at the linearised interface position $y = f_0$ as shown in figure 3.12.

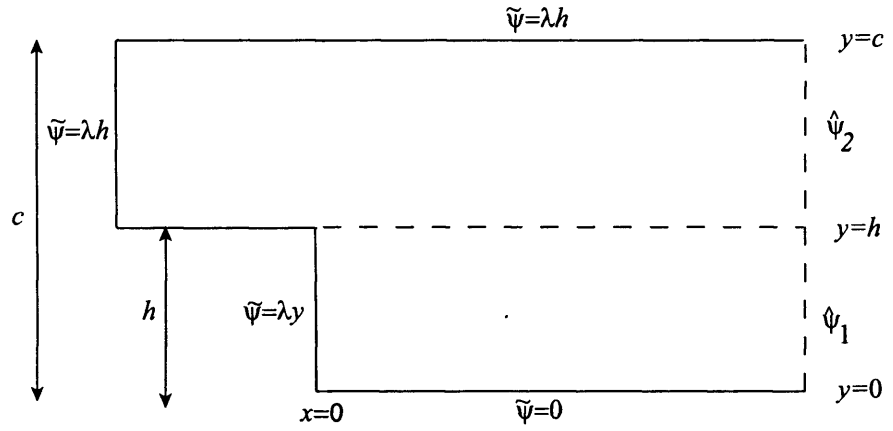

Figure 3.12: The geometry of the linearised problem and the relevant boundary conditions for the perturbation to the stream-function $\tilde{\psi}$. Here γ is the velocity perturbation in the glue.

3.2.2 A simple first example

We first take $(u_0)_1 = (u_0)_2 = 1$. As the flow is symmetric in the line $y = 0$ we only need to consider half the shape considered in section 3.1. Hence it remains to solve Laplace's equation in the geometry shown in figure 3.12, with conditions (3.35) and (3.36) at the linearised interface position $y = h = f_0$ and with other boundary conditions as shown in the figure.

To complete the boundary conditions we need to find the values of $\tilde{\psi}$ far downstream denoted $\hat{\psi}_1$ and $\hat{\psi}_2$ in the glue and blood respectively. Far downstream we assume that the solution is independent of x, hence we set $\hat{\psi}_1 \to \hat{\psi}_1(y)$ in the glue and $\hat{\psi}_2 \to \hat{\psi}_2(y)$ in the blood, and hence Laplace's equation reduces to $\hat{\psi}_{1yy} = 0$ and $\hat{\psi}_{2yy} = 0$. Hence on integration we find $\hat{\psi}_1 = a_1 y$ and $\hat{\psi}_2 = a_2 y + b_2$, for constants a_1, a_2 and b_2. These constants are found by matching the streamfunction at the top and bottom of the domain as well as the interface $y = h$. Matching at the top and bottom of the domain, $y = 0$

and $y = \pi/2$. We find

$$a_1 = \frac{\lambda h}{h + \rho(c-h)}, \tag{3.37}$$

$$a_2 = \frac{\rho\lambda h}{h + \rho(c-h)}, \tag{3.38}$$

$$b_2 = \lambda h \left[\frac{-c\rho}{h + \rho(c-h)} + 1 \right]. \tag{3.39}$$

Hence the downstream conditions are

$$\hat{\psi}_1 = \frac{\lambda h}{h + \rho(c-h)} y, \tag{3.40}$$

$$\hat{\psi}_2 = \frac{\rho\lambda h}{h + \rho(c-h)} y + \lambda h \left[\frac{-c\rho}{h + \rho(c-h)} + 1 \right], \tag{3.41}$$

where again c is the channel half-width and h is the catheter half-width. Now all the boundary and interface conditions are in place, an overview of the method of the solution is given.

3.2.3 Solution of Laplace's equation

Initially the solution to Laplace's equation was considered by using series expansions. Three different series expansions were posed in three different regions: in the glue and in the blood just for $x > 0$, and then in the blood in the region $x < 0$. The only unknowns in the series were the constants multiplying the individual terms in the series. The glue coefficients were found using the boundary condition at the catheter and by using orthogonality. The coefficients in the blood in the region $x > 0$ were then found equating the two series at $y = h$ in view of equation (3.36). This however left the only unknown being the coefficients in the series of the blood solution in the region $x < 0$. However both continuity of $\tilde{\psi}$ and $\tilde{\psi}_x$ were needed at the point $x = 0$ so there are too many equations for the number of unknowns. Hence the series solution was abandoned and a numerical solution was attempted instead.

A successive over-relaxation technique was used to solve the problem. Details of this method are given later in chapter 8. The usual five point stencil for the Laplacian is used here. However, the linearised pressure condition must also be satisfied, so for points lying on the interface the Laplacian stencil is abandoned and instead we impose the discrete form of (3.34). So again taking a second order accurate representation of the derivative in the y-direction leads to the discrete formula for ψ at the linearised interface position $y = h$ as

$$\tilde{\psi}_{i,j} = \frac{1}{3+3\rho}(4\tilde{\psi}_{i,j+1} + 4\rho\tilde{\psi}_{i,j-1} - \rho\tilde{\psi}_{i,j-2} - \tilde{\psi}_{i,j+2}), \tag{3.42}$$

as $\tilde{\psi}$ is continuous across $y = h$, from equation (3.36). Here the discrete level of the interface is at the point j. So the iteration is continued until the discrete version of Laplace's equation is satisfied at every interior point other than those lying on $y = h$, and when equation (3.42) is satisfied on the interior points lying on the line $y = h$.

3.2.4 Results

Results for the cases $\rho = 1, 10, 0.1, 0.5$ are shown in figures 3.14 and 3.15. In each of the figures three plots are shown: the solution $\tilde{\psi}$, and the 'total' streamfunction $\psi_0 \pm \epsilon\tilde{\psi}$. The streamfunction for the incident flow is given by $\psi_0 = y$ and is shown in figure 3.13. Here we take $\epsilon = 1$, as smaller values of ϵ resulted in streamlines which varied very little from the incidence streamfunction ψ_0.

The case where $\rho = 1$ shows that the streamlines are slightly displaced from the incidence profile. When the density of the glue is larger than that of the blood, the streamlines are displaced quicker and the flow of the glue is fast. In the case where the density ratio is small, there is little displacement of the streamlines in the glue, as indicated by figure 3.15. The analysis is continued for the two limits $\rho \gg 1$ and $\rho \ll 1$, where some progress can be

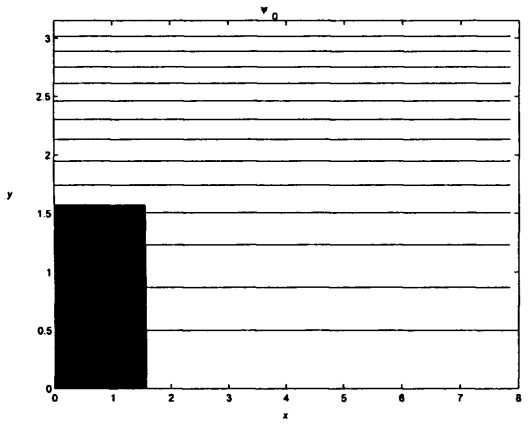

Figure 3.13: The undisturbed value $\psi_0(y) = y$.

made analytically.

The case where $\rho \gg 1$

When the density of the blood is much less than that of the glue, some simplifications to the analysis are possible. First we examine the behaviour of the constants a_1, a_2 and b_2 in this limit. Analysis of equations (3.37)-(3.39) shows that $a_1 \sim 1/\rho$, while both a_2 and b_2 are of order unity, provided λ, h and c are all of order unity. As the density ratio also appears in the interface conditions we have $\tilde{\psi}_{1y} \sim 1/\rho$. So the form of the solution to the linearised problem in this limit takes the form

$$\tilde{\psi}_1 = \tilde{\psi}_{11} + \rho^{-1}\tilde{\psi}_{12} + \cdots, \tag{3.43}$$

$$\tilde{\psi}_2 = \tilde{\psi}_{21} + \rho^{-1}\tilde{\psi}_{22} + \cdots. \tag{3.44}$$

The interface condition (3.34) now becomes $\partial\tilde{\psi}_{11}/\partial y = 0$ at $y = h$, in this limit. Far downstream the conditions are found by taking a Taylor expansion of equations (3.40) and (3.41) in powers of ρ^{-1}. This means that at leading order the glue problem is closed, hence we may calculate $\tilde{\psi}_{11}$: see figure 3.16.

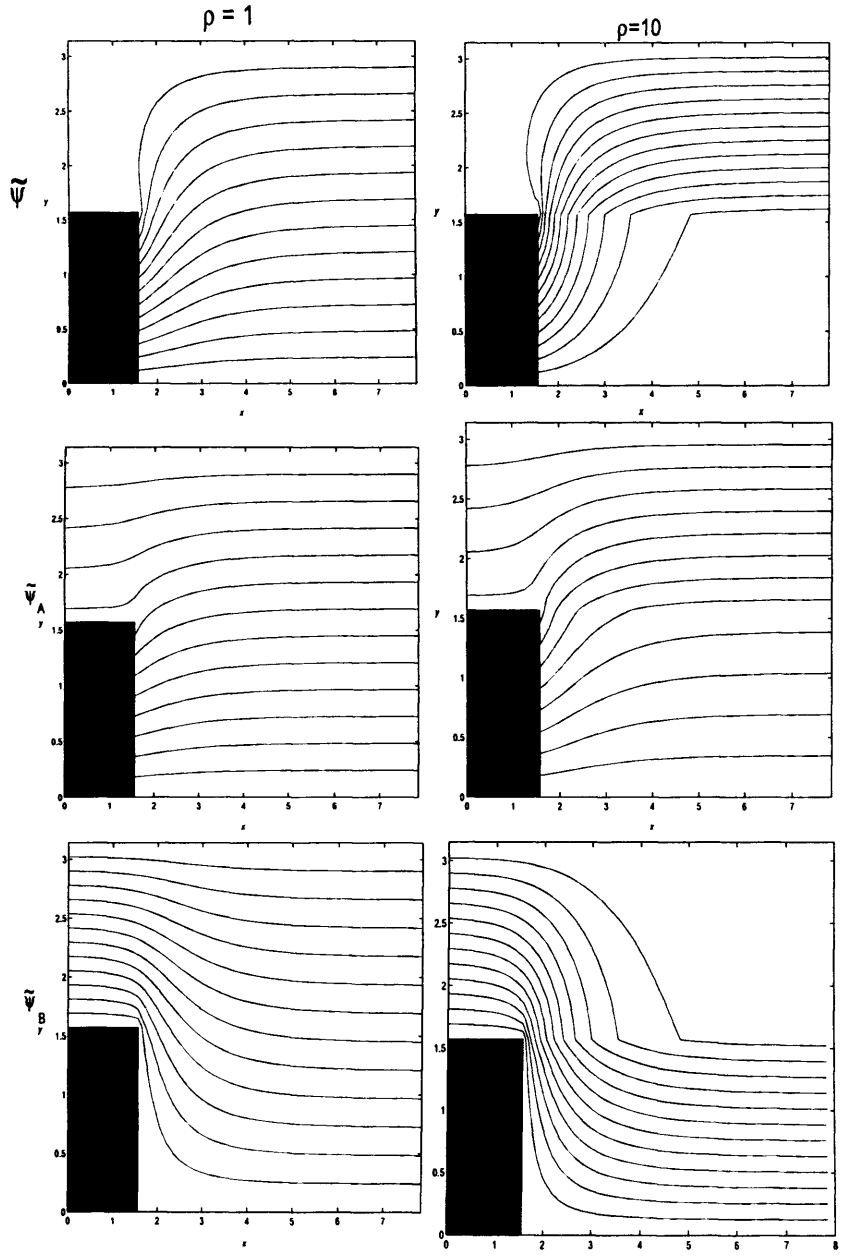

Figure 3.14: Solutions for $\tilde{\psi}$, $\tilde{\psi}_A = \psi_0 + \tilde{\psi}$ and $\tilde{\psi}_B = \psi_0 - \tilde{\psi}$ from top to bottom. Case $\rho = 1$ left and $\rho = 10$ right.

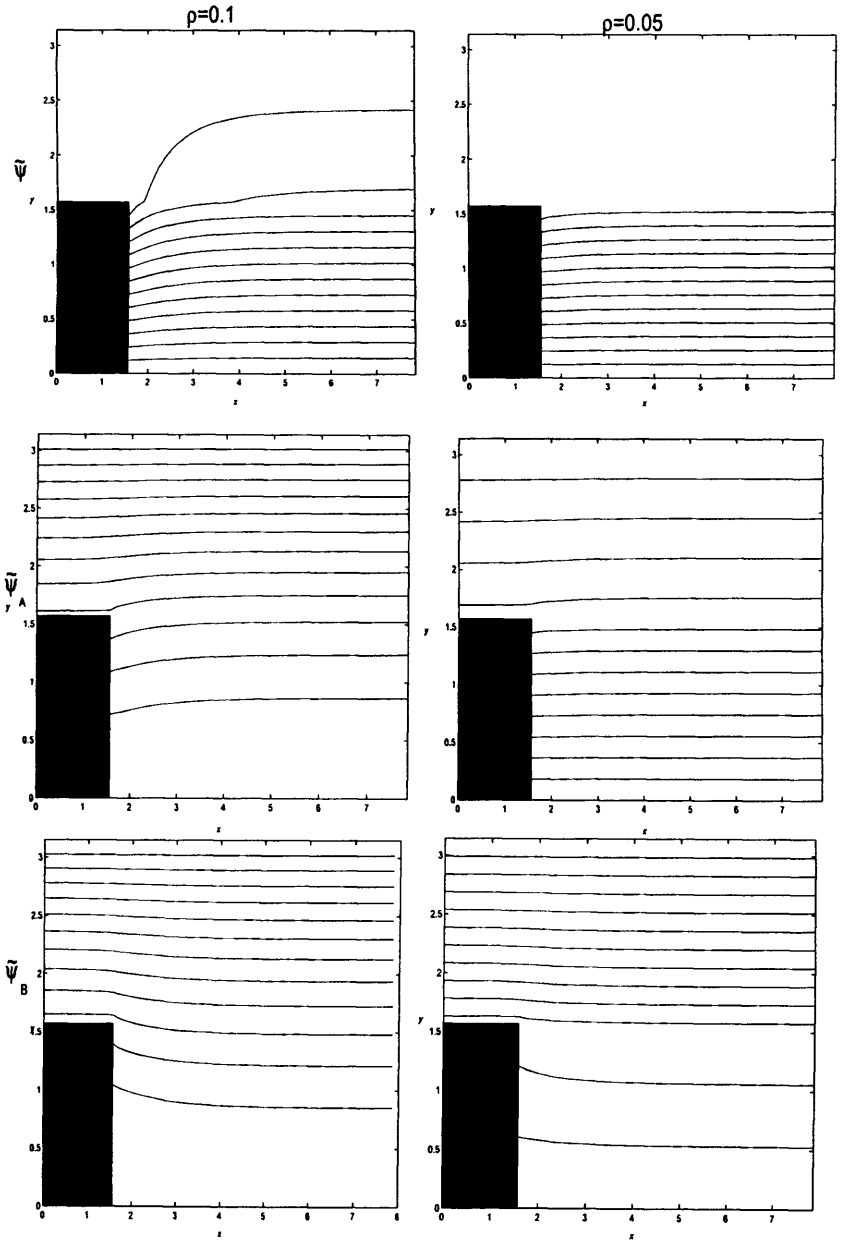

Figure 3.15: Solutions for $\tilde{\psi}$, $\tilde{\psi}_A = \psi_0 + \tilde{\psi}$ and $\tilde{\psi}_B = \psi_0 - \tilde{\psi}$ from top to bottom. Case $\rho = 0.1$ left and $\rho = 0.05$ right.

When this is calculated the leading order solution to the blood problem may be calculated using the previously calculated $\tilde{\psi}_{11}$ for the boundary conditions at the bottom of the blood domain. Thus the first order solution may be found by solving Laplace's equation separately in each fluid. At the next order the boundary conditions for the glue solution are supplied by the leading order blood solution, resulting in another closed problem for solving Laplace's equation in the glue at this order. Then again the solution in the blood at second order may be calculated using this solution, as shown in the figure.

To recap, the leading order glue solution is found first, resulting in the leading order blood solution. Next the glue solution is found at second order, followed by the second order blood solution and so on.

The case where $\rho \ll 1$

Now we consider the case where the density ratio ρ is small. We expand the solution as

$$\tilde{\psi}_1 = \tilde{\psi}_{11} + \rho\tilde{\psi}_{12} + \cdots, \tag{3.45}$$

$$\tilde{\psi}_2 = \tilde{\psi}_{21} + \rho\tilde{\psi}_{22} + \cdots. \tag{3.46}$$

The interface condition (3.34) now becomes $\partial\tilde{\psi}_{21}/\partial y = 0$, so this provides all the boundary conditions for the leading order problem in the blood. So we now find that in this case we solve in the blood first and using the blood solution set the boundary conditions for the glue problem, the reverse of the previous case where ρ was taken to be large. This makes sense physically though, if, for instance, we were considering a free surface problem where the blood was negligible to leading order, we would solve in the glue first and vice-versa. In fact it turns out that at leading order both the blood and glue have simple

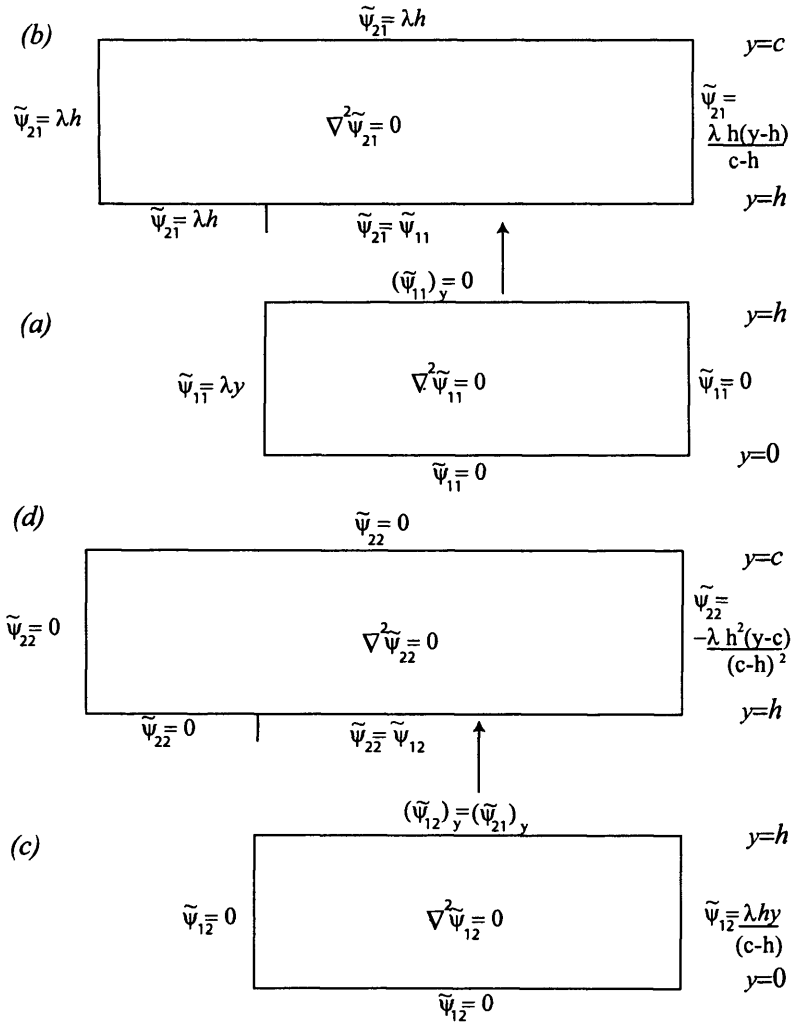

Figure 3.16: The structure for the solution for the $\rho \gg 1$ problem. First the solution is found in the glue for $\tilde{\psi}_{11}$, step(a). This solution is used to set the boundary conditions in order to solve in the blood (b) for $\tilde{\psi}_{21}$. Again this solution sets the boundary conditions for the solution of $\tilde{\psi}_{12}$, step (c), which again in turns sets the boundary conditions in order to solve in the blood (d) for $\tilde{\psi}_{22}$.

solutions, namely,

$$\tilde{\psi}_{11} = \lambda y, \tag{3.47}$$

$$\tilde{\psi}_{21} = \lambda h. \tag{3.48}$$

Again figure 3.17 shows the problem, now with $\rho \ll 1$. By substituting the expansions into the interface conditions we find at $O(\rho)$ that the kinematic condition becomes

$$\frac{\partial \tilde{\psi}_{22}}{\partial y} = \frac{\partial \tilde{\psi}_{11}}{\partial y} = 0, \qquad \text{at } y = h, \tag{3.49}$$

which is known to be zero from the first order solution. The only boundary conditions involving ρ are the downstream conditions, so all other boundary conditions are set to zero. Far downstream we find

$$\tilde{\psi}_{12} = \frac{\lambda}{h}(h - c)y, \tag{3.50}$$

$$\tilde{\psi}_{22} = \lambda(y - c), \tag{3.51}$$

after taking a Taylor expansion and equating at order ρ. Note that $\tilde{\psi}$ is still continuous at $y = h$ at this order as required by the interface conditions. The problem is summarized in fig 3.17.

3.2.5 Discussion of the fully non-linear problem

As outlined earlier making progress on the fully non-linear problem is not so straightforward. We defer discussion of this problem (as sketched in figure 3.18) until chapter 8. There similar problems are tackled directly using the Volume of Fluid method.

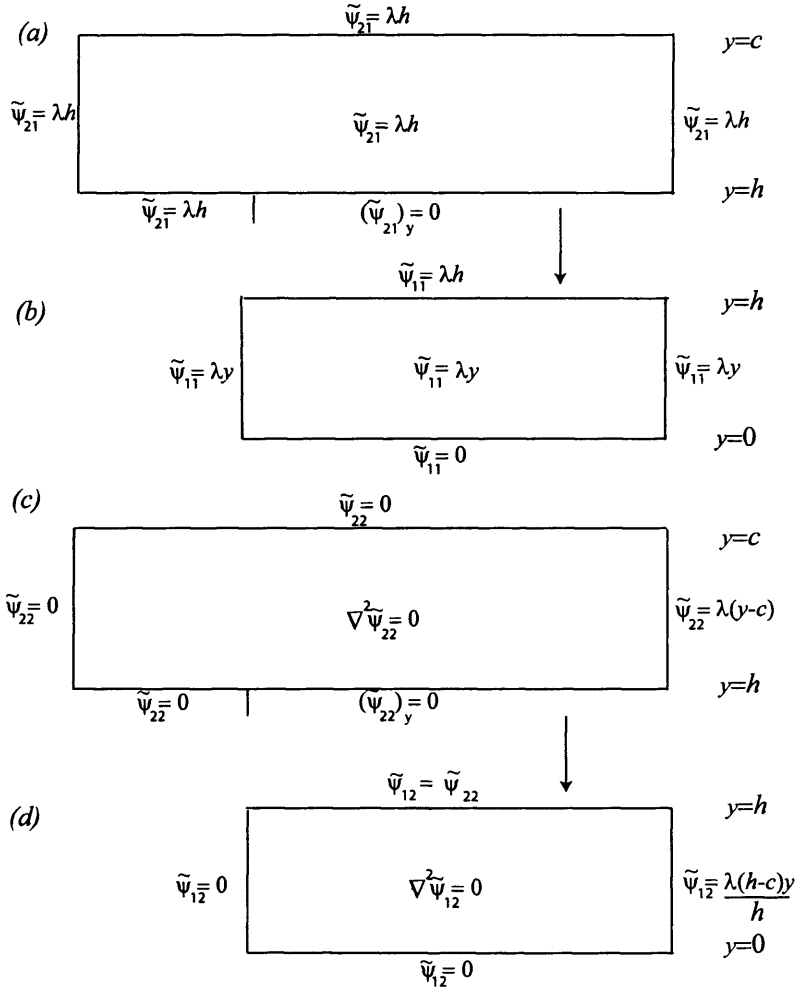

Figure 3.17: The structure for the solution for the $\rho \ll 1$ problem. First the solution is found in the blood for $\tilde{\psi}_{21} = \lambda h$, step(a). This solution is used to set the boundary conditions in order to solve in the glue (b) for $\tilde{\psi}_{11} = \lambda y$. Again this solution sets the boundary conditions for the solution of $\tilde{\psi}_{22}$, step (c), which again in turns sets the boundary conditions in order to solve in the glue (d) for $\tilde{\psi}_{12}$.

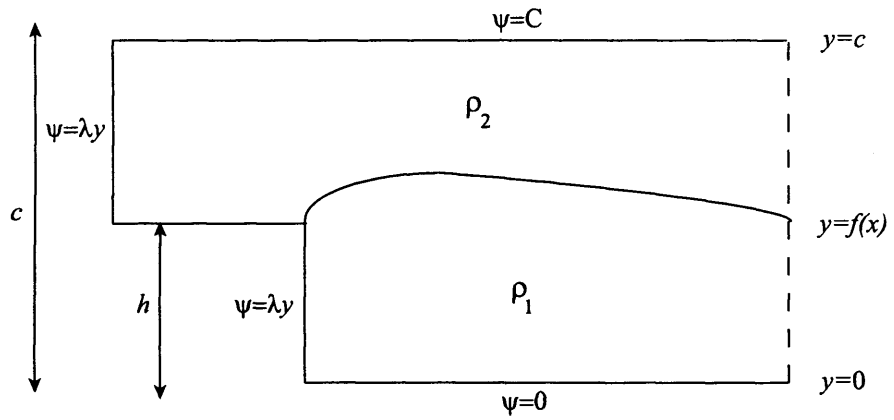

Figure 3.18: Setup for the fully non-linear problem. Here the interface position $y = f(x)$ is still an unknown.

Chapter 4

Wall layer flow: Equations of motion and numerical treatment

In many cases when treating AVMs by embolization, it is desirable for the catheter to take up most of the feeding artery, in which instance the catheter is said to be 'wedged'. In this case the glue being injected may occupy most of the mother vessel. It seems reasonable therefore to consider a case where the core of the artery is full of glue and the interface between the two fluids is located in a thin boundary layer near the wall of the artery, so that the depth of the lower fluid is comparable with the thin wall layer thickness. So in this chapter the flow of both fluids in the wall layer is considered first over a slight roughness on the wall and subsequently into two symmetric bifurcating daughters. As noted in [85] the Reynolds number for blood flow through AVMs can be as high as 300 and so an asymptotic theory based on high Reynolds number, $\mathrm{Re} \to \infty$, seems valid in this case also where two fluids are present, and similarly high values of the Reynolds number are expected.

We assume that the flow can be categorized in two main areas: the core of the artery where, as the Reynolds number is high, the dynamics can be assumed to be inviscid, and a thin wall layer where viscous effects are assumed to be

important and the no-slip boundary condition can be applied. Also vorticity throughout the flow is in general non-zero. The flow is assumed to be quasi-steady due to the short length scales at the branching site and hence short typical time scales compared with the long-scale oncoming flow [85]. First a derivation of the appropriate non-dimensionalisation for the problem is given. This non-dimensionalisation for a two fluid problem is not unique however; an alternative description is given by chapter 11 and by Brotherton-Radcliffe [13], where the non-dimensionalisation is based on individual fluid properties rather than below, where it is based on the pressure gradient far upstream of the surface roughness. Two different problems are studied in this and the subsequent chapter: the flow over a surface roughness and the flow into two large daughters, followed by a combination of both problems. It is hoped that significant insight into the dynamics will be gained from this asymptotic theory, especially concerning the position of the interface in different configurations and with different viscosity ratios. This follows in chapter 5, whereas in the present chapter details of the numerical method and results are given.

4.1 Governing equations and non-dimensionalisation

Consider the flow of two fluids of different viscosity and density in a channel as shown in figure 4.1. The dimensional governing equations were stated in chapter 2 and are given by equations (2.2) and (2.3) for conservation of momentum and mass respectively. Here we examine the steady equations given in dimensional form as

$$(\mathbf{u}_1.\nabla)\mathbf{u}_1 = -\frac{1}{\rho_1}\nabla p_1 + \nu_1\nabla^2\mathbf{u}_1, \tag{4.1}$$

$$(\mathbf{u}_2.\nabla)\mathbf{u}_2 = -\frac{1}{\rho_2}\nabla p_2 + \nu_2\nabla^2\mathbf{u}_2, \tag{4.2}$$

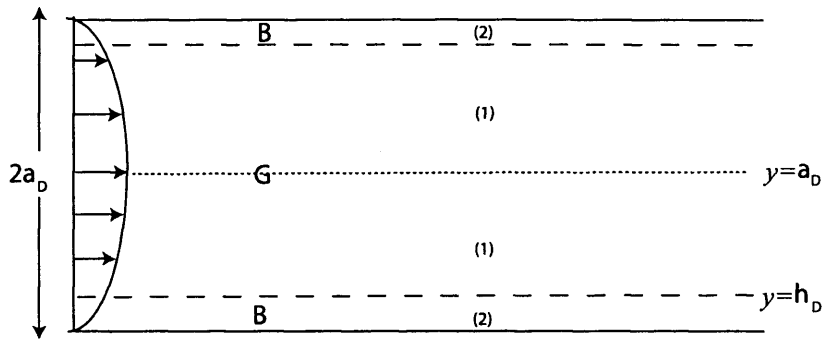

Figure 4.1: Flow of glue and blood in a channel with symmetry in the line $y = a_D$ and fully developed Poiseuille flow upstream in both the glue and the blood. All variables are dimensional in this figure, with the dimensional interface position given by $y = h_D$. Here region (1) specifies the glue region and region (2) that of the blood.

for the glue and the blood respectively, with associated dimensional continuity equations in each fluid given by equation (2.3).

From now on in this chapter dimensional quantities are denoted with a subscript D, whereas non-dimensional values have no subscript assigned to them. In this section details of the non-dimensionalisation of the Navier-Stokes equations are given as well as the simplified conditions at the interface. The flow of glue and blood in a straight channel is considered for now, where the channel half width is taken to be a_D, and the flow is assumed to be symmetric in the line $y = a_D$. We consider the flow far upstream with an oncoming Poiseuille velocity profile in both the glue and the blood, with the velocity vanishing at the artery walls $y = 0$ and $y = 2a_D$. The dimensional pressure gradient in the streamwise direction is denoted G_D, thus the relevant equations of motion in the glue and blood for the incident uni-directional velocity profiles $u_1(y)$ and $u_2(y)$ are respectively

$$\mu_{1D}\frac{\partial^2 u_{1D}}{\partial y_D^2} = G_D, \tag{4.3a}$$

$$\mu_{2D}\frac{\partial^2 u_{2D}}{\partial y_D^2} = G_D, \tag{4.3b}$$

from imposing a uni-directional solution $u(y)$ in each fluid and substituting the respective expressions into equations (4.1) and (4.2). The velocity in each fluid is strictly positive in the x-direction and the velocity profile of the glue is symmetric about the centre of the mother artery $y_D = a_D$. Integrating each of the above in turn twice gives

$$u_{1D} = \frac{G_D}{\mu_{1D}}\left(y_D^2/2 - a_D y_D + \hat{A}_D\right), \tag{4.3c}$$

$$u_{2D} = \frac{G_D}{\mu_{2D}}\left(y_D^2/2 + \hat{B}_D y_D\right), \tag{4.3d}$$

with the as yet unknown constants $\hat{A}_D$ and $\hat{B}_D$ to be determined. The constant a_D multiplying the linear term in (4.3c) is implied by imposing a vanishing velocity gradient at the centreline of the channel $y_D = a_D$. The constants $\hat{A}_D$ and $\hat{B}_D$ are found by applying the conditions of continuity of velocity and shear at the interface. These are essentially a simplified form of equation (2.7) and (2.20), a description of their derivation in this context being given in the next section: see equations (4.21a). Applying these conditions at the horizontal interface $y_D = h_D$ say gives

$$\hat{A}_D = \left(\frac{\mu_{1D}}{\mu_{2D}} - 1\right)\left(\frac{h_D^2}{2} - h_D a_D\right), \tag{4.3e}$$

$$\hat{B}_D = -a_D, \tag{4.3f}$$

for the constants $\hat{A}_D$ and $\hat{B}_D$.

The set-up for the problem is shown in figure 4.1. The fact that the velocity profile must be linear in region (2) means that we must have $h_D \ll a_D$, when substituting for the velocity in the blood at the interface. Next the equations

are non-dimensionalised on blood quantities, which of course remain fixed. The dimensional wall shear in the blood is given by

$$\tau_D = \mu_2 \frac{\partial u_{2D}}{\partial y_D}\bigg|_{y_D=0} = -G_D a_D. \tag{4.4}$$

For the configurations studied below we non-dimensionalise based on equations (4.3c)-(4.3f), and the variables can now be written as

$$x_D = a_D x, \tag{4.5}$$

$$y_D = a_D y, \tag{4.6}$$

$$\mathbf{u}_D = \frac{-G_D a_D^2}{\mu_{2D}}\mathbf{u}, \tag{4.7}$$

$$p_D = \rho_{2D}\kappa_D^2 p. \tag{4.8}$$

Here the non-dimensionalisation for the velocity applies in each of the two fluids. So using these expressions and the dimensional momentum equations, we find the non-dimensional equations in the glue are given by

$$(\mathbf{u}.\nabla)\mathbf{u}\left(\frac{\kappa_D^2}{a_D}\right) = -\nabla p_1\left(\frac{\rho_{2D}\kappa_D^2}{\rho_{1D}a_D}\right) + \frac{\mu_{1D}\kappa_D}{\rho_{1D}a_D^2}\nabla^2\mathbf{u}, \tag{4.9}$$

where $\kappa_D = \frac{-G_D a_D^2}{\mu_{2D}}$. The form of the continuity equation is unchanged and the values denoted with subscript D can be replaced by those without, due to the coordinate scalings on the velocity components and those in the lateral and axial directions. We rewrite the momentum equations in the form

$$(\mathbf{u}_1.\nabla)\mathbf{u}_1 = -\left(\frac{\rho_2}{\rho_1}\right)\nabla p_1 + \frac{1}{\mathrm{Re}}\left(\frac{\nu_1}{\nu_2}\right)\nabla^2\mathbf{u}_1, \tag{4.10}$$

with the Reynolds number given by

$$\mathrm{Re} = \frac{\kappa_D a_D}{\nu_{2D}}. \tag{4.11}$$

These scalings also leave the steady Navier-Stokes equations in the blood in familiar form

$$(\mathbf{u}_2.\nabla)\mathbf{u}_2 = -\nabla p_2 + \frac{1}{\mathrm{Re}}\nabla^2\mathbf{u}_2. \tag{4.12}$$

So now in non-dimensional variables we have that the walls of the channel are situated at $y = 0$ and $y = 2$. Non-dimensionalised velocities far upstream are found by substituting the expressions (4.5)-(4.8) into the expressions for the dimensional velocity profiles (4.3c) and (4.3d). Hence we have

$$u_1 = \mu(y - y^2/2) + (1 - 1/\mu)\left(\bar{h} - \frac{\bar{h}^2}{2}\right), \tag{4.13}$$

$$u_2 = y - y^2/2, \tag{4.14}$$

far upstream, where $\bar{h} \ll 1$ is the non-dimensional interface position h_D/a_D.

4.2 High Reynolds numbers : the wall-layer equations

Next we consider large Reynolds number solutions for the flow over a roughness. Now the unknown interface is given by $y = f(x)$, and as outlined above the flow is assumed to be steady, so the time derivatives in the interface conditions are omitted. We consider the flow of both fluids over the roughness given by $y = hg(x)$, where h is an $O(1)$ height and $g(x)$ a known wall shape. Assuming the Reynolds number is sufficiently large, a boundary layer will form on the bottom surface, where the velocity may vary very rapidly in the lateral direction from the value of zero at the wall to the effective value of the streamwise velocity of the inviscid free stream at the edge of the wall layer. The thickness of the wall layer is found by an order of magnitude analysis of the Navier-Stokes equations akin to that in [40] or [85]. In the wall layer region viscous effects and inertial forces must balance, leading to the relation $uu_x \sim \mathrm{Re}^{-1}u_{yy}$, assuming the kinematic viscosity ratio $\nu = O(1)$. Taking the x-scale of order unity and an oncoming unit shear as in equation (4.14) gives the wall layer thickness $y \sim \mathrm{Re}^{-1/3}$. With these scalings for the longitudinal and transverse directions, the continuity equation implies the following

expansions for the boundary layer thickness, velocities and pressure,

$$y = \mathrm{Re}^{-1/3}Y + \cdots, \tag{4.15}$$

$$u = \mathrm{Re}^{-1/3}U(x,Y) + \cdots, \tag{4.16}$$

$$v = \mathrm{Re}^{-2/3}V(x,Y) + \cdots, \tag{4.17}$$

$$p = \mathrm{Re}^{-2/3}P(x,Y) + \cdots, \tag{4.18}$$

with U, V, P and Y all of order-one. These expressions are valid in both fluids and take the relevant subscripts. The interface between the fluids is now denoted by $Y = F(x)$, in scaled variables, where $F = \mathrm{Re}^{1/3}f$. The situation is shown in figure 4.2. When the expansions (4.15)-(4.18) are substituted into the y-momentum equation we obtain $\partial P/\partial Y = 0$, at leading order, leaving the unknown scaled pressure P as a function of x only, as anticipated. The equations of continuity and momentum in the glue and the blood become at leading order

$$\frac{\partial U_1}{\partial x} + \frac{\partial V_1}{\partial Y} = 0, \; U_1\frac{\partial U_1}{\partial x} + V_1\frac{\partial U_1}{\partial Y} = -\left(\frac{\rho_2}{\rho_1}\right)\frac{dP}{dx} + \left(\frac{\nu_1}{\nu_2}\right)\frac{\partial^2 U_1}{\partial Y^2}, \tag{4.19}$$

$$\frac{\partial U_2}{\partial x} + \frac{\partial V_2}{\partial Y} = 0, \; U_2\frac{\partial U_2}{\partial x} + V_2\frac{\partial U_2}{\partial Y} = -\frac{dP}{dx} + \frac{\partial^2 U_2}{\partial Y^2}. \tag{4.20}$$

As the interface is in the thin wall-layer, it is assumed to be approximately horizontal, i.e. parallel to the wall. Using this fact as well as the fact that velocity gradients in the streamwise direction are small compared with those perpendicular to the wall, the dynamic condition reduces to $P_1 = P_2$, which in essence is already taken in $P = P(x)$. The simplified forms of the continuity of velocity, tangential-stress and kinematic relations are easily found to be:

$$\left.\begin{aligned} U_1 &= U_2 \\ \mu_1\tfrac{\partial U_1}{\partial Y} &= \mu_2\tfrac{\partial U_2}{\partial Y} \\ V_1 &= U_1 F_x \\ V_2 &= U_2 F_x \end{aligned}\right\} \quad \text{on} \quad Y = F(x), \tag{4.21a}$$

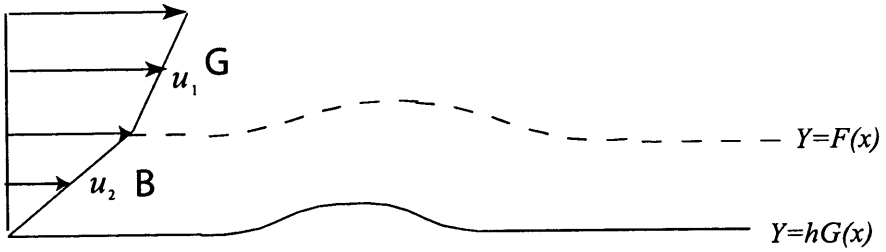

Figure 4.2: Flow of glue and blood in a channel over a roughness given by $Y = hG(x)$ in scaled variables. Here the upstream velocity profiles are given in the glue and blood by equations (4.21e) and (4.21f) respectively. The interface is assumed to be within the wall layer.

in scaled variables for this quasi-steady motion. The other boundary conditions are

$$U_2 = 0 \quad \text{at} \quad Y = hG(x), \tag{4.21b}$$

$$V_2 = 0 \quad \text{at} \quad Y = hG(x), \tag{4.21c}$$

$$U_1 \sim \mu Y + f_0(1-\mu) \quad \text{as} \quad Y \to \infty, \tag{4.21d}$$

$$(U_1, V_1, P) \to (\mu(Y - f_0) + f_0, 0, 0) \quad \text{as} \quad x \to -\infty, \tag{4.21e}$$

$$(U_2, V_2, P) \to (Y, 0, 0) \quad \text{as} \quad x \to -\infty, \tag{4.21f}$$

where f_0 is the undisturbed interface position far upstream and $G(x)$ is the scaled wall shape, given by $G(x) = \mathrm{Re}^{1/3} g(x)$. The equations are respectively for no-slip on the surface of the hump roughness (4.21b), (4.21c), matching with the core-flow solution (4.21d) and matching upstream in the glue and the blood (4.21e), (4.21f). It should be noted that the velocity profiles in each fluid given by (4.21e), (4.21f) are the only velocity profiles which satisfy all the interface and boundary conditions upstream. The above equations constitute a closed problem, which we will compare to the problem of flow into two daughter vessels as discussed in [85] for a single fluid and later on here in section 4.5. In

[85] the wall layer problem is driven by a slip velocity $u_W(x)$ which is added to the right hand side of (4.21d), and is found by solving the inviscid core equations. More details are given in section 4.5.

In our work the main challenge is to solve equations (4.19) and (4.20) together with the boundary and interface conditions (4.21a)-(4.21f). The calculation of the wall shear, pressure and seeking any separation (flow reversal) that may occur as well as presence of upstream influence, are all factors which are of interest. The main methods to be used are a purely numerical approach in this chapter, followed by an asymptotic analysis where the factor μ is assumed small, in chapter 5. Extensions to deal with flow into two symmetric daughters is examined in section 4.5.

4.2.1 Numerical procedure for $h = O(1)$

As the equations of motion are non-linear, with complicated non-linear interface conditions, a numerical treatment is opted for when the density and viscosity ratios ρ and ν are both of order-one. The numerical method used here is due to Davis and is also reported in [95]. This finite-difference method, marching from the point x to $x + \Delta x$ say with a step length Δx essentially linearises the governing equations by insisting that non-linear contributions are treated using known values from the previous x-station, where the solution has already been determined. As the boundary layer equations in each fluid are locally parabolic, a marching scheme in the streamwise direction is appropriate, with the form of the solution known far upstream of the roughness and given in the glue and blood respectively by equations (4.21e) and (4.21f). The numerical approach uses a fixed Cartesian grid and it is desirable to implement the boundary and interface conditions at grid points, rather than at points lying between grid points and using interpolation. As it turns out, both the interface and wall conditions can be applied at constant values coin-

ciding with grid lines. This is done by using two Prandtl-transformations of the vertical coordinate, one for the wall shape and one for the interface shape. Details of these transformations will now be given, resulting in transformed governing equations, which are in suitable form for numerical treatment. After this, details of the method of solution of the equations will be given.

4.2.2 Transformation of the governing equations

Initially we take a Prandtl-shift of the form

$$\begin{aligned} X &= x, \\ \hat{Y} &= Y - hG(X). \end{aligned}$$

This leaves the governing equations in the glue and blood as

$$\frac{\partial U_1}{\partial X} + \frac{\partial \hat{V}_1}{\partial \hat{Y}} = 0, \; U_1\frac{\partial U_1}{\partial X} + \hat{V}_1\frac{\partial U_1}{\partial \hat{Y}} = -\left(\frac{\rho_2}{\rho_1}\right)\frac{dP}{dX} + \left(\frac{\nu_1}{\nu_2}\right)\frac{\partial^2 U_1}{\partial \hat{Y}^2} \quad (4.22)$$

$$\frac{\partial U_2}{\partial X} + \frac{\partial \hat{V}_2}{\partial \hat{Y}} = 0, \; U_2\frac{\partial U_2}{\partial X} + \hat{V}_2\frac{\partial U_2}{\partial \hat{Y}} = -\frac{dP}{dX} + \frac{\partial^2 U_2}{\partial \hat{Y}^2}, \quad (4.23)$$

where the form of the transverse component of the velocity is given in each fluid by

$$\hat{V}_i = V_i - hG'(X)U, \quad (4.24)$$

where $i = 1, 2$ represents the glue and blood respectively as normal. More details on the Prandtl-transformation can be found in [40]. Crucially the no-slip condition is now applied at $\hat{Y} = 0$, making numerical implementation much more straightforward. The new position of the interface is given by $\hat{Y} = (F - hG)(X) = \tilde{f}(X)$, say. The transformed boundary conditions in full are given by

$$\left.\begin{aligned} U_1 &= U_2 \\ \mu_1\frac{\partial U_1}{\partial \hat{Y}} &= \mu_2\frac{\partial U_2}{\partial \hat{Y}} \\ \hat{V}_1 &= U_1\tilde{f}'(X) \\ \hat{V}_2 &= U_2\tilde{f}'(X) \end{aligned}\right\} \quad \text{on} \quad \hat{Y} = \tilde{f}(X). \quad (4.25)$$

The other conditions, those of no-slip and matching with the core flow are

$$U_2 = 0 \quad \text{at} \quad \hat{Y} = 0, \tag{4.26}$$

$$\hat{V}_2 = 0 \quad \text{at} \quad \hat{Y} = 0, \tag{4.27}$$

$$U_1 \sim \mu\hat{Y} + f_0(1-\mu) + \mu h G(X) \quad \text{as} \quad \hat{Y} \to \infty, \tag{4.28}$$

in terms of the new variables. Now we employ further transpositions in view of the interface. It is again beneficial to apply the interface conditions at a constant value of the transverse coordinate. Now however we must choose two different transpositions for each fluid, with care taken so that the wall boundary conditions in the blood are still imposed at a zero value of the given co-ordinate system. The transformations in the glue and blood are defined as

$$\overline{Y} = \hat{Y} - \tilde{f}(X), \tag{4.29}$$

$$\eta = \frac{\hat{Y}}{\tilde{f}}, \tag{4.30}$$

The blood is now defined in the region $0 < \eta \leq 1$ and the glue by $\overline{Y} \geq 0$. The structure of the transformations is the same as the first transformation for the glue, but now in the blood we have the relations $\partial_{\hat{Y}} \to 1/\tilde{f}\partial_\eta$ and $\partial_X \to \partial_X - \eta\tilde{f}'/\tilde{f}\partial_\eta$. Substituting into the equations of momentum and continuity in both fluids leads to [1]

$$\frac{\partial U_1}{\partial X} + \frac{\partial \bar{V}_1}{\partial \bar{Y}} = 0, \; U_1\frac{\partial U_1}{\partial X} + \bar{V}_1\frac{\partial U_1}{\partial \bar{Y}} = -\frac{1}{\rho}\frac{dP}{dX} + \frac{1}{\nu}\frac{\partial^2 U_1}{\partial \bar{Y}^2}, \tag{4.31}$$

$$\frac{\partial(\tilde{f}U_2)}{\partial X} + \frac{\partial \bar{V}_2}{\partial \eta} = 0, \; \tilde{f}^2 U_2\frac{\partial U_2}{\partial X} + \tilde{f}\bar{V}_2\frac{\partial U_2}{\partial \eta} = -\tilde{f}^2\frac{dP}{dX} + \frac{\partial^2 U_2}{\partial \eta^2}, \tag{4.32}$$

where the velocity components are now given by

$$\overline{V}_1 = \hat{V}_1 - U_1\tilde{f}'(X), \tag{4.33}$$

$$\overline{V}_2 = \hat{V}_2 - \eta\tilde{f}'(X)U_2. \tag{4.34}$$

[1] Although strictly speaking the transpositions take the variable $X \to \hat{X}$, we retain the variable X for convenience

The form of the continuity equation in the glue remains unchanged, but in the blood it becomes

$$\tilde{f}\frac{\partial U_2}{\partial X} + \tilde{f}'(X)U_2 + \frac{\partial \bar{V}_2}{\partial \eta} = 0. \tag{4.35}$$

The transformed interface conditions are evaluated at $\bar{Y} = 0, \eta = 1$ and are given by

$$\left.\begin{aligned} U_1 &= U_2 \\ \mu_1 \tfrac{\partial U_1}{\partial \bar{Y}} &= \tfrac{\mu_2}{\tilde{f}} \tfrac{\partial U_2}{\partial \eta} \\ \overline{V}_1 &= 0 \\ \overline{V}_2 &= 0 \end{aligned}\right\} \quad \text{on} \quad \bar{Y} = 0\,, \quad \eta = 1, \tag{4.36}$$

which are again for continuity of tangential velocity, continuity of shear and the kinematic boundary condition. The wall-boundary and outer conditions are given by

$$U_2 = 0 \quad \text{at} \quad \eta = 0, \tag{4.37}$$

$$\overline{V}_2 = 0 \quad \text{at} \quad \eta = 0, \tag{4.38}$$

$$U_1 \sim \mu\bar{Y} + f_0(1-\mu) + \mu h G(X) + \mu\tilde{f}(X) \quad \text{as} \quad \bar{Y} \to \infty. \tag{4.39}$$

As the limits are fixed, i.e. $0 \leq \eta \leq 1$ and $0 \leq \bar{Y} < \infty$, we can start the numerical solution. (It should be noted that the Prandtl-shift used in the glue would lead to extra complications if used in the blood too. In this case the wall boundary conditions would be evaluated at $\hat{Y} = -\tilde{f}$.) The numerical solution is accomplished using a semi-explicit finite-difference method which is second order accurate in Y and η, and first order accurate in X. Next follows a precise account of the discretizations used for the derivatives along with a full account of the method.

4.2.3 Discretization of terms

A Cartesian grid is used in this problem; so the finite-difference expressions are well known and many details are omitted. The discretizations used are

the same in each fluid so in this section subscripts will be dropped, while for purposes of clarity of explanation we omit hats or tilded independent variables. The solution at the first X-station is known from the incident flow and in general the solution at the previous station which is also known is denoted by a barred variable. Explicit formulae to be used in the momentum equation are

$$UU_x = \bar{U}_j \frac{U_j - \bar{U}_j}{\Delta X}, \tag{4.40}$$

$$VU_y = \bar{V}_j \frac{U_{j+1} - U_{j-1}}{2\Delta Y}, \tag{4.41}$$

$$P'(x) = \frac{P_j - \bar{P}_j}{\Delta X}, \tag{4.42}$$

$$U_{yy} = \frac{U_{j+1} - 2U_j + U_{j-1}}{\Delta Y^2}. \tag{4.43}$$

Here dependent variables with bars, for instance $\bar{U}$, are actually shorthand for the known value at the previous X-station $U_{i-1,j}$ and similarly for other variables. All variables with no bar are variables which are unknown and which are to be calculated at the current X-station. The step lengths in the $X-$ and Y-directions are respectively given by ΔX and ΔY. In the glue Y is replaced by $\bar{Y}$, and in the blood Y is replaced by η.

We now substitute these expressions into the momentum equations for both glue and blood. Again for ease of explanation and to avoid two subscripts we now set the discrete velocity in the blood to lower case
$\mathbf{u} = (u_0, u_1, u_2, \cdots u_{N-1}, u_N)^T$ and the glue velocity to upper case
$\mathbf{U} = (U_0, U_1, U_2, \cdots U_{M-1}, U_M)^T$, and similarly for $\mathbf{v}, \mathbf{V}$, so we calculate the blood velocity at N separate points and the glue velocity at M points where M and N are not necessarily equal. So substituting expressions (4.40)-(4.43) into the momentum equations gives a linear system for the unknowns $u_{i,j}$ or $U_{i,j}$ in the respective fluids. Denoting the pressure gradient in the x-direction as q, the linear system in the blood can be solved by inverting the matrix problem

$$Su = F. \tag{4.44}$$

Here the matrix S is given by

$$S = \begin{bmatrix} A_1 & C_2 & & & & & \\ B_1 & A_2 & C_3 & & & & \\ & \ddots & \ddots & \ddots & & & \\ & & B_{j-1} & A_j & C_{j+1} & & \\ & & & \ddots & \ddots & \ddots & \\ & & & & B_{N-3} & A_{N-2} & C_{N-1} \\ & & & & & B_{N-2} & A_{N-1} \end{bmatrix}, \tag{4.45}$$

and $u = (u_1, u_2, \cdots u_{N-1})^T$. In fact the solution in both fluids is accomplished separately and so two matrix inversions must be carried out. In the blood the value u_0 is the velocity at the wall and is always set to zero to satisfy the no slip condition. This value and the value for the velocity at the interface u_N assumed to be known at the moment are taken out of the vector so as to make S a tri-diagonal matrix of dimensions $(N-1 \times N-1)$. The coefficients of the matrix S in the blood are given by

$$A_j = \left(\frac{\bar{u}_j \bar{\bar{f}}^2}{\Delta X} + \frac{2}{\Delta \eta^2} \right), \tag{4.46}$$

$$B_j = \left(\frac{-\bar{v}_j \bar{\bar{f}}}{2\Delta \eta} - \frac{1}{\Delta \eta^2} \right), \tag{4.47}$$

$$C_j = \left(\frac{\bar{v}_j \bar{\bar{f}}}{2\Delta \eta} - \frac{1}{\Delta \eta^2} \right), \tag{4.48}$$

for the main, sub-diagonal and super-diagonal respectively. In the diffusive term in the blood equations we take the value $\bar{\bar{f}}$ to be the known value from

the previous X-station. The entries for the known vector F are given by

$$F_j = \left(-\bar{\bar{f}}^2 q + \frac{\bar{u}_j^2 \bar{\bar{f}}^2}{\Delta X}\right), \qquad \text{for } 2 \leq j \leq N-1, \tag{4.49}$$

$$F_1 = \left(-\bar{\bar{f}}^2 q + \frac{\bar{u}_1{}^2 \bar{\bar{f}}^2}{\Delta X}\right) - u_0 A_1, \tag{4.50}$$

$$F_N = \left(-\bar{\bar{f}}^2 q + \frac{\bar{u}_1{}^2 \bar{\bar{f}}^2}{\Delta X}\right) - C_{N-1} u_N. \tag{4.51}$$

To repeat, all the variables with a bar are known, hence the only unknowns are the U_j and the system is linear, provided the pressure gradient q and the velocity at the interface u_N are known. So the U-velocities are found by inverting the matrix problem (4.44). Once found the V_j can be obtained directly from the continuity equation. The discretization associated with the continuity equation in the blood is

$$\frac{\bar{\bar{f}}}{2}\left(\frac{u_j - \bar{u}_j}{\Delta X}\right) + \frac{\bar{\bar{f}}}{2}\left(\frac{u_{j-1} - \bar{u}_{j-1}}{\Delta X}\right) + \left(\frac{\bar{u}_j + \bar{u}_{j-1}}{2}\right)\frac{\tilde{f}_{i,j} - \bar{\bar{f}}_j}{\Delta X} + \frac{v_j - v_{j-1}}{\Delta \eta} = 0. \tag{4.52}$$

The entries F_1 and F_{N-1} are determined with the help of the boundary conditions; in fact the no-slip condition $u_0 = 0$ means that F_1 is of the same form as other values F_j in this case. As all the u_j are known now and the value for the v-velocity is known at the wall, i.e. $v_0 = 0$, all the v-velocities can be calculated using the continuity equation (4.52), assuming the current transformed interface position f is known.

Similar formulae hold in the glue. Again we are solving the matrix problem (4.44) but with M replaced by N and the vector $\mathbf{u}$ replaced by $\mathbf{U}$. The

coefficients are given by

$$A_j = \left(\frac{\bar{U}_j}{\Delta X} + \frac{2}{\nu \Delta Y^2}\right), \tag{4.53}$$

$$B_j = \left(\frac{-\bar{V}_j}{2\Delta Y} - \frac{1}{\nu \Delta Y^2}\right), \tag{4.54}$$

$$C_j = \left(\frac{\bar{V}_j}{2\Delta Y} - \frac{1}{\nu \Delta Y^2}\right), \tag{4.55}$$

again for the main, sub-diagonal and super-diagonal respectively. The discretizations associated with the continuity equation are

$$U_x = \frac{1}{2}\left(\frac{U_j - \bar{U}_j}{\Delta X}\right) + \frac{1}{2}\left(\frac{U_{j-1} - \bar{U}_{j-1}}{\Delta X}\right), \tag{4.56}$$

$$V_{\bar{Y}} = \frac{V_j - V_{j-1}}{\Delta \bar{Y}}. \tag{4.57}$$

Again the velocity vector in the glue is $U = (U_1, U_2, \cdots, U_{M-1})^T$, and V takes a similar form. As in the blood, the velocity at the bottom and the top have been taken out of the vector to make the matrix problem suitable for inversion. The velocity U_0 is now just set to the top blood velocity u_N to satisfy the continuity of velocity at the interface. The velocity U_M is also known from the matching condition, hence, as in the blood taking these two values out of the vector only affects the first and last values of the vector F. These are now given by

$$F_j = \left(-\frac{q}{\rho} + \frac{\overline{U}_j^{\,2}}{\Delta X}\right) \qquad \text{for } 2 \leq j \leq M-1, \tag{4.58}$$

$$F_1 = \left(-\frac{q}{\rho} + \frac{\overline{U}_1^{\,2}}{\Delta X}\right) - (u_N)_B A_1, \tag{4.59}$$

$$F_N = \left(-\frac{q}{\rho} + \frac{\overline{U}_1^{\,2}}{\Delta X}\right) - C_{M-1} U_M. \tag{4.60}$$

where $(u_N)_B$ is the blood velocity at the interface. In practice the matrix inversion is carried out using the well known Thomas algorithm for tri-diagonal systems [55]. However at the start of the computational procedure the pressure gradient q_i and the interface position f and hence $\tilde{f}$ are unknown. When both have been determined they may be simply substituted into the equations

and the velocities found straight away. Both quantities are determined using guessed values and simple linear interpolation. Before the implementation of the full solution is explained we will concentrate on a case where the interface position is known, namely a one fluid problem. After this a full detailed explanation of the complete system will be given.

4.3 A simplified problem

We consider here just a single fluid with governing equation (4.20), boundary conditions given by (4.21b)-(4.21d) and and initial solution (4.21f) holding. So at the first X-station the solution is known, at the next x-station the only unknown is the pressure gradient q. With q known, the U-velocities can be calculated by inverting the matrix M and the V-velocities follow straight away from the continuity equation. To find the correct pressure gradient denoted from now on as $q^\star$, we take two guesses q_1 and q_2. With each of the guesses the $U-$ and V-velocities are calculated using the method described above. However with these guessed pressure gradients there is no guarantee that the matching condition equation (4.39) is satisfied; all other conditions will be satisfied though. If we substitute equation (4.39) into the momentum equation and ignore the term involving the interface for the time being, the equation simplifies to

$$(\mu\bar{Y} + f_0(1-\mu) + \mu hG(X))\mu hG'(X) + \mu V_M \sim -q\rho^{-1} \qquad \text{as } \bar{Y} \to \infty. \quad (4.61)$$

So with each guess q_1 and q_2 the U-velocities are first found and then the V-velocities are calculated from the discrete continuity equation as outlined in the previous section. The V-velocity at the top of the computational domain, V_M is found typically at $Y = 20$ and the magnitude of the error in equation

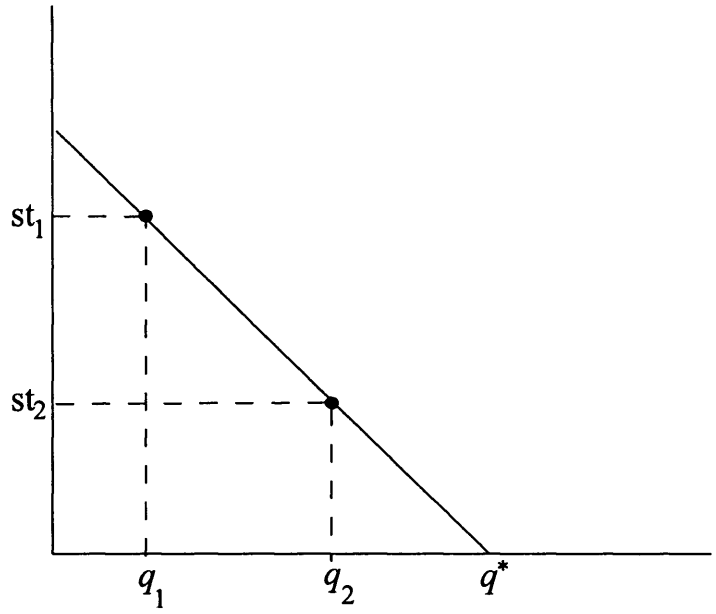

Figure 4.3: Interpolation to find the correct value q^*,

(4.61) is stored; for the two guesses we have

$$st_1 = (\mu\bar{Y} + f_0(1-\mu) + \mu hG(X))\mu hG'(X) + \mu V_{M1} + \rho^{-1}q_1, \quad (4.62)$$

$$st_2 = (\mu\bar{Y} + f_0(1-\mu) + \mu hG(X))\mu hG'(X) + \mu V_{M2} + \rho^{-1}q_2, \quad (4.63)$$

where the values V_{M1} and V_{M2} in equations (4.62) and (4.63) are those calculated with respective guesses q_1 and q_2. A simple linear interpolation, as shown in figure 4.3, gives the exact value for the pressure gradient as

$$q^* = \frac{-st_2q_1 + q_2st_1}{st_1 - st_2}, \quad (4.64)$$

due to the problem being linear. So now the exact pressure gradient is known, the actual values of U and V can be determined by following exactly the same procedure as outlined above with the correct pressure gradient q^*. The updated pressure is given by

$$p = \overline{p} + q^*dX. \quad (4.65)$$

All values at the current X-station are now known and the calculation may progress onto the next station in the streamwise direction. The problem of two fluids, i.e. the problem we wish to solve is a little more complicated due to the fact that now the pressure gradient is still unknown at a general X-station and the interface position is also unknown there. However essentially the same methodology still applies here, and both quantities can be found using simple interpolation methods.

4.4 Solution of equations (4.31) -(4.39)

As outlined above, the computational solution to equations (4.31)-(4.39) is complicated by the fact that the pressure gradient q and the interface position f are unknown and both must be determined at every X-station. In practice this is again achieved by guessing the values of the variables and correcting by using linear interpolation for each pair of guesses, based on the linearity of the scheme. Actually the only equations where the current interface condition is needed are in the continuity equation in the blood and the matching condition with the core flow in the glue. So first here we take a guess at the current interface position, f_1 say. With this guessed value we first proceed to find the associated pressure gradient. However another issue arises here as the transformed kinematic condition $\hat{V} = 0$ at the interface must be satisfied. No numerical value however is given for the velocity at the interface u_N or equivalently U_1 in advance and so again two guessed values for u_N are taken and once the resulting v-velocities are found, the correct u value can be determined by interpolation relating to the requirement $\hat{V} = 0$.

With this effective upper boundary condition in the blood in place, we can now find all the $u-$ and $v-$velocities in the blood with the kinematic relation $\hat{V} = 0$ satisfied. At the interface the u-velocities are continuous, so the top

boundary condition in the blood becomes effectively the bottom boundary condition in the glue and feeds into equation (4.59). The upper condition in the glue is also known explicitly and so now all the u-velocities in the glue can be found by using the Thomas algorithm again to invert equation (4.44). The corresponding v-velocities are also found using the continuity equation. So now we have calculated all the velocities in the glue and blood using a guessed pressure gradient for a guessed interface position. The kinematic condition has been satisfied but at present the continuity of shear at the interface and the matching condition for the v-velocities are in general not satisfied.

So next we take another guess at the pressure gradient q_2 with the same guessed interface position and calculate all the velocities in the glue and blood as above. As in the previous section we now correct the pressure gradient based on the matching condition, to give the true pressure gradient associated with the interface position f_1. By substituting equation (4.39) into the momentum equation we find that at the top of the glue

$$(\mu\bar{Y} + \mu(1 - f_0) + \mu hG(X) + \mu\tilde{f}(X))(\mu hG'(X) + \mu\tilde{f}'(X)) + V_M\mu = -\rho^{-1}q. \tag{4.66}$$

So the values for V at the top can be stored and the pressure gradient is corrected so that the top condition is satisfied to machine accuracy. Once this has been done the process is repeated with the correct pressure gradient, q^* say and all velocities are calculated in the glue and blood.

Now because f_1 was only a guessed interface position, the shear condition at the interface will still not be satisfied in general. So we now take another guessed value, f_2, and repeat the process to find the pressure gradient, a second q^* value associated with this interface position. Again all the velocities in both fluids are calculated and are stored. As the interface position f is present explicitly in the shear condition, it can be corrected using this equation. Once again the magnitude of the error in the condition with each interface position

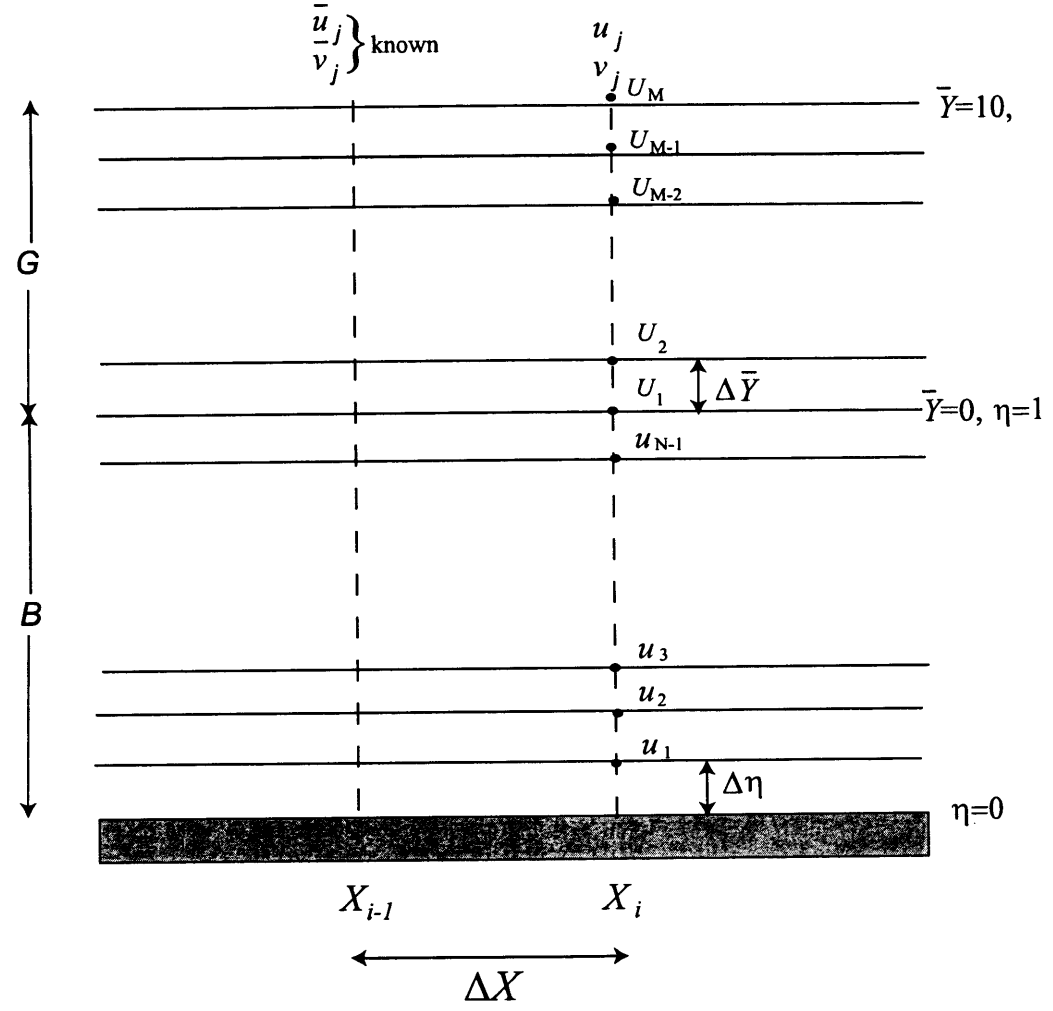

Figure 4.4: Computational grid used for the wall layer problem. Here the solution is known already at the position X_{i-1} and the known velocity components are denoted $\bar{u}_j, \bar{v}_j$. The points show where both the $u-$ and v-velocities are evaluated. Due to ease of explanation u here represents the blood velocities, i.e. u_2 and U the glue velocities u_1. We take N points in the blood, not including the wall where the velocity is zero, and M points in the glue; the relations $N\Delta\eta = 1$ and $M\Delta\bar{Y} = 10$ must be satisfied for the case $0 \leq \bar{Y} \leq 10$ shown.

is found. In fact the discrete version is given by

$$st = \tilde{f}\left(\frac{-3u_N + 4u_{N-1} - u_{N-2}}{2\Delta\eta}\right) - \mu\left(\frac{3U_1 - 4U_2 + U_3}{2\Delta\bar{Y}}\right), \tag{4.67}$$

where of course, the velocities U_1 and u_N are equal. This expression is again second order accurate. The value is found for the two different guesses at the interface position f_1 and f_2 and stored as st_1 and st_2 say and then the correct interface position is found according to

$$f^* = \frac{-st_2 f_1 + f_2 st_1}{st_1 - st_2}. \tag{4.68}$$

Now that the correct interface position is deduced, again the correct pressure gradient associated with it must be found. As previously, this is obtained using two guesses and correction via the matching condition at the top of the wall layer. Once the correct pressure gradient is found, all the velocities are determined and these velocities will satisfy all the governing equations and boundary conditions. Thus the computation is ready to proceed to the next X-station and the whole process is repeated.

4.4.1 Results

In the computations we take $0 \leq \eta \leq 1$ which is actually fixed by the Prandtl-shifts chosen and $0 \leq \bar{Y} \leq 10$. The upper edge of 10 was found to be sufficient in most cases examined. We take the surface roughness to be of the form

$$G(X) = \begin{cases} h(1 - X^2)^2 & \text{if} - 1 \leq X \leq 1, \\ 0 & \text{otherwise.} \end{cases} \tag{4.69}$$

The wall shape and its derivative are continuous at $X = \pm 1$, and here h is generally an order-one constant. To validate the numerical method, first we set the wall shape $G(X) = 0$, to make sure then that the incident flow solution is now the solution at every X-station. Next the viscosity and density of each

of the fluids are taken to be equal, which effectively results in a single fluid problem again, as studied in [40]. We take $\mu = 1$ and $\rho = 1$ with the wall shape as given by equation (4.69) and the height parameter set to $h = 1.7$ to compare to Rothmayer and Smith's results. The interface position f now is effectively a streamline for the flow. The results obtained for this case are presented in figures 4.5 to 4.7 and are in good agreement with [40] for both pressure and wall shear. The wall shear is calculated from

$$\tau_W(X) = \mu_2 \frac{\partial u_2}{\partial y}\bigg|_{y=0} = \frac{\mu_2}{\tilde{f}} \left(\frac{4u_1 - u_2}{2\Delta\eta} \right), \tag{4.70}$$

using a second-order discretization for the first derivative and using the no-slip condition at the solid surface.

The results for the flow over the roughness are shown in figures 4.7 to 4.19, which give the wall shear, pressure and interface position for different values of μ. The wall shape is taken to be that in equation (4.69), we take values of the height parameter $h = 1, 1.7$ and 3 to make comparisons with the results of Rothmayer and Smith's work on the one fluid problem [40]. In general, larger values of h produced large separation for $\mu = \rho = 1$ and indeed a breakdown in the numerical routine. Figure 4.7 gives the shear for the case $h = 1.7$. It can be seen that separation occurs for $\mu = 1$, but taking smaller values of μ results in no flow reversal. Indeed for the one fluid case, i.e. $\rho = \mu = 1$, $h = 1.7$ is the smallest height at which separation occurs.

The interface position for small values of μ is shown in figure 4.8. It shows that the smaller the value of μ taken, the higher the interface travels over the roughness, but the quicker it returns to its un-disturbed downstream position, after the roughness has been negotiated. For instance with $\nu = 0.1$ the interface returns to $f_0 = 1$ at the point 1.05, i.e. just after the hump. Larger values of μ result in the interface gaining less height as it travels over the hump and taking longer to return to the undisturbed position. When $\nu = 1$ the interface returns to f_0 at approximately $X = 6$, when the computations are run for

larger streamwise length scales (not shown in the figures). The pressure for these cases is shown in figure 4.10. As expected, the larger μ ratio provokes a greater negative pressure response, and the smaller μ values result in the pressure returning to $p = 0$ quickly after the flow has passed the roughness, as in line with the results of the interface position.

Figures 4.11 to 4.13 show the same problem but now with the height parameter increased to $h = 3$. Results are not shown for $\mu = 1$ as large separation occurs here and the numerical routine breaks down in the strong region of reversed flow. However similar trends compared to the $h = 1.7$ case are seen here, with the critical viscosity ratio for separation now being approximately 0.4, see figure 4.11.

Although the case where the viscosity of the blood is greater than that of the glue is of less relevance to the embolization process, results were obtained for this case anyway. Figures 4.14 to 4.16 show the interface position, pressure and wall shear, but now with $h = 1$, as larger values of h again lead to separation for these large μ values. Figures 4.14 to 4.16 show the interface position for the cases where $\mu = 1, 5, 10$ and 20. As can be seen from the figures, the higher the value of the viscosity ratio, the longer the interface takes to return to the position f_0 as was found with the smaller values of h. The pressures for these cases are shown in fig 4.16. It should be noted that the smaller the viscosity ratio, the less likely the chance of any flow reversal. Indeed figure 4.14 shows that for the case $\nu = 0.1$ the value for the skin friction returns to its incident value of unity very soon after the flow has negotiated the surface roughness.

So it appears that when the viscosity ratio is small, $\mu_1 \gg \mu_2$ as is the case for embolization, we see no flow reversal and the interface travels over the roughness with approximately the shape of the roughness. This will be shown to be the analytic asymptotic solution as $\mu \to 0$ in the next section.

Computations were also carried out where the viscosity ratio was kept con-

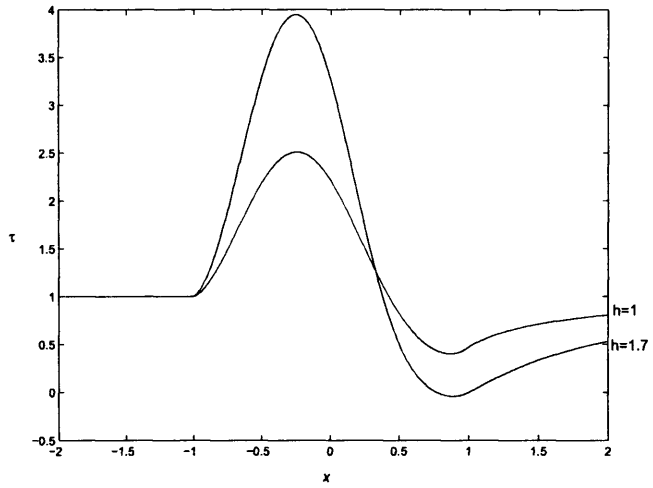

Figure 4.5: Wall shear for $\mu = 1, \rho = 1$, i.e. the one fluid problem, with hump heights $h = 1$ and $h = 1.7$. Very good comparison with Rothmayer and Smith's [40] results are seen.

stant $\mu = 1$ and the density varied. Results for wall-shear, pressure and interface position are shown in figures 4.17 to 4.19. These figures show the case where $\rho = 0.1, 1$ and 10, and the hump height is again taken to be $h = 1.7$. As can be seen from the figures when the density ratio is taken to be large, values for the wall shear are much lower than for smaller ρ. When $h = 1.7$, figure 4.17 shows that separation occurs in all three cases with the greatest displacement of the interface coming for smaller values of ρ.

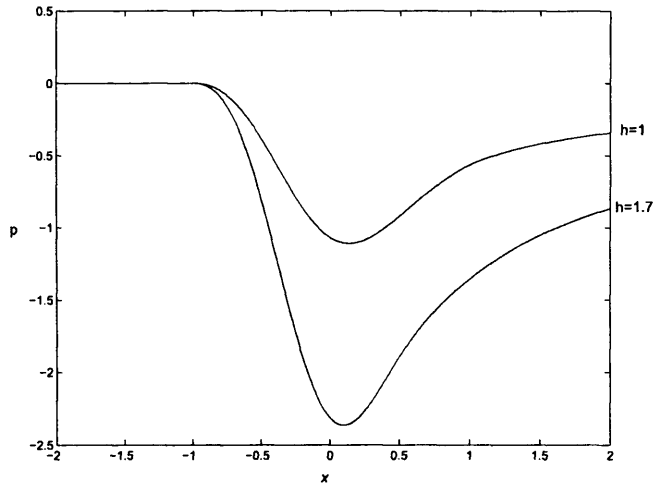

Figure 4.6: Pressure for $\mu = 1, \rho = 1$, for hump heights $h = 1$ and $h = 1.7$.

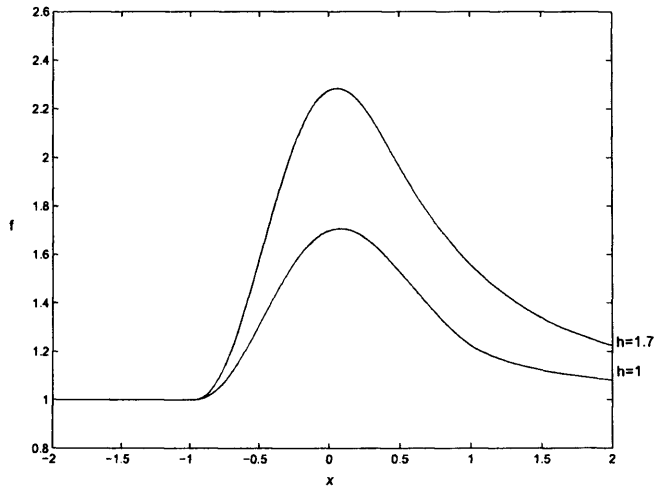

Figure 4.7: Effective interface position for $\mu = 1, \rho = 1$, i.e. the one fluid problem, with hump heights $h = 1$ and $h = 1.7$. In essence the plots show the pathlines of an individual fluid particles trajectory over the roughness, where the particle starts at $y = 1$.

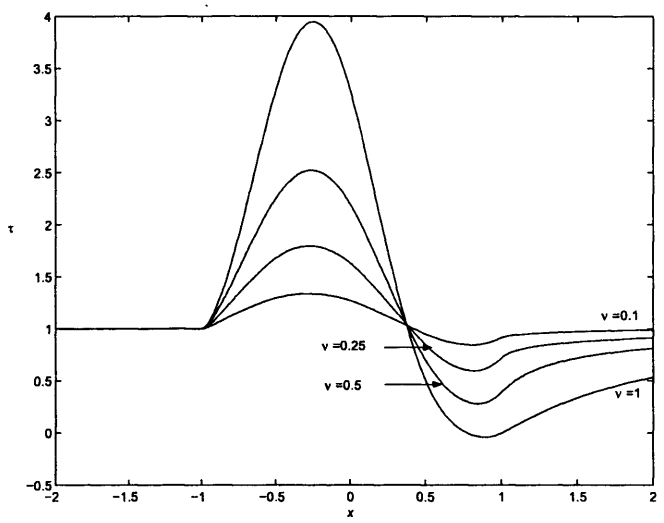

Figure 4.8: Wall shear for $h = 1.7$ and values $\nu = \mu = 0.1, 0.25, 0.5, 1$, $\rho = 1$.

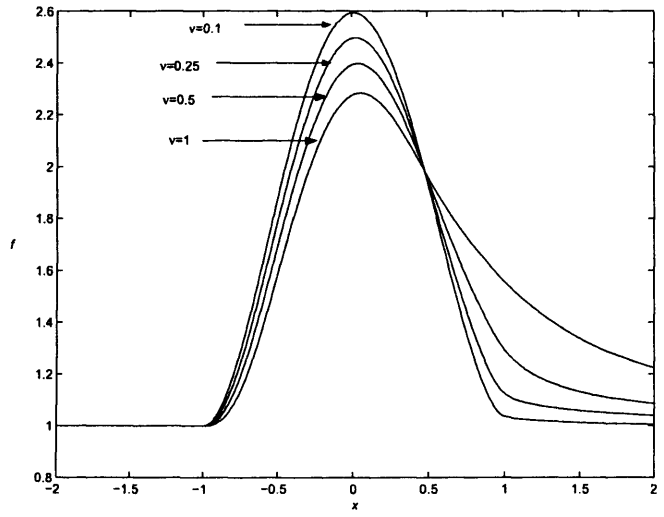

Figure 4.9: Interface position for $h = 1.7$ and values $\nu = \mu = 0.1, 0.25, 0.5, 1$, $\rho = 1$.

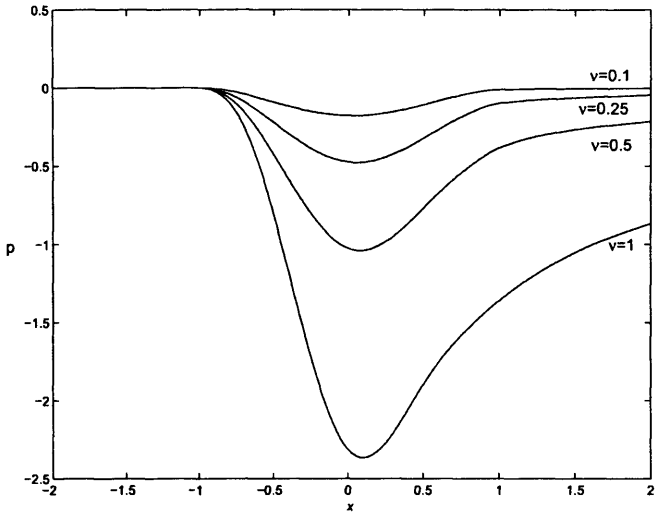

Figure 4.10: Pressure for $h = 1.7$ and values $\mu = \nu = 0.1, 0.25, 0.5, 1$, $\rho = 1$.

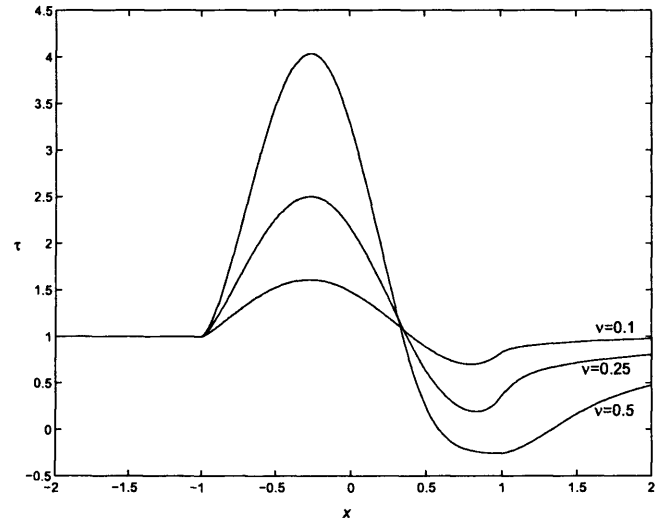

Figure 4.11: Wall shear for $h = 3$ and values $\mu = \nu = 0.1, 0.25, 0.5$, $\rho = 1$. Large separation occurs for the value $\mu = 1$ and the numerical routine breaks down in the strong region of reversed flow.

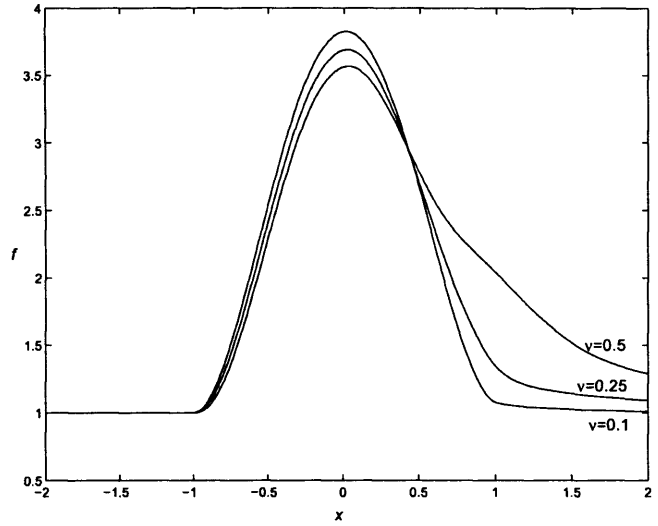

Figure 4.12: Interface position for $h = 3$ and values $\mu = \nu = 0.1, 0.25, 0.5$, $\rho = 1$

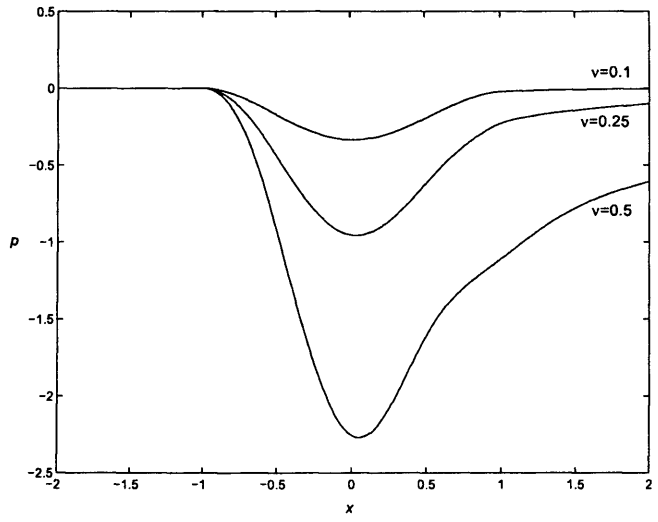

Figure 4.13: Pressure for $h = 3$ and values $\mu = \nu = 0.1, 0.25, 0.5$, $\rho = 1$.

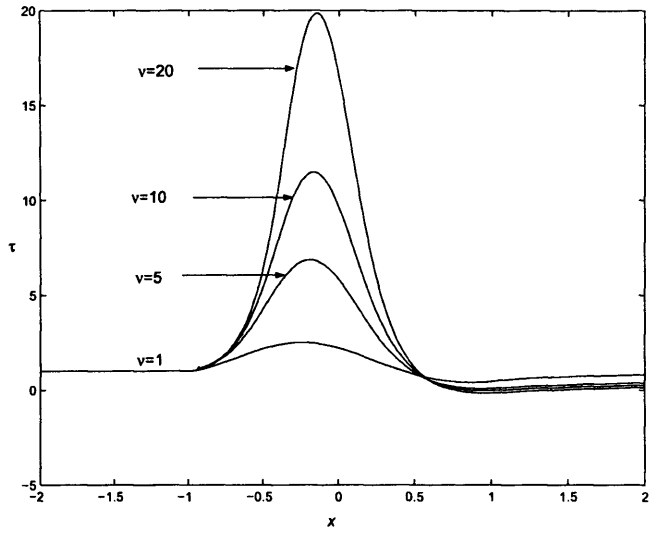

Figure 4.14: Wall shear for $h = 1$ and values of $\nu \geq 1$, $\rho = 1$.

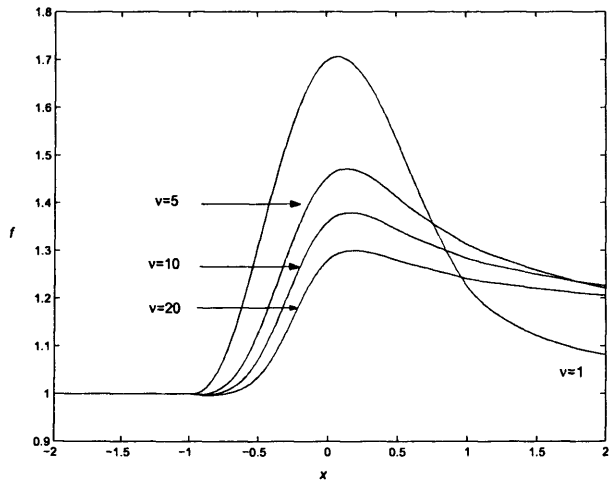

Figure 4.15: Interface position for $h = 1$ and values of $\nu \geq 1$, here $\rho = 1$.

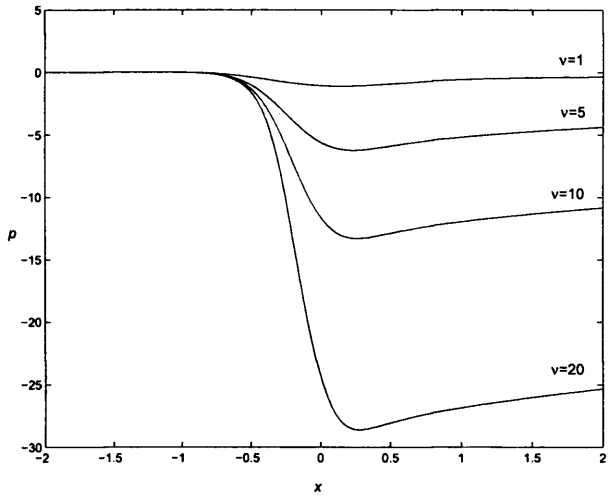

Figure 4.16: Pressure for $h = 1$, and values of $\nu \geq 1$, $\rho = 1$.

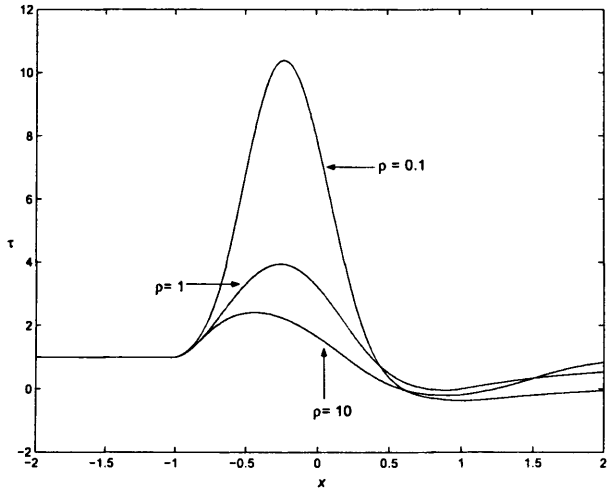

Figure 4.17: Wall shear for $h = 1$, $\rho = 0.1, 1$ and 10. Here $\mu = 1$.

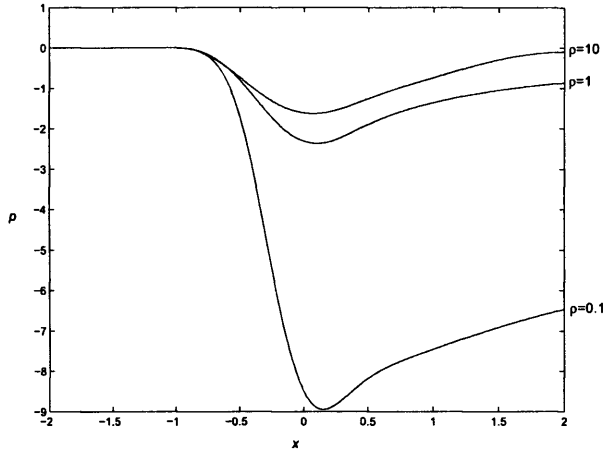

Figure 4.18: Pressure values for $h = 1$, $\rho = 0.1, 1$ and 10. Here $\mu = 1$.

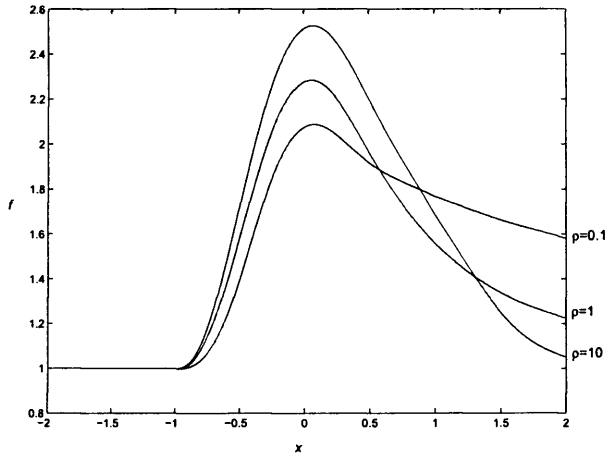

Figure 4.19: Interface position for $h = 1$ $\rho = 0.1, 1$ and 10. Here $\mu = 1$.

4.5 Flow into two large daughters

The flow to two daughters was investigated for a single fluid in [85]. Here we aim to tackle exactly the same problem, but applied to two fluids.

The branching starts at the position $x = 0$ say, to tie in with [85], and again the divider has shape $y = y_1 + \mathrm{Re}^{-1/3} f_1^{\pm}(x)$, with f_1 order-one throughout. Here we will consider a linear divider, hence $f_1^{\pm}(x) = \pm hx$, with $h \geq 0$ in this setting, starting at $x = 0$. In fact, due to symmetry we only will need to consider the part $f_1^{-}(x) = -hx$, as the flow is symmetric in the line $y_1 = 1$. As the divider begins in the core, the streamwise component of the oncoming flow is order-one typically, and so on the divider itself there is a Blasius boundary layer of thickness $\mathrm{Re}^{-1/2}$. This is safely ignored in this setting as it is small in comparison with the thicker $\mathrm{Re}^{-1/3}$ layer at the wall. As outlined earlier the flow to two symmetric daughters requires the solution of two problems: solution of the equations in the wall layer must be preceded by solution in the inviscid core, from which a slip velocity is calculated, that in effect drives the wall layer flow. This slip effect is discussed fully in [82] and results in an effective wall layer displacement at $O(\mathrm{Re}^{-1/3})$.

The slip velocity is defined by $u_W(x) = \partial\tilde{\psi}/\partial y|_{y=0}$ where $\tilde{\psi}$ represents the disturbance to the streamfunction. In general this slip velocity is non-zero even prior to any branching and so significant upstream influence is expected to occur here. In order to be able to tackle the wall layer problem we must first solve the core problem to find the at present unknown slip velocity $u_W(x)$.

4.5.1 The flow in the core

The core where glue only is present can be taken to be inviscid, as outlined earlier. The wall layer flow though provokes a perturbation to the initial Poiseuille flow of order of the thickness of the boundary layer, $O(\mathrm{Re}^{-1/3})$, and

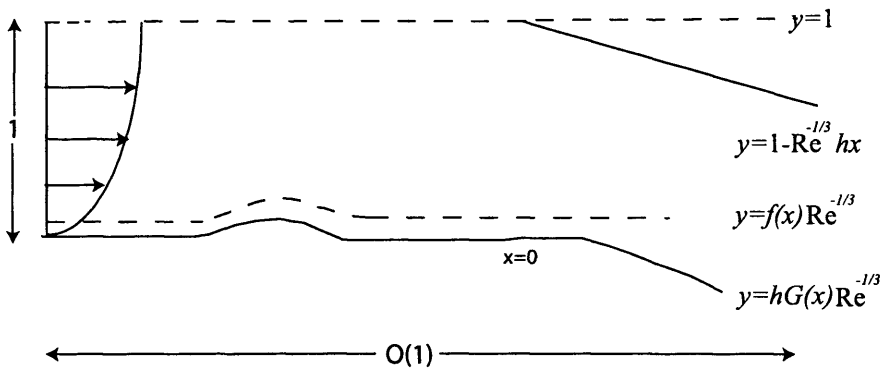

Figure 4.20: Flow to two large daughters, showing wall shape, interface and the thin divider. Symmetry in the line $y = 1$ is assumed throughout. The x-length scale under consideration here is order-one.

hence the relevant expansions with this disturbance are given as

$$\psi = \mu\psi_0(y) + \mathrm{Re}^{-1/3}\tilde{\psi}(x,y) + \cdots, \tag{4.71}$$

$$u = \mu u_0(y) + \mathrm{Re}^{-1/3}\tilde{u}(x,y) + \cdots, \tag{4.72}$$

$$v = \mathrm{Re}^{-1/3}\tilde{v}(x,y) + \cdots, \tag{4.73}$$

$$p = \mathrm{Re}^{-1/3}\tilde{p}(x,y) + \cdots. \tag{4.74}$$

Again all tilded variables are of order unity, as are x, y and μu_0 (the initial velocity far upstream). Substitution of these expressions into the governing Euler-equations yields at leading order

$$u_0\nabla^2\tilde{\psi} = u_0''\tilde{\psi}, \tag{4.75}$$

an equation independent of μ and in fact identical to that solved in [85]. This equation can be recast in terms of pressure as discussed in [85], however this equation is in terms of the derivative p_y rather than p as noted on page 6. The correct equation is solved for three dimensional flows later on in the paper. The boundary conditions here also are analogous to those in [85], the only change

being for the tangential flow condition on the divider, where the viscosity ratio μ now enters play. The full boundary conditions are

$$\tilde{\psi} = -\mu u_0(1) f^-(x) = \mu h x u_0(1) \quad \text{at } y = 1, x > 0, \tag{4.76}$$

$$\tilde{\psi} = 0 \quad \text{at } y = 1, x < 0, \tag{4.77}$$

$$\tilde{\psi} \to 0 \quad \text{as } x \to -\infty, \tag{4.78}$$

$$\tilde{\psi} = 0 \quad \text{at } y = 0; \tag{4.79}$$

with divider shape $f_1 = -hx$. The conditions are respectively for tangential flow on the divider, flow symmetry in the line $y = 1$, matching to the known unperturbed flow far upstream and the tangential flow condition on the lower wall. The condition for tangential flow on the divider is obtained by setting $\psi = 0$ at the divider $y = 1 + \mathrm{Re}^{-1/3} f^-(x)$ and equating terms at $O(\mathrm{Re}^{-1/3})$ after taking a Taylor expansion.

Similar analyses may be applied for more than one divider/daughter, n daughters say, where n is an order-one number and the divider shapes are of the form $y_n = 1 + \mathrm{Re}^{-1/3} f_n^{\pm}(x)$. In this case the boundary conditions remain the same and are supplemented by the tangential flow conditions on all dividers, given by $\tilde{\psi} = -\mu u_0(y_n) f_n^{\pm}(x)$ at $y = y_n$. However situations such as these, with flow to more than two daughters, are not studied in this work.

4.5.2 Solution of the core-flow problem

The initial velocity in the glue $\mu u_0(y)$ is taken to be $\mu y(1 - y/2)$, in line with (4.13) and with $\bar{h}$ small so that the velocity vanishes at the walls $y = 0$ and $y = 2$ and is symmetric about the centre of the channel $y = 1$ where $u_0(1) = 1/2$. The governing equation for the perturbed system (4.75) becomes of Helmholtz type

$$y(1 - y/2)\nabla^2 \tilde{\psi} = -\frac{1}{2}\tilde{\psi}. \tag{4.80}$$

The solution to equation (4.80) subject to the boundary conditions (4.76)-(4.79) can be written in closed form [94]. Here a complex variable method is used and the resulting solution is written in series form as

$$\bar{\psi}(x,y) = \begin{cases} \sum_1^\infty \sigma_n e^{\beta_n x} s_n(y) & \text{for} \quad x < 0, \\ hxu_0 + \sum_1^\infty \sigma_n e^{-\beta_n x} s_n(y) & \text{for} \quad x \geq 0. \end{cases} \tag{4.81}$$

with normalised eigenfunctions $s_n(y)$ and corresponding eigenvalues β_n. Here $s_n'(0) = 1$ and $s_n(1) = 0$, see also [13], [85]. The values for β_n found in [94] were found to be incorrect however and here we use the values calculated in [85], also values for σ are taken to be h times those of β. The first five values of β used here, are those calulated in [85] and are given by

$$(\beta_1, \cdots, \beta_5) = (2.5895, 5.9705, 9.1978, 12.33857, 15.5568), \tag{4.82}$$

$$(\sigma_1, \cdots, \sigma_5) = (0.3145, -0.1003, 0.06061, -0.04361, 0.03412). \tag{4.83}$$

By definition the slip velocity can be written down straight away from equation (4.81) as

$$u_W(x) = \begin{cases} \sum_1^\infty \sigma_n e^{\beta_n x} & \text{for} \quad x < 0, \\ hx + \sum_1^\infty \sigma_n e^{-\beta_n x} & \text{for} \quad x \geq 0. \end{cases} \tag{4.84}$$

We see from (4.84) that both u_W and its derivative are continuous at $x = 0$, and in fact it is these conditions that determine the β_n and σ_n. Results for the slip velocity with other incident profiles (those of shear and constant velocity) are given in [85]; the slip velocity found in both cases is very close to that for Poiseuille flow. We also note that far downstream we have that $u_W \sim x$ as $x \to \infty$. Figure 4.21 shows the slip velocity for various values of μ.

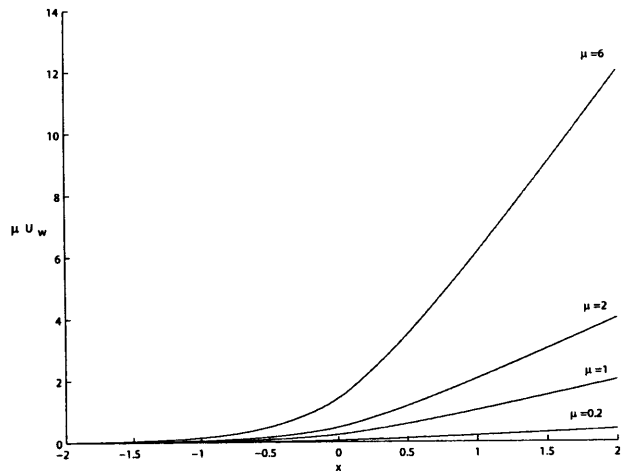

Figure 4.21: Slip velocity μu_W against x, for a range of μ.

4.5.3 Effect of the divider on the wall-layer equations

To include the divider in the numerical routine we must change the top condition in the glue. Indeed the matching of the wall layer flow and that of the core now requires the condition

$$u \sim \mu(Y - f_0) + f_0 + \mu u_W(x) \qquad \text{as } Y \to \infty, \tag{4.85}$$

where no Prandtl-shifts have been taken. Other governing equations remain the same as those for the wall layer roughness problem, i.e. equations (4.19)-(4.21c), (4.21e) and (4.21f), and the same transformed versions of these equations after the two Prandtl-shifts.

Now the slip velocity has been found it can be substituted into the matching condition. (4.85). After the two transformations (4.39) then becomes in this setting

$$U_1 \sim \mu\bar{Y} + \mu(1 - f_0) + \mu h G(x) + \mu\tilde{f}(x) + \mu u_W(x) \quad \text{as} \quad \bar{Y} \to \infty. \tag{4.86}$$

When the pressure is corrected, this equation must be substituted into the

momentum equation as discussed in section 4.4, hence we now have

$$(\mu\bar{Y}+\mu(1-f_0)+hG(x)+\tilde{f}(x)+\mu u_W(x))\mu(hG'(x)+\tilde{f}'(x)+u'_W(x))+V\mu = -\rho^{-1}q. \tag{4.87}$$

The derivative $u'_W(x)$ is calculated from equation (4.84). All the other governing equations remain the same though, equations (4.86) and (4.87) are the only changes needed for the whole numerical routine.

4.5.4 Results for divider and $G(x) = 0$.

In contrast to the flow over hump roughness, significant upstream influence is expected for the flow into two large daughters due to the slip velocity $u_W(x)$ being non-zero even prior to any branching which commences at $x = 0$. To reiterate points in the previous section the slip effect only enters play in the matching condition to the core flow and thus acts as an effective displacement function, given by $A(x)$ in triple deck theory [83].

Here we take the divider to be linear as outlined above and set the constant to 1, so the divider shape is

$$f^-(x) = -x. \tag{4.88}$$

Figures 4.22 to 4.24 show the shear, pressure and interface position for a thin linear divider with $h = 1$. As can be seen from the figures, the skin friction increases as the viscosity ratio is increased; this plot should be compared to the plot for the slip velocity, figure 4.21. The interface position is shown again for the values of μ being 0.1, 0.2, 1, 5. The larger the value of μ, the quicker the interface position approaches the wall, which of course is flat here. Running the program for larger values of x showed that the interface position approached the wall for all values of the viscosity ratio, so the glue takes up all of the daughter artery whatever the value of μ, but when μ is larger the daughter is filled more quickly. Pressures for the different cases are shown in figure 4.24,

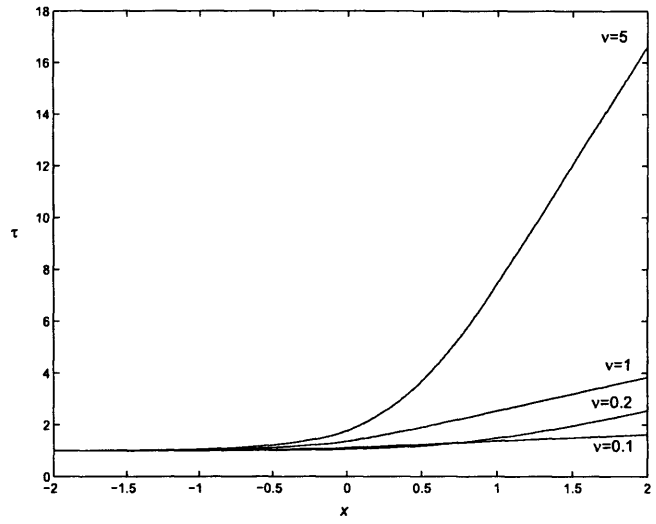

Figure 4.22: Wall shear for the flow into two daughters where the divider shape is given by $y = -x$. Plots for $\mu = \nu = 0.1, 0.2, 1$ and 5, $\rho = 1$.

with $\nu = 5$ having the largest negative pressure as expected from the other results. Section 5.5, in the next chapter deals with analysis far downstream.

4.5.5 Results for divider and $G(x) \neq 0$.

Taking the same wall shape as in equation (4.69), with $h = 1$ and keeping the divider of the same form as the previous section, we now solve the problem with both of these features incorporated. As can be seen from the figures, the results here are quite different from the other problems studied. Upstream influence for the flow is clearly seen in the plot for the interface position and is more noticeable for larger values of μ due to the increased slip velocity in this case. The larger values of μ also produce the larger values of the wall shear far downstream.

In the next chapter we consider the problems of flow over a roughness and to two large daughters, but now using an asymptotic approach.

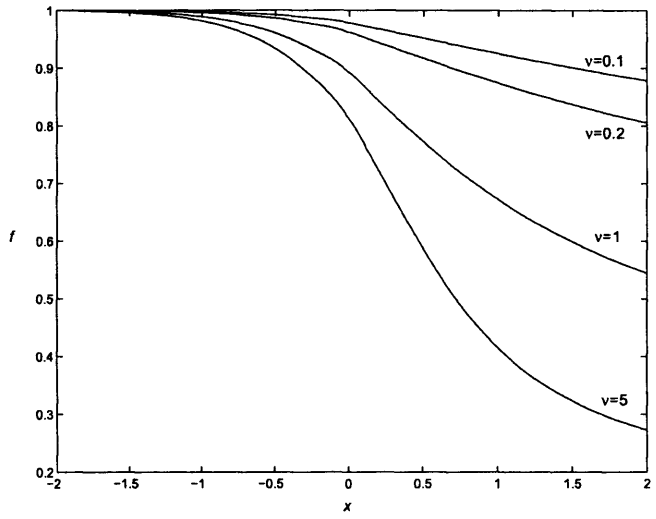

Figure 4.23: Interface position for the flow into two daughters where the divider shape is given by $y = -x$. Plots for $\mu = \nu = 0.1, 0.2, 1$ and 5, $\rho = 1$.

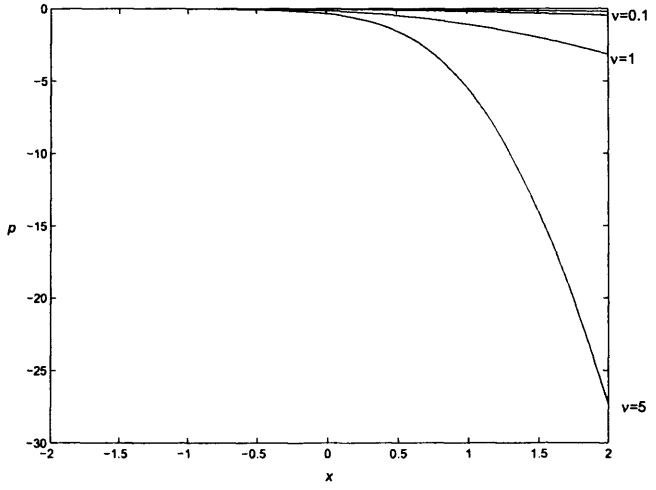

Figure 4.24: Pressure values for the flow into two daughters where the divider shape is given by $y = -x$. Plots for $\mu = \nu = 0.1, 0.2, 1$ and 5, $\rho = 1$.

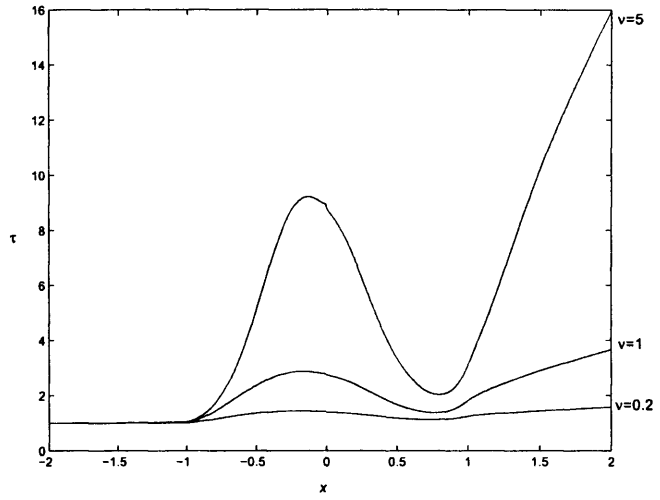

Figure 4.25: Wall shear for flow over roughness and to two daughters. Here the roughness shape is $G(x) = (1 - x^2)^2$ and the divider shape $y = -x$.

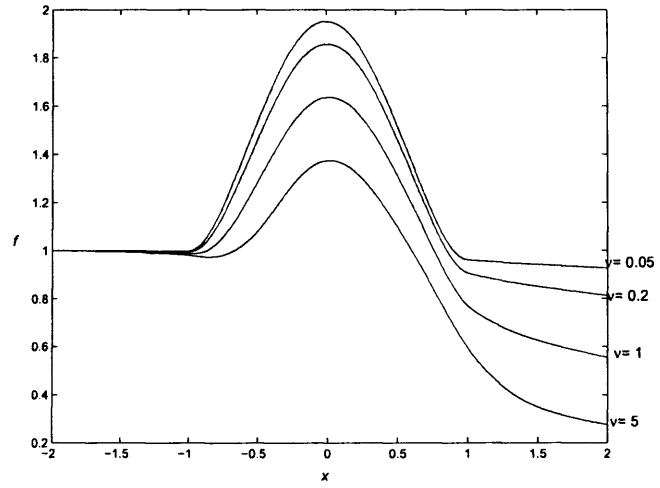

Figure 4.26: Interface position for flow over roughness and to two daughters. Here the roughness shape is $G(x) = (1 - x^2)^2$ and the divider shape $y = -x$.

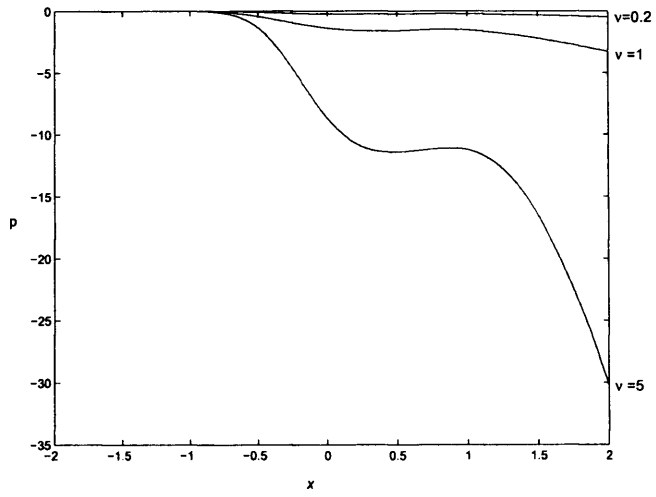

Figure 4.27: Pressure values for flow over roughness and to two daughters. Here the roughness shape is $G(x) = (1 - x^2)^2$ and the divider shape $y = -x$.

Chapter 5

Analytical properties of the wall layer equations

5.1 Equivalent governing equations

For convenience we study the wall layer problem analytically with the factors ν and ρ appearing in the blood momentum equations rather than the factors ρ^{-1} and ν^{-1} appearing in those of the glue in the system of equations (4.19), (4.20). The two systems are equivalent, although non-dimensionalising on blood quantities, as outlined earlier, seems to make more sense physically as the blood density and viscosity will always remain effectively constant.

The relationship between the two systems is

$$[U, V, Y, P, x] = \left[\left(\frac{\nu_1}{\nu_2}\right)^{1/2} u_N, \left(\frac{\nu_1}{\nu_2}\right)^{1/2} v_N, \left(\frac{\nu_1}{\nu_2}\right)^{1/2} Y_N, \left(\frac{\mu_1}{\mu_2}\right)^{1/2} p_N, \left(\frac{\nu_1}{\nu_2}\right)^{1/2} x_N\right], \tag{5.1}$$

in each fluid; then this leaves the momentum equations of the same form, but

now the factors of ρ and μ appear in the blood equations

$$\frac{\partial u_1}{\partial x}+\frac{\partial v_1}{\partial Y} = 0, \quad u_1\frac{\partial u_1}{\partial x}+v_1\frac{\partial u_1}{\partial Y} = -\frac{dp}{dx}+\frac{\partial^2 u_1}{\partial Y^2}, \tag{5.2a}$$

$$\frac{\partial u_2}{\partial x}+\frac{\partial v_2}{\partial Y} = 0, \quad u_2\frac{\partial u_2}{\partial x}+v_2\frac{\partial u_2}{\partial Y} = -\left(\frac{\rho_1}{\rho_2}\right)\frac{dp}{dx}+\left(\frac{\nu_2}{\nu_1}\right)\frac{\partial^2 u_2}{\partial Y^2}, \tag{5.2b}$$

where the subscripts N have been dropped for convenience. This also leaves the boundary conditions in the same form; to repeat they are

$$u_2 = 0 \quad \text{at} \quad Y = hG(x), \tag{5.2c}$$

$$v_2 = 0 \quad \text{at} \quad Y = hG(x), \tag{5.2d}$$

$$u_1 \sim \mu Y + f_0(1-\mu) \quad \text{as} \quad Y \to \infty, \tag{5.2e}$$

$$(u_1, v_1, p) \to (\mu(Y-f_0)+f_0, 0, 0) \quad \text{as} \quad x \to -\infty, \tag{5.2f}$$

$$(u_2, v_2, p) \to (Y, 0, 0) \quad \text{as} \quad x \to -\infty. \tag{5.2g}$$

This system will be known from now on as system (2) whereas the system which was based on non-dimensionalising on blood quantities is denoted system (1). The subsequent analysis will be undertaken using system (2), after we verify next that systems (1) and (2) give the same results using the numerical method.

Verification of numerical results using systems (1) and (2)

Both systems were tested numerically and were found to give identical computational results, namely those given in chapter 4. In the present chapter we perform the analysis with system (2), i.e. with equations (5.2a) and (5.2b) and boundary conditions (5.2c)-(5.2g), and interface condition (4.21a). Similar analysis would of course be applicable to system (1) with the appropriate transformation of the variables.

5.2 Linearised solution

The analysis in this section is based on the quantity h multiplying the wall shape $G(x)$ being assumed to be small. We suppose that the incident solution suffers a slight perturbation. The following expansions are posed

$$(u_1, v_1, p_1) = \left(\frac{\mu_2}{\mu_1}(Y - f_0) + f_0, 0, 0\right) + h(\overline{u}_1, \overline{v}_1, \overline{p}_1) + O(h^2), \quad (5.3)$$

$$(u_2, v_2, p_2) = (Y, 0, 0) + h(\overline{u}_2, \overline{v}_2, \overline{p}_2) + O(h^2), \quad (5.4)$$

in the glue and the blood respectively. Now substituting these quantities into the boundary conditions and equating at $O(h)$ we find that the linearised form of these equations are

$$\overline{u}_2 = -G(x) \quad \text{at } Y = 0, \quad (5.5)$$

$$\overline{v}_2 = 0 \quad \text{at } Y = 0, \quad (5.6)$$

$$\overline{v}_1 = \overline{v}_2 = f_0(f_1)_x \quad \text{at } Y = f_0, \quad (5.7)$$

$$\overline{u}_1 = \overline{u}_2 + f_1\left(1 - \frac{\mu_2}{\mu_1}\right) \quad \text{at } Y = f_0, \quad (5.8)$$

$$\overline{u}_{1y} = \mu\overline{u}_{2y} \quad \text{at } Y = f_0, \quad (5.9)$$

$$\overline{u}_1 \to 0 \quad \text{as } Y \to \infty, \quad (5.10)$$

where the interface is now given by $Y = f_0 + f_1 h + O(h^2)$ and the wall shape is expanded as $Y = hG(x) + O(h^2)$ with f_0 and $G(x)$ both of order unity. Now substituting the expansions (5.3) and (5.4) into the momentum equations gives the linearised equations at order h, in the glue and the blood respectively, as

$$\frac{\partial\overline{u}_1}{\partial x} + \frac{\partial\overline{v}_1}{\partial Y} = 0, \qquad (Y - \alpha)\frac{\partial\overline{u}_1}{\partial x} + \overline{v}_1 = \left(\frac{\mu_1}{\mu_2}\right)\left[-\frac{d\overline{p}}{dx} + \frac{\partial^2\overline{u}_1}{\partial Y^2}\right], \quad (5.11)$$

$$\frac{\partial\overline{u}_2}{\partial x} + \frac{\partial\overline{v}_2}{\partial Y} = 0, \qquad Y\frac{\partial\overline{u}_2}{\partial x} + \overline{v}_2 = -\left(\frac{\rho_1}{\rho_2}\right)\frac{d\overline{p}}{dx} + \left(\frac{\nu_2}{\nu_1}\right)\frac{\partial^2\overline{u}_2}{\partial Y^2}, \quad (5.12)$$

where the constant $\alpha = f_0\left(1 - \frac{\mu_1}{\mu_2}\right)$. Netx taking the Fourier transform of each equation, we obtain the transformed equations in the glue and the blood

$$i\omega\overline{u}_1^* + \frac{\partial\overline{v}_1}{\partial Y}^* = 0, \qquad i\omega(Y - \alpha)\overline{u}_1^* + \overline{v}_1^* = -i\omega\left(\frac{\mu_1}{\mu_2}\right)\overline{p}^* + \left(\frac{\mu_1}{\mu_2}\right)\frac{\partial^2\overline{u}_1}{\partial Y^2}^*, \quad (5.13)$$

$$i\omega\overline{u}_2^* + \frac{\partial \overline{v_2}}{\partial Y}^* = 0, \qquad i\omega Y\overline{u}_2^* + \overline{v}_2{}^* = -i\omega\left(\frac{\rho_1}{\rho_2}\right)\overline{p}^* + \left(\frac{\nu_2}{\nu_1}\right)\frac{\partial^2\overline{u}_2}{\partial Y^2}^*. \quad (5.14)$$

The two transformed equations in each fluid can now be combined to eliminate $\overline{v}_i{}^*$ and the pressure term $\overline{p}^*$ to obtain an equation for the transformed tangential velocity perturbation in both of the fluids. If we differentiate the transformed momentum equations with respect to Y and combine with the associated continuity equation we obtain a single equation in the glue and the blood, respectively given by

$$i\omega\frac{\partial\overline{u}_1}{\partial Y}^*[Y-\alpha] = \left(\frac{\mu_1}{\mu_2}\right)\frac{\partial^3\overline{u}_1}{dY^3}^*, \quad (5.15)$$

$$i\omega Y\frac{\partial\overline{u}_2}{\partial Y}^* = \left(\frac{\nu_2}{\nu_1}\right)\frac{\partial^3\overline{u}_2}{dY^3}^*. \quad (5.16)$$

Equations (5.15) and (5.16) are essentially Airy's equation for $\partial\overline{u}^*/dY$. The solutions are given by,

$$\frac{\partial\overline{u}_1}{\partial Z}^* = C(\omega)\mathrm{Ai}\left[\left(\frac{i\omega\mu_2}{\mu_1}\right)^{1/3}Z\right], \quad (5.17)$$

$$\frac{\partial\overline{u}_2}{\partial Y}^* = A(\omega)\mathrm{Ai}\left[\left(\frac{i\omega\nu_1}{\nu_2}\right)^{1/3}Y\right] + B(\omega)\mathrm{Bi}\left[\left(\frac{i\omega\nu_1}{\nu_2}\right)^{1/3}Y\right], \quad (5.18)$$

in the glue and the blood. Here we have made use of the origin shift $Z = Y - \alpha$ and both $\left(\frac{i\omega\nu_1}{\nu_2}\right)^{1/3}$ and $\left(\frac{i\omega\mu_2}{\mu_1}\right)^{1/3}$ have a branch cut along the positive imaginary axis.

5.2.1 Analysis of equations

We would like to be able to determine the functions $A(\omega)$, $B(\omega)$ and $C(\omega)$ in order to obtain an explicit solution to equations (5.17) and (5.18). Integrating (5.17) we find

$$\overline{u_1}^*|_{Y=f_0} = -\int_{f_0-\alpha}^{\infty} C\mathrm{Ai}\left[\left(\frac{i\omega\mu_2}{\mu_1}\right)^{1/3}Z\right]dZ. \quad (5.19)$$

Now integrating (5.18) in the blood from the wall to the interface and using boundary condition (5.5) we have

$$\overline{u_2}^*|_{Y=f_0} = \int_0^{f_0} \left(A\mathrm{Ai}\left[\left(\frac{i\omega\nu_1}{\nu_2}\right)^{1/3} Y\right] + B\mathrm{Bi}\left[\left(\frac{i\omega\nu_1}{\nu_2}\right)^{1/3} Y\right]\right) dY - G^*(\omega). \tag{5.20}$$

Using equations (5.13) and (5.14) as well as the boundary conditions (5.5)-(5.9) we can determine A, B and C. However these equations are also in terms of both the pressure perturbation and the the wall shape perturbation f_1^*, both of which are unknown so there are in fact five unknowns, if we assume that the wall shape transform G^* is given. Thus we will need five equations in order to determine $A(\omega)$, $B(\omega)$, $C(\omega)$, $\overline{p}^*$ and f_1^*. Applying a suitable change of variables

$$\xi = (\mu i\omega)^{1/3}, (Y-\alpha) \quad \eta = \left(\frac{i\omega}{\nu}\right)^{1/3} Y,$$

to simplify the subsequent analysis, we now find five equations for the five unknowns in the system A,B and C as well as $\overline{p}^*$ and f_1^*. These are given by

$$C\mathrm{Ai}(\xi_0) = \mu(A\mathrm{Ai}(\eta_0) + B\mathrm{Bi}(\eta_0)), \tag{5.21}$$

$$\rho i\omega\overline{p}^* = \nu\left(\frac{i\omega}{\nu}\right)^{1/3} \{A\mathrm{Ai}'(0) + B\mathrm{Bi}'(0)\}, \tag{5.22}$$

$$(1-\rho)i\omega\overline{p}^* = (\mu i\omega)^{1/3} C\mathrm{Ai}'(\xi_0) - \nu\left(\frac{i\omega}{\nu}\right)^{1/3} \{A\mathrm{Ai}'(\eta_0) + B\mathrm{Bi}'(\eta_0)\}, \tag{5.23}$$

$$\begin{aligned} f_0 i\omega &\left\{ f_1^* - G^* + \int_0^{\eta_0} [A\mathrm{Ai}(\eta) + B\mathrm{Bi}(\eta)] d\eta \left(\frac{i\omega}{\nu}\right)^{-1/3} \right\} \\ &= -\rho i\omega\overline{p}^* + \left(\frac{i\omega}{\nu}\right)^{1/3} \nu \left(A\mathrm{Ai}'(\eta_0) + B\mathrm{Bi}'(\eta_0)\right), \end{aligned} \tag{5.24}$$

$$G^* - (1-\mu) f_1^* = \int_0^{\eta_0} [A\mathrm{Ai}(\eta) + B\mathrm{Bi}(\eta)] d\eta \left(\frac{i\omega}{\nu}\right)^{-1/3} + C\int_{\xi_0}^{\infty} \mathrm{Ai}(\xi)(\mu i\omega)^{-1/3} d\xi, \tag{5.25}$$

where

$$\xi_0 = \frac{(\mu i\omega)^{1/3}}{\mu} f_0, \quad \eta_0 = \left(\frac{i\omega}{\nu}\right)^{1/3} f_0, \quad \rho = \rho_1/\rho_2, \quad \nu = \nu_2/\nu_1, \quad \mu = \mu_2/\mu_1. \tag{5.26}$$

These equations follow respectively from the stress condition (5.9), the momentum equation in the blood (5.13) evaluated at $Y = 0$, the difference of the two momentum equations (5.13), (5.14), the momentum equation in the blood (5.14) and the continuity of tangential velocities at the interface (5.8). Expressions for the unknowns would undoubtedly be long and cumbersome involving integrals which can only be integrated numerically and so they were not evaluated at this stage.

We will now look at the case where the viscosity of the glue is much larger then that of the blood. This should simplify the equations of motion considerably and allow the quantities $A(\omega)$, $B(\omega)$ and $C(\omega)$ to be determined numerically.

5.2.2 Numerical investigation

To transform the problem into real variables we make the substitution $\kappa = i\omega = 1$ and we take $\rho = 1$ to start with. The undisturbed interface position f_0 is taken to be 1, as is the transformed wall shape G^* in this simplified situation. The solution to equations (5.21) to (5.25) was obtained using a direct matrix inversion for different values of μ. However, care must be taken when dealing with the Airy functions, indeed here we favour the asymptotic representations for these functions as given in [7] rather than the computational value for values of very small μ. Table 5.1 shows the results for A, B, C, $\overline{p}^*$ and f_1^* for various values of μ. It can clearly be seen that the solution is converging to the solution

$$f_1^* \to 1 = G^*, \qquad A, B, \overline{p}^* \to 0, \tag{5.27}$$

μ	A	B	C	$\overline{p}^*$	f_1^*
0.5	2.4069	0.0359	2.2825	-0.3823	0.6785
0.1	1.5314	0.00064	28.0301	-0.0848	0.8420
0.05	1.2278	0.0011	41.5901	-0.0431	0.8911
0.01	1.0e-27	1.0e-29	-389.05	-0.0000	1.0000

Table 5.1: Table showing the numerical solution to the linearised wall layer problem. The solution is approaching $A, B, \overline{p}^* \to 0$, $f_1^* \to 1$ as $\mu \to 0$.

as $\mu \to 0$. Although the values for C are still large, numerical integration of equation (5.17) shows that $\overline{u}_1^*$ approaches zero for all values of Z as $\mu \to 0$. Values for $\overline{u}_1^*$ are shown in table 5.2 for a range of values of μ. Calculations with other values of ρ and κ confirmed these trends.

So taking $f_1 = G$ leaves the boundary conditions in the form

$$\begin{aligned} \overline{u}_2 &= -G \quad \text{at } Y = 0, \\ \overline{u}_2 &= -G. \quad \text{at } Y = f_0. \end{aligned}$$

So a simple solution in the blood is now

$$\overline{u}_2 = -G, \tag{5.28}$$

$$\overline{v}_2 = YG'. \tag{5.29}$$

In full, the linearised small μ solution is given by

$$u_1 = \mu(Y - f_0) + f_0 + O(h^2), \tag{5.30a}$$

$$v_1 = hf_o(f_1)_x + O(h^2), \tag{5.30b}$$

$$u_2 = Y - hG + O(h^2), \tag{5.30c}$$

$$v_2 = hYG' + O(h^2), \tag{5.30d}$$

$$p = \mu f_0 f_1 + O(h^2), \tag{5.30e}$$

$$f = f_0 + hG + O(h^2). \tag{5.30f}$$

Z	$\mu = 0.1$	$\mu = 0.05$	$\mu = 0.02$
10	0.0022	-	-
20	5.0e-11	1.0e-16	-
50	2.3e-14	1.2e-18	1.3e-12
100	3.0e-18	0	1.0e-18
150	0	0	0

Table 5.2: Table showing the values for $\overline{u}_1^*$, for the values $\mu = 0.1, 0.05, 0.02$ at different values of Z. These are calculated by numerical integration of equation (5.17).

So in this very simplistic setting, the interface just rides up and over the wall shape, with the exact shape of the wall shape and remains a constant distance f_0 away from it.

So based on a linearised analysis on $h \ll 1$ a relatively simple solution was found for the case $\mu \ll 1$. Now we turn attention to the fully non-linear analysis where asymptotic expansions for the flow variables are posed in each of the two fluids and where we still insist $\mu \ll 1$. It is hoped that this will give meaningful insight into the solution in this limit.

5.3 Asymptotic expansions in the general regime for the case $\mu_1 \gg \mu_2$

When the viscosity of the glue is much greater than that of the blood, the ratio μ becomes small, as was studied in the previous section. Hence we can construct a perturbation series using this small parameter and investigate the flow dynamics in this case. In this section we tackle the general system, equations (5.2a)-(5.2g) in this limit.

We take a large streamwise length scale with $x \sim 1/\mu$ in both fluids. The transverse scaling in each fluid will be different however, due to the ν factor multiplying the diffusive term in the blood equations and its balance with the advective term, i.e. $uu_x \sim \nu u_{YY}$. If we take a thin layer in the blood, specifically $Y \sim \mu^{-1/2}$, with $u_1 \sim 1$, the subsequent scalings are then fixed as

$$u_1 \sim 1, \tag{5.31}$$

$$v_1 \sim \mu^{1/2}, \tag{5.32}$$

$$p \sim 1. \tag{5.33}$$

If we again fix the streamwise velocity component in the blood to be order-one, we find $Y \sim 1$ and the velocity and pressure components are scaled as

$$u_2 \sim 1, \tag{5.34}$$

$$v_2 \sim \mu, \tag{5.35}$$

$$p \sim 1, \tag{5.36}$$

from the continuity and momentum balance. Hence considering the second and third order corrections also, we impose the following expansions in the glue

$$u_1 = \overline{u}_1 + \mu^{1/2}\overline{\overline{u}}_1 + \mu\overline{\overline{\overline{u}}}_1 + \cdots, \tag{5.37}$$

$$v_1 = \mu^{1/2}\overline{v}_1 + \mu\overline{\overline{v}}_1 + \mu^{3/2}\overline{\overline{\overline{v}}}_1 + \cdots, \tag{5.38}$$

$$p = \overline{p}_1 + \mu^{1/2}\overline{\overline{p}}_1 + \mu\overline{\overline{\overline{p}}}_1 + \cdots, \tag{5.39}$$

with $Y = \overline{Y}\mu^{-1/2}$ and $x = \mu^{-1}\overline{x}$. The expansions in the blood take the form

$$u_2 = \overline{u}_2 + \mu^{1/2}\overline{\overline{u}}_2 + \mu\overline{\overline{\overline{u}}}_2 + \cdots, \tag{5.40}$$

$$v_2 = \mu\overline{v}_2 + \mu^{3/2}\overline{\overline{v}}_2 + \mu^2\overline{\overline{\overline{v}}}_2 \cdots, \tag{5.41}$$

with p being expanded exactly as above, and we still have $x = \mu^{-1}\overline{x}$, but we examine a thicker layer, $Y \sim 1$ here. The interface $Y = f(x)$ is expanded as

$$f = \overline{f} + \mu^{1/2}\overline{\overline{f}} + \mu\overline{\overline{\overline{f}}} + \cdots. \tag{5.42}$$

The expressions are substituted into the equations of continuity and momentum above and solutions at successive orders of the perturbation parameter are found. Once these are found they are substituted back into the expansion and we go on to solve for the next order terms and so on. Applying this procedure twice leads to the following refined expressions for the velocities and pressure in the glue,[1]

$$u_1 = f_0 + \mu^{1/2}\overline{Y} + \mu\overline{u}_1 + \cdots, \tag{5.43}$$

$$v_1 = \mu f_0 \overline{f}' + \mu^{3/2}\overline{v}_1 + \cdots, \tag{5.44}$$

$$p = \mu\overline{p}_1 + \cdots, \tag{5.45}$$

where the undisturbed interface position can now be written as $f_0 = \overline{f} - G$. Hence the leading order contribution to the interface position in equation (5.42) is $\overline{f} = f_0 + G$. Both the solutions at $O(\mu^{1/2})$ and $O(\mu)$ satisfy all the relevant transformed boundary conditions given earlier. The same process is applied in order to find the expansions in the blood. After two such successive calculations we obtain the following asymptotic form for the two velocity components in the blood as

$$u_2 = (Y - G) + \mu\overline{u}_2 + \cdots, \tag{5.46}$$

$$v_2 = \mu G'(Y - G) + \mu^2\overline{v}_2 + \cdots, \tag{5.47}$$

$$f = (f_0 + G) + \mu\overline{\overline{f}} + \cdots. \tag{5.48}$$

We now go on to determine the next order terms in the expansions, $\overline{u}_1, \overline{v}_1, \overline{u}_2, \overline{v}_2$. Substituting expressions (5.43)-(5.45) into the governing equations in the glue gives

$$\frac{\partial\overline{u}_1}{\partial\overline{x}} + \frac{\partial\overline{v}_1}{\partial\overline{Y}} = 0, \tag{5.49}$$

$$f_0\frac{\partial\overline{u}_1}{\partial\overline{x}} + f_0\frac{\partial\overline{f}}{\partial\overline{x}} = -\frac{d\overline{p}}{d\overline{x}} + \frac{\partial^2\overline{u}_1}{\partial\overline{Y}^2}. \tag{5.50}$$

[1]Here the triple bar has been replaced by single bar for convenience and is dropped on blood quantities from (5.46) onwards.

Here the boundary conditions are

$$\overline{u}_1 \rightarrow -f_0 \quad \text{as} \quad \overline{Y} \rightarrow \infty, \tag{5.51}$$

$$\overline{u}_1 \rightarrow \tilde{u}_2(\overline{x}) + \overline{\overline{\overline{f}}} \quad \text{as} \quad \overline{Y} \rightarrow 0+, \tag{5.52}$$

$$\overline{u}_1 \rightarrow -f_0 \quad \text{as} \quad \overline{x} \rightarrow -\infty, \tag{5.53}$$

$$\overline{v}_1 \rightarrow 0 \quad \text{as} \quad \overline{Y} \rightarrow 0+, \tag{5.54}$$

$$\frac{\partial \overline{u}_1}{\partial \overline{Y}} \rightarrow 0 \quad \text{as} \quad \overline{Y} \rightarrow 0+. \tag{5.55}$$

At the interface we have $\overline{Y} = \mu^{1/2}(\overline{f} + \cdots)$, so as $\mu \ll 1$ the interfacial conditions are now given by $\overline{Y} \rightarrow 0+$. These equations follow from the matching with the core flow solution, continuity of tangential velocity at the interface, matching with the incident solution, the kinematic condition at the interface and the shear condition at the interface. Using equation (5.50) and letting $\overline{Y} \rightarrow \infty$, we find the pressure is of the form

$$\overline{p} = -f_0\overline{f} + c, \tag{5.56}$$

where the constant c is determined to be f_0^2, so that the pressure vanishes far upstream and indeed far downstream. The relatively simple solution at this order in the glue is given by

$$\overline{u}_1 = -f_0, \qquad \overline{v}_1 = 0, \qquad \overline{p} = -f_0 G. \tag{5.57}$$

This solution effectively sets the top boundary condition for the blood equations. Indeed from equation (5.52), the interfacial blood velocity is given by

$$\tilde{u}_2(\overline{x}) = -f_0 - \overline{\overline{\overline{f}}}. \tag{5.58}$$

The blood equations obtained by substituting these expressions in the thin-layer equations and equating at $O(\mu^2)$ are

$$(Y-G)\frac{\partial \overline{u}_2}{\partial \overline{x}} + G'\left((Y-G)\frac{\partial \overline{u}_2}{\partial Y} - \overline{u}_2\right) + \overline{v_2} = -\rho\frac{d\overline{p}}{d\overline{x}} + \frac{\nu}{\mu}\frac{\partial^2 \overline{u}_2}{\partial Y^2}, \tag{5.59}$$

$$\frac{\partial \overline{u}_2}{\partial \overline{x}} + \frac{\partial \overline{v}_2}{\partial Y} = 0, \tag{5.60}$$

where the factor $\nu/\mu = \rho$ is of order-one. The boundary and interface conditions are given by

$$\overline{u}_2 = 0 \quad \text{at} \quad Y = G(\overline{x}), \tag{5.61}$$

$$\overline{v}_2 = 0 \quad \text{at} \quad Y = G(\overline{x}), \tag{5.62}$$

$$\overline{u}_2 = \tilde{u}_2(\overline{x}) \quad \text{at} \quad Y = \overline{f}(\overline{x}), \tag{5.63}$$

$$\overline{v}_2 = \tilde{u}_2(\overline{x})G'(\overline{x}) + f_0\overline{\overline{\overline{f}}}' \quad \text{at} \quad Y = \overline{f}(\overline{x}), \tag{5.64}$$

$$\frac{\partial \overline{u}_2}{\partial Y} = 0 \quad \text{at} \quad Y = \overline{f}(\overline{x}), \tag{5.65}$$

which again are the conditions of no slip on the solid surface, continuity of tangential velocity, the kinematic condition and the tangential stress condition at the interface. Hence equation (5.64) can be written in the form

$$\overline{v}_2 = (-f_0 - \overline{\overline{\overline{f}}})G'(\overline{x}) + f_0\overline{\overline{\overline{f}}}' \quad \text{at} \quad Y = \overline{f}\,(\overline{x}), \tag{5.66}$$

using equation (5.58). The relatively simple solution to the glue equations (5.57) sets the pressure, which is of course the same in both fluids. The blood equations do not have such a straightforward solution, but by making a suitable transformation of variables we can transform equations (5.59) and (5.60) to a convenient linear form. We would like to determine the induced pressure along with the skin friction on the hump surface for the small μ case and find out if any separation occurs for the case $G \sim 1$, given that equation (5.46) already shows that the skin friction is a small perturbation from the incident value which is μ_2.

5.3.1 Solution of the blood problem

In order to make progress with the blood equations we make use of a Prandtl-shift, setting

$$\hat{Y} = Y - G(\hat{x}), \qquad \overline{x} = \hat{x}. \tag{5.67}$$

So again $\partial_{\overline{x}} \rightarrow \partial_{\hat{x}} - G'(\hat{x})\partial_{\hat{Y}}$ and $\partial_Y \rightarrow \partial_{\hat{Y}}$. The equations of motion (5.59) and (5.60) then take the linearised form

$$\hat{Y}\frac{\partial \overline{u}_2}{\partial \hat{x}} + \hat{v}_2 = -\rho\frac{d\overline{p}}{d\hat{x}} + \rho\frac{\partial^2 \overline{u}_2}{\partial \hat{Y}^2}, \tag{5.68}$$

$$\frac{\partial \overline{u}_2}{\partial \hat{x}} + \frac{\partial \hat{v}_2}{\partial \hat{Y}} = 0, \tag{5.69}$$

where $\hat{v}_2 = \overline{v}_2 - \overline{u}_2 G'(\hat{x})$, and in this notation $\nu/\mu = \rho$. The boundary conditions in the new coordinates are

$$\overline{u}_2 = 0 \quad \text{at} \quad \hat{Y} = 0, \tag{5.70}$$

$$\hat{v}_2 = -f_0\overline{\overline{f}}' \quad \text{at} \quad \hat{Y} = f_0, \tag{5.71}$$

$$\frac{\partial \overline{u}_2}{\partial \hat{Y}} = 0 \quad \text{at } \hat{Y} = f_0, \tag{5.72}$$

and here $\overline{p} = -f_0(\overline{f} - f_0) = -f_0 G$.

Taking Fourier transforms of (5.68) and (5.69) and combining by differentiating with respect to $\hat{Y}$ gives

$$\frac{\partial \overline{u}_2}{\partial \hat{Y}}^* = K(\omega)\mathrm{Ai}[(iw/\rho)^{1/3}\hat{Y}] + L(\omega)\mathrm{Bi}[(iw/\rho)^{1/3}\hat{Y}], \tag{5.73}$$

where * denotes Fourier transform as defined earlier and $(i\omega/\rho)^{1/3}$ has a branch cut along the positive imaginary axis. The boundary conditions for the problem are exactly those in (5.70)-(5.72) but with variables suitably transformed. Evaluating equation (5.73) at $\hat{Y} = f_0$ along with the transformed version of equation (5.72) leads to

$$K(\omega)\mathrm{Ai}[(iw/\rho)^{1/3}f_0] + L(\omega)\mathrm{Bi}[(iw/\rho)^{1/3}f_0] = 0, \tag{5.74}$$

and evaluating the transformed version of equation (5.68) at $\hat{Y} = 0$ gives

$$\left(\frac{i\omega}{\rho}\right)^{1/3}[K(\omega)\mathrm{Ai}'(0) + L(\omega)\mathrm{Bi}'(0)] = -i\omega f_0 G^*. \tag{5.75}$$

Hence $L(\omega)$ and $K(\omega)$ may be found and so an expression for the transformed wall shear is

$$\overline{\tau}_W^* = \mu_2 \frac{-i\omega f_0 G^*[\mathrm{Bi}(0) - \theta\mathrm{Ai}(0)]}{(i\omega/\rho)^{1/3}[\mathrm{Bi}'(0) - \theta\mathrm{Ai}'(0)]}, \tag{5.76}$$

where $\theta = \mathrm{Bi}(\chi)/\mathrm{Ai}(\chi)$ and $\chi = (i\omega/\rho)^{1/3} f_0$. After some manipulation of the Airy functions, the ratio θ can be expressed as

$$\theta = \frac{1}{\pi}\left[\int_0^{\chi} \frac{dx}{\mathrm{Ai}^2(x)}\right] + \sqrt{3}. \tag{5.77}$$

Hence we arrive at the expression for the perturbation to the shear stress as

$$\bar{\tau}_W(x) = \frac{\mu_2}{2\pi}\int_{-\infty}^{\infty} \frac{-i\omega f_0 G^*[\mathrm{Bi}(0) - \theta\mathrm{Ai}(0)]}{(i\omega/\rho)^{1/3}[\mathrm{Bi}'(0) - \theta\mathrm{Ai}'(0)]} e^{i\omega x} d\omega. \tag{5.78}$$

No attempt was made to evaluate this integral in general, but when small values of ω, corresponding to large values of x are considered, the integrand is much simpler to deal with. Indeed for small ω or small χ we find

$$\frac{\mathrm{Bi}(0) - \theta\mathrm{Ai}(0)}{\mathrm{Bi}'(0) - \theta\mathrm{Ai}'(0)} \sim -\chi + C_4\chi^4 + C_7\chi^7 + \cdots, \tag{5.79}$$

for $\chi \to 0$. Here the terms χ^2 and χ^3 do not appear in the expansions as the constants multiplying them vanish. For instance, the constant multiplying χ^2 is

$$C_2 = \frac{\mathrm{Ai}''(0)\mathrm{Bi}(0) - \mathrm{Ai}(0)\mathrm{Bi}''(0)}{\mathrm{Ai}(0)\mathrm{Bi}'(0) - \mathrm{Ai}'(0)\mathrm{Bi}(0)} = 0. \tag{5.80}$$

as the values $\mathrm{Ai}''(0)=\mathrm{Bi}''(0) = 0$, from Airy's equation. Similarly the constants C_3, C_5 and C_6 vanish and the only constants that do not vanish are those of the form $3n + 1$, where $n \in \mathbb{Z}$.

So in this setting an approximation to the wall shear perturbation is given by

$$\bar{\tau}_W(x) = \frac{\mu_2 i f_0^2}{2\pi}\int_{-\infty}^{\infty} \omega G^*(\omega) e^{i\omega x} d\omega - \frac{\mu_2 C_4 f_0^5}{2\pi\rho}\int_{-\infty}^{\infty} (i\omega)^2 G^*(\omega) e^{i\omega x} d\omega + \cdots. \tag{5.81}$$

The first of the integrals in equation (5.81) is just the derivative of the wall shape, which is of course zero as $x \to \infty$, and hence can safely be ignored. The next order contribution is just the second derivative and taking the next term would give the third derivative of the wall shape and so on, which are all

of course zero when $x > 1$. Hence for large x it seems that there is virtually no contribution at this order, as is shown in figure 5.4.

If the integral (5.78) is considered, a branch cut is needed along the positive imaginary axis, as shown in figure 5.1. By examining equation (5.78) we would like to determine whether or not the integrand has any poles, to look for any downstream influence. Letting $(i\omega)^{1/3} = r^{1/3}e^{i\theta/3}e^{i\pi/6}$ where $-3\pi/2 < \theta < \pi/2$, we examine the negative imaginary axis given by $\theta = -\pi/2, r = \kappa$. On this line we find $(i\omega)^{1/3} = \kappa^{1/3}$. However we find that the denominator of the integrand in equation (5.78) does not vanish for positive values of κ. This is due to the fact that $\mathrm{Bi}'(0) > 0$ and $\mathrm{Ai}'(0)\kappa < 0$ for positive κ. Hence there are no poles in both the upper and lower half planes, and so there is virtually no expected upstream or downstream influence, although this may be found at the next order.

Figure 5.4 shows the numerically calculated skin friction, given by the solid line, and the asymptotic small μ approximation, given by the dotted line. The figure shows plots for values of $\mu = 0.1, 0.05$. The plots seem to agree well with the analysis and hence as $\mu \to 0$ there is neither upstream or downstream influence.

5.3.2 Summary

To summarise, for small μ glue expansions are

$$u_1 = f_0 + \mu^{1/2}\overline{Y} - \mu f_0 + \cdots, \tag{5.82}$$

$$v_1 = \mu f_0 G' + O(\mu^2), \tag{5.83}$$

$$p = -\mu f_0 G + O(\mu^2), \tag{5.84}$$

where $\overline{Y} = Y\mu^{1/2}$. In the blood $Y \sim 1$ and the solution is given by

$$u_2 = (Y - G) + \mu\overline{u}_2 + \cdots, \tag{5.85}$$

$$v_2 = \mu G'(Y - G) + \mu^2\overline{v}_2 + \cdots, \tag{5.86}$$

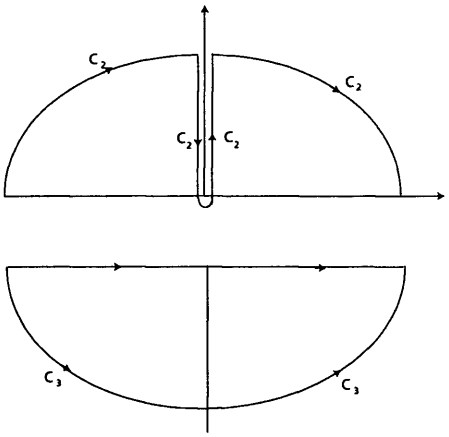

Figure 5.1: Contour for the wall shear calculation. Here there is a branch point at $\omega = 0$, and a branch cut is made along the positive imaginary axis. The contour traverses the origin in a small circle, no branch cut is necessary along the negative imaginary axis.

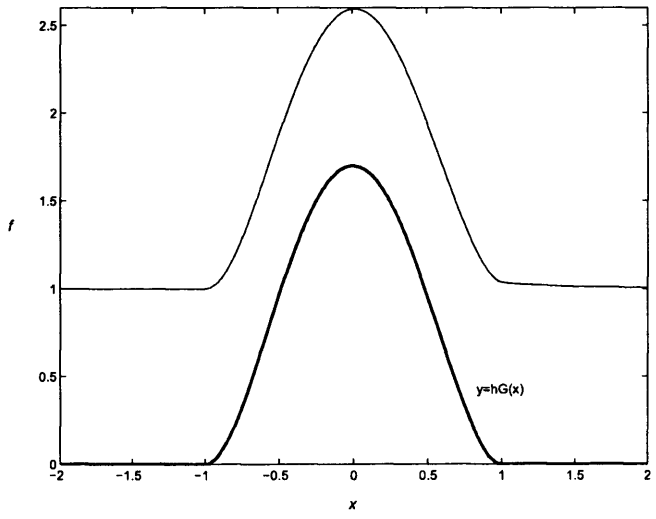

Figure 5.2: Interface position for the case $\mu = 0.1$, $\rho = 1$, over a roughness and no divider. As can be seen the solution here is almost exactly the asymptotic value $1 + G(x)$.

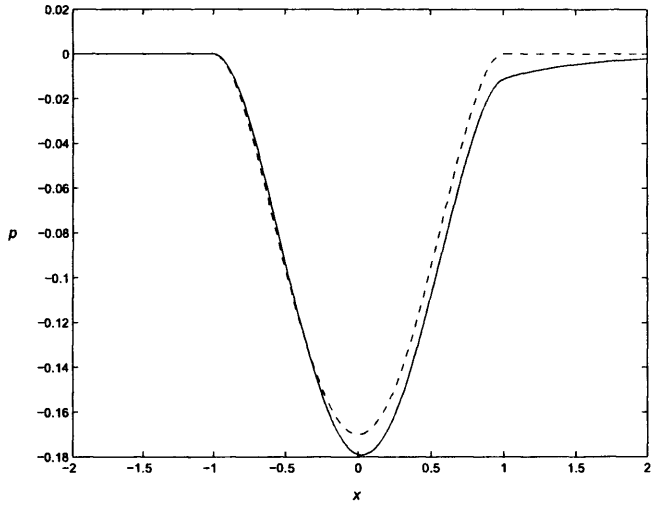

Figure 5.3: Pressure for $\mu = 0.1$ and $\rho = 1$, full line and the asymptotic value dashed line. Closer agreement is found for smaller values of μ, indeed the value $\mu = 0.01$ is not plotted as it coincides almost exactly with the asymptote.

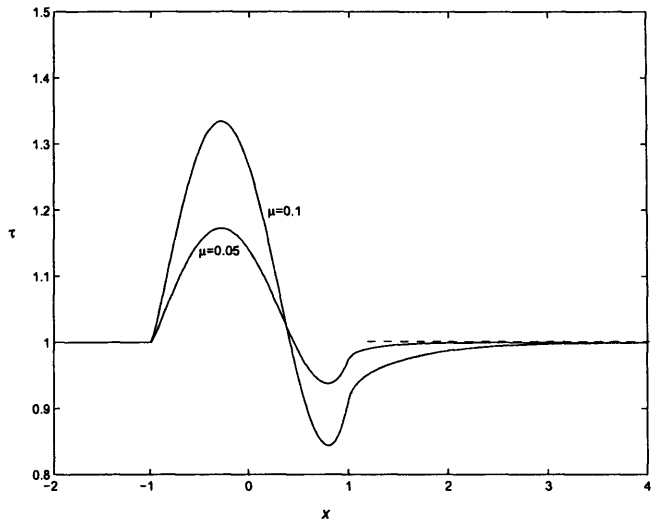

Figure 5.4: Wall shear for $\mu = 0.1, 0.05, \rho = 1$. Here the full line represents the numerical solution and the dotted line the large x asymptote.

with the interface given by

$$f = (f_0 + G) + \mu\overline{\overline{\overline{f}}} + \cdots . \tag{5.87}$$

Thus for small μ the interface effectively just rides up and over the wall shape and returns to its undisturbed value of f_0 downstream. Figure 5.2 shows the computational results for the interface when $\mu = 0.1$, along with the asymptotic result. Even for such a moderately small value of μ a good agreement is found and better agreement found with smaller values of μ. Figures 5.3 and 5.4 show the pressure and wall shear again for the case $\mu = 0.1$ and the asymptotic values; again good agreement is found.

There is an $O(\mu^{1/2})$ correction for the streamwise velocity in the glue but not in the blood. The $O(\mu)$ term in the blood was not calculated directly but the perturbation of the wall shear was found far downstream in equation (5.81). An extended analysis to the next order of μ would probably determine

the unknown correction to the interface $\overline{\overline{f}}$.

5.3.3 Analysis of the flow to two large daughters

We can extend the analysis of the previous section to consider the case where a divider is present rather than the roughness. The governing equations are the same as in the previous section and, as outlined previously the only change to the boundary conditions is the condition of matching with the core flow, which to repeat is

$$u_1 \sim \mu y + f_0(1-\mu) + \mu u_W. \tag{5.88}$$

So following the same analysis and omitting the details, we find the only change comes to the form of the glue expansions at $O(\mu)$. Indeed the solutions at $O(1)$ and $O(\mu^{1/2})$ can be retained. At $O(\mu)$ the conditions (5.52)–(5.55) are of the same form but the matching condition with the core flow is changed to $\overline{u}_1 \sim -f_0 + u_W$. This sets the glue solution as

$$\overline{u}_1 = u_W - f_0, \qquad \overline{v}_1 = \overline{Y} u_W, \qquad \overline{p} = -f_0(u_W + G). \tag{5.89}$$

The blood expansions are of course unchanged at leading order and hence the leading order interface position is still given by f_0+G. The only change though comes in the calculation to the wall shear, where a factor of $i\omega u_W^*$ appears on the right hand side of equation (5.75). Hence the perturbed wall shear is given as

$$\bar{\tau}_W(x) = \frac{1}{2\pi}\int_{-\infty}^{\infty} \frac{-i\omega f_0(G^* + u_W^*)[\mathrm{Bi}(0) - \theta \mathrm{Ai}(0)]}{(i\omega/\rho)^{1/3}[\mathrm{Bi}'(0) - \theta \mathrm{Ai}'(0)]} e^{i\omega x} d\omega. \tag{5.90}$$

Again this integral must in general be calculated numerically due to the transform of the slip velocity in general being a numerical exercise.

5.4 Increasing the surface roughness height

Given the linear behaviour holding in the previous configuration, it is interesting to ask now at what stage non-linear effects re-enter play as the roughness height is increased, in the setting of μ being small.

We take a Prandtl-shift again but now at the start of the analysis with $\hat{Y} = Y - G(x)$, hence the form of the governing equations (5.2a) and (5.2b) remain unchanged, but with $V = v - G'(x)U$ replacing v in each fluid. Hence the equations are now

$$\frac{\partial u_1}{\partial x} + \frac{\partial V_1}{\partial \hat{Y}} = 0, \; u_1\frac{\partial u_1}{\partial x} + V_1\frac{\partial u_1}{\partial \hat{Y}} = -\frac{dp}{dx} + \frac{\partial^2 u_1}{\partial \hat{Y}^2}, \tag{5.91}$$

$$\frac{\partial u_2}{\partial x} + \frac{\partial V_2}{\partial \hat{Y}} = 0, \; u_2\frac{\partial u_2}{\partial x} + V_2\frac{\partial u_2}{\partial \hat{Y}} = -\left(\frac{\rho_1}{\rho_2}\right)\frac{dp}{dx} + \left(\frac{\nu_2}{\nu_1}\right)\frac{\partial^2 u_2}{\partial \hat{Y}^2}. \tag{5.92}$$

The boundary conditions here are

$$u_2 = 0 \quad \text{at} \quad \hat{Y} = 0, \tag{5.93}$$

$$V_2 = 0 \quad \text{at} \quad \hat{Y} = 0, \tag{5.94}$$

$$u_2 \to \hat{Y} \quad \text{as } x \to -\infty, \tag{5.95}$$

$$u_1 \sim \mu(\hat{Y} + G) + f_0(1-\mu) \quad \text{as} \quad \hat{Y} \to \infty. \tag{5.96}$$

$$\left.\begin{aligned} u_1 &= u_2 \\ \mu_1\tfrac{\partial u_1}{\partial \hat{Y}} &= \mu_2\tfrac{\partial u_2}{\partial \hat{Y}} \\ V_1 &= u_1\tilde{f}' \\ V_2 &= u_1\tilde{f}' \end{aligned}\right\} \quad \text{on} \quad \hat{Y} = \tilde{f}(x), \tag{5.97}$$

where $\tilde{f}(x) = f - G$ again. In the previous section we assumed that the hump shape G was of order-one. Here we again consider the case where $\mu \ll 1$ and $G \sim \mu^{-1} \gg 1$, indeed we set $G = \mu^{-1}\tilde{G}$. The form of the scalings of the axial coordinate are the same as in section 5.3, hence we set $\hat{Y} = \mu^{-1/2}\overline{Y}$ in the glue and $\hat{Y} \sim 1$ in the blood, where again $x = \mu^{-1}\overline{x}$. The scalings for the velocities

in this new case are given by

$$u_1 = O(1), \tag{5.98}$$

$$V_1 = \mu^{1/2}\tilde{V}_1, \tag{5.99}$$

$$p = O(1), \tag{5.100}$$

$$u_2 = O(1), \tag{5.101}$$

$$V_2 = \mu\tilde{V}_2. \tag{5.102}$$

This again leaves the boundary layer equations in the form

$$\frac{\partial u_1}{\partial \bar{x}} + \frac{\partial \tilde{V}_1}{\partial \bar{Y}} = 0, \qquad u_1\frac{\partial u_1}{\partial \bar{x}} + \tilde{V}_1\frac{\partial u_1}{\partial \bar{Y}} = -\frac{dp}{d\bar{x}} + \frac{\partial^2 u_1}{\partial \bar{Y}^2}, \tag{5.103}$$

$$\frac{\partial u_2}{\partial \bar{x}} + \frac{\partial \tilde{V}_2}{\partial \hat{Y}} = 0, \qquad u_2\frac{\partial u_2}{\partial \bar{x}} + \tilde{V}_2\frac{\partial u_2}{\partial \hat{Y}} = -\rho\frac{dp}{d\bar{x}} + \nu\frac{\partial^2 u_2}{\partial \hat{Y}^2}. \tag{5.104}$$

The boundary and interface conditions for the transformed problem are given by

$$u_1 \to f_0 + \overline{G}(\overline{x}) \quad \text{as} \quad \overline{Y} \to \infty, \tag{5.105}$$

$$u_1 \to f_0 \quad \text{as} \quad \overline{x} \to -\infty, \tag{5.106}$$

$$\tilde{V}_1 \to 0 \quad \text{as} \quad \overline{Y} \to 0+, \tag{5.107}$$

$$\frac{\partial u_1}{\partial \overline{Y}} \to 0 \quad \text{as} \quad \overline{Y} \to 0+, \tag{5.108}$$

where we have again assumed $\mu \ll 1$. Again these conditions follow respectively from matching with the core flow solution, matching far downstream, the kinematic condition at the interface and the tangential stress condition at the interface. So the glue solution can be written as

$$u_1 = \overline{G} + f_0, \qquad \tilde{V}_1 = -\overline{G}'\overline{Y}, \qquad p = -(f_0 + \overline{G})\overline{G}'. \tag{5.109}$$

However the leading order interface position $\tilde{f}$ is still not able to be determined at this stage. Again the solution in the blood is not so straightforward and we

are left with solving the non-linear wall-layer equations with known pressure-gradient

$$u_2\frac{\partial u_2}{\partial \bar{x}} + \tilde{V}_2\frac{\partial u_2}{\partial \hat{Y}} = \left(\frac{\rho_1}{\rho_2}\right)(f_0+\overline{G})\overline{G}' + \left(\frac{\nu_2}{\nu_1}\right)\frac{\partial^2 u_2}{\partial \hat{Y}^2}. \tag{5.110}$$

The interface conditions are

$$\left.\begin{aligned} u_2 &= f_0+\overline{G} \\ \mu_1\tfrac{\partial u_2}{\partial \hat{Y}} &= 0 \\ \tilde{V}_2 &= u_2\tilde{f}' \end{aligned}\right\} \quad \text{on} \quad \hat{Y}=\tilde{f}(x), \tag{5.111}$$

and the conditions at the wall and matching far upstream are given by

$$u_2 = 0 \quad \text{at} \quad \hat{Y}=0, \tag{5.112}$$

$$\tilde{V}_2 = 0 \quad \text{at} \quad \hat{Y}=0, \tag{5.113}$$

$$u_2 \to \hat{Y} \quad \text{as} \quad x\to-\infty. \tag{5.114}$$

So with $G\sim\mu^{-1}$, the blood problem remains non-linear and will in general need to be solved numerically. Again linearised solutions of the blood equations may be possible as in section 5.2 but are not calculated here.

5.5 Analysis for flow into two daughters far downstream $x\to\infty$

Far downstream the condition of matching tangential velocity with the core equation (4.85) is dominated by the slip velocity contribution for which we have $u\sim\mu u_W\sim\mu x$ at large positive x. The balance of inertial and viscous terms demands that $uu_x\sim u_{YY}$, giving $Y\sim 1$ if μ is of $O(1)$ in this situation. Hence we are led to the following expansions far upstream

$$u(x,Y) = \mu x\hat{u}(Y)+\cdots, \tag{5.115}$$

$$v(x,Y) = \mu\hat{v}(Y)+\cdots, \tag{5.116}$$

$$p(x) = \mu^2x^2\hat{p}+\cdots, \tag{5.117}$$

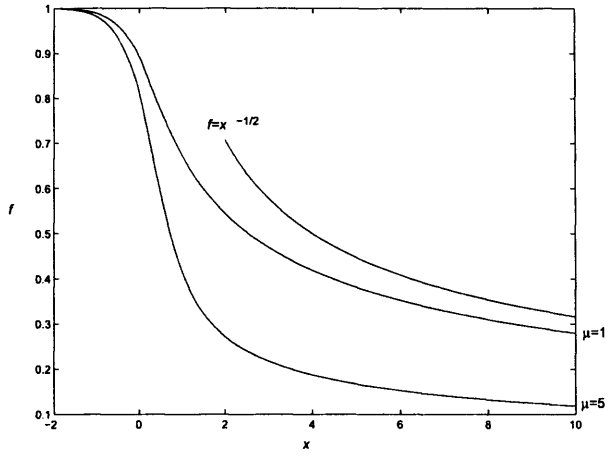

Figure 5.5: Interface shape far downstream for the values $\mu = 1$ and 5, and comparison with the asymptotic solution $x^{-1/2}$.

where $\hat{p}$ is a constant here. Substitution of the expansions into the momentum and continuity equations (5.2a) and (5.2b) gives

$$\hat{u}^2 + \hat{v}\frac{d\hat{u}}{dY} = -2\rho\hat{p} + \rho\frac{d^2\hat{u}}{dY^2}, \tag{5.118}$$

$$\hat{u}(Y) = -\frac{d\hat{v}}{dY}. \tag{5.119}$$

Combining these two equations leads to a third order ordinary differential equation for $\hat{v}$,

$$\rho\hat{v}'''(Y) - \hat{v}\hat{v}''(Y) + [\hat{v}'(Y)]^2 + 2\rho\hat{p} = 0. \tag{5.120}$$

Setting $\hat{v} = -V\rho$ transforms the equation to

$$V'''(Y) + VV''(Y) - [V'(Y)]^2 + 1 = 0, \tag{5.121}$$

holding in the glue. Here $\hat{p} = -\rho/2$ as a consequence of Bernoulli's theorem at the outer edge inviscid free stream.

The boundary conditions are now $V'(\infty) = 0, V'(0) = 0$ and $V''(0) = 0$. The equation and boundary conditions are now identical to those of a front

stagnation point with $\alpha = 1$ and $\beta = 1$. The numerical solution to equation (5.121) is given in [73] on page 232. The kinematic relation enables us to determine the downstream behaviour of the interface. For small $\hat{Y}$ we set the following expansions

$$U \sim \lambda x \hat{Y} + O(\hat{Y}^2), \tag{5.122}$$

$$V \sim -\lambda \hat{Y}^2/2 + \cdots, \tag{5.123}$$

here λ is the constant again given by Rosenhead. Thus the kinematic balance gives

$$-\lambda \hat{Y}^2/2 \sim \lambda x \hat{Y} F'(x), \tag{5.124}$$

at leading order, so on integration we find the asymptotic description of the interface shape is given by

$$F(x) \sim x^{-1/2} \qquad \text{as} \quad x \to \infty, \tag{5.125}$$

valid for values of μ and ρ of order unity. This asymptotic form agrees well with the computations for all values of ρ, μ of order-one. Figure 5.5 shows the case of the interface far downstream for the cases $\mu = 1$ and $\mu = 5$ and also the shape of the asymptote for comparison. It can be seen for both of these values of the viscosity ratio that the interface is close to the shape of the asymptote.

5.6 Analysis for large ρ

When the density ratio is taken to be large, significant simplifications can be made to the equations of motion governing the blood flow. Indeed taking $\rho \gg 1$ and with $\rho \sim \nu$ and $\mu \sim 1$, the momentum equation in the blood reduces to

$$\rho \frac{\partial p}{\partial x} = \nu \frac{\partial^2 u_2}{\partial Y^2}. \tag{5.126}$$

Taking a Prandtl-transformation also helps again here so as usual we take $\hat{Y} = Y - G$. The boundary conditions on the u-velocity reduce to

$$u_2 = 0 \quad \text{on } \hat{Y} = 0, \tag{5.127}$$

$$u_2 = \hat{u}_2 \quad \text{on } \hat{Y} = \tilde{f}, \tag{5.128}$$

where again $\tilde{f} = f - G$. Thus integrating equation (5.126) twice and using the boundary conditions above we find the velocity in the blood as

$$u_2 = \frac{p'\hat{Y}^2}{2\mu} + \left(\frac{2\mu\hat{u}_2 - p'\tilde{f}^2}{2\mu\tilde{f}}\right)\hat{Y}. \tag{5.129}$$

Next using the continuity equation we find

$$\frac{\partial}{\partial x}\left\{\int_0^{\tilde{f}} \left(\frac{p'\hat{Y}^2}{2\mu} + \left(\frac{2\hat{u}_2 - p'\tilde{f}^2}{2\mu\tilde{f}}\right)\hat{Y}\right) d\hat{Y}\right\} = 0. \tag{5.130}$$

So on integration of the above equation and imposing the boundary conditions far upstream we find

$$p' = \frac{-6}{\tilde{f}^3}\left(1 - \hat{u}_2\tilde{f}\right). \tag{5.131}$$

Here the conditions far upstream are $f = 1$, $p'(x) = 0$, $\hat{u}_2 = 1$ as have been used. So in this case the form of the pressure solution is found from the blood solution and then substituted into the glue equations, the opposite to the small μ analysis. Hence the equations in the glue are the normal boundary layer equations with known pressure gradient, given by

$$u_1\frac{\partial u_1}{\partial x} + V_1\frac{\partial u_1}{\partial \hat{\hat{Y}}} = \frac{-6}{\tilde{f}^3}\left(1 - \hat{u}_2\tilde{f}\right) + \frac{\partial^2 U_1}{\partial \hat{\hat{Y}}^2}, \tag{5.132}$$

where $\hat{\hat{Y}} = \hat{Y} - f$ and $V_1 = v_1 + u_1 f'(x)$. The interface conditions become

$$\left.\begin{aligned} u_1 &= u_2 \\ \mu_1\tfrac{\partial u_1}{\partial \hat{\hat{Y}}} &= \mu_2\tfrac{\partial u_2}{\partial \hat{\hat{Y}}} \\ \hat{V}_1 &= u_1\tilde{f}' \\ \hat{V}_2 &= u_1\tilde{f}' \end{aligned}\right\} \quad \text{on } \hat{\hat{Y}} = 0, \tag{5.133}$$

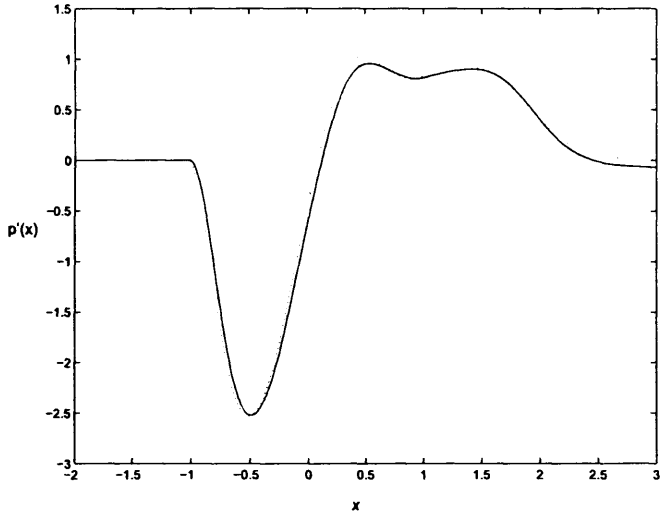

Figure 5.6: Calculation of the pressure for the density ratio $\rho = 10$ and $\mu = 1$, over the hump roughness $G(x) = (1 - x^2)^2$. (a)-dotted line asymptotic value given by equation (5.131), (b)-full line, the numerical solution.

So in this case, although the solution has not been found explicitly, the solution in the blood takes a simpler form than the solution in the glue. As with the small μ analysis, perturbations around the small parameter ρ^{-1} could be taken and the leading order solution calculated, however because of time constraints this was not considered here. Also, as the glue and blood are of roughly equal densities, it was not a problem that was directly relevant to the embolization process.

To continue the wall layer analysis we introduce chemical interaction of the two fluids at the interface. The formulation of this problem and associated analysis is presented in the next chapter.

Chapter 6

The Wall Layer (2) - A simple model of chemical effects

The present chapter describes the possible beginnings of a further account of interfacial effects between the blood and the glue. A simple model is investigated. The problem involved is found to have features which are interesting in their own right.

6.1 Formulation and equations of motion

The previous analysis of the steady wall layer flow in chapters 4 and 5 did not take account of any chemical interaction between the glue and the blood. Here we investigate a simple condition as a starting point to model such interaction, which we model by mass exchange at the moving interface. The problem is also made unsteady. The governing equations of unsteady motion are again the wall layer equations, with the factors ρ and ν appearing in the blood momentum equations to tie in with the analysis of the previous chapter. The time dependent kinematic condition at the interface is now changed to

$$v_i = \frac{\partial f}{\partial t} + u_i \frac{\partial f}{\partial x} + C_i, \tag{6.1}$$

for $i = 1, 2$ where C_1 and C_2 may or may not be constants. A new condition to attempt to model simple chemical effects is included at the interface, in that we impose the balance

$$\rho_1 C_1 = \rho_2 C_2, \tag{6.2}$$

which essentially conserves mass, in view of equation (6.1) and determines C_2 if C_1 is given.

To start with, we seek a simple solution to the unsteady wall layer equations in both fluids; hence we set

$$u_i = u_i(y, t), \tag{6.3}$$

from which the continuity equation imposes $v_i = v_i(x, t)$, independent of y. Substitution of these expressions into the wall layer equations then gives

$$\frac{\partial u_1}{\partial t} + v_1 \frac{\partial u_1}{\partial y} = -\frac{\partial p}{\partial x} + \frac{\partial^2 u_1}{\partial y^2}, \tag{6.4}$$

$$\frac{\partial u_2}{\partial t} + v_2 \frac{\partial u_2}{\partial y} = -\rho \frac{\partial p}{dx} + \nu \frac{\partial^2 u_2}{\partial y^2}, \tag{6.5}$$

for the glue and blood respectively. Again we have the pressure $p = p(x, t)$ from the y-momentum balance. The boundary conditions for the problem are now

$$u_2 = v_2 = 0 \quad \text{at} \quad y = 0, \tag{6.6}$$

$$u_1 \sim \Gamma y + A(t) \quad \text{as} \quad y \to \infty, \tag{6.7}$$

$$\left.\begin{aligned} u_1 &= u_2 \\ \mu_1 \tfrac{\partial u_1}{\partial y} &= \mu_2 \tfrac{\partial u_2}{\partial y} \\ v_1 &= f_t + C_1 \\ v_2 &= f_t + C_2 \end{aligned}\right\} \quad \text{on} \quad y = f(x, t), \tag{6.8}$$

where Γ is the shear determined from the core flow solution and $A(t)$ is the unknown displacement effect. The conditions are respectively for no-slip at the wall, matching with the inviscid core solution, the continuity of tangential

velocity, the tangential stress condition and the kinematic condition at the interface, in the glue and the blood respectively.

The velocities in the normal direction are now in general not equal at the interface and indeed equality is only realised in the case $\rho_1 = \rho_2$.

Next as $v_2 = v_2(x,t)$ and $v_2 = 0$ at $y = 0$ we must have $v_2 = 0$ everywhere in the blood. The glue condition, the final equation in (6.8), reduces to $f_t + C_2 = 0$ and so the interface can be defined explicitly as

$$f = f^* - C_2 t, \tag{6.9}$$

where the constant f^* is the interface position at time $t = 0$. The velocity v_1 can then be written as $v_1 = C_1 - C_2 = \Delta C$ and thus is another constant in the problem. The pressure gradient is now a function of t only and is denoted $q(t)$. The equations of motion reduce to

$$\frac{\partial u_1}{\partial t} + \Delta C \frac{\partial u_1}{\partial y} = -q(t) + \frac{\partial^2 u_1}{\partial y^2}, \tag{6.10}$$

$$\frac{\partial u_2}{\partial t} = -\rho q(t) + \nu \frac{\partial^2 u_2}{\partial y^2}. \tag{6.11}$$

The boundary and interface conditions are now given by

$$\left.\begin{aligned} u_1 &= u_2 \\ \mu_1 \tfrac{\partial u_1}{\partial y} &= \mu_2 \tfrac{\partial u_2}{\partial y} \end{aligned}\right\} \quad \text{on} \quad y = f^* - C_2 t, \tag{6.12}$$

$$u_2 = 0 \quad \text{at} \quad y = 0, \tag{6.13}$$

$$u_1 \sim \Gamma y + A(t) \quad \text{as} \quad y \to \infty. \tag{6.14}$$

Here the constants Γ and C_1 and hence C_2 are assumed to be known. The solution for (6.10)-(6.14) will now be discussed where f^*, C_1 act as the parameters in the model.

Substitution of the matching condition (6.14) into the momentum equation (6.10) gives the form of the derivative of the unknown displacement function

$A(t)$ to be

$$A'(t) = -(\Gamma \Delta C + q). \tag{6.15}$$

There is usually no simple solution for this set of equations but in a special case we seek a similarity solution.

6.2 Similarity solution for negative times

To continue analysis of the system, we seek the solution of the governing equations at negative values of t, since touchdown $f \to 0$ seems a possibility. In this setting the scaling $y \sim |t|^{1/2}$ in each fluid allows the system to be transformed to two ordinary differential equations using a similarity variable η say. So the following expressions are posed

$$u_1 = |t|^{1/2}\hat{u}_1(\eta) + \cdots, \tag{6.16}$$

$$u_2 = |t|^{1/2}\hat{u}_2(\eta) + \cdots, \tag{6.17}$$

$$\eta = y/|t|^{1/2}, \tag{6.18}$$

$$q = \overline{q}|t|^{-1/2} + \cdots, \tag{6.19}$$

based on the orders of magnitude in equations (6.10) to (6.14). Also the chemical-model parameters are taken now in the form

$$C_1 = \tilde{C}_1|t|^{-1/2} \text{ and } C_2 = \tilde{C}_2|t|^{-1/2}, \tag{6.20}$$

to balance terms in equation (6.10). Here $\tilde{C}_1$ and $\tilde{C}_2$ are constants. In this setting the spatial and temporal derivatives in terms of the new variables are given as

$$\partial_y = \frac{1}{|t|^{1/2}}\partial_\eta, \tag{6.21}$$

$$\partial_t = -\partial_{|t|} + \frac{\eta}{2|t|}\partial_\eta. \tag{6.22}$$

Also the constant $f^* = 0$, and so the interface is given by $\eta = \tilde{C}_2$. Substitutions of these expressions into the governing equations yield linear ordinary differential equations in both fluids. These are

$$\frac{d^2\hat{u}_2}{d\eta^2} - \frac{1}{2\nu}\eta\frac{d\hat{u}_2}{d\eta} + \frac{1}{2\nu}\hat{u}_2 - \frac{1}{\mu}\overline{q} = 0, \tag{6.23}$$

$$\frac{d^2\hat{u}_1}{d\eta^2} - \left(\frac{\eta}{2} + \Delta\tilde{C}\right)\frac{d\hat{u}_1}{d\eta} + \frac{1}{2}\hat{u}_1 - \overline{q} = 0, \tag{6.24}$$

where $\Delta\tilde{C} = \tilde{C}_1 - \tilde{C}_2$. The transformed boundary and interface conditions are

$$\hat{u}_2 = 0 \quad \text{at} \quad \eta = 0, \tag{6.25}$$

$$\hat{u}_2 = \hat{u}_1 \quad \text{at} \quad \eta = \tilde{C}_2, \tag{6.26}$$

$$\frac{\partial\hat{u}_1}{\partial\eta} = \mu\frac{\partial\hat{u}_2}{\partial\eta} \quad \text{at} \quad \eta = \tilde{C}_2, \tag{6.27}$$

$$\hat{u}_1 \sim \Gamma\eta + 2(\Gamma\Delta\tilde{C} + \overline{q}) \quad \text{as} \quad \eta \to \infty. \tag{6.28}$$

The matching condition in equation (6.28) is found by substituting expansions (6.19) and (6.20) into expression (6.15) and integrating with respect to $|t|$.

We notice that $c\eta + 2\rho\overline{q}$ (where c is a constant) is an exact solution of the blood equation (6.23); hence we can then easily write down the full solution to (6.23) as

$$\hat{u}_2(\eta) = a_1\eta + a_2\eta\int_{\eta_0}^{\eta}\frac{1}{\overline{\eta}^2}e^{\overline{\eta}^2/4\nu}d\overline{\eta} + 2\rho\overline{q}, \tag{6.29}$$

for constants a_1 and a_2. The solution of the glue equation takes the same form as (6.29) but we notice that there is exponential growth in the integral as $\eta \to \infty$, so the constant multiplying this expression must be set to zero. The full solution in the glue that satisfies the condition as $\eta \to \infty$ is then simply

$$\hat{u}_1(\eta) = \Gamma(\eta + 2\Delta\tilde{C}) + 2\overline{q}. \tag{6.30}$$

The three constants a_1, a_2 and $\overline{q}$ are now determined from the no-slip boundary condition and the continuity of velocity and tangential stress conditions at the interface.

6.2.1 Determination of the constants

Applying the no-slip condition at the wall means we must examine (6.29) as $\eta \to 0$. The integral in the second term of (6.29) is

$$S = \int_{\eta_0}^{\eta} \frac{1}{\eta^2} e^{\eta^2/4\nu} d\eta = \int_{\eta_0}^{\eta} \frac{1}{\eta^2} \left(e^{\eta^2/4\nu} - 1 \right) d\eta + \int_{\eta_0}^{\eta} \frac{1}{\eta^2} d\eta. \tag{6.31}$$

Here the first integral on the right hand side is finite as $\eta \to 0$. Hence by evaluating the second integral we find

$$\eta S \sim -1 \qquad \text{as} \quad \eta \to 0. \tag{6.32}$$

So applying the no slip condition in equation (6.29) gives

$$a_2 = 2\rho\bar{q}. \tag{6.33}$$

Next we obtain two equations demanding that both the velocity and the shear conditions are satisfied at the interface. Using (6.29) and (6.30) along with interface conditions (6.26) and (6.27) these are

$$\Gamma(\tilde{C}_2 + 2\Delta\tilde{C}) = a_1\tilde{C}_2 + a_2\tilde{C}_2 I + 2(\rho - 1)\bar{q}, \tag{6.34}$$

$$\Gamma = \mu(a_1 + a_2\tilde{C}_2\theta + a_2 I), \tag{6.35}$$

where

$$I = \int_{\eta_0}^{\tilde{C}_2} \frac{1}{\eta^2} e^{\eta^2/4\nu} d\eta \quad \text{and} \quad \theta = \frac{e^{\tilde{C}_2^2/4\nu}}{\tilde{C}_2^2}, \tag{6.36}$$

for suitably chosen η_0. The constants a_1, a_2 and $\bar{q}$ are then found from (6.33), (6.34) and (6.35), which is a linear system of three equations for three unknowns. These are found to be

$$a_1 = \frac{\Gamma}{\mu} - \rho\frac{(I + \tilde{C}_2\theta)\Gamma(\Sigma\mu - \tilde{C}_2)}{\mu(-1 + \rho - \tilde{C}_2^2\theta\rho)}, \tag{6.37}$$

$$a_2 = \rho\frac{\Gamma(\Sigma\mu - \tilde{C}_2)}{\mu(-1 + \rho - \tilde{C}_2^2\theta\rho)}, \tag{6.38}$$

$$\bar{q} = \frac{\Gamma(\Sigma\mu - \tilde{C}_2)}{2\mu(-1 + \rho - \tilde{C}_2^2\theta\rho)}, \tag{6.39}$$

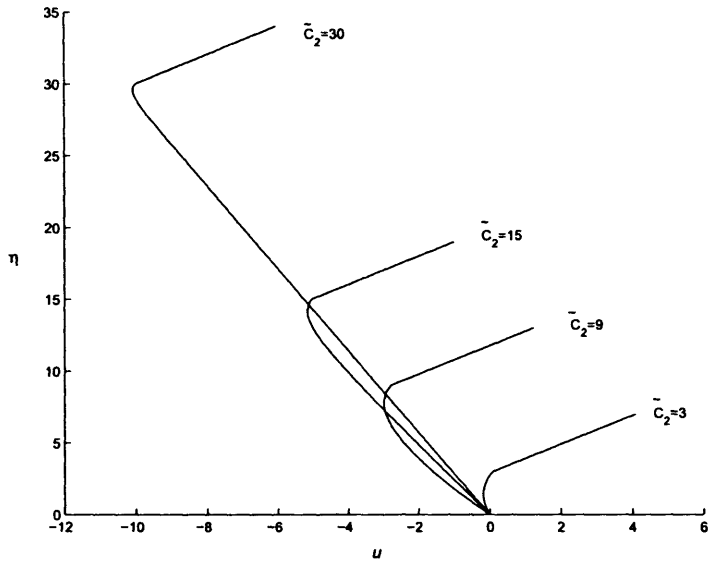

Figure 6.1: Velocity profiles for $\rho = 3$, $\mu = 3$, for larger values of $\tilde{C}_2$.

where $\Sigma = (\tilde{C}_2 + 2\Delta\tilde{C}) = \tilde{C}_2\left(\frac{2}{\rho} - 1\right)$. So the solution to (6.23) and (6.24) is now fully determined.

Figures 6.1 and 6.2 show some velocity profiles for the case $\Gamma = 1$, $\rho = 3$, $\mu = 3$ and different $\tilde{C}_2$. Large values of $\tilde{C}_2$ seem to suggest the occurrence of reversed flow, whereas when $\tilde{C}_2$ is small the flow is all forward. On the other hand, figure 6.3 shows the velocity profiles for the cases $\rho = 1/3, \mu = 3$ and again $\Gamma = 1$ here. It seems here that no reversed flow occurs irrespective of the values of $\tilde{C}_2$ which are taken. A similar situation is seen for the velocity profiles in the case where $\rho = 1/2, \mu = 1/2$ which is shown in figure 6.4. It turns out the occurrence of flow reversal is dependent on the density ratio ρ, which will be further discussed in the next section.

We now analyse the above solution in the limits $\tilde{C}_2 \to \infty$ and $\tilde{C}_2 \to 0$. These analyses provide insight when we consider moving on to values of C_1 and C_2 being constants of order unity, which are studied in sections 6.3 and 6.4.

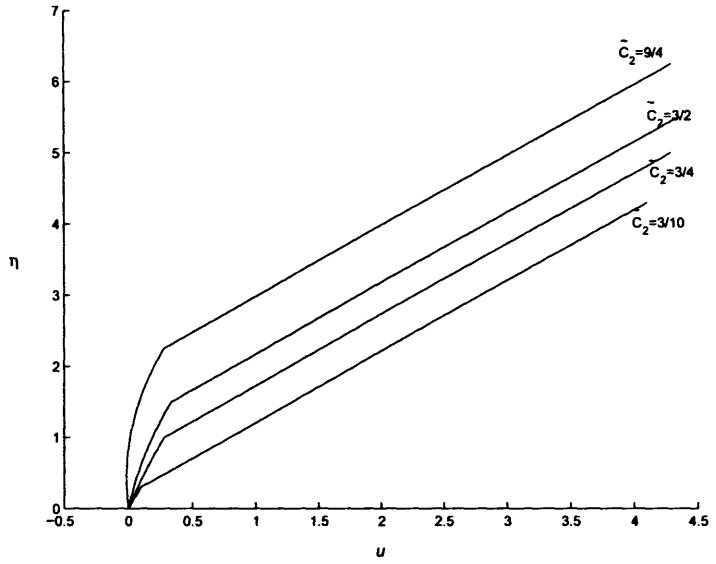

Figure 6.2: Velocity profiles for $\rho = 3$, $\mu = 3$, for smaller values of $\tilde{C}_2$.

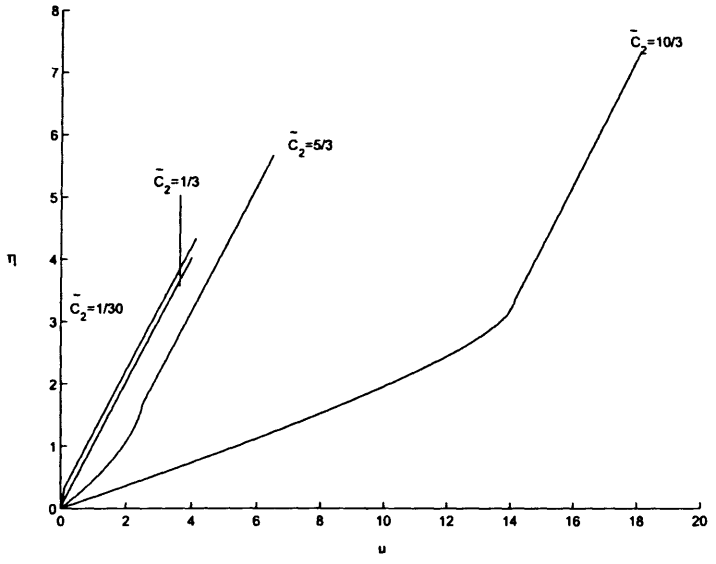

Figure 6.3: Velocity profiles for $\rho = 1/3$, $\mu = 3$.

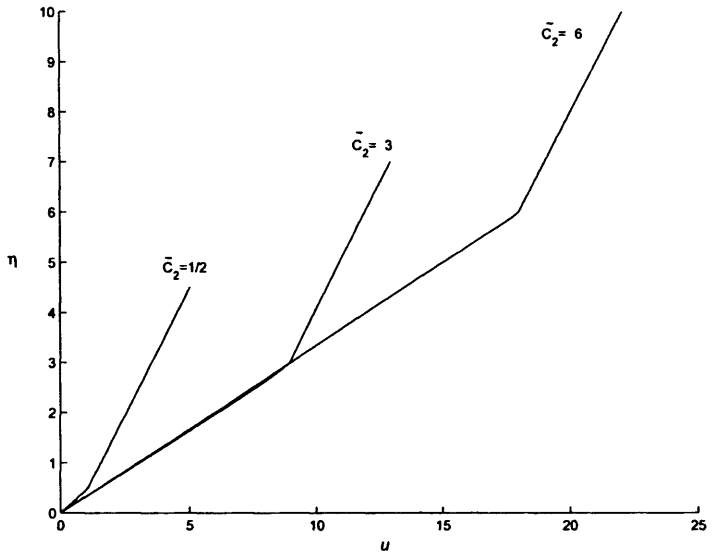

Figure 6.4: Velocity profiles for $\rho = 1/2$, $\mu = 1/2$. The flow is forward here and in figure 6.3 for all values of $\tilde{C}_2$.

6.2.2 Solution for large $\tilde{C}_2$

For large $\tilde{C}_2$ the interface $\eta = \tilde{C}_2$ is far from the wall. First the behaviour of the constants a_1, a_2 and $\overline{q}$ is considered in this limit. By using (6.37)-(6.39) we can see that as $\tilde{C}_2 \rightarrow \infty$ the constants a_2 and $\overline{q} \rightarrow 0$. When considering the limit of a_1 we need to consider

$$\lim_{\tilde{C}_2 \rightarrow \infty} \frac{\int_{\eta_0}^{\tilde{C}_2} \frac{1}{\eta^2} e^{\eta^2/4\nu} d\eta}{e^{\tilde{C}_2^2/4\nu}}; \tag{6.40}$$

integration by parts in the numerator shows that the ratio vanishes in the limit, hence the limiting behaviour of a_1 is given by

$$a_1 \rightarrow \Gamma(2/\rho - 1), \tag{6.41}$$

as $\tilde{C}_2 \to \infty$.[1] The asymptotic representations for the constants a_2 and $\overline{q}$ are given respectively by

$$a_2 \sim -\frac{\Gamma\rho}{\mu}\left(\frac{2\mu}{\rho} - \mu - 1\right)\tilde{C}_2 e^{-\tilde{C}_2{}^2/(4\nu)}, \tag{6.42}$$

$$\overline{q} \sim -\frac{\Gamma}{2\mu}\left(\frac{2\mu}{\rho} - \mu - 1\right)\tilde{C}_2 e^{-\tilde{C}_2{}^2/(4\nu)}. \tag{6.43}$$

Asymptotic expansion for large $\tilde{C}_2$

When $\tilde{C}_2$ is large the substitution $\eta = \tilde{C}_2 Y$ is made, so that $0 \leq Y \leq 1$ in the blood. Equation (6.23) becomes

$$\epsilon\frac{d^2\hat{u}_2}{dY^2} - \frac{1}{2\nu}Y\frac{d\hat{u}_2}{dY} + \frac{1}{2\nu}\hat{u}_2 - \frac{1}{\mu}\overline{q} = 0, \tag{6.44}$$

where $\epsilon = 1/\tilde{C}_2^2$ and is assumed to be a small parameter. Hence neglecting the $O(\epsilon)$ term in equation (6.44) leaves a first order equation. The solution satisfying no slip at the wall is

$$\hat{u}_2(Y) = \hat{\gamma}Y, \tag{6.45}$$

as equation (6.43) shows that $\overline{q}$ is exponentially small in this setting and so is neglected. Near the interface however this expression is not valid as the shear Γ in the glue at the interface is taken as positive and so the shear in the blood must also be positive, but $\hat{\gamma}$ is unknown at this stage. The glue solution is unchanged in this setting and is still given by (6.30), but without the $\overline{q}$ term.

The above indicates the presence of a thin interfacial sub-layer in order for the shear condition at the interface to hold. In the new variables the interface is given by $Y = 1$ and so we take an expansion at the upper edge of the blood

$$Y = 1 + \epsilon Z \tag{6.46}$$

for $-\infty < Z < 0$. Substitution into the governing equation (6.44) yields the leading order equation

$$\frac{d^2\hat{u}_2}{dZ^2} - \frac{1}{2\nu}\frac{d\hat{u}_2}{dZ} = 0. \tag{6.47}$$

[1] We note a_2 and $\overline{q}$ vanish when $2\mu = (\mu + 1)\rho$

We remark that $\hat{u}_2$ need not be scaled yet since (6.44) is linear and $\overline{q}$ remains negligible. The solution to this equation is given by

$$\hat{u}_2(Z) = A + Be^{Z/(2\nu)}. \tag{6.48}$$

We now find the constants $\hat{\gamma}$, A and B. First $\hat{\gamma}$ is found from matching the tangential velocity component of the blood at the interface in (6.45) and (6.48), giving

$$\hat{\gamma} = A. \tag{6.49}$$

Second, matching the shear in both fluids at the interface determines the constants A and B. By relating the co-ordinates in the glue to those in the interfacial sub-layer we find $\eta = \tilde{C}_2(1 + \tilde{C}^{-2} Z)$, hence we have the relation $\partial_\eta = \tilde{C}_2 \partial_Z$. Thus we find

$$A = \Gamma \tilde{C}_2 \left(\frac{2}{\rho} - 1\right), \tag{6.50}$$

$$B = \frac{2\Gamma\nu}{\mu \tilde{C}_2}, \tag{6.51}$$

from continuity of velocity and continuity of shear at the interface respectively. Although A is large whereas B is small, the results (6.48)-(6.51) are found to remain valid.

So for large $\tilde{C}_2$ the solutions in the glue and blood are respectively given by

$$\hat{u}_1 = \Gamma \left[\eta + 2\tilde{C}_2 \left(\frac{1}{\rho} - 1\right)\right] \quad \text{for } \eta > \tilde{C}_2, \tag{6.52}$$

$$\hat{u}_2 = \Gamma \tilde{C}_2 \left(\frac{2}{\rho} - 1\right) Y \quad \text{for } 0 < Y < 1, \tag{6.53}$$

$$\hat{u}_2 = \Gamma \tilde{C}_2 \left(\frac{2}{\rho} - 1\right) + \frac{2\Gamma\nu}{\mu \tilde{C}_2} e^{Z/(2\nu)} \quad \text{for } -\infty < Z < 0. \tag{6.54}$$

These solutions agree with the trends in the plots of the velocity profiles for large $\tilde{C}_2$. Figure 6.5 shows the solution for the case $\tilde{C}_2 \to \infty$. In particular equation (6.53) shows that for $\rho > 2$ the velocity in the blood is negative but the presence of the interfacial sub-layer changes the value of the shear in the

interfacial region and hence matches with both the glue shear and glue velocity at the interface, as shown in figure 6.5. Also in this limit the wall shear is given

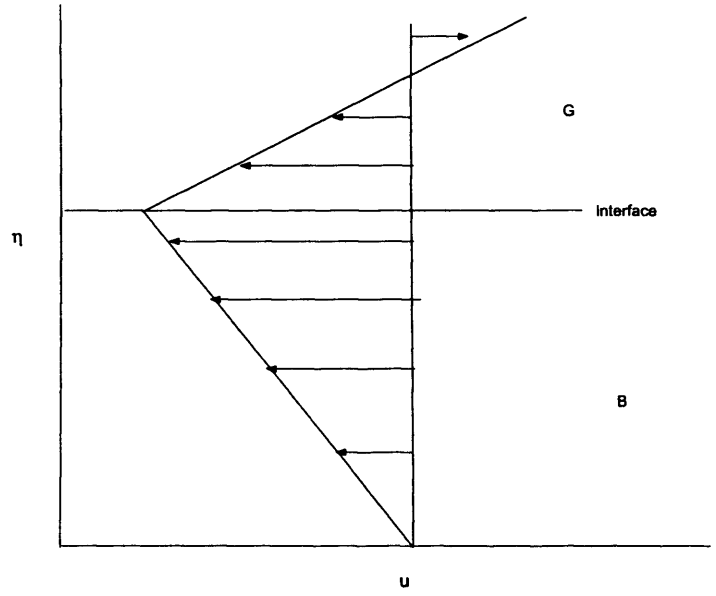

Figure 6.5: Velocity profile in the limit $\tilde{C}_2 \to \infty$ and $\rho > 2$.

by

$$\tau_W = \mu\Gamma\left[\frac{2}{\rho} - 1\right]. \tag{6.55}$$

The interfacial sublayer can also be seen for the cases where $\tilde{C}_2$ is large and $\rho < 2$ as seen for instance in figure 6.3 for the case $\tilde{C}_2 = 10/3$. Here a sharp change in gradient of the velocity profile is seen near the interface $\eta = \tilde{C}_2$.

6.2.3 The case where $\tilde{C}_2$ is small

Next the limiting solution when $\tilde{C}_2$ is small is studied. Figures 6.2-6.4 seem to suggest that small values of $\tilde{C}_2$ result in flow that is forward, no matter what value we take for ρ.

We again make the substitution $\eta = \tilde{C}_2 Y$ but $\tilde{C}_2$ is now small and therefore $\epsilon \gg 1$. The governing equation (6.23) becomes,

$$\epsilon \frac{d^2\hat{u}_2}{dY^2} - \frac{1}{2\nu} Y \frac{d\hat{u}_2}{dY} + \frac{1}{2\nu}\hat{u}_2 - \frac{1}{\mu}\overline{q} = 0, \tag{6.56}$$

therefore has solution $u_2(Y) = \tilde{A}Y$ to leading order. To determine the constant $\tilde{A}$ we match to the glue solution at the interface $\eta = \tilde{C}_2$, giving

$$\tilde{A} = \Gamma \tilde{C}_2 \left(\frac{2}{\rho} - 1\right) + 2\overline{q}, \tag{6.57}$$

and the no-slip condition at the wall is automatically satisfied. The tangential stress condition at the interface demands that

$$\Gamma = \mu\Gamma \left(\frac{2}{\rho} - 1\right) + \frac{2\overline{q}}{\tilde{C}_2}\mu. \tag{6.58}$$

So rearranging for $\overline{q}$ we find

$$\overline{q} = -\frac{\Gamma \tilde{C}_2}{2\mu}\left(\frac{2\mu}{\rho} - \mu - 1\right). \tag{6.59}$$

As a check (6.59) is consistent with the leading order term in the limit $\tilde{C}_2 \to 0$ obtained by analysing equation (6.43).

For $\tilde{C}_2 \ll 1$, plots of the velocity field figures 6.2 and 6.3 seem to suggest that $\hat{u}_2$ is positive (i.e. the flow is forward) no matter which values of ρ and μ we choose, in contrast to the large $\tilde{C}_2$ analysis in the previous section where $\rho = 2$ provided a crossover case.

The quantity $\tilde{A}$ can also be written as $\tilde{A} = \Sigma + 2\overline{q}$ using the notation of section 6.2.2. If $\rho > 2$ we find $\Sigma < 0$, $2\overline{q} > 0$ but $|2\overline{q}| > |\Sigma|$. For $\rho < 2$, $\Sigma > 0$, $2\overline{q} < 0$ but now $|2\overline{q}| < |\Sigma|$. Thus for all values of ρ and μ and $\Gamma > 0$

$$\tilde{A} > 0. \tag{6.60}$$

Accordingly $\hat{u}_2$ is always positive and the flow is forward as figures 6.2 to 6.4 suggest. The velocity profiles in the glue and blood are given by

$$\hat{u}_1 = \Gamma\left[\eta + 2\tilde{C}_2\left(\frac{1}{\rho} - 1\right)\right] + 2\overline{q} \text{ for } \eta \geq \tilde{C}_2, \tag{6.61}$$

$$\hat{u}_2 = \left[\Gamma\tilde{C}_2\left(\frac{2}{\rho} - 1\right) + 2\overline{q}\right] Y \text{ for } 0 \leq Y \leq 1. \tag{6.62}$$

Substituting equation (6.59) into (6.62) gives the leading order blood solution

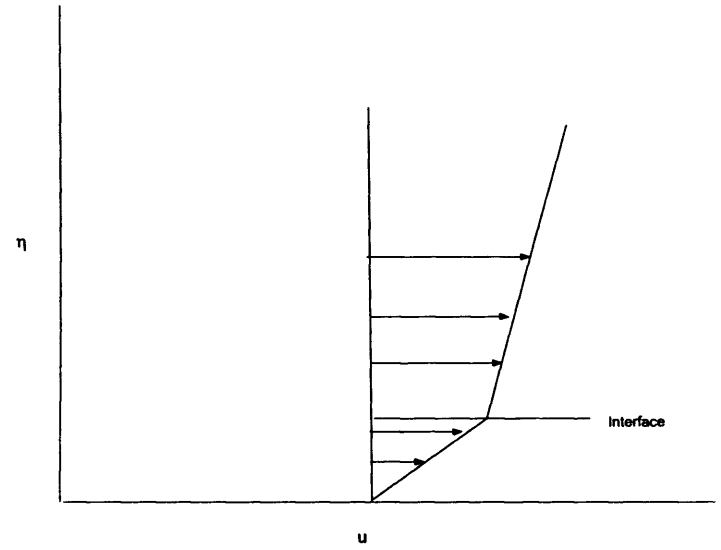

Figure 6.6: Velocity profiles in the limit $\tilde{C}_2 \to 0$ and $\mu < 1$.

as $\hat{u}_2 = \Gamma\tilde{C}_2/\mu$. Hence in this limit the velocity gradient in the blood is $1/\mu$. The limiting velocity profiles are given in figure 6.6 and 6.7, where the form of each is dependent on the viscosity ratio μ. The connection with the results in figures 6.2-6.4 for decreasing $\tilde{C}_2$ values seems clear.

In summary, the case $\tilde{C}_2 \gg 1$ results in an essentially inviscid solution except for a very thin interfacial sub-layer, whereas for $\tilde{C}_2 \ll 1$ the equations reduce to a lubrication approximation. However in this lubrication approximation the pressure gradient term $\overline{q}$ was shown to be small and hence the the second derivative of u stands alone at leading order and the velocity profile is linear. As was shown in this limit, the flow is forward for all values of μ and ρ.

The similarity solution to the negative-time problem with constant $\tilde{C}_1, \tilde{C}_2 \sim 1$ has been fully determined then. Using this analysis as a guide the cases where C_1, C_2 are constant instead will now be examined.

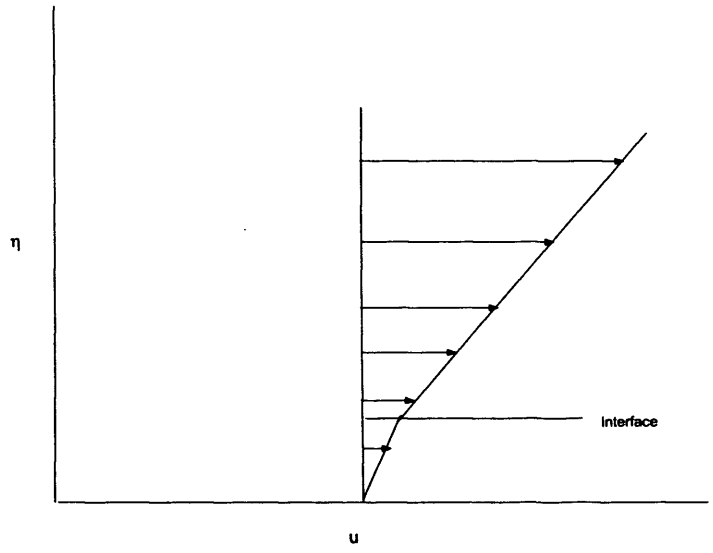

Figure 6.7: Velocity profiles in the limit $\tilde{C}_2 \to 0$ and $\mu > 1$

6.3 The case where C_1, C_2 are constants

In the previous analysis we made use of the relation

$$C_1 = \tilde{C}_1|t|^{-1/2}, \quad C_2 = \tilde{C}_2|t|^{-1/2}, \tag{6.63}$$

with $\tilde{C}_1$ and $\tilde{C}_2$ constants. To consider C_1 and C_2 being order-one constants with time being large and negative we need to take $\tilde{C}_2 \sim |t|^{1/2}$ large as studied in section 6.2.2 to provide a guideline. Again the flow has a similar structure. The transverse scaling now in both the glue and blood is $y \sim |t|$ with t again being large and negative and so we make use of a similarity variable $\hat{\eta} = y/|t|$. The flow again can be split into three distinct regions. We turn our attention to the sub-layer at the interface where viscous effects are still important. From the previous section, we found that the scaling for the sublayer when $\tilde{C}_2 \sim |t|^{1/2}$ was given by equation (6.46). Hence replacing Y in this equation with η and

y in turn leads to the expression for the scaling of the sub-layer

$$y = \tilde{C}_2 |t|^{1/2} + \frac{1}{\tilde{C}_2} |t|^{1/2} Z, \tag{6.64}$$

Now using equation (6.63) we see that when C_1 and C_2 are of order-one the viscous sub-layer has the scaling

$$y = C_2 |t| + \frac{1}{C_2} Z, \tag{6.65}$$

where again $Z = O(1)$. So the flow structure can again be divided into three distinct areas as as shown in figure 6.8, described by:

- $y \sim |t|$ in the blood,
- $y = C_2|t| + \frac{1}{C_2} Z$ in the interfacial sub-layer,
- $y \sim |t|$ in the glue.

First we examine the regions where $y \sim |t|$ in each fluid and set $\hat{\eta} = y/|t|$. Hence the form of the sub-layer is

$$\hat{\eta} = C_2 + \frac{Z}{C_2|t|}, \tag{6.66}$$

for $-\infty < Z \leq 0$. The asymptotic expansions in the glue and the blood in the main regions are given by

$$u_1 = |t|\overline{u}_1(\hat{\eta}) + \cdots, \tag{6.67}$$

$$u_2 = |t|\overline{u}_2(\hat{\eta}) + \cdots. \tag{6.68}$$

Substitution of the expansion for the blood into the governing equation (6.23) shows that the viscous term can be neglected and so we are left with solving

$$-\left(\overline{u}_2 - \hat{\eta}\frac{d\overline{u}_2}{d\hat{\eta}}\right) = 0, \tag{6.69}$$

where q is exponentially small again, as guided by the analysis from section 6.2.2. The simple solution is given by

$$\overline{u}_2 = \delta\hat{\eta}, \tag{6.70}$$

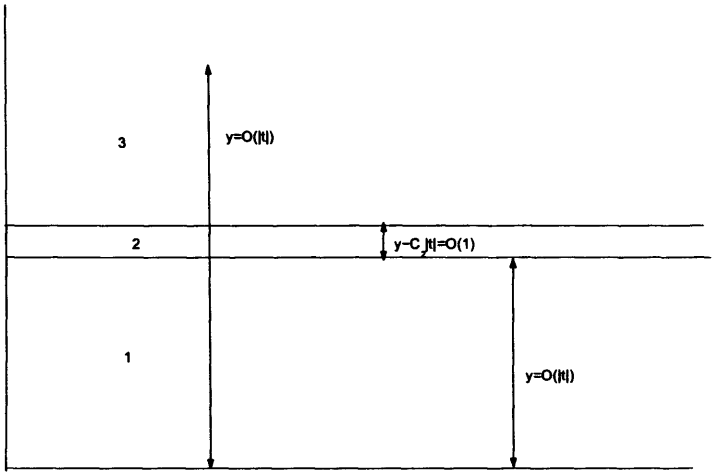

Figure 6.8: The structure for large negative times and $C_2 \sim 1$.

which automatically satisfies the no-slip condition at $\hat{\eta} = 0$. Similarly in the glue, the governing equation now reduces to

$$-\left(\overline{u}_1 - \hat{\eta}\frac{d\overline{u}_1}{d\hat{\eta}}\right) + \Delta C\frac{d\overline{u}_1}{d\hat{\eta}} = 0, \tag{6.71}$$

which has the simple solution

$$\overline{u}_1(\hat{\eta}) = \Gamma(\hat{\eta} + \Delta C). \tag{6.72}$$

So again the glue and blood have fairly simple solutions in the main region $y \sim |t|$.

In the interfacial sub-layer, we have the relations $\partial_y \rightarrow C_2\partial_Z$ and $\partial_t \rightarrow -\partial_{|t|} + C_2^2\partial_Z$. In this region we pose the asymptotic expansion as

$$\hat{u}_2(Z,t) = |\,t|\,\hat{u}_{21}(Z) + \hat{u}_{22}(Z) + \cdots. \tag{6.73}$$

After substitution into the governing equation (6.11) we find balances at $O(|t|)$ and $O(1)$ are

$$\frac{d\hat{u}_{21}}{dZ} = \nu\frac{d^2\hat{u}_{21}}{dZ^2}. \tag{6.74}$$

$$\frac{d\hat{u}_{22}}{dZ} = \nu \frac{d^2\hat{u}_{22}}{dZ^2} + \frac{\hat{u}_{21}}{C_2^2}. \tag{6.75}$$

So the main term in the sub-layer is

$$\hat{u}_{21}(Z) = A_{21} + B_{21}e^{Z/\nu}, \tag{6.76}$$

where, however, the interfacial conditions show that $B_{21} = 0$. Solving the next order term gives

$$\hat{u}_{22}(Z) = A_{22} + B_{22}e^{Z/\nu} + A_{21}Z/C_2^2, \tag{6.77}$$

We use the same method to find the constants A, B, and δ as in the previous section, as the glue solution has already been determined explicitly. Matching the velocity between the blood and the glue using equations (6.70) and (6.76) leads to

$$A_{21} = \Gamma C_1. \tag{6.78}$$

Next matching the two expressions for the blood velocity, that of the sub-layer and the main layer at the interface gives

$$\delta = \frac{\Gamma C_1}{C_2}. \tag{6.79}$$

Next matching the shear we note $\partial_\eta = \frac{1}{C_2}\partial_Z$ and so

$$\Gamma = \mu \left(C_2 \left(\frac{B_{22}}{\nu} + \frac{A_{21}}{{C_2}^2} \right) \right), \tag{6.80}$$

and thus the solution is fully determined. In summary the solution is

- $u_2(\hat{\eta},|t|) = |t|\,\Gamma(C_1/C_2)\hat{\eta} = |t|\,\Gamma\rho\hat{\eta} \quad 0 < \hat{\eta} < C_2,$
- $u_2(Z,|t|) = |t|\,\Gamma C_1 + A_{22} + \left(\frac{\nu\Gamma}{\mu C_2} - \frac{\Gamma C_1 \nu}{C_2^2}\right) e^{Z/\nu} + \frac{\Gamma C_1 Z}{C_2^2} \quad -\infty < Z < 0,$
- $u_1(\hat{\eta},|t|) = |t|\,\Gamma(\hat{\eta} + \Delta C) \quad \hat{\eta} > C_2.$

Here the constant value A_{22} would be determined from the next order, but is small compared to the $O(|t|)$ term and does not affect the matching of shear directly. So in contrast to the previous section, it appears that the flow in the blood is forward at large negative times. This is because of the different chemical-model parameters here.

So this concludes the case where $\tilde{C}_2 \gg 1$ and $C_2 \sim 1$. Hence for large negative times, the positive wall shear is given by

$$\tau_W = \mu\Gamma(C_1/C_2). \tag{6.81}$$

6.4 Small time solution for C_1, C_2 being order-one constants

In a similar vein to the large negative time solution of the $C_2 \sim 1$ problem we can use the analysis from section 6.2.3 where $\tilde{C}_2$ is small and investigate the case where $C_2 \sim 1$ and $|t| \ll 1$. We expect the flow to have a similar structure to that in section 6.2.2, suggesting the asymptotic expansions in the glue and the blood

$$u_1 = |t|\,\overline{u}_1(\hat{\eta}) + |t|^2\overline{\overline{u}}_1(\eta) + \cdots, \tag{6.82}$$

$$u_2 = |t|\,\overline{u}_2(\hat{\eta}) + |t|^2\overline{\overline{u}}_2(\eta) + \cdots, \tag{6.83}$$

$$q = \overline{q} + O(|t|), \tag{6.84}$$

where once more $\eta = y/|t|$. Again the equations of motion are (6.10)-(6.14). As was the case in the previous section the form of the function $A(t)$ is

$$A(t) = (\Gamma\Delta C + \overline{q})|t|\,. \tag{6.85}$$

Substitution of the expansions into the governing equations gives a linear velocity profile again in each fluid, similar to the case where $\tilde{C}_2$ is small as studied

in section 6.2.3. So to satisfy the no-slip condition the constant is set to zero. The matching condition given by $\overline{u}_1 \sim \Gamma(\hat{\eta} + \Delta C) + \overline{q}$ effectively sets the glue solution for all values of $\hat{\eta}$. The solutions in the glue and blood are now given respectively by

$$\overline{u}_1 = \Gamma[\hat{\eta} + \Delta C] + \overline{q} \quad \text{for } \hat{\eta} > C_2, \tag{6.86}$$

$$\overline{u}_2 = \frac{\hat{\eta}}{C_2}\left(\Gamma\frac{C_2}{\rho} + \overline{q}\right) \text{ for } \hat{\eta} < C_2. \tag{6.87}$$

Continuity of velocity at the interface is satisfied and once again the tangential stress condition determines the leading order solution of the pressure gradient $\overline{q}$ to be

$$\overline{q} = \frac{\Gamma C_2}{\mu}\left(1 - \frac{\mu}{\rho}\right). \tag{6.88}$$

Hence substituting this expression back into the velocity profiles in each fluid gives

$$\overline{u}_1 = \Gamma\hat{\eta} + \Gamma C_2\left(\frac{1}{\mu} - 1\right) \quad \text{for } \hat{\eta} > C_2, \tag{6.89}$$

$$\overline{u}_2 = \frac{\Gamma\hat{\eta}}{\mu} \text{ for } \hat{\eta} < C_2. \tag{6.90}$$

It should be noted that as $\hat{\eta} \geq C_2$ in the glue the flow is always forward if C_2 is chosen to be positive. In this regime the wall shear is given by

$$\tau_w = \frac{\Gamma}{\mu}. \tag{6.91}$$

6.5 Overview

When the constants C_1 and C_2 were scaled as $|t|^{-1/2}$, the solution to the governing equations were found to be given by (6.29) and (6.30), where the constants are given by (6.37)-(6.39). The solution of the problem for the two limits $\tilde{C}_2 \to \infty$ and $\tilde{C}_2 \to 0$, were then studied. Analysis and direct computation showed that in the limit $C_2 \to \infty$ reversed flow occurred for

$\rho > 2$. Indeed in this limit an interfacial sub-layer changed the gradient of the velocity profile to match with that in the glue, where the gradient Γ is taken to be positive.

For small values of $\tilde{C}_2$ the flow is forward for all values of ρ and μ and the pressure gradient term $\overline{q}$ cannot be ignored. Again a linear velocity profile is found in both fluids and the interface is now very close to the wall.

For values of C_1 and C_2 of order-one, analysis at large negative times showed that the flow had a similar structure to the case where $\tilde{C}_1$ was large. Again the velocity profiles were linear in each fluid and an interfacial sub-layer was also found. However in this case the flow was always found to be forward in each of the two fluids.

For small negative times, the procedure as explained in section 6.4 is similar to the analysis where $\tilde{C}_2$ was small. Again the velocity profiles in this limit were found to be linear and no flow reversal occurred. Further details are deferred to chapter 11.

An extensive analysis of the wall layer flow has been presented, both with and without chemical effects being incorporated into the model. For the remainder of the thesis it is assumed that both fluids are present in the core of the artery and a numerical approach is used. The next two chapters give a detailed account of the method.

Chapter 7

Review of computational approaches to multiphase flow and the Volume of Fluid method

7.1 Computational approaches to multiphase flow

The solution of the equations of multiphase flow is a difficult task as outlined above. In general the solution of such flows is complicated by the fact that the free surface or interface position is not known in advance and must be determined in the numerical procedure. This, coupled with large density and viscosity ratios between the two fluids and accurate description of surface tension forces at the interface makes multiphase flow dynamics a considerable problem.

The interface must somehow be accurately represented in the numerical model. There are in practice many ways of doing this, a choice of either a fixed grid, a grid that moves with the interface or a grid that moves with the

entire flow may be used. A very brief review of these methods will be given in section 7.1.1.

Whichever method one chooses, there are three main routines that need to be used in the solution of such problems: finding the interface position, solving the equations of motion for each fluid, and moving the interface according to the velocity field. All three of these tasks are complicated in their own right due to the associated non-linearity in the Navier-Stokes equations and interface conditions. Many methods have been developed over the years to try to deal with these complicated flow situations. Here begins a brief review of the main methods, in particular the Volume of Fluid method, which is the method used in this work.

7.1.1 Eulerian and Lagrangian approaches to multiphase flow modelling

There are two main numerical approaches to modelling interfacial fluid flow or fluid flow in general; these are known as Lagrangian and Eulerian methods. In general Lagrangian attempts use a mesh that is not fixed in space to calculate approximations to the equations governing the flow, commonly known as an adaptive grid. In such simulations, grids with high levels of deformation can be used so that the interface actually lies on the grid lines and the interface conditions such as the kinematic condition can be applied easily and accurately. In some cases though, especially when the interface becomes very distorted, problems may arise and mesh entanglement may severely restrict both the accuracy and stability of the numerical procedure [56]. Many techniques have been formulated in order to try and remove such problems; a brief review of these are given by [56]. Generally Lagrangian techniques move points on the interface after the governing equations have been solved to find the location of these points at the next time step. The interface can be found by fitting a

curve through these points to give the new position of the interface.

Eulerian methods, on the other hand, make use of a grid that is fixed in time and space. Using such methods, the fluid underneath the interface is advected rather than just the points on the interface themselves. In general the interface is approximated using some known volumetric data, such as how much fluid is in a particular cell on the grid.

Numerical methods for multiphase flow may also be divided into a further two classes: volume tracking and interface tracking. A brief description of each is now given, although more details of volume tracking methods are given as this is the category into which the Volume of Fluid method belongs.

7.1.2 Volume tracking and interface tracking methods

Computational methods for the simulation of multiphase or free surface flow are generally composed of interface tracking methods and volume tracking methods. In the former the free surface is considered to be a sharp interface whose motion is followed usually with the help of a boundary fitted grid. Interface tracking methods track the individual points x_i on the free surface or interface and aim to solve the equation

$$\frac{dx_i}{dt} = u_i, \tag{7.1}$$

where u_i is the velocity of the interface at the point x_i. This Lagrangian formulation has been studied extensively, see references in [77] and can produce accurate results.

Volume tracking methods on the other hand use a fixed grid and the free surface is allowed to move smoothly over the grid cells. Volume tracking methods do not store an accurate description of the interface but rather construct it only when necessary. The shape of the interface is determined by analysis of cells that are partly full of fluid. The amount of fluid in such cells determines

the shape of the interface using reconstructive methods which will be discussed in the next section. Methods of this type use a grid which is fixed in time and space.

Both types of method have their advantages and disadvantages. For instance, moving grids may be inaccurate when the free surface shape is changing dramatically and the grid can become highly skewed. Unstructured grids attempt to overcome these limitations but complex flow dynamics can still not be handled with these methods. Volume tracking methods can, on the other hand, deal with phenomena such as breaking waves and reconnection of fluid interfaces. There may be problems implementing the free surface boundary conditions in the volume tracking methods though. Traditionally the first method of this type was the Marker and Cell method [31]. Although this method started out as a method for free surface flows, it became a very popular method for solving the Navier-Stokes equations with no free surface in two and three dimensions in the 1970s and 1980s. There are limitations to this method though and now the main two volume tracking methods used are the Volume of Fluid (VOF) method and Level Set Method.

7.1.3 Interface tracking methods

The best known types of interface capturing methods are the boundary integral method and front tracking. Front tracking is a Lagrangian technique on a fixed grid and works by moving marker particles which represent the interface. It is distinguished from the Marker particle method in that the particles are located only on the interface, rather than in a volume region near the interface. Typically one or two particles are used per cell and so it is significantly faster than other marker type methods. Figure 7.1.4 shows a given distribution of marker particles. Care must be taken that the marker particles are evenly distributed over the interface for accurate solution to these problems.

The boundary integral or boundary element method again uses marker particles and the solution to the flow in the whole domain is calculated just from this information. The main advantage of such methods is that they transfer a two-dimensional problem to a one dimensional problem and avoid discontinuities of variables across the material interface [100].

7.1.4 Volume tracking methods

Marker and Cell method

The Marker and Cell (MAC) method is due to Harlow and Welch [31], [99] and was one of the first main numerical methods used for free surface flow calculations. This volume tracking type algorithm again uses massless marker particles but now distributed over the total fluid not just the interface. These particles define the position of the free surface on a fixed Cartesian grid. Once the governing equations of the flow are solved, the particles are advected with this velocity field in a Lagrangian manner. Cells with no marker particles are supposed to be free of fluid, and cells with an empty neighbour define cells with a free surface.

Originally the MAC-method was used only for free surface flows but it was developed for multiphase flows in [99] and the Rayleigh-Taylor instability was studied between two fluids of differing densities. A drawback of the Marker and Cell method is that keeping a sharp boundary between the two fluids can be difficult; this can affect the implementation of boundary/interface conditions, especially conditions on the pressure.

Many of the ideas in the Marker and Cell method extend naturally to the VOF method. Although this method is dated and not computationally efficient, it can deal with complicated flow scenarios such as breaking waves and splashing.

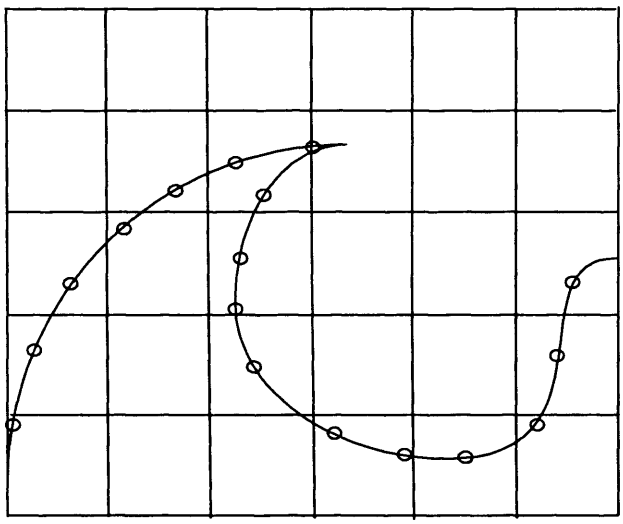

Figure 7.1: Markers particles representing the interface as used in the Markers method.

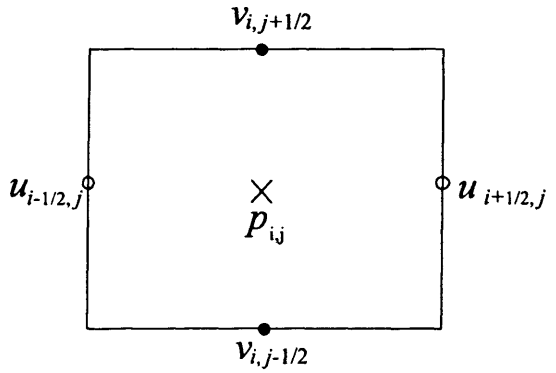

Figure 7.2: Marker and Cell type grid.

Level Set method

The Level Set method is a method for analysing the motion of an interface in two and three dimensional flows, and was first described in [80]. Here a continuous function $\phi(\mathbf{x},t)$ is introduced where ϕ gives the distance of the point $\mathbf{x}$ from the interface. Here ϕ is given by

$$\phi(\mathbf{x},t) > 0 \quad \text{if } \mathbf{x} \in \Omega_1, \tag{7.2}$$

$$\phi(\mathbf{x},t) < 0 \quad \text{if } \mathbf{x} \in \Omega_2, \tag{7.3}$$

$$\phi(\mathbf{x},t) = 0 \quad \text{if } \mathbf{x} \in \partial\Omega, \tag{7.4}$$

where Ω_1 and Ω_2 refer to two different fluids and $\partial\Omega$ represents the interface. So the interface is defined to be the set $\Gamma(t) = \{x| : \phi(\mathbf{x},t) = 0\}$. Similarly to the VOF method, we wish to solve the non-linear advection equation

$$\frac{\partial\phi}{\partial t} + \mathbf{u}.\nabla\phi = 0, \tag{7.5}$$

where $\mathbf{u}$ is the velocity of the interface. The solution to the advection equation only needs to be solved locally near the interface. A Level Set procedure generally consists of solving this equation coupled with a re-initialisation scheme. In the Level Set method the interface is not sharply reconstructed, it does however have a finite thickness and properties such as viscosity and density vary smoothly over this transition region. Typically a Heaviside function is used to calculate the density and viscosity in this transitional region. In this region no conditions need to be set at the interface which is a main difficulty in other numerical methods. Once equation (7.5) has been solved, estimates to the normal and curvature can be obtained from

$$\mathbf{n} = \frac{\nabla\phi}{|\nabla\phi|}, \qquad \kappa = \nabla.\left(\frac{\nabla\phi}{|\nabla\phi|}\right). \tag{7.6}$$

The reinitialization scheme makes sure that ϕ retains a value for distance from the interface and basically ensures that the interface thickness is constant in

time. This stage involves the solution of a Hamilton-Jacobi type equation [81] and can often be the source of error in Level Set methods.

The discretization of equation (7.5) is very important for the mass conservation properties of the method. Generally Level Set methods do not conserve mass as well as VOF methods. However the calculation of the interface normal and curvature are more accurate than in VOF methods; this is due to the fact that the advection equation is solved for a continuous function rather than the discontinuous colour function in the VOF method. Both methods are Eulerian in nature and recent work [90] has seen them combined to give the CLSVOF Coupled Level-Set Volume of Fluid algorithm which uses the most desirable features of each method.

Overview

Generally the main attributes that a numerical scheme involving the evolution of an interface should possess are

- Mass conservation of each fluid,
- Easily extendable to three dimensions and complex geometries,
- Ability to incorporate additional physical features such as surface tension, phase change etc.

There are difficulties in obtaining the desired features listed above. The interfacial boundary conditions are of non-linear type (kinematic boundary condition) and involve singular force terms such as surface tension. To calculate the surface tension across an interface, an accurate estimate of the curvature must be found which again can cause difficulties. The jump in density and viscosity at the interface also causes problems in the solution of the Navier-Stokes equations; this will be described in chapter 8.

There are many other numerical schemes used for interfacial flows which will not be discussed in depth here. Some examples are Smoothed Particle Hydrodynamics (SPH), where no mesh is needed; an idea borrowed from astrophysics [88], The Particle In Cell method (PIC) [19]; and the Diffuse Interface method [22] in which a Cahn-Hilliard type equation is solved for the evolution of the interface, an analogue of equation (7.5). A very powerful method for free surface flows is the Arbitrary Euler-Lagrange method (ALE method) [34]. Here the most desirable parts of the Eulerian and Lagrangian approaches are kept. The advantage of this method is that it allows a very accurate description of the free surface or interface but the problem of mesh tangling when the interface is geometrically complicated is reduced [56].

Although all the methods probably could be applied here to the problem of embolization, the Volume of Fluid method was chosen. As well as being extremely accurate, the VOF method does not require a large amount of computer memory and does not require any complicated meshing techniques compared to some of the methods described above. A Cartesian grid is used throughout.

7.2 Volume of Fluid method

The first VOF methods where introduced at Los Alamos in the late 1970s and came to prominence in the early 1980s [35]. The method is used in numerical solution to multiphase flows or flows where a free surface is involved. The VOF method does not aim to track the interface explicitly, but rather the volume of fluid in each computational cell is calculated at each time step by solving a non-linear advection equation; from this the new volumes in each computational cell are updated. The interface is now reconstructed at this time step using the new volumes, although a given distribution of volume data does not guarantee

a unique interface [72]. The main advantage of the VOF method over other schemes is that no special treatment is needed if the interface breaks up, for example droplet deformation, and breaking waves can be treated accurately. Also the method can be extended to deal with three dimensional problems.

In general the VOF method itself consists of two main parts: reconstructing the interface by using some volumetric given data, and advecting the interface with the current velocity field. After advection, new volumes are found and then the interface can be reconstructed again. In practice there are many different methods for each of these two steps: a review of the main reconstruction and advection algorithms will be given in section 7.3.

Examples of flows that have been studied with the VOF method are: waves at a ship side [43] and tsunamis, splashing of droplets [68], [70], and atomization [11]. The method can also deal with complexities such as turbulence [16], non Newtonian flows [42] and flows with changes of state, for example solidification [69].

7.2.1 VOF codes

The first codes devoted to modelling free surface flows were introduced in Los Alamos using the Marker and Cell approach [31]. The MAC method [99] was later followed by the Simplified Marker and Cell (SMAC) method [3]. The first main code developed at Los Alamos using the VOF method was the code SOLA-VOF, [59] an extension of the SOLA algorithm [32] to treat free surface flows. This could handle free surface viscous flow and was the starting point for many other codes developed there. The next development was the code NASA-2DVOF [96], which used an Eulerian approach for solving the interface advection and again a finite-difference formulation for the governing equations. This was followed by NASA-3DVOF, an extension of the algorithm to three dimensions. RIPPLE [44], also developed at Los Alamos, is able to incorporate

the effects of contact angle at a solid surface and surface tension effects. It also uses a partial cell treatment for cells which are only partially open to flow. More recently the codes SURFER [45] and GERRIS have come to prominence. GERRIS [66] is open source software with many powerful features, such as adaptive mesh refinement, multigrid methodology for the solution of Poisson type equations, second-order Godunov-type advection scheme and ability to handle complex boundaries.

7.2.2 General outline of the method

In order to determine the position of the interface, we need some measure of how much fluid is in each computational cell, as explained in the previous section. We define the colour function C to be a discrete analogue of the well known characteristic function $\chi(x, y, t)$ which, in this context, is given by

$$\chi(x,y,t) = \begin{cases} 1 & \text{if the point } (x,y) \text{ is in fluid (1),} \\ 0 & \text{if the point } (x,y) \text{ is in fluid (2).} \end{cases} \tag{7.7}$$

The colour function is defined to be 1 if the cell under consideration is full of fluid (1), 0 if the cell is full of fluid (2). When $0 < C < 1$, the cell is cut by the interface or free surface and is termed an interface cell. The value of the colour function in this case is the fraction of the cell that is full of fluid. Hence we can write

$$C_{ij} = h^2 \int \int_S \chi(x,y,t) dx dy, \tag{7.8}$$

where S indicates the (i,j)th cell, and h is the side of the square cell. [1] Figure 7.3 gives an example of different volume fractions associated with the given interface. Values for the colour function are known at the start of the computational cycle and are updated at every time step, indeed only values

[1] Throughout we will assume that the grid has equal grid spacing in all directions, however this method is easily extended to non uniform Cartesian grids.

for the colour function are needed to reconstruct the interface. There are many different ways of reconstructing the interface and a brief review will be given in the next section. In this thesis we make use of the Piecewise Linear Interface calculation (PLIC) method [109]. After the interface position has been found it must be advected with the current velocity field; this is the second main ingredient of VOF algorithms. The equation for advection of the colour function is given by

$$\frac{\partial C}{\partial t} + \mathbf{u}.\nabla C = 0. \tag{7.9}$$

This equation is essentially a discrete version of the kinematic condition. There are in practice many ways of solving such hyperbolic equations: common methods include FCT (Flux corrected transport) [74], ENO (Essentially non-oscillatory) and 5th order WENO (Weighted essentially non-oscillatory schemes) [48]. Here we use a Lagrangian approach to solve this evolution equation for the colour function, similar to [50]. This method is of a geometric nature and involves the calculation of areas in 2 dimensions and volumes in three dimensions. In this work we employ a direction split approach, so the equation is solved in two stages, first in the x-direction and then in the y-direction. This simplifies the solution of the advection equation considerably. As stated earlier, the two main components of the VOF method are the reconstruction of the interface and the advection of the interface with the given velocity field. Before the method of choice in this work is described, the PLIC method, a brief review of the most fundamental reconstruction and advection algorithms is given.

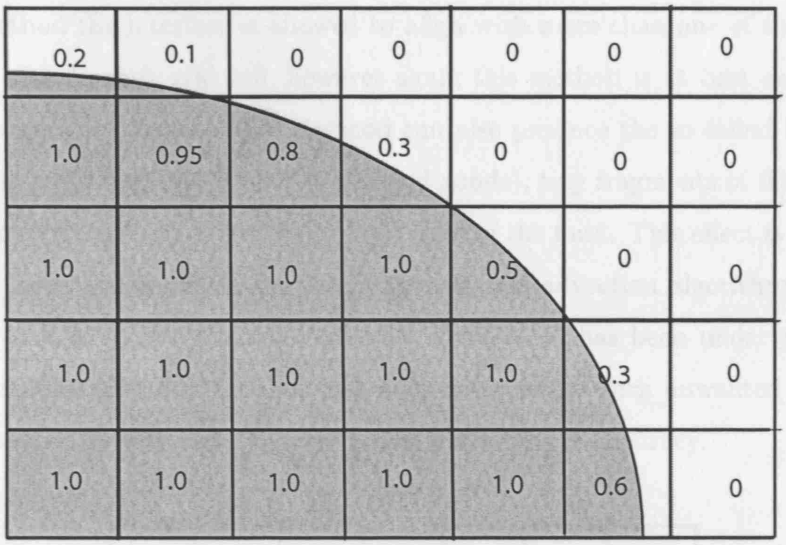

Figure 7.3: Volume fractions on a regular Cartesian grid. Shaded volumes represent fluid.

7.3 Review of interface reconstruction and advection methods

7.3.1 Simple line interface calculation (SLIC)

The oldest method of reconstructing the interface given the volume fractions, is the Simple Line Interface calculation (SLIC) [60]. In this method the interface is aligned to be parallel to either of the coordinate axes in the given cell. The interface is reconstructed using the volume fractions in a row of three cells, where the central cell contains the interface. This algorithm uses an operator split approach and the direction of advection for the interface is performed separately in the two or three spatial dimensions. Hirt and Nichols extended the SLIC method to a stair stepped direction split method [35]. In

this method the interface is allowed to align with more than one of the coordinate axes in each grid cell, however again this method is at best only first order accurate [67]. The SLIC method can also produce the so called flotsam (floating wrecking) and jetsam (jettisoned goods), tiny fragments of fluid that disconnect from the free surface or main bulk of the fluid. This effect is caused by the lack of accuracy in the reconstruction and advection algorithms. Due to the lack of accuracy of such schemes, much work has been undertaken to find a reconstruction algorithm that does not produce such unwanted results and that can reconstruct the interface to second order accuracy.

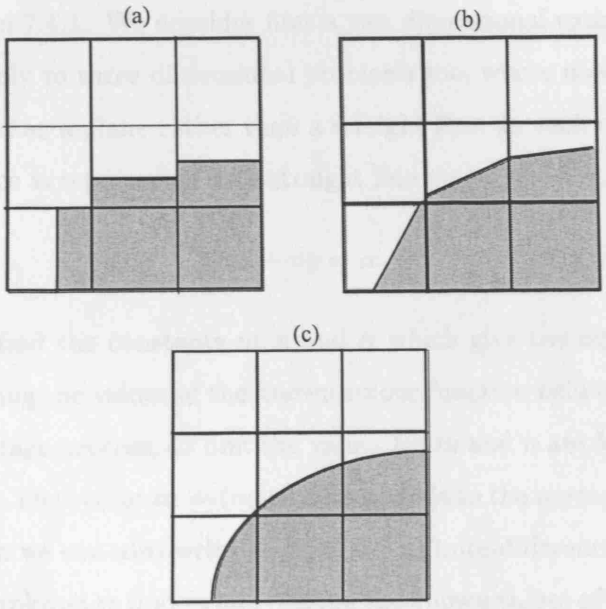

Figure 7.4: (a) The SLIC representation of the interface, (b) PLIC, and (c) the actual interface position.

7.3.2 Piecewise Linear interface calculation (PLIC)

An improvement to SLIC type algorithms is the piecewise linear interface calculation type reconstruction. Here the interface is not forced to align with the mesh and can cut arbitrarily through the cells. This gives a much more accurate representation of the interface in general, although in three dimensions efficient algorithms are difficult to find. In these methods the segments of interface in each cell are again not forced to join up, and so the interface remains discontinuous. The first main type of PLIC type reconstruction was formulated by Youngs [109]; this is the method used here and it will be described in detail in section 7.4.1. We consider first a two dimensional example but generalizations apply to three dimensional problems too, where now the interface is approximated as a plane rather than a straight line. In each computational cell the interface is represented as a straight line

$$mx + ny = \alpha. \tag{7.10}$$

The aim is to find the constants m, n and α which give the equation for the straight line using the values of the known colour function field only. This is in essence a two stage process, so first the values for m and n are found and then the constant α. The vector $\mathbf{m} = (m, n)$ corresponds to the normal vector to the interface, which we can also write as $\mathbf{m} = \nabla C$. Finite-difference forms of this equation are employed to find m and n using the known values of the scalar field C; usually a block of (3 x 3) computational cells are used in this estimation. Once the normal vector is found, the slope of the approximate interface is known and so the problem reduces to finding the equation of a straight line with known slope, which bounds an area Ch^2 for each computational cell. Hence the given equation for the segment of interface in the computational cell is determined.

An improvement to Youngs' method is the Efficient Least squares Volume

of Fluid interface reconstruction algorithm (ELVIRA) [65]. This method is an extension to the well known LVIRA algorithm and is second order accurate.

There are many other reconstruction algorithms that are currently in use, for example the center of mass algorithm and the linear and quadratic least squares fit methods described in [65].

7.3.3 Review of the main advection schemes used in the Volume of Fluid method

As stated previously, both Eulerian and Lagrangian techniques have been used to solve such equations. Three popular advection schemes that are direction split are

- Lagrange explicit-Lagrange explicit (LE-LE) method,
- Euler explicit-Euler explicit (EE-EE) method,
- Lagrange explicit-Euler implicit (LE-EI) method.

The governing equation for the interface advection equation (7.9) can be rewritten in the conservative form

$$\frac{\partial C}{\partial t} + \nabla.(\mathbf{u}C) = 0. \tag{7.11}$$

This effectively states that the conservation of mass of the system is equivalent to the conservation of volume of each phase of the two or more fluids [78]. The Lagrangian scheme used here uses operator splitting. This is the method of choice for this work and it is described fully in section 7.5. In this scheme the interface is advected, and afterwards fluxes to the nearby cells are calculated geometrically and the colour function is updated. Eulerian attempts to solve the advection equation have been used for many years in VOF type problems for instance in SOLA-VOF [59] and are probably more commonly used for such

problems. Explicit Eulerian methods such as those used in NASA 2D-VOF [96] and RIPPLE [44] take explicit finite-differences of equation (7.9) and solve directly for the value of the colour function at the next time step. This is very similar to the Lagrange explicit (LE-LE) method [28]. The only difference now is in the calculation of the fluxes. In the LE-LE method the interface is advected and then the fluxes calculated and the reverse is true for the Eulerian method. Recent advances [72] recast the advection equation (7.9) as

$$\frac{\partial C}{\partial t} + \mathbf{u}.\nabla C = C\nabla.\mathbf{u}, \tag{7.12}$$

with the term on the right hand side being known as the divergence correction. With this term on the right hand side of the equation it is found that volume-filling constraints are adhered to more closely [72]. This equation is integrated from time level n to $n+1$. Again this is an operator split method and the finite-difference form of equation (7.9) is solved as

$$C_{i,j}^{(*)} = C_{i,j}^{(n)} + (F_{\text{left}} - F_{\text{right}}) + C_{i,j}^{(n)}(u_{\text{right}} - u_{\text{left}})\tau/h, \tag{7.13}$$

in the x-direction and

$$C_{i,j}^{(n+1)} = C_{i,j}^{(*)} + (G_{\text{bottom}}^{*} - G_{\text{top}}^{*}) + C_{i,j}^{(n+1)}(v_{\text{bottom}} - v_{\text{top}})\tau/h, \tag{7.14}$$

in the y-direction. Here F and G are the fluxes in the x- and y-directions respectively, and τ is the time step. It should be noted that this method is implicit in nature as $C^{(n+1)}$ appears on the right hand side of the equation for the second step and the fluxes G^{*} are calculated with the colour function field $C^{(*)}$. Replacement of the term $C^{(n+1)}$ on the right hand side of equation (7.9) with $C^{(n)}$ gives the discrete representation of the Euler explicit or Lagrange explicit case, although the fluxes are calculated differently here as remarked on above. Although these methods are adequate they do not conserve mass exactly [78].

A further improvement to these methods is the LE-EI method as described by [78], however the split version still does not conserve mass. A recent development to this is an un-split version which uses an area preserving linear mapping method. Details are given in [6]. It is found that the method both conserves mass and obeys the consistency relation

$$0 \leq C_{i,j} \leq 1. \tag{7.15}$$

This method can also be extended to three dimensions.

Next follows a detailed description of the method used in this thesis, Youngs' method for reconstruction and a Lagrangian advection algorithm, the LE-LE method.

7.4 Volume of Fluid method using Youngs reconstruction and an explicit Lagrangian approach for advection

7.4.1 Parker and Youngs method

The reconstruction of the interface used in this work uses the Parker and Youngs algorithm [109], [50]. Although only a first order accurate method it has a proven ability to deal with deforming interfaces and complex interface topology. The method has been described for two dimensional flow simulations by [50] and its extension to three dimensions in [77].

Again at the beginning of the computational cycle we have values for the colour function in each computational cell in the domain. Using these we can find an estimate to the normal vector to the interface: here it is given by

$$\mathbf{m} = \nabla C, \tag{7.16}$$

where, as described in section 7.3.2 we take the normal to the interface to be the vector $\mathbf{m} = (m, n)$. In order to find the normal we need to discretize equation (7.16), where here the scalar field C is known. We find an estimate to equation (7.16) at each of the four corners of the cell, for example at the top right hand corner, the derivatives of the colour function in the x- and y-directions are given respectively by

$$m_{i+1/2,j+1/2} = \frac{1}{2h}(C_{i+1,j} + C_{i+1,j+1} - C_{i,j} - C_{i,j+1}), \tag{7.17}$$

$$n_{i+1/2,j+1/2} = \frac{1}{2h}(C_{i,j+1} + C_{i+1,j+1} - C_{i,j} - C_{i+1,j}), \tag{7.18}$$

where again h is the side length of the cell. Similar expressions are easily reproduced for the other three corners. Then the two components for the normal of the (i, j) th cell are given as the average of the respective components at the four corners

$$\mathbf{m}_{ij} = \frac{1}{4}(\mathbf{m}_{i+1/2,j+1/2} + \mathbf{m}_{i-1/2,j-1/2} + \mathbf{m}_{i+1/2,j-1/2} + \mathbf{m}_{i-1/2,j+1/2}). \tag{7.19}$$

In order to find the equation of the straight line we need to find the line constant, i.e. α from equation (7.10). However as the slope of the line is known from the normal calculation, and the area under the line $C_{i,j}$ is also known, this task is straightforward.

Calculation of the constant α

Consider a cell of length h in both the $x-$ and y-direction, with associated volume fraction C. The area under the interface and bounded by the cell is then given by $A = Ch^2$. If we suppose that the equation of the interface in each cell is given by $mx + ny = \alpha$, then we need now to find the constant α such that the line with gradient $-m/n$ bounds an area Ch^2.

Let us first assume that $0 < m \leq n$, with $m, n < 0$. We see that there are three ways in which the line can cut the side of the square, as shown in

figure 7.5. The area under the line and bounded by the square is of course Ch^2. When the interface passes through the bottom right hand corner of the cell, the area is given by $m/2n$ and when it passes though the top right hand corner it is $1 - m/2n$. It turns out that the method of determining α depends on which of the situations in figure 7.5 that we are considering. By finding the area under the interface in each of the three situations and rearranging for α we find that

$$\alpha = h\sqrt{2Cmn} \quad \text{if} \quad 0 < C \leq C_1, \tag{7.20a}$$

$$\alpha = h(2Cn + m)/2 \quad \text{if} \quad C_1 < C < C_2, \tag{7.20b}$$

$$\alpha = h\left(n + m - \sqrt{2mn(1-C)}\right) \quad \text{if} \quad C_2 \leq C \leq 1, \tag{7.20c}$$

where here $C_1 = m/2n$ and $C_2 = 1 - C_1$. Once α is found the interface has been reconstructed in each of the computational cells where $0 < C < 1$.

When $0 < n \leq m$, the values of m and n can be interchanged and α calculated with the above formulae. Here we are effectively just rotating the interface to one of the three cases in figure 7.5, but crucially the area under the interface is still exactly the same. All other combinations of positive and negative values of m and n can be transformed to these three cases using basic symmetry arguments. With α now known explicitly, the equation of the straight line representing the interface is at hand.

It must be pointed out that the Parker and Youngs' scheme is only first order accurate, compared to the ELVIRA algorithm which is truly a second order accurate method. In three dimensional flows, the present calculation for α is usually replaced with a Newton iteration scheme or Brent's algorithm. In this case, planes rather than straight lines represent the interface and many combinations of the planes cutting the computational cells are possible.

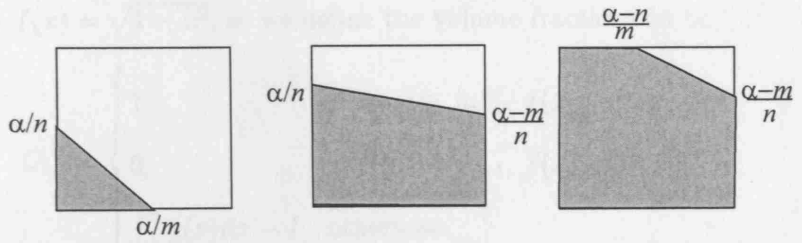

Figure 7.5: The three different ways the interface can cut the cell when $0 < m \leq n$.

7.4.2 Tests on the stationary reconstruction algorithm

A traditional Marker and Cell type grid is used for the position of the velocity components, for each cell the component of velocity in the x-direction is positioned on the right hand side of the cell and the vertical velocity is positioned in the centre of the top edge of the cell as shown in figure 7.2. The scalar quantities, pressure and colour function are defined in the centre of the cell. The left hand edge of the cell is defined to be the position x_{i-1} and the right hand side x_i and similarly the bottom is given by y_{i-1} and the top y_i. In this work we will always have that $\Delta x = \Delta y$ so that the grid spacing will be the same throughout the grid.

The Parker and Youngs algorithm described above is tested on the reconstruction of two simple shapes, namely a circle and an ellipse. Considering the circle first, we take a circle of unit radius positioned inside a uniform square Cartesian grid of length 2. The first thing to do is to calculate the volume fractions in each cell in the computational domain. As both the circle and ellipse are symmetric we only need to calculate the volume fractions in one quadrant; we choose the positive x- and positive y-quadrants here for convenience. We define the position of the (i, j)th cell to be such that in the cell $x_i \leq x \leq x_{i+1}$ and $y_j < y < y_{j+1}$. The explicit form of the interface in this quadrant is given

by $y = f(x) = \sqrt{1-x^2}$, so we define the volume fractions to be

$$C_{i,j} = \begin{cases} 1 & \text{if } f(x_i) > y_{j+1},\ f(x_{i+1}) > y_{j+1}, \\ 0 & \text{if } f(x_i) < y_{j+1},\ f(x_{i+1}) < y_{j+1}, \\ \int_0^h g(x)dx - I & \text{otherwise.} \end{cases} \tag{7.21}$$

Here $g(x)$ is defined as

$$g(x) = \begin{cases} h & \text{if } f(x) > h, \\ 0 & \text{if } f(x) < 0, \\ f(x) & \text{otherwise,} \end{cases} \tag{7.22}$$

and I is the area under the curve but not in the cell under consideration. There are four ways in which the interface in this quadrant can pass through the cell as shown in figure 7.6. The area under the curves in these cells is calculated by numerical integration using the trapezoidal rule. Care must be taken to find the area just in the cell rather than the total area under the curve. In case (2) we need to calculate the total area under the curve from the points x_L to x_R and then subtract the area beneath the (i,j) th cell. We use the same method also for the other three cases. Here though we must also find the x-or y-points where the curve cuts through the (i,j)th cell.

Once the volume fractions are found, the constants m and n are calculated in each cell from equations (7.17)-(7.19). Then α is found from equations (7.20a)-(7.20c).

7.5 Advection of the interface

Once the interface has been reconstructed, the computational cycle is ready to proceed to the next stage, moving the interface with the prescibed velocity field. As outlined above, the method of choice here is the direction split explicit

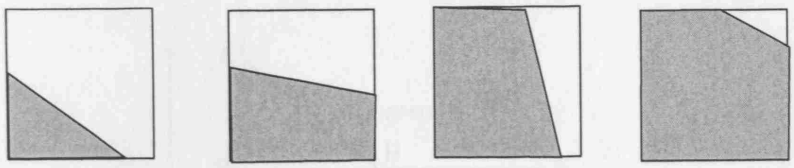

Figure 7.6: Initialisation of volume fractions. The four different ways that an interface can pass through a cell, when considering the positive quadrant.

Lagrangian method, or LE-LE method. The advection is carried out separately in each spatial direction by means of a geometric calculation of area in 2 dimensions and volume in 3 dimensions. The method is the CIAM (Calcul d'interface affine par-morceaux) method of Li and Zaleski described in two dimensions in French by [50] and 3 dimensions by [28].

7.5.1 Calculation of area, the area function A

We turn now to the evaluation of the area under the interface in the given computational cell, i.e. calculating the colour function given the equation of the interface, in this case $mx + ny = \alpha$. Figure 7.7 demonstrates a certain situation where $m > n > 0$. It turns out that we will need to be able to evaluate this area on an $[h_1 \times h_2]$ rectangle even if we are using a grid where the mesh spacing is equal in both the coordinate directions. The area of the rectangle bounded by the line is given by

$$A = \frac{\alpha^2}{2mn}\left[1 - H(\alpha - mh_1)\left(\frac{\alpha - mh_1^2}{\alpha}\right) - H(\alpha - nh_2)\left(\frac{\alpha - nh_2^2}{\alpha}\right)\right], \tag{7.23}$$

where $H(x)$ is the Heaviside function given by

$$H(x) = \begin{cases} 0 & \text{if } x < 0, \\ 1 & \text{if } x \geq 0. \end{cases} \tag{7.24}$$

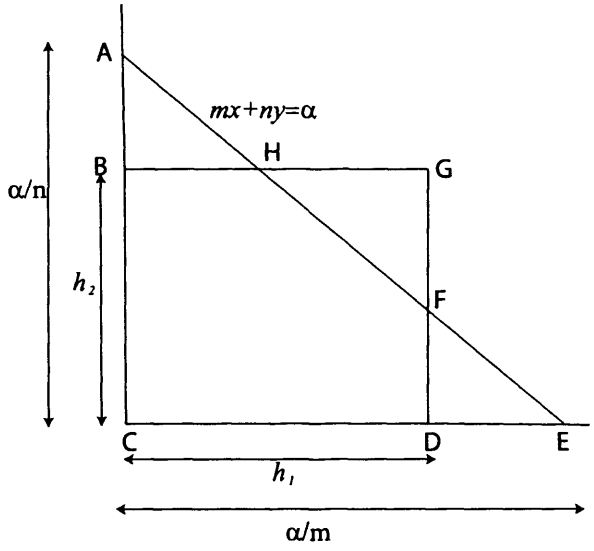

Figure 7.7: The interface cutting through the computational cell. Given the volume fraction C and the slope of the line, a unique line constant α determines the equation of the interface.

Here the first term corresponds to the area of the large triangle ACE and the second two terms correspond to the two smaller triangles ABH and FDE. So given the equation for the straight line in the form $mx + ny = \alpha$, equation (7.23) gives us the area. In this work a function $\text{vol}(m, n, \alpha, a, b)$ gives the area bounded by the straight line $mx + ny = \alpha$ in the $[a \times b]$ rectangle. The situation in figure 7.7 is for the case where $m < 0$ and $n < 0$ but the others apply again using symmetry arguments. So now we have the two results: The forward formulae, i.e. given the equation of the interface, calculate the area or volume fraction, and the backward formula, i.e. given the area find the equation of the interface. In practice the interface is advected and the new volume fractions are found using the forward formula. With these new volume fractions the new position of the interface is determined using the backwards formula, first calculating the normal to the interface and then the line constant

α as discussed in section 7.4.1.

7.5.2 Equation of interface after advection

Let us consider an interface segment in cell (i, j) with equation $mx + ny = \alpha$. First the line segment is moved in the x-direction. The velocities in this direction are only defined on the sides of the cells but a simple linear interpolation gives the velocity at any point across the width of the cell as

$$u(x) = u_{i-1/2,j}\left(1 - \frac{x}{h}\right) + u_{1+1/2,j}\frac{x}{h}, \tag{7.25}$$

where $0 \leq x \leq h$. It should be noted though that this component of velocity is taken not to vary over the edge of the cell where it is assigned. To consider the motion of the interface in a time step $\tau = t^{n+1} - t^n$, we must find how the equation for the interface segment changes. During a time step a point on the interface x will be moved to a new point x^* given by

$$x^* = x + u(x)\tau, \tag{7.26}$$

$$= x + \left(u_{i-1/2,j}\left(1 - \frac{x}{h}\right) + u_{1+1/2,j}\frac{x}{h}\right)\tau. \tag{7.27}$$

Rearranging for x we find

$$x = \frac{x^* - u_{i-1/2j}\tau}{1 - u_{i-1/2,j}\tau/h + u_{i+1/2,j}\tau/h}. \tag{7.28}$$

So substituting back into the original equation for the interface gives

$$m^*x^* + ny = \alpha^*, \tag{7.29}$$

where

$$m^* = \frac{m}{1 - u_{i-1/2,j}\tau/h + u_{i+1/2,j}\tau/h}, \tag{7.30}$$

$$\alpha^* = \alpha + \frac{m\tau u_{i-1/2j}}{1 - u_{i-1/2,j}\tau/h + u_{i+1/2,j}\tau/h}. \tag{7.31}$$

Thus (7.29) gives the new equation for the interface after advection. As expected, if the two velocities $u_{i-1/2,j}$ and $u_{i+1/2,j}$ are equal the slope of the segment remains the same and only the constant α is different, so the interface is moving with a constant velocity in the x-direction in this case.

7.5.3 Calculation of new volume fractions

Once the new position of the interface has been found we need to find the new volume fractions associated with its new position. For each cell three calculations are made.

- ϕ_R:- The amount of fluid entering the cell $(i+1, j)$ from the cell (i, j),
- ϕ_0:- The amount of fluid which is still in the cell (i, j),
- ϕ_L:- The amount of fluid entering the cell $(i-1, j)$ from the cell (i, j).

Figure 7.8 shows a typical scenario where in this case the velocity $u_{i-1/2,j}$ is positive and $u_{i+1/2,j}$ is negative. In this situation there are three contributions to the new volume fraction in the cell (i, j).

If, for instance, the velocity $u_{i+1/2,j}$ were positive, there would be no contribution ϕ_R. First we describe how ϕ_0 is calculated. So the equation of the advected interface in the cell (i, j) is $m^*x^* + ny = \alpha^*$. The left hand edge of this segment travels a distance $u_{i-1/2,j}\tau$ after one time step, as is shown in figure 7.8. We now change the coordinate system so this left edge lies on the axis, hence we let

$$\overline{x} = x^* - u_{i-1/2,j}\tau. \tag{7.32}$$

This is carried out so the area may be calculated more easily, indeed in this case we may use equation (7.23) directly to find ϕ_0. Using this transformation, the equation of the interface segment is now

$$m^*\overline{x} + ny = \alpha^* - mu_{i-1/2,j}\tau = \alpha. \tag{7.33}$$

Similar transformations are used in order to calculate the other two contributions ϕ_R and ϕ_L.

The three components for the (i,j)th cell are given by

$$\phi_0 = \mathrm{vol}(m^*, n, H(u_{i-1/2,j})\alpha + H(-u_{i-1/2,j})\alpha_L^*, \Phi, h), \tag{7.34}$$

$$\phi_L = H(-u_{i-1/2,j})\,\mathrm{vol}(m^*, n, \alpha_L^*, u_{i-1/2,j}\tau, h), \tag{7.35}$$

$$\phi_R = H(u_{i+1/2,j})\,\mathrm{vol}(m^*, n, \alpha_R^*, u_{i+1/2,j}, \tau, h), \tag{7.36}$$

where $\Phi = h + \min(u_{1+1/2}\tau, 0) - \max(u_{1-1/2}\tau, 0)$, $\alpha_L^* = \alpha_R^* = \alpha^* - m^*h$. Here $H(x)$ is the Heaviside function defined in equation (7.24). So the updated volume fraction of the cell (i,j) is

$$C_{i,j}^* = (\phi_{Ri-1,j} + \phi_{0i,j} + \phi_{Li+1,j})h^{-2}. \tag{7.37}$$

throughout the computational grid.

Once the advection in the x-direction has been carried out, the interface is again reconstructed using the updated colour function field C^* and then an analogous routine is performed for the y-direction. This then yields the updated value for the colour function at the next time step $C^{(n+1)}$, which in turn leads to the a reconstruction of the interface at this time step. Neumann conditions are usually chosen for the colour function at boundaries of the domain; this will be discussed further in chapter 7.

It is vital in the computational routine that the colour function obeys the consistency relation

$$0 \leq C_{i,j} \leq 1. \tag{7.38}$$

Crucially this relation is satisfied using this method [6]. Also the Courant-Friedrichs-Lewy (CFL) condition must be satisfied so the interface does not move more than a cell width in one time step. This condition on the time step is stricter than some of those used in other numerical routines and is given by

$$\frac{\max(\mathbf{u})\tau}{h} \leq \frac{1}{2}, \tag{7.39}$$

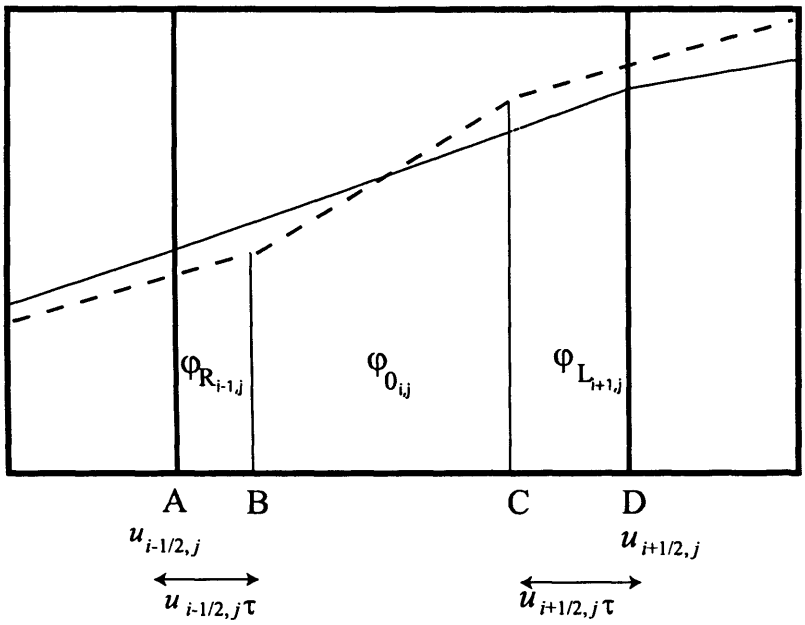

Figure 7.8: The interface cutting through the computational cell before advection is given by the straight black line. The point A is advected to the point B and the point D is moved to the point C, by the velocities $u_{i-1/2,j}$ and $u_{i+1/2,j}$ respectively. The point B is given by $\tau u_{i-1/2,j}$ and C given by $h-\tau u_{i+1/2,j}$. The new equations of the straight lines (the dashed lines) are found as described in the text and then the areas ϕ_L, ϕ_0 and ϕ_R are found. Then the new volume fraction is found by adding these three quantities and normalising on the total area of the cell. It should be noted that in this example the velocity $u_{i+1/2,j}$ is negative; if it were positive, there would be no contribution ϕ_L.

in view of equations (7.28), (7.30) and (7.31). More details on the CFL criteria for convergence will be given in the next chapter.

Usually when values of the colour function are greater than $1-\epsilon$ or less than ϵ, where ϵ is typically 10^{-6}, the values for the colour function are set to 1 and 0 respectively. Care must be taken here though. When the interface

moves only a very small amount in a given time step it may be that the user is inadvertently stopping the interface progressing, i.e. it is being reset to 1 after every time step, whereas other interface segments where this resetting is not applied are moving freely. This causes kinks to develop in the interface and the accuracy of the solution is lost extremely quickly.

This method can be extended to three dimensions although the computation of the line constant here is more complicated. Now, volumes under planes are calculated rather than areas under lines: a detailed description is given in [77] and related papers. There are few disadvantages to the Volume of Fluid method overall. Perhaps the main two are that the reconstruction of the interface is not unique, due to the fact that the colour function field may have some irregularities resulting in a normal vector to the interface that in fact is not representative of the situation at hand. Also the method as a whole requires many logical operations to determine the equation of each interface segment. This does not cause too much difficulty in two dimensions, but becomes more of a problem in three dimensions.

7.6 Tests on the interface advection algorithm

The advection scheme discussed in section 7.5 can now be tested with some examples where the velocity field is given. The simplest advection studied is just a simple translation of a circle under the velocity field $(u, v) = (1, 1)$. This effectively translates the circle from the bottom left to top right of the grid and is identical to the test used in [50]; the plots are not shown here. The scheme above gave good results, which improved when the direction of advection is alternated at every time step. The next test on the algorithm was a rotation of a circle of radius 0.25. Initially the circle is positioned at the point (1.75,

0.23) and a velocity field

$$(u, v) = (-y, x),$$

is applied to the whole domain. This rotational velocity field moves the circle as shown in figure 7.9, and again good accuracy was obtained. Another common test for VOF reconstruction and advection algorithms is Zalesak's slotted disk problem [111]. This however was not considered here due to time constraints.

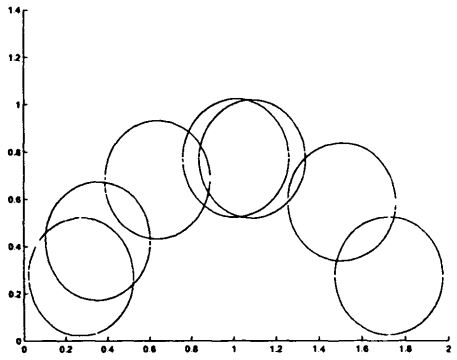

Figure 7.9: Rotation of a circle.

7.6.1 Single vortex problem

Although the tests for the Volume of Fluid PLIC scheme in the last section prove to be useful to test the method, they are simple velocity fields and the shape of the interface is not or should not be changing over time. A more stringent test on the algorithm is the so-called single vortex, which is due to Kothe [72]. A single vortex with stream-function

$$\psi(x, y) = \frac{1}{\pi} \sin^2(\pi x) \cos^2(\pi y), \tag{7.40}$$

is defined over a unit square where a circle of radius 0.15 is positioned at the point (0.5,0.75) as shown in figure 7.10. The velocity components for the flow

are obtained as $u = \partial\psi/\partial y$ and $v = -\partial\psi/\partial x$. When the circle is placed in this velocity field it spirals around the centre, approximately twice by $t = 3$ compared with Rider and Kothe results [72]. Indeed [72] gives the 'exact' solution which is very close to the results obtained here. They are shown in figure 7.11 which gives the particle positions at times $t = 1, 2, 3$ and 4. The figure shows the results for two different resolutions of mesh 64 by 64 on the left, and 128 by 128 on the right. At $t = 3$ the results are almost identical to Kothe's, other than a slight breakup or tear of the 'tail'. It is common for this to happen when studying this problem with the VOF method, however further grid refinement would hopefully alleviate this slight problem.

Another variant of this problem is the time reversed problem [49]. Here the stream-function is changed to

$$\psi(x, y) = \frac{1}{\pi} \cos\left(\frac{\pi t}{T}\right) \sin^2(\pi x) \cos^2(\pi y), \tag{7.41}$$

where here T is the total time and the flow is reversed after a time $t = T/2$. So

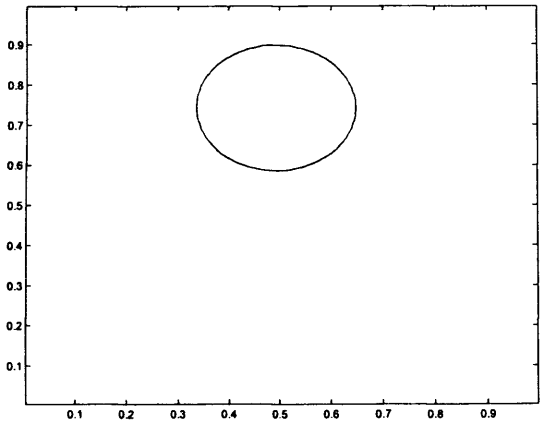

Figure 7.10: Initial configuration for the single vortex problem. A circle of radius 0.15 is positioned in a square of side 1, with its centre at (0.5, 0.75).

after a time T the circle should have returned to its initial state. Figure 7.12

shows the situations for the relatively small time T=2, again with the same two different grids. The finer grid shows the circle returns to approximately its initial position, although the coarser of the grids shows reasonable results and good comparisons are made with [43] and [72]. In [43] results for this problem are given using four different methods: the Hirt and Nicholls method, the same method with local height function, Youngs' method (as used here) and Youngs' method with local height function. Best results seem to be obtained using Youngs' method without the local height function.

The methodology that has been used in the present chapter is made use of in the next three chapters.

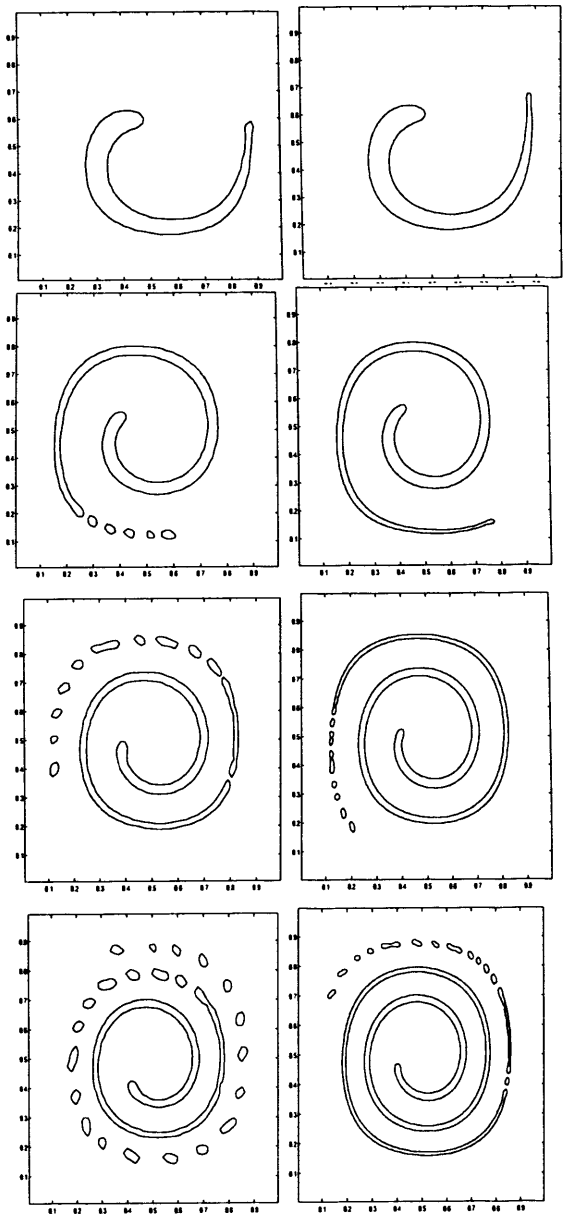

Figure 7.11: Single vortex test with grid (64 by 64) left and (128 by 128) right. From top to bottom times $t = 1, t = 2, t = 3$ and $t = 4$.

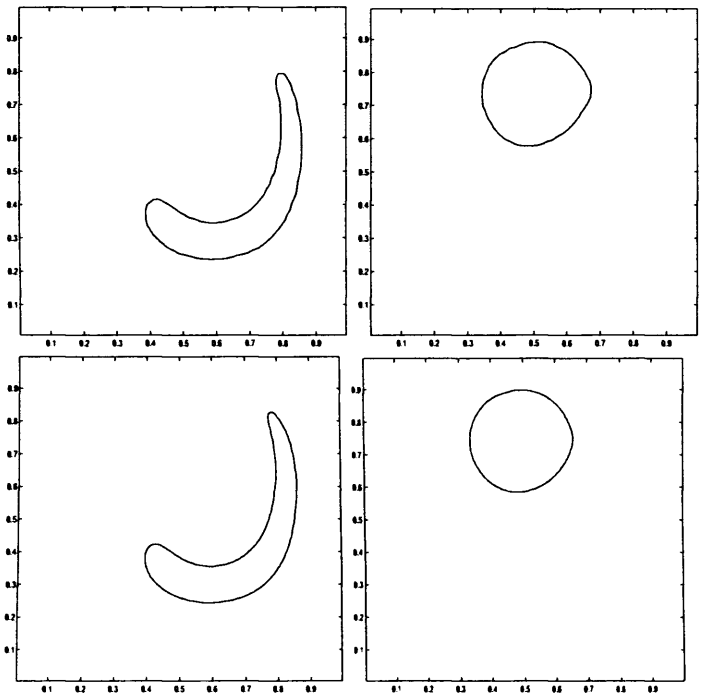

Figure 7.12: The reversed vortex for T=2. Top shows interface for t =T/2= 1, the maximum deformation of the original droplet and t =T on a 64 by 64 grid, below same problem on a 128 by 128 grid.

Chapter 8

Solution of the governing equations for free-surface or multiphase flow problems

8.1 Free surface flows

The flow of two different fluids with large density and viscosity ratios has widespread occurrence, water and air being a common example. In many such situations because one of the fluids, in this case air, has a very small density and viscosity compared to water, it can be neglected and instead the flow of just one fluid and a free surface can be studied. Although this formulation makes the solution of the governing equations more straightforward, the application of interface or now boundary conditions is in general a more complicated task compared to applying the interfacial conditions between two different but comparable fluids. The difficulty in the current numerical terms generally arises due to the fact that in order to set the desired conditions at the free surface, velocities and pressures must be set outside the fluid, i.e. in the vacuum or void; these points will be referred to as interior ghost points

from now on. These points are not to be confused with ghost points at the edges of the domain where the boundary conditions such as no-slip and slip conditions of the velocity at a solid wall are applied. Such points are outside the domain of the flow and there is no possibility that fluid can enter these cells.

8.1.1 Definition of cell types

When considering free surface flow on a Cartesian grid, grid cells are classified differently depending on their location relative to the free surface. A cell which contains no fluid at all is called an E-cell (Empty cell). A cell is defined to be a Surface or S-cell when one of its neighbours is an empty cell. A cell which is totally or partly full of fluid and has no empty neighbours is defined to be an F-cell or Full cell. It must be pointed out here that the term full cell is misleading as an F-cell is not necessarily full of fluid, as shown by the central cell in the figure 8.1. Finally the cells which are neighbouring the domain are termed G-cells or ghost cells; all other cells are denoted O-cells or obstacle cells, and represent solid obstacles in the domain. These cells are totally closed for flow. No values for pressure or velocities are needed in such cells. Also velocities between cells of different class are defined. So the velocity between a Full and Surface cell is called an FS velocity, and between an empty cell and a surface cell is called an SE velocity, and all other combinations are denoted accordingly.

The assigning of such velocities is an important issue. Different equations are used to approximate the flow equations at different classes of nodes. The momentum equations are used to calculate FF, FS, SS and SF velocities. In these cases there is some fluid in the cell under consideration and some fluid in the adjacent cell. Boundary conditions are set at SE velocity points using the continuity equations. Some EE points also need to be assigned a velocity.

A thorough discussion of setting the free surface conditions will be given in section 8.1.11.

8.1.2 The computational grid

The choice of grid used in this work is an orthogonal Cartesian grid. The variables are staggered, as shown in figure 7.2 in the previous chapter. So each computational cell has two velocities associated with it, $u_{i+1/2,j}$ and $v_{i,j+1/2}$, as well as a pressure and a value for volume fraction both defined in the centre of the cell. The staggered grid is used in order to prevent the checkerboard pressure distribution [4], which can often be found in situations where a co-located grid is used, i.e. a grid where velocities and pressures are calculated at the same position. The total numbers of cells in the $x-$ and y-directions respectively are given by imax and jmax. So excluding the ghost cells at each edge of the domain, the total number of cells open to flow is imax-2 in the x-direction , jmax-2 in the y-direction. The left and right hand faces of the cell (i, j) are given by the coordinates $x_{i-1/2}$ and $x_{i+1/2}$ respectively. The top and bottom faces are given by $y_{j-1/2}$ and $y_{j+1/2}$. At the beginning of the computational cycle the geometry of the domain is set. First the length of the domain in the two coordinate directions is set and the constant grid spacings in the x- and y-direction are chosen.

Solid obstacles are incorporated into the routine by effectively blocking out cells. As outlined in the previous section, obstacle cells are defined to be those to which no fluid can enter, so either a cell is a Flow cell (a cell which fluid can enter) or an obstacle cell. Cells are either totally open for flow or totally closed; hence the obstacle boundaries are aligned with those of the mesh.

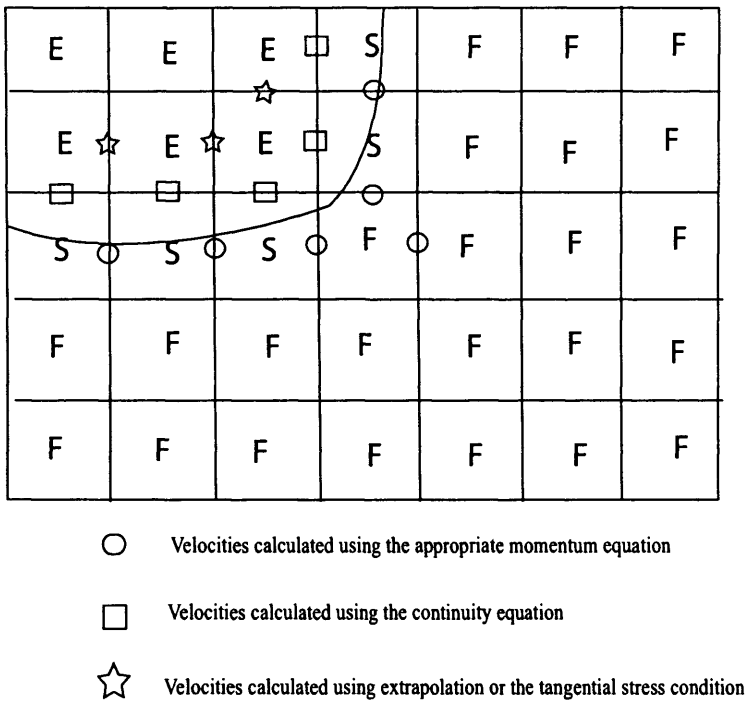

Figure 8.1: Velocities at the free surface. It should be noted that although the central cell is not full of fluid it is still denoted an F-cell as it has no adjacent empty neighbours in the top, bottom, left and right positions.

8.1.3 General outline of the solution

A common method for the solution of the Navier-Stokes equations for either single or multiphase dynamics is the so-called projection method. This method is commonly used in incompressible fluid flows and is due to Chorin [17]. It is in essence a fractional step method. First the momentum equations are integrated without the pressure gradient terms to give a velocity field which, is in general, not solenoidal. The second major part of the algorithm is a correction which when applied gives a divergence-free velocity field as required. The second step is known as the projection step and involves the solution of a Poisson

type equation. There are in practice many different discretization methods for the solution of the Navier-Stokes equations. One common method is to use the Adams-Bashforth differencing for the advective terms and Crank-Nicholson differencing for the viscous terms, the resulting discretization being

$$\frac{\mathbf{u}^{(n+1)}-\mathbf{u}^{(n)}}{\Delta t} = -\left(\frac{3}{2}\mathbf{u}^{(n)}.\nabla\mathbf{u}^{(n)} - \frac{1}{2}\mathbf{u}^{(n-1)}.\nabla\mathbf{u}^{(n-1)}\right) - \frac{1}{\rho}\nabla p^{(n+1)} - \frac{1}{\rho}\mathbf{F}^{(n)} + \frac{\mu}{2\rho}\nabla^2\left(\mathbf{u}^{(n)}+\mathbf{u}^{(n+1)}\right). \quad (8.1)$$

A more straightforward differencing is used in this thesis. The discretization of the Navier-Stokes equations we choose here is fully explicit and is given by

$$\frac{\mathbf{u}^{(n+1)}-\mathbf{u}^{(n)}}{\Delta t} = -\mathbf{u}^{(n)}.\nabla\mathbf{u}^{(n)} - \frac{1}{\rho}\nabla p^{(n+1)} - \frac{1}{\rho}\mathbf{F}^{(n)} + \frac{\mu}{\rho}\nabla^2\mathbf{u}^{(n)}, \quad (8.2)$$

$$\nabla.\mathbf{u}^{(n+1)} = 0. \quad (8.3)$$

Here Δt is the time step and as we are considering the flow of just one fluid with a free surface to start with, the quantities μ and ρ are assumed constant. The second of the equations ensures continuity of mass at the next time step. So an intermediate velocity $\tilde{\mathbf{u}}$ is calculated using the momentum equation but neglecting the pressure gradient,

$$\frac{\tilde{\mathbf{u}}^{(n)}-\mathbf{u}^{(n)}}{\Delta t} = -\mathbf{u}^{(n)}.\nabla\mathbf{u}^{(n)} - \frac{1}{\rho}\mathbf{F}^{(n)} + \frac{\mu}{\rho}\nabla^2\mathbf{u}^{(n)}. \quad (8.4)$$

However using equation (8.2) we then find that

$$\frac{\mathbf{u}^{(n+1)}-\tilde{\mathbf{u}}^{(n)}}{\Delta t} = -\frac{1}{\rho}\nabla p^{(n+1)}. \quad (8.5)$$

Since the velocity field at the $(n+1)$th time step must be divergence-free,

$$\nabla.\tilde{\mathbf{u}}^{(n)} = \Delta t\nabla^2\left(\frac{p^{(n+1)}}{\rho}\right). \quad (8.6)$$

So the different stages of the computational procedure can be listed as follows:

- Calculate $\tilde{\mathbf{u}}$ using equation (8.4), [1]

[1] This velocity field will be referred to as the tentative velocity field.

- Solve the Poisson equation (8.6) for the pressure field,
- Calculate the new velocity field $\mathbf{u}^{(n+1)}$ using equation (8.5).

There now follows a detailed description of the method, including the difference approximations for the derivatives and the implementation of free surface, interfacial and solid wall boundary conditions. At the start of this work the semi-implicit method for pressure linked equations (SIMPLE) algorithm was used to solve the flow equations. This method was found to give accurate results but was abandoned due to the increased amount of running time of the programs, compared to the projection method described above. A detailed description of the algorithm is given in Appendix B.

8.1.4 Discretization of terms

We use a simple finite-difference based method for the discretization of the governing equations. The discretization is based on that of the SOLA-VOF algorithm developed by Hirt and Nicholls [59], with the well known Marker and Cell grid [99]. Thus as outlined in section 8.1.2 there are two velocities to calculate in each computational cell namely $u_{i+1/2,j}$ and $v_{i,j+1/2}$. Figure 8.2 shows all the velocities that are needed in the calculations of $u_{i+1/2,j}$ and $v_{i,j+1/2}$ respectively. These velocities are taken from the previous time step and this velocity field is already known. Consider first the continuity equation (8.3). The discrete version of this equation is given by

$$D_{i,j} = \frac{u_{i+1/2,j} - u_{i-1/2,j}}{\Delta x} + \frac{v_{i,j+1/2} - v_{i,j-1/2}}{\Delta y} = 0. \tag{8.7}$$

This equation must be satisfied by every cell containing fluid. Details now will be given of the differencing used in the convective viscous and pressure force terms. Although this method uses finite-difference formulae for the spatial and temporal derivatives, essentially the same set of equations is obtained

from a finite-volume simulation with the control volumes as shown in figure 8.2. All velocities in subsequent sections are evaluated at the nth time level but the superscript (n) is now abandoned for brevity. The scheme is first order accurate in time and space.

Convective term

Consider now the momentum equation in the x-direction for the cell (i, j). The values Δx and Δy are the length of the cells, i.e. $x_{i+1/2} - x_{i-1/2}$ and $y_{j+1/2} - y_{j-1/2}$. These are taken to be constant over the whole domain in this work, although this method can be used where the cell widths vary over the domain [96]. We define the following derivatives

$$\left(\frac{\partial u}{\partial x}\right)_{i+1,j} = \frac{u_{i+3/2,j} - u_{i+1/2,j}}{\Delta x}, \tag{8.8a}$$

$$\left(\frac{\partial u}{\partial x}\right)_{i,j} = \frac{u_{i+1/2,j} - u_{i-1/2,j}}{\Delta x}, \tag{8.8b}$$

$$\left(\frac{\partial u}{\partial y}\right)_{i+1/2,j+1/2} = \frac{u_{i+1/2,j+1} - u_{i+1/2,j}}{\Delta y}, \tag{8.8c}$$

$$\left(\frac{\partial u}{\partial y}\right)_{i+1/2,j-1/2} = \frac{u_{i+1/2,j} - u_{i+1/2,j-1}}{\Delta y}. \tag{8.8d}$$

These are effectively the u-velocity derivatives to the right, left, top and bottom of the velocity node respectively: see figure 8.2. Similar difference equations apply to the v-component of the velocity, which are given by

$$\left(\frac{\partial v}{\partial x}\right)_{i+1/2,j+1/2} = \frac{v_{i+1,j+1/2} - v_{i,j+1/2}}{\Delta x}, \tag{8.9a}$$

$$\left(\frac{\partial v}{\partial x}\right)_{i-1/2,j+1/2} = \frac{v_{i,j+1/2} - v_{i-1,j+1/2}}{\Delta x}, \tag{8.9b}$$

$$\left(\frac{\partial v}{\partial y}\right)_{i,j} = \frac{v_{i,j+1/2} - v_{i,j-1/2}}{\Delta y}, \tag{8.9c}$$

$$\left(\frac{\partial v}{\partial y}\right)_{i,j+1} = \frac{v_{i,j+3/2} - v_{i,j+1/2}}{\Delta y}. \tag{8.9d}$$

So now using these expressions, first order accurate finite-difference formulae for the convection terms can be obtained. The convective term in the x-direction centered at the point $(i+1/2, j)$ is given by

$$(\mathbf{u}.\nabla)u_{i+1/2,j} = \left(u\frac{\partial u}{\partial x}\right)_{i+1/2,j} + \left(v\frac{\partial u}{\partial y}\right)_{i+1/2,j}. \tag{8.10}$$

Treating the two components individually we have

$$\left(u\frac{\partial u}{\partial x}\right)_{i+1/2,j} = \frac{u_{i+1/2,j}}{2}\left[(1-\alpha_1)\left(\frac{\partial u}{\partial x}\right)_{i+1,j} + (1+\alpha_1)\left(\frac{\partial u}{\partial x}\right)_{i,j}\right], \tag{8.11}$$

$$\left(v\frac{\partial u}{\partial y}\right)_{i+1/2,j} = \frac{v_{i+1/2,j}}{2}\left[(1-\alpha_2)\left(\frac{\partial u}{\partial y}\right)_{i+1/2,j+1/2} + (1+\alpha_2)\left(\frac{\partial u}{\partial y}\right)_{i+1/2,j-1/2}\right]. \tag{8.12}$$

Here

$$v_{i+1/2,j} = \frac{1}{4}(v_{i,j+1/2} + v_{i,j-1/2} + v_{i+1,j+1/2} + v_{i+1,j-1/2}), \tag{8.13}$$

$$\alpha_1 = A\,\mathrm{sign}(u_{i+1/2,j}), \tag{8.14}$$

$$\alpha_2 = A\,\mathrm{sign}(v_{i+1/2,j}). \tag{8.15}$$

Here A is an interpolation parameter. When $A = 0$ we just have a central differencing procedure and when $A = 1$ this differencing for the convection terms amounts to a first order upwinding process where the derivative upwind of the given point is used. The advective component in the y-direction is given by

$$(\mathbf{u}.\nabla)v_{i,j+1/2} = \left(u\frac{\partial v}{\partial x}\right)_{i,j+1/2} + \left(v\frac{\partial v}{\partial y}\right)_{i,j+1/2}, \tag{8.16}$$

where

$$\left(u\frac{\partial v}{\partial x}\right)_{i,j+1/2} = \frac{u_{i,j+1/2}}{2}\left[(1-\alpha_3)\left(\frac{\partial v}{\partial x}\right)_{i+1/2,j+1/2} + (1+\alpha_3)\left(\frac{\partial v}{\partial x}\right)_{i-1/2,j+1/2}\right], \tag{8.17}$$

$$\left(v\frac{\partial v}{\partial y}\right)_{i,j+1/2} = \frac{v_{i,j+1/2}}{2}\left[(1-\alpha_4)\left(\frac{\partial v}{\partial y}\right)_{i,j+1} + (1+\alpha_4)\left(\frac{\partial v}{\partial y}\right)_{i,j}\right], \tag{8.18}$$

and

$$u_{i,j+1/2} = \frac{1}{4}(u_{i+1/2,j} + u_{i-1/2,j} + u_{i+1/2,j+1} + u_{i-1/2,j+1}), \quad (8.19)$$

$$\alpha_3 = A\,\mathrm{sign}(u_{i,j+1/2}), \quad (8.20)$$

$$\alpha_4 = A\,\mathrm{sign}(v_{i,j+1/2}). \quad (8.21)$$

It was pointed out in [59] that central differencing for the convective terms may lead to an unstable numerical method.

Viscous term

The components of the stress tensor are given in Appendix A. The first component of the vector $\nabla.\mathbf{T}$ is

$$\frac{\partial T_{xx}}{\partial x} + \frac{\partial T_{yx}}{\partial y}, \quad (8.22)$$

and so a discretization at the cell edge leads to

$$\left(\frac{\partial T_{xx}}{\partial x} + \frac{\partial T_{yx}}{\partial y}\right)_{i+1/2,j} = \frac{T_{xx\,i+1,j} - T_{xx\,i,j}}{\Delta x} + \frac{T_{xy\,i+1/2,j+1/2} - T_{yx\,i+1/2,j-1/2}}{\Delta y}. \quad (8.23)$$

The individual components of the shear stresses are actually defined at cell centres. Here the individual components are given by

$$T_{xx\,i+1,j} = 2\mu\left(\frac{u_{i+3/2,j} - u_{i+1/2,j}}{\Delta x}\right), \quad (8.24)$$

$$T_{xx\,i,j} = 2\mu\left(\frac{u_{i+1/2,j} - u_{i-1/2,j}}{\Delta x}\right), \quad (8.25)$$

$$T_{yx\,i+1/2,j+1/2} = \mu\left(\frac{u_{i+1/2,j+1} - u_{i+1/2,j}}{\Delta y} + \frac{v_{i+1,j+1/2} - v_{i,j+1/2}}{\Delta x}\right), \quad (8.26)$$

$$T_{yx\,i+1/2,j-1/2} = \mu\left(\frac{u_{i+1/2,j} - u_{i+1/2,j-1}}{\Delta y} + \frac{v_{i+1,j-1/2} - v_{i,j-1/2}}{\Delta x}\right). \quad (8.27)$$

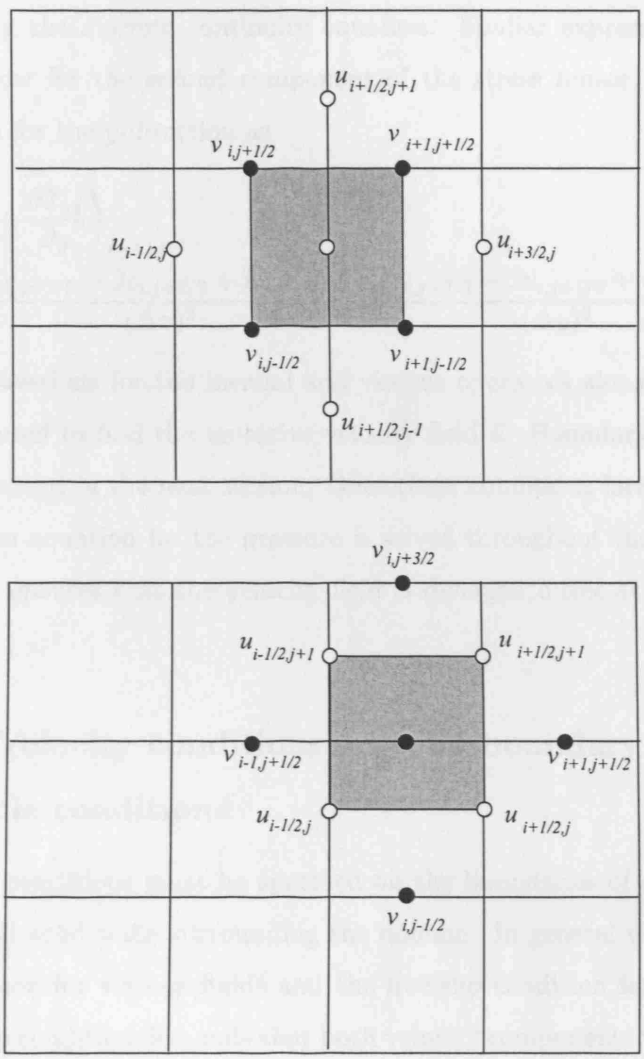

Figure 8.2: Velocities needed for the momentum equation: (a) x-direction, here the velocity being evaluated is $u_{i+1/2,j}$; (b) y-direction for the velocity is $v_{i,j+1/2}$. The shaded areas represent the associated control volumes used in the finite-volume method.

In the free surface calculations the viscosity is constant and so a simple central differencing is recovered for the viscous terms, hence we have

$$\left(\frac{\partial T_{xx}}{\partial x} + \frac{\partial T_{yx}}{\partial y}\right)_{i+1/2,j}$$
$$= \frac{u_{i+3/2,j} - 2u_{i+1/2,j} + u_{i-1/2,j}}{(\Delta x)^2} + \frac{u_{1+1/2,j+1} - 2u_{i+1/2,j} + u_{i+1/2,j-1}}{(\Delta y)^2}, \quad (8.28)$$

upon using the discrete continuity equation. Similar expressions to (8.24)-(8.27) follow for the second component of the stress tensor, leading to the expression for the y-direction as

$$\left(\frac{\partial T_{yx}}{\partial x}+\frac{\partial T_{yy}}{\partial y}\right)_{i,j+1/2} = \frac{v_{i+1,j+1/2}-2v_{i,j+1/2}+v_{i-1,j+1/2}}{(\Delta x)^2}+\frac{v_{i,j+3/2}-2v_{i,j+1/2}+v_{i,j-1/2}}{(\Delta y)^2}. \quad (8.29)$$

These expressions for the inertial and viscous operators along with equation (8.4) are used to find the tentative velocity field $\tilde{u}$. Boundary conditions for $\tilde{\mathbf{u}}$ are discussed in the next section. Once these conditions have been applied, the Poisson equation for the pressure is solved throughout the domain. This effectively ensures that the velocity field is divergence free at the next time-step.

8.1.5 Velocity conditions on solid boundary and obstacle conditions

Boundary conditions must be specified on the boundaries of obstacles in the flow and all solid walls surrounding the domain. In general we apply the no-slip condition for viscous fluids and the free-slip condition for inviscid flows. The no-slip condition demands that both velocity components vanish at a solid wall while the free-slip condition sets the velocity component normal to the wall to zero and imposes a Neumann condition for the tangential component. These conditions are set by using ghost cells just outside the flow domain. In this work the boundaries of the domain coincide with the grid cells as shown in the figure 8.4. Here we apply the following second order accurate boundary conditions:

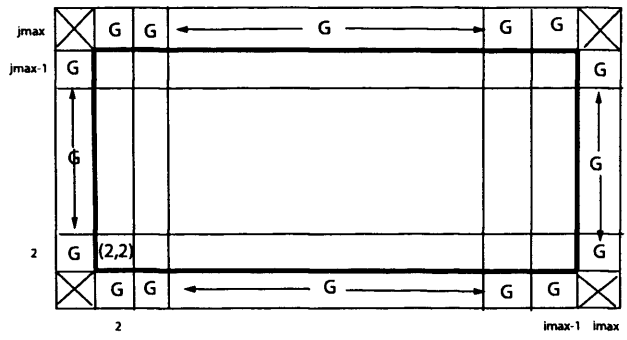

Figure 8.3: The Cartesian grid. Ghost cells are marked G and no values are stored for velocity or pressure in corner cells.

For example, considering the left edge of the domain we set

$$u_{1,j} = 0, \tag{8.30}$$

$$v_{2,j+1/2} = v_{1,j+1/2}, \tag{8.31}$$

for inviscid flows. For viscous flows the velocities to be set are

$$u_{1,j} = 0, \tag{8.32}$$

$$v_{2,j+1/2} = -v_{1,j+1/2}. \tag{8.33}$$

Analogous formulae hold on the right, top and bottom of the domain. In fact these conditions are also applied to the tentative velocity field $(\tilde{u}, \tilde{v})$. This, combined with a careful treatment of pressure at solid walls to be described in section 8.1.8, ensures that the newly calculated velocity field **u** satisfies the boundary conditions and the divergence free constraint in the cells bordering a solid object.

8.1.6 Inflow and outflow conditions

At the beginning of the computational cycle the conditions at the inlet and outlet must be set. In general the outflow boundary conditions are the more

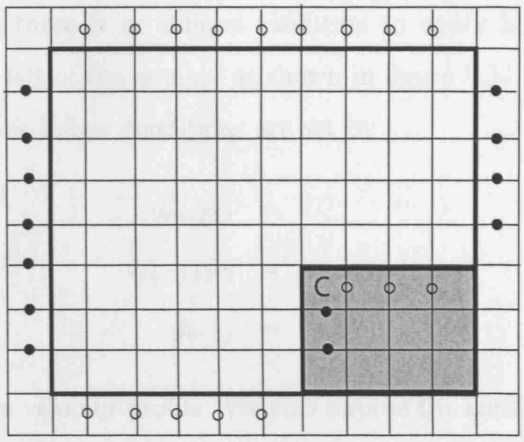

Figure 8.4: Velocities that must be assigned in ghost and obstacle cells. For inviscid flow the velocities are extrapolated from the interior, for viscous flow the no slip condition is set using the negative value of the normal velocity. Here ○ represents the u-velocity, and • the v-velocities. Here the cell C is a corner cell.

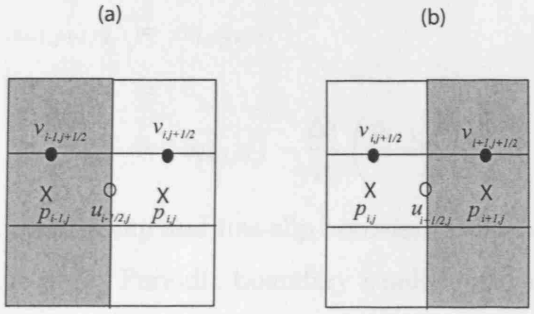

Figure 8.5: Velocities that must be assigned in ghost cells at the inflow case (a) and the outflow case (b). Here values for pressure are used in the ghost cells and special conditions for the velocity and intermediate velocity field are also applied.

difficult to set as there is no unique condition to apply here. Consider the ghost cells to the left of the domain as shown in figure 8.34. In this thesis the inviscid and viscous inflow conditions are set by

$$u_{i+1/2,j} = U, \tag{8.34}$$

$$v_{i+1,j+1/2} = v_{i,j+1/2}, \tag{8.35}$$

$$p_{i-1,j} = p_{i,j}, \tag{8.36}$$

where U is a given velocity profile. We also impose the condition $u = \tilde{u}$ at the inflow which is consistent with equation (8.36) in the above. For the outflow condition, we prescribe that the derivatives of the two velocity components must vanish. This is achieved by extrapolation of these fields to the ghost cells. Hence the following conditions are set on the final fluid cells at the right of the domain

$$\tilde{u}_{i+1/2,j} = \tilde{u}_{i-1/2,j}, \tag{8.37}$$

$$v_{i-1,j+1/2} = v_{i,j+1/2}, \tag{8.38}$$

$$p_{i+1,j} = 0, \tag{8.39}$$

$$u_{i+1/2,j} = \tilde{u}_{i+1/2,j} - \frac{\Delta t}{\rho}\left(\frac{p_{i+1,j} - p_{i,j}}{\Delta x}\right). \tag{8.40}$$

In certain calculations no slip and free-slip boundary conditions are applied at these points on the grid. Periodic boundary conditions may also be used in some Volume of Fluid simulations, in particular for simulations of the Rayleigh-Taylor instability for viscous fluids [67], however they are not used in this work.

When the flow is viscous a Poiseuille type velocity profile is applied, whereas when the flow is inviscid the velocities at the inflow are usually taken to be constants.

8.1.7 Discretization of the Poisson equation

Using the expressions in section 8.1.4 allows the calculation of $\tilde{\mathbf{u}}$. So the next stage of the calculation is the solution to the Poisson equation (8.6) for the pressure field. Finite- differencing is also used to solve this equation. Central-differencing is used here. Noting that the density is constant in the free surface case we obtain

$$\frac{\tau}{\rho}\left(\frac{p_{i+1,j}-2p_{i,j}+p_{i-1,j}}{(\Delta x)^2}+\frac{p_{i,j+1}-2p_{i,j}+p_{i,j-1}}{(\Delta y)^2}\right) = \frac{\tilde{u}_{i+1/2,j}-\tilde{u}_{i-1/2,j}}{\Delta x}+\frac{\tilde{v}_{i,j+1/2}-\tilde{v}_{i,j-1/2}}{\Delta y}. \quad (8.41)$$

The right hand side is of course already known and so the equation is of elliptic type. This differencing is used for all F-cells, however at S-cells this equation is not valid and the free surface condition must be applied. The boundary conditions at the free surface for an inviscid fluid reduce to

$$p = p_{\mathbf{atm}}, \quad (8.42)$$

where $p_{\mathbf{atm}}$ is the atmospheric pressure. In general this condition is set by using linear interpolation from the neighbouring fluid cell. First a check is made as to whether the interface is more horizontal or vertical. In practice this is done using the already computed normal to the interface. Then the fluid cell in the normal direction is chosen to be the interpolating cell. Figure 8.6 shows an example.

So the height of the interface from the centre of the interpolating cell is defined to be d. As the pressure at the interface is given by $p_{\mathbf{atm}}$ the pressure in the centre of the S-cell is given by

$$p_S = p_{\mathbf{atm}} + (1-\bar{h})p_F, \quad (8.43)$$

where $\bar{h} = d/\Delta y$. In general $\bar{h}$ can be calculated in quite a straightforward manner. As the volume fraction is known and the length of the sides of the

cells are known, we can find $\hat{h} = C_{i,j}\,\Delta x$ where $\hat{h} = |d - \Delta y|$, in the case of a horizontal interface and a cell where $\Delta x = \Delta y$. Similar reasoning follows for a vertical interface.

For viscous free surface flow, the condition for the normal stress balance is

$$p + 2\nu\frac{\partial u_n}{\partial n} = p_{\mathbf{atm}}. \tag{8.44}$$

Because the flows considered here are at high Reynolds number, the viscous term is assumed to be negligible, and hence the condition reduces the inviscid description above. For low Reynolds number flows where this term may be dominant we choose the SIMPLE algorithm in order to solve the Navier-Stokes equations. This method is preferred to the projection method as the velocity field is updated after every iteration and so a precise discretized version of equation (8.44) may be set at the interface. Using the projection method there is only one outer iteration per time step and so the velocity from the previous time step must be used for the viscous free surface condition, which of course will give less meaningful results.

8.1.8 Boundary conditions for the Poisson equation

No equations for the boundary conditions are directly available for the Poisson equation for the pressure. However it turns out that in fact no condition is needed. The setting of the normal velocity component to zero is applied whether the flow is inviscid or viscous. If we consider the situation of a right-wall, the momentum equation for the velocity is not needed as this velocity is set to zero at once using the no-slip or free slip condition. So now the continuity equation for this cell reduces to

$$D_{i,j} = \frac{-u_{i-1/2,j}}{\Delta x} + \frac{v_{i,j+1/2} - v_{i,j-1/2}}{\Delta y} = 0. \tag{8.45}$$

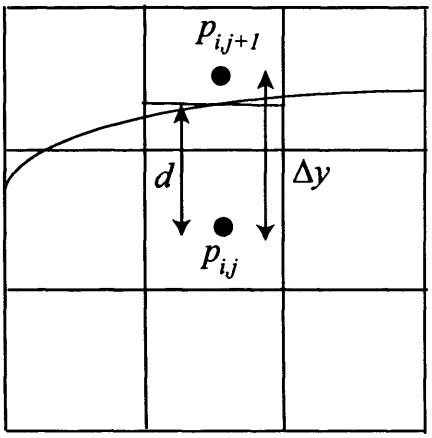

Figure 8.6: Pressure interpolation at the free surface. In this case the interface is more horizontal and so the interpolating cell is $p_{i,j}$. Here d is the distance between cell centres and h the distance from the F-cell centre to the interface.

Substituting the relevant expressions from the momentum equation leads to the balance

$$\frac{\Delta t}{\rho}\left(\frac{-p_{i,j}+p_{i-1,j}}{(\Delta x)^2}+\frac{p_{i,j+1}-2p_{i,j}+p_{i,j-1}}{(\Delta y)^2}\right)=\frac{-\tilde{u}_{i-1/2,j}}{\Delta x}+\frac{\tilde{v}_{i,j+1/2}-\tilde{v}_{i,j-1/2}}{\Delta y}. \tag{8.46}$$

This equation actually can be obtained from (8.41) by imposing a ghost pressure $p_{i+1,j}$ by using a Neumann boundary condition. Care must be taken using this method though, at corner obstacle cells where the pressure would become double valued. So modified equations such as (8.46) are set in all cells neighbouring solid walls or obstacle cells. The resulting set of linear equations can be solved by a variety of different methods. The system essentially involves inverting a penta-diagonal matrix. Here the successive over-relaxation method is used. Another technique of an iterative nature, the Incomplete Cholesky-conjugate gradient method is described in [41] and [44]. An extension of this method to simulate three-dimensional flows would probably benefit from this type of solver.

8.1.9 Solution of the Poisson equation

The well known successive over-relaxation method is popular for solving linear equation systems due to the low amount of computer memory needed and its relative simplicity to program. Many more sophisticated methods for solving Poisson type equations can be found in the literature. The recent advances in multigrid techniques have improved the time for running such simulations immensely. Such techniques typically can use only 3 to 10 iterations for problems which could take as many as 500 using an over-relaxation or Gauss-Seidel method. The SOR routine is chosen here though, as it is easy to set up, and all work done here is in two dimensions and so there is less of a demand on computational efficiency.

So the first guess at the pressure field is the pressure field from the last time step $p^{(n)}$. Then we find a value for the residual $\overline{p}$ as

$$\overline{p} = \frac{\tau}{\rho}\left(\frac{p^{(k)}_{i+1,j} - 2p^{(k)}_{i,j} + p^{(k)}_{i-1,j}}{(\Delta x)^2} + \frac{p^{(k)}_{i,j+1} - 2p^{(k)}_{i,j} + p^{(k)}_{i,j-1}}{(\Delta y)^2}\right) - \left(\frac{\tilde{u}_{i+1/2,j} - \tilde{u}_{i-1/2,j}}{\Delta x} + \frac{\tilde{v}_{i,j+1/2} - \tilde{v}_{i,j-1/2}}{\Delta y}\right). \quad (8.47)$$

This value is then averaged with the previous iterate value, using a relaxation parameter ω,

$$p^{(k+1)} = \omega\overline{p} + (1-\omega)p^{(k)}. \quad (8.48)$$

The iteration is continued until convergence, typically a value of 10^{-6} for the residual. The choice of the parameter ω is extremely important in order to achieve convergence for the method and to optimise the number of iterations to achieve convergence. It is found [55] that the best choice of ω is

$$\omega = \frac{4}{2 + \sqrt{4 - (\cos(\pi/(m-1)) + \cos(\pi/(n-1)))^2}}, \quad (8.49)$$

where m and n are the number of grid points in the $x-$ and y-directions respectively.

This equation is only applied in F-cells; for S-cells the interpolation method discussed in section 8.1.7 is used. Pressure in E-cells is automatically set to zero.

8.1.10 Finding the velocity

Once the pressure field is found the velocities are updated using equation (8.5). Now when the relevant expressions for each velocity are substituted using the momentum equation, we obtain

$$u_{i+1/2,j}^{(n+1)} = \tilde{u}_{i+1/2,j} - \frac{\Delta t}{\rho}\left(\frac{p_{i+1,j}^{(n+1)} - p_{i,j}^{(n+1)}}{\Delta x}\right), \tag{8.50}$$

$$v_{i,j+1/2}^{(n+1)} = \tilde{v}_{i,j+1/2} - \frac{\Delta t}{\rho}\left(\frac{p_{i,j+1}^{(n+1)} - p_{i,j}^{(n+1)}}{\Delta y}\right). \tag{8.51}$$

These ensure a divergence-free velocity field in all F-cells. Now velocities are set in S-cells so the continuity equation is satisfied here and in E-cells to satisfy the tangential stress condition.

8.1.11 Velocity boundary conditions at the free surface

Although there are no physical boundary conditions on the velocity field at the free surface, velocities must be imposed here for two reasons. Firstly mass must be conserved in all cells that contain fluid, so we must have $D_{i,j} = 0$ in all F- and S-cells. Also velocities must be assigned to some interior ghost nodes, i.e. in empty cells. This is due to the fact that the calculation of velocities in some cells requires velocities outside the fluid, which come into the momentum equations.

There are five types of velocities that can arise between different neighbouring cells. These are FF, FS, SS, SE and EE velocities. The first three are solved directly using the momentum equation. In all these cases there is some fluid in the neighbouring cell, the cell to the right for the calculation of u-velocities

and the cell to the top for the calculation of the v-velocities. However the SE and EE type velocities are treated differently. SE velocities are set using the continuity equation and EE velocities that are needed are set using the condition of zero tangential stress for viscous fluids and simple extrapolation for inviscid fluids. If we consider an S-cell, there are fifteen ways in which this cell[2] can have one or more neighbouring empty cells. These are shown in figure 8.7. The following list of the equations is used for setting the free surface velocity conditions.

$$u_{i+1/2,j} = u_{i-1/2,j} - \frac{\Delta x}{\Delta y}(v_{i,j+1/2} - v_{i,j-1/2}), \tag{8.52a}$$

$$v_{i,j+1/2} = v_{i,j-1/2} - \frac{\Delta y}{\Delta x}(u_{i+1/2,j} - u_{i-1/2,j}), \tag{8.52b}$$

$$u_{i+1/2,j} = u_{i-1/2,j}, \tag{8.52c}$$

$$u_{i-1/2,j} = u_{i+1/2,j} + \frac{\Delta x}{\Delta y}(v_{i,j+1/2} - v_{i,j-1/2}), \tag{8.52d}$$

$$u_{i-1/2,j} = u_{i+1/2,j}, \tag{8.52e}$$

$$v_{i,j+1/2} = v_{i,j-1/2}, \tag{8.52f}$$

$$v_{i,j-1/2} = v_{i,j+1/2} + \frac{\Delta y}{\Delta x}(u_{i+1/2,j} - u_{i-1/2,j}), \tag{8.52g}$$

$$v_{i,j-1/2} = v_{i,j+1/2}, \tag{8.52h}$$

$$u_{i-1/2,j} = u_{i-1/2,j-1}, \tag{8.52i}$$

$$u_{i+1/2,j} = u_{i+1/2,j-1}, \tag{8.52j}$$

$$v_{i,j-1/2} = v_{i-1,j-1/2}, \tag{8.52k}$$

$$v_{i,j+1/2} = v_{i-1,j+1/2}, \tag{8.52l}$$

$$u_{i-1/2,j} = u_{i-1/2,j+1}, \tag{8.52m}$$

$$u_{i+1/2,j} = u_{i+1/2,j+1}, \tag{8.52n}$$

$$v_{i,j+1/2} = v_{i+1,j-1/2}, \tag{8.52o}$$

$$v_{i-1/2,j} = v_{i+1,j+1/2}. \tag{8.52p}$$

[2]This generalizes to 63 in three dimensions

Cell type	Equation used 8.52-()
1	(a)
2	(b)
3	(c), (f)
4	(d)
5	(i), (a)
6	(e), (f)
7	(i), (j), (b)
8	(g)
9	(c), (h)
10	(k), (b)
11	(k), (l), (a)
12	(e), (h)
13	(m), (n), (g)
14	(o), (p), (d)
15	(a)

Table 8.1: Different equations used for different configurations of E and S-cells. Note the order in which the conditions are set does matter.

When the cell under consideration has one empty neighbour, the velocity can be calculated exactly using the discrete continuity equation. If there are two empty neighbours which are adjacent then the continuity equation is split into $\frac{\partial u}{\partial x} = 0$ and $\frac{\partial v}{\partial y} = 0$. This method cannot be applied however when an S-cell is adjacent to two E-cells to the top and bottom or left and right. Here an extrapolation routine is used to find one of the velocities and then the continuity equation is used to find the other velocity using the other three on the cell's edge. When there are three empty neighbours a similar technique is

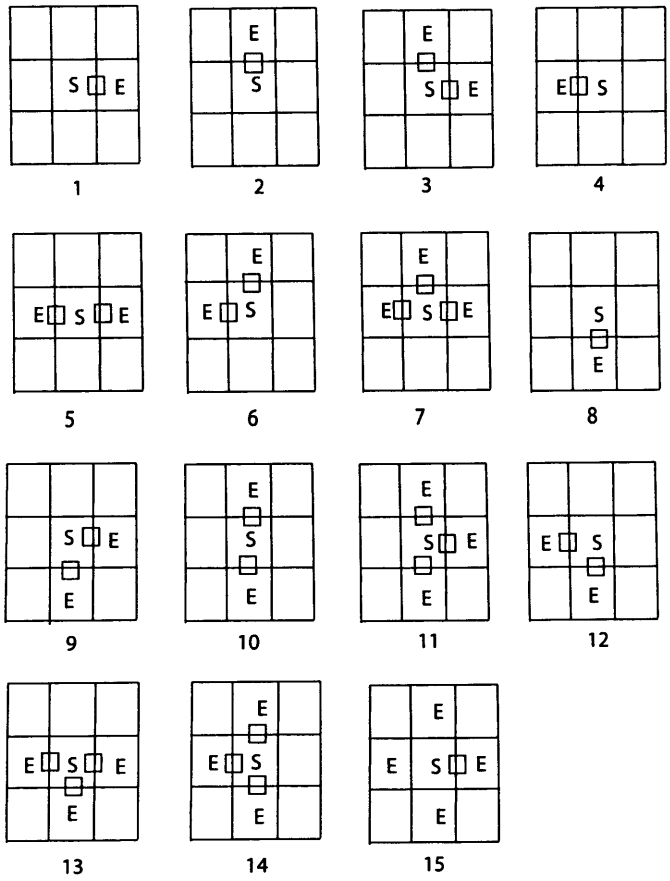

Figure 8.7: The fifteen different configurations of an S-cell and at least one empty neighbour. The integer associated with each is calculated depending on the position and number of empty neighbours as described above.

employed. The velocities are interpolated from the neighbouring surface cell and the remaining velocity is again found from the continuity equation.

For ease of programming, the exact arrangement of the S-cell is defined to be an integer from 1 to 15. This integer is initialised to zero. If the cell $(i+1, j)$ is empty then 1 is added to the integer, if $(i, j+1)$ is empty 2 is added, if $(i-1, j)$ is empty 4 is added and if $(i, j-1)$ is empty 8 is added. The resulting sum gives an integer between 1 and 15 which is unique to the given geometry of cells. The integer obtained corresponds to the figure with the same number in Figure 8.7.

8.1.12 Conditions on the EE velocities

EE type velocities are not needed everywhere, indeed they are only needed due to the fact that certain points need a value for velocity at an EE position when they are solved using the momentum equation. Figure 8.1 gives an example of such a case where the SS velocity at the left edge of the domain is calculated using the momentum equation, and this demands a value for the velocity at the point EE directly above the position where the velocity is to be calculated.

There are in fact only four different configurations of S/E-cells where it is necessary to assign a value. These four cases are shown in figure 8.8. In each case a Surface cell is at the position (i, j). The velocities set are given as

$$v_{i+1,j+1/2} = v_{i,j+1/2}, \tag{8.53a}$$

$$u_{i+1/2,j+1} = u_{i+1/2,j}, \tag{8.53b}$$

$$v_{i-1,j+1/2} = v_{i,j+1/2}, \tag{8.53c}$$

$$u_{i+1/2,j-1} = u_{i+1/2,j}. \tag{8.53d}$$

These conditions correspond to the cases shown in (a), (b), (c) and (d) respectively in figure 8.8.

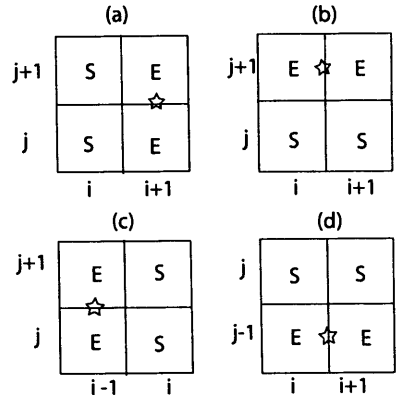

Figure 8.8: The four different types of configuration where EE velocities denoted by a star need to be set.

When the flow is viscous the equations generalize to

$$v_{i+1,j+1/2} = v_{i,j+1/2} - \frac{\Delta x}{\Delta y}(u_{1+1/2,j+1} - u_{i+1/2,j}), \tag{8.54a}$$

$$u_{i+1/2,j+1} = u_{i+1/2,j} - \frac{\Delta y}{\Delta x}(v_{i,j+1/2} - v_{i+1,j+1/2}), \tag{8.54b}$$

$$v_{i-1,j+1/2} = v_{i,j+1/2} + \frac{\Delta x}{\Delta y}(u_{1-1/2,j+1} - u_{i-1/2,j}), \tag{8.54c}$$

$$u_{i+1/2,j-1} = u_{i+1/2,j} + \frac{\Delta y}{\Delta x}(v_{1+1,j-1/2} - v_{i,j-1/2}). \tag{8.54d}$$

So in general the points where the momentum equations are used are solved for first, then using these velocities the SE velocities are set using the continuity equation. Then using both these velocities and the velocities from the momentum equation the EE velocities are calculated using either the tangential stress condition or extrapolation as discussed above. The order of setting these conditions is crucial though. If for instance the tangential condition was used before the continuity equation, incorrect velocities would be assigned and the algorithm would break down straight away.

8.1.13 Boundary conditions for the colour function

In general the condition $\partial C/\partial n = 0$ is used at solid walls, where n is normal to the boundary. This effectively sets a constant contact angle of $\pi/2$. Also the condition sets the interpolating cell for the free surface pressure calculation to be a fluid cell rather than a ghost cell which would clearly cause the algorithm to be inaccurate. Figure 8.9 shows two situations where this situation arises. The figure on the top, part (a), has an interface that is more horizontal and so the interpolating cell is the ghost cell. However by setting the $C_{i,j-1} = C_{i,j}$ this situation is avoided and the interpolating cell is the neighbouring fluid cell $(i-1, j)$. The condition $C = 0$ in ghost cells can be applied in some Volume of Fluid simulations [70]. This corresponds to a flow or impact onto a super-hydrophobic surface. This however is not of interest in this work. Care must be taken at obstacle corners where here the colour function is discontinuous. Here two different values for the colour function must be stored and each used individually when the interface normal is calculated, for example in the corner obstacle cell in figure 8.4 cell C. One value will be used to find the normal in the cell $(i-1, j)$ and another for the cell $(i, j+1)$.

8.1.14 Velocity boundary conditions for flows involving impacts

The boundary conditions and free surface conditions when a free surface is about to impact on a solid body can cause problems in numerical routines.

Such impacts onto solid boundaries are also studied in other contexts [39] and complications can arise. If for example a droplet is approaching a solid obstacle, when the free surface enters the last row or column of grid cells next to the boundary, a normal velocity of zero is applied on the wall and this is used in the calculation at the next time step, even before the droplet has

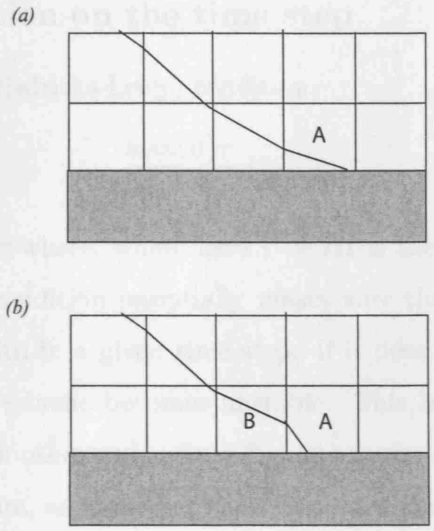

Figure 8.9: (a) An example of a case where the interpolating cell for the pressure condition for cell A is a ghost cell, not allowed. (b) The interpolating cell is now cell B, when using Neumann conditions for the Colour function at the boundary.

touched the wall. The boundary condition on the colour function also alters the flow when the free surface enters this row of grid cells. So the presence of the boundary is felt before the free surface comes into contact with the boundary.

One way of removing this slight error is to impose boundary conditions on the colour function and velocities only when individual segments of interface have touched the wall. Once the interface has touched the wall though these conditions must be set at all subsequent time steps. Further details on this idea are given in [39], [99].

8.1.15 Restriction on the time step

The CFL (Courant-Friedrichs-Lewy) condition

$$\frac{\max(\mathbf{u})\tau}{h} \leq \frac{1}{2}, \tag{8.55}$$

must be satisfied everywhere, where here $\tau = \Delta t$ is the time step, and $h = \max(\Delta x, \Delta y)$. This condition essentially makes sure that the interface does not cross one cell width in a given time step. If it does cross a cell width or more then the PLIC scheme becomes unstable. This is a stricter condition than is usually used in other methods and is due to the Lagrangian nature of the advection algorithm, as discussed in section 7.5.3 and in [28].

8.2 Summary of the calculation for free surface flows

Below is a summary of the method for a free surface flow calculation for a single time step:

1. Initially the velocity field is known and values for the colour function are also known.
2. The velocity field is advected in the x-direction.
3. The interface is reconstructed from the colour function field.
4. A check is made as to the status of every individual cell. Each cell is defined to be either E, S, F, G or O. Boundary conditions are set on the free surface and solid walls.
5. The interface is advected in the y-direction.
6. Step 3 is repeated.

7. Step 4 is repeated.

8. The value for $\bar{h}$ is determined in all S-cells.

9. The tentative velocity field $\tilde{u}$ is found.

10. The Poisson equation is solved for p.

11. The velocity field is updated.

So this gives the velocity field at time step $(n+1)$. In general the direction of advection is reversed every time step. At the next time step, the first guess for the new pressure will be $p^{(n+1)}$.

8.3 Solution to the two fluids problem

When considering the flow of two fluids, certain simplifications can be made to the previous discussion, but also more complexities arise. We use the same computational grid, but now assume that each cell is either a fluid cell or an obstacle cell, hence there is no need to categorise cells as previously. Indeed now we apply the momentum equations at all cells other than boundary and obstacle cells.

The routine for the two fluids problem is similar to that of the free surface problem. We now solve for the velocity field $\tilde{u}$ at all points as well as solving the Poisson equation for pressure throughout the domain. As there are now two fluids, we choose one fluid, fluid 1 say, as a reference fluid and so the values for the colour function correspond to the amount of this fluid present in the cell. So now when the value of the colour function is zero the cell is completely full of fluid 2 . We can thus use exactly the same algorithm to track the interface in the two fluid case as we used in the single fluid calculations.

8.3.1 Interfacial conditions

It turns out that the applications of interfacial conditions cause no problems to the solver. Running the solver over the whole domain, the conditions

$$\mathbf{u}_1.\mathbf{n} = \mathbf{u}_2.\mathbf{n}, \tag{8.56}$$

$$\left(-p + 2\mu_1 \frac{\partial u_n}{\partial n}\right)_1 = \left(-p + 2\mu_2 \frac{\partial u_n}{\partial n}\right)_2, \tag{8.57}$$

are satisfied automatically. The second of these is essentially the momentum equation applied at interfacial cells. Again the kinematic condition is satisfied using the advection scheme for the colour function outlined in chapter 4. The tangential condition

$$\mu_1 \left(\frac{\partial u_n}{\partial t} + \frac{\partial u_t}{\partial n}\right)_1 = \mu_2 \left(\frac{\partial u_n}{\partial t} + \frac{\partial u_t}{\partial n}\right)_2, \tag{8.58}$$

is also satisfied automatically [99].

8.3.2 Discretization of viscosity and density

The viscosity and density discretizations used in this thesis are similar. The arithmetic mean is used for both the density and the viscosity. We define two densities here, a density ρ at the point $i + 1/2, j$ essentially giving the average of the two densities from cells (i, j) and $(i + 1, j)$ and a density ρ at the point $i, j + 1/2$ giving the average of the two cells in the y-direction. These are given respectively by

$$\rho_{i+1/2,j} = \frac{1}{2}\left(C_{i,j} + C_{i+1,j}\right)\rho_1 + \left(1 - \frac{C_{i,j} + C_{i+1,j}}{2}\right)\rho_2, \tag{8.59}$$

$$\rho_{i,j+1/2} = \frac{1}{2}\left(C_{i,j} + C_{i,j+1}\right)\rho_1 + \left(1 - \frac{C_{i,j} + C_{i,j+1}}{2}\right)\rho_2. \tag{8.60}$$

Here the colour function refers to fluid 1. We also need the density at cell centres for certain calculations; this is given by

$$\rho_{i,j} = \rho_1 C_{i,j} + \rho_2(1 - C_{i,j}). \tag{8.61}$$

As the components of the stress tensor are defined in the centre of the cells, we also define the viscosity at this position, hence only one viscosity is needed. Its discrete version is

$$\mu_{i,j} = \mu_1 C_{i,j} + \mu_2(1 - C_{i,j}). \tag{8.62}$$

Some practitioners of the VOF method choose the harmonic mean over the arithmetic mean. This choice seems to give better results when there is a large viscosity gradient near the interface. A full discussion is given in [21].

With the discrete version of the viscosity, the form of the pressure Poisson equation is now changed. It becomes in the (i,j)th cell

$$\frac{1}{\rho_{i+1/2,j}}\left(\frac{p_{i+1,j}-p_{i,j}}{\Delta x}\right) - \frac{1}{\rho_{i-1/2,j}}\left(\frac{p_{i,j}-p_{i-1,j}}{\Delta x}\right) + \frac{1}{\rho_{i,j+1/2}}\left(\frac{p_{i,j+1}-p_{i,j}}{\Delta y}\right) - \frac{1}{\rho_{i,j-1/2}}\left(\frac{p_{i,j}-p_{i,j-1}}{\Delta y}\right) = \Delta t\left(\frac{\tilde{u}_{i+1/2,j}-\tilde{u}_{i-1/2,j}}{\Delta x} + \frac{\tilde{v}_{i,j+1/2}-\tilde{v}_{i,j-1/2}}{\Delta y}\right). \tag{8.63}$$

Again this is solved using a successive over-relaxation technique. It must be noted here though that as the boundary condition $\partial p/\partial n = 0$ is used everywhere on the boundary, the solution is only unique to an additive constant. This of course does not affect the calculation of the velocities at the next time step, as the calculation of these quantities involves only the derivatives of pressure.

The divergence-free velocities are then given by

$$u^{(n+1)}_{i+1/2,j} = \tilde{u}_{i+1/2,j} - \frac{\Delta t}{\rho_{i+1/2,j}}\left(\frac{p^{(n+1)}_{i+1,j} - p^{(n+1)}_{i,j}}{\Delta x}\right), \tag{8.64}$$

$$v^{(n+1)}_{i,j+1/2} = \tilde{v}_{i,j+1/2} - \frac{\Delta t}{\rho_{i,j+1/2}}\left(\frac{p^{(n+1)}_{i,j+1} - p^{(n+1)}_{i,j}}{\Delta y}\right). \tag{8.65}$$

Other than these minor alterations the method for the two phase flow problem is identical to that of the free surface flows. A summary of the steps involved with the calculation is given in section 8.3.5. First though we turn attention to difficulties that can arise in such calculations.

8.3.3 Extreme density ratio

Near the interface, the density and viscosity undergo a large jump if these properties of the individual fluids vary markedly. This can cause problems in the solution of the Poisson pressure equation.

One popular technique to overcome this problem is to smooth the density field near the interface where sharp gradients exist. Smoothing the density or viscosity fields essentially involves only smoothing the colour function field, hence formulae such as

$$\hat{C}_{i,j} = \frac{1}{2}C_{i,j} + \frac{1}{8}(C_{i,j-1} + C_{i,j+1} + C_{i-1,j} + C_{i+1,j}) \tag{8.66}$$

can be applied. This smoothed field allows a smoother jump in the colour function and hence in viscosity and density near the interface. Smoothing can be repeated two or more times. Higher order methods involving convolving the colour function with a smoothing kernel have also been studied [9].

Use of a multigrid method to solve the Poisson equation is the other main technique to help solve the problem of a large density difference between the two fluids, for example the red black method as described in [28]. Rudman [75] uses a traditional marker and cell type grid, but uses a different grid for the solution of the equations governing the evolution of colour function and the Navier-Stokes equations. The multigrid method used in his work has been used to solve the Poisson equation where the density ratio is 1000:1, indeed he concluded at the end of his section (2.6) that this extreme density ratio uses only twice the number of work units compared to the case of a density ratio of 1.1:1.

Adaptive mesh refinement is another commonly used technique to try to overcome the problems in the interfacial area, [1], [66]. Adaptive mesh refinement has been extensively studied and is particularly useful for problems with interfaces, for example droplet impact problems where at impact very

high pressures and rapidly changing velocities occur, whereas both pressure and velocities may be changing only very slowly in other parts of the computation domain. Adaptive mesh refinement was not considered in this work, but would be a natural next step in improving the accuracy of the numerical model, especially for flows with large density ratios or flows with impacts as described above.

8.3.4 Extension to irregular vessel geometries

In the current work, the boundary of the computational domain is taken to be along grid cells in either coordinate direction. Thus simulations that involve curved boundaries in this case can only be approximated using a 'staircase' type geometry. This approach however can be very inaccurate and is not attempted here directly. There are three main methods of treating such boundaries relating to interfacial fluid problems: these are finite-difference methods using partial cell treatment [96], cut-cell finite-volume modelling [43], [33] and boundary fitted grids.

Perhaps the easiest of the three choices to implement is the finite-difference method. Here a variable $\theta_{i,j}$ is introduced and is defined as the area open for flow in cell (i, j). However these codes use an explicit Eulerian advection scheme for the colour function, and no details of similar methods using Lagrangian advection methods, such as the one used in this thesis, can be found in the literature. Cut-cell finite-volume type methods have been used to study the impact of a wedge on a pool of water [43]. The results found draw close comparison with the experiments found. Boundary fitted grids are another option, although if the geometry is very complicated, the calculations of setting up the grid can become very laborious and indeed in some cases can be more time-consuming than the solution of the governing equations. The immersed boundary method introduced by Peskin has also been using in conjunction

with the VOF method [64].

8.3.5 Summary of the calculation for two-phase flow

The main stages of the computational algorithm for two phase flow are given below. In essence this is the same as the free surface routine but now there is no need to check on the status of each cell.

1. Initially the velocity field is known and values for the colour function are also known.
2. The velocity field is advected in the x-direction.
3. The interface is advected in the y-direction.
4. The tentative velocity field $\tilde{\mathbf{u}}$ is found.
5. The Poisson equation is solved for p throughout the domain.
6. The velocity field is updated.

8.4 Combining the PLIC method with the projection method for solution of the Navier-Stokes equations

Now that both parts of the routine have been discussed, the main routine is now assembled by putting both parts together. The overall routine is summarized by the flowchart figure 8.10. Below a brief description of the subroutines is given.

- MESHSET - Initialises the mesh, grid spacing etc. including solid obstacles. Also fluid properties such as viscosity and density are initialised

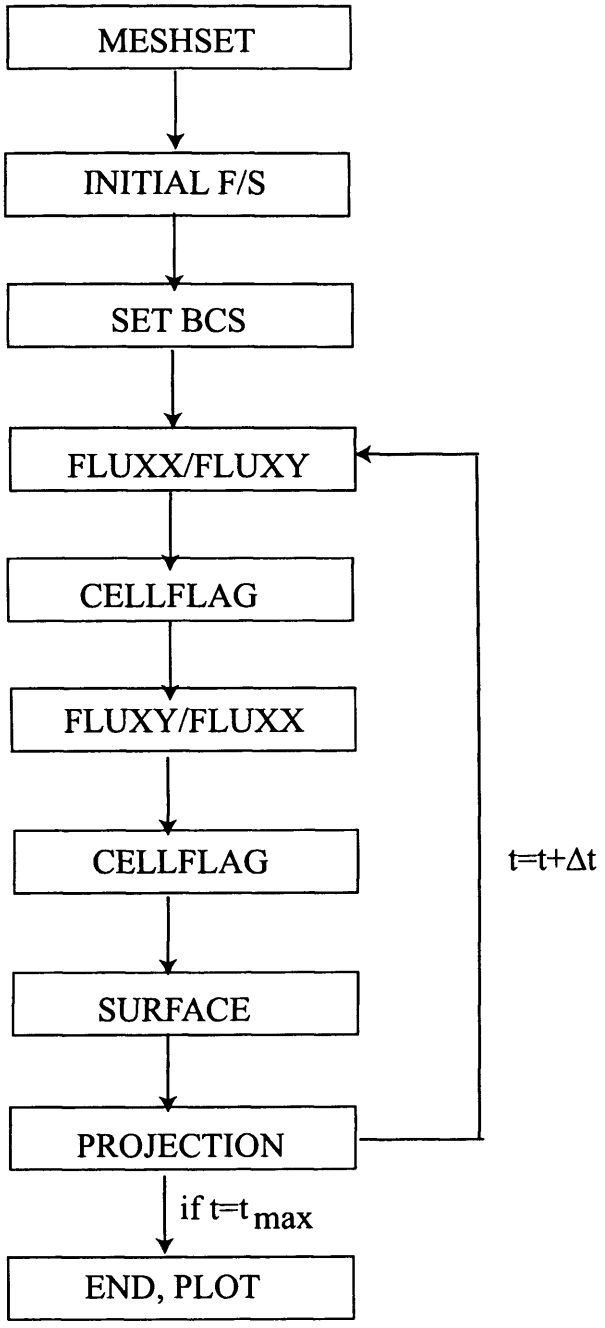

Figure 8.10: VOF/PLIC program flowchart.

along with the time step for the routine. In general the time step is kept constant throughout the routine. However the program will stop if the CFL number reaches the value of 0.5. The user then can reduce the time step manually and the computation can proceed.

- SET BCS - Set the choice of boundary conditions for the given problem, choices are slip or no slip. Periodic boundary conditions are not used in this work.

- INITIAL F/S - Calculates the volume fractions for the initial free surface/interface configuration. The interface is given in the form $y = f(x, 0)$.

- FLUXX - Calculates the new volume fractions after advection of the interface in the x-direction and reconstructs the interface.

- FLUXY - Advection in the y-direction and reconstruction. [3]

- CELLFLAG - Determines the configuration of each S-cell and imposes velocities at the free surface.

- SURFACE - Calculates the interpolation factor needed for the free surface pressure calculation.

- PROJECTION - Solves the Euler/Navier-Stokes equations using the SOR method for the solution of the Poisson equation. Returns a divergence-free velocity field and current pressure field.

- PLOT - Plots the streamfunction for the flow and the free surface/interface position. There are two methods used here to draw the free surface at a given time step. The first more straightforward method draws the

[3]It should be noted that the position of FLUXX and FLUXY should be changed at every time step, as shown in the flowchart, to get rid of any directional bias. See chapter 7.

$C = 0.5$ contour, however this does not always give particularly accurate results especially when droplets detach from the main flow. The second method plots all the individual discontinuous interface portions. Although not ideal for a coarse grid, this method gives better images on highly resolved grids.

Chapter 9

Tests of the Volume of fluid method

9.1 Test on the impulsively started lid-driven cavity problem

The lid-driven cavity problem has become a popular test case for solvers of the Navier-Stokes equations since the pioneering work of Burggraf [14]. The test is popular due to the simple boundary conditions as well as the abundance of literature on the subject. Details of the problem for steady state flow and impulsively started flow can be found in [25], [29], and [76]. Extensions to three dimensions can be found in [37]. We concentrate on the impulsively started flow here to use as a test for the viscous flow solver. Although the boundary conditions are straightforward, there is a singularity at the top corners. This can be resolved using higher order methods such as the Chebychev collocation method [2].

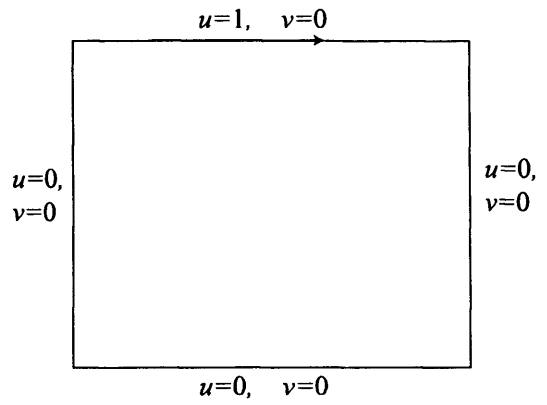

Figure 9.1: The velocity boundary conditions for the lid-driven cavity flow.

9.1.1 Problem set-up

No-slip boundary conditions are applied to the left, bottom and right of a 1×1 domain. The velocity condition at $y = 1$ is given by $\mathbf{u} = (1, 0)$, see figure 9.1. Pressure at the boundaries is treated as in section 8.1.8, so again there is no need to implement any boundary conditions on pressure. As no interface is present here, the only part of the algorithm that is needed is the projection method. We start from a zero velocity field. The equations of motion here are the non-dimensionalized Navier-Stokes equations given by

$$\frac{\partial \mathbf{u}}{\partial t} + (\mathbf{u}.\nabla)\mathbf{u} = -\nabla p + \frac{1}{\mathrm{Re}}\nabla^2\mathbf{u}, \qquad \nabla.\mathbf{u} = 0. \tag{9.1}$$

This form of the equations was chosen so direct comparison with [76] could be performed. Indeed details of the non-dimensionalization for the problem can be found in this reference.

9.1.2 Results

Figures 9.2– 9.11 show the streamlines and $u-$ and v-centreline velocities for the cases Re=400 and Re=1000. The results seem to be in good agreement

with others previously obtained. Flow is driven by the upper wall. A vortex known as the Primary vortex forms near the top right hand corner of the cavity and moves towards the centre of the cavity at later times at higher Reynolds numbers. At Reynolds number of 400, two vortices form in the bottom left and right corners and stay there for all later times. At Re=1000 an eddy is formed at the right wall, and subsequently another eddy at the bottom right hand corner. At later times the two eddies merge and form a large eddy in the bottom right hand corner of the cavity as pointed out in [76]. At larger Reynolds numbers, the calculations become more difficult due to the presence of boundary layers near the walls and also due to the presence of a Hopf-bifurcation [9].

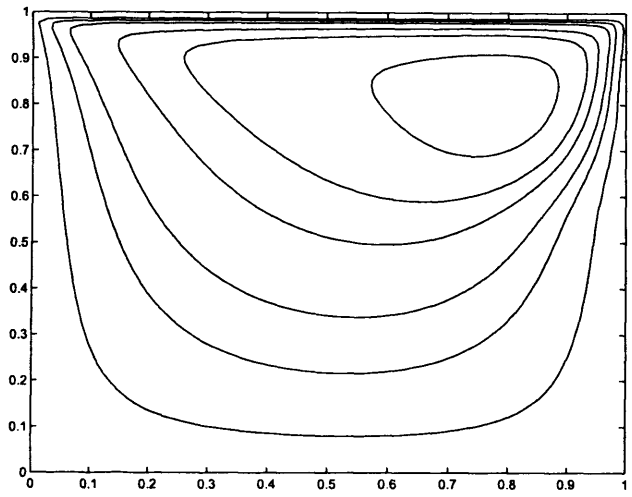

Figure 9.2: Streamlines for Re=400 and $t = 2$.

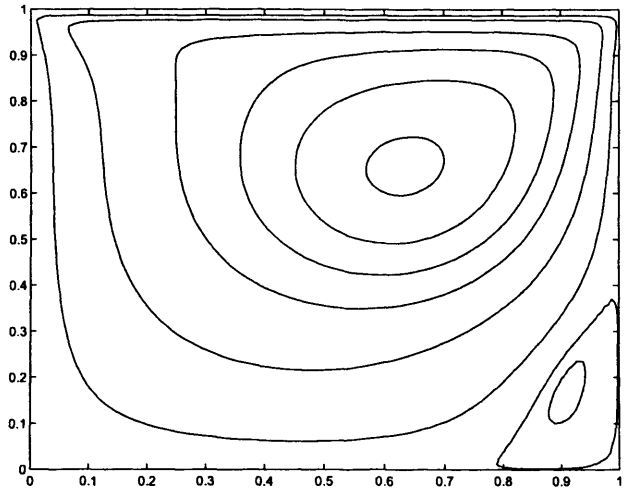

Figure 9.3: Streamlines for Re=400 and $t = 6$.

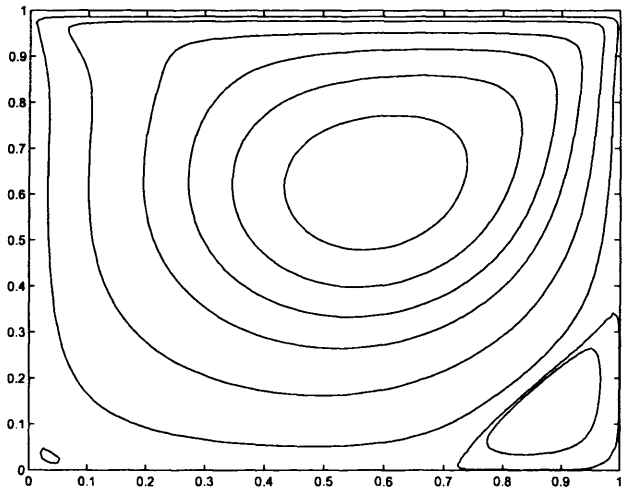

Figure 9.4: Streamlines for Re=400 and $t = 10$.

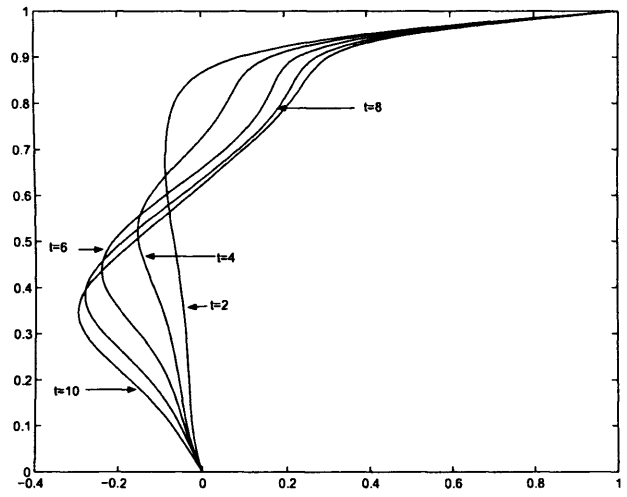

Figure 9.5: The centreline u-velocity for Re=400 at non-dimensional times $t = 2, 4, 6, 8$ and 10.

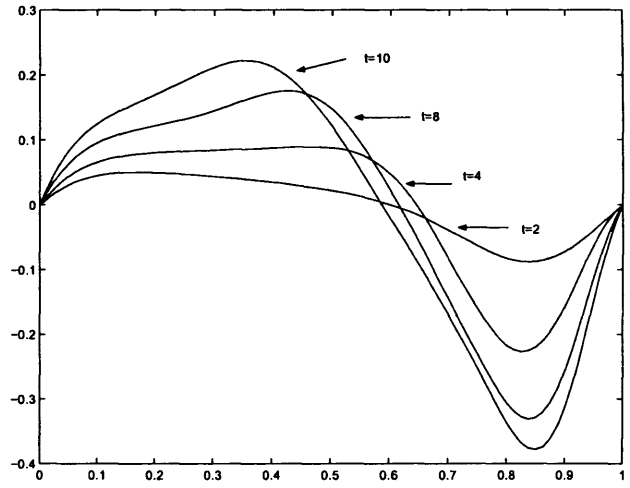

Figure 9.6: The centreline v-velocity for Re=400 at non-dimensional times $t = 2, 4, 8$ and 10.

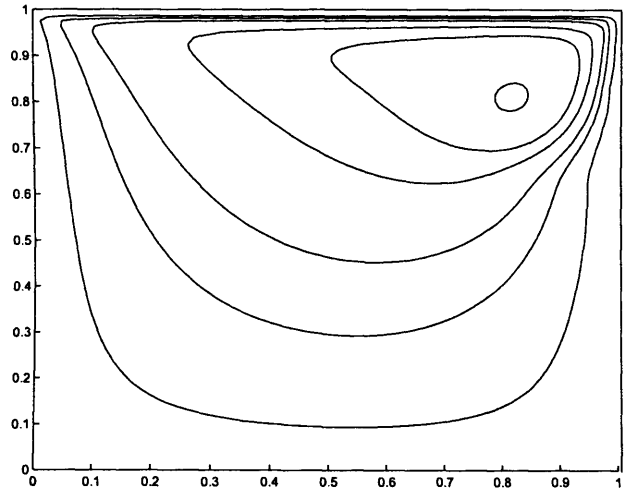

Figure 9.7: Streamlines for Re=1000 at non-dimensional time $t = 2$.

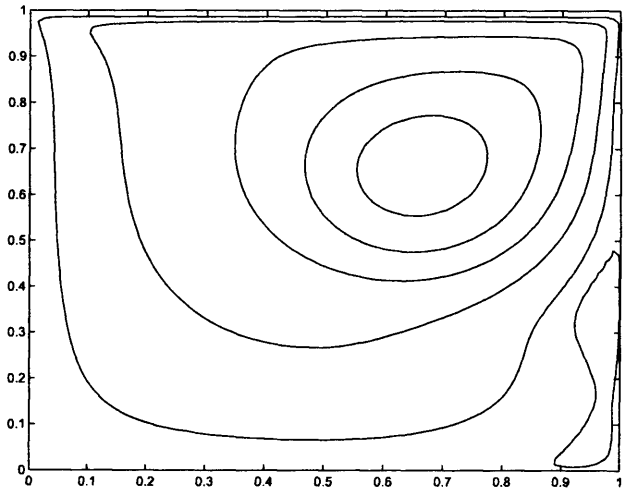

Figure 9.8: Streamlines for Re=1000 at non-dimensional time $t = 6$.

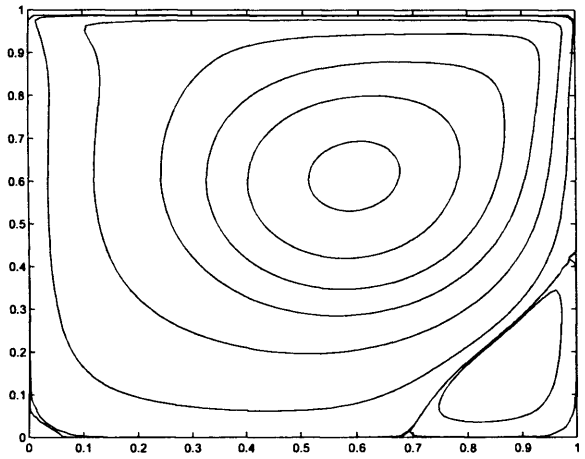

Figure 9.9: Streamlines for Re=1000 at non-dimensional time $t = 10$.

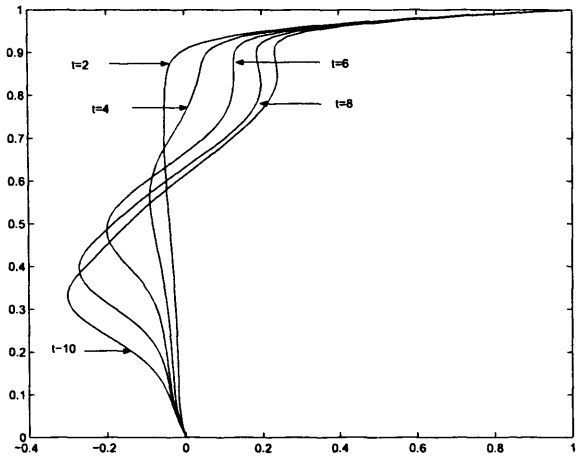

Figure 9.10: The centreline u-velocity for Re=1000 at non-dimensional times $t = 2, 4, 6, 8$ and 10.

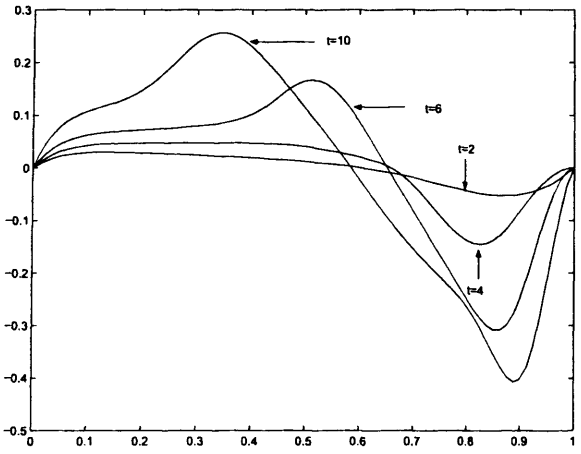

Figure 9.11: The centreline v-velocity for Re=1000 at non-dimensional times $t = 2, 4, 6$ and 10.

	Present	Sahin [76]	Present	Sahin [76]
	u_{min}, y_{min}	u_{min}, y_{min}	v_{min}, x_{min}	v_{min}, x_{min}
$t = 2$	-0.062, 0.716	-0.058 , 0.710	-0.050, 0.882	-0.048, 0.875
$t = 4$	-0.096, 0.524	-0.092 , 0.525	-0.149, 0.826	-0.178, 0.825
$t = 6$	-0.201, 0.482	-0.210 , 0.480	-0.310, 0.846	-0.335, 0.856
$t = 8$	-0.283, 0.390	-0.289, 0.384	-0.382, 0.876,	-0.395, 0.884

Table 9.1: Comparison of results for the lid-driven cavity flow at Re = 400. The first two columns compare the minimum values of u along $x = 0.5$, along with the corresponding y coordinate. The third and fourth columns show the minimum values of v along $y = 0.5$, with the corresponding x-position.

These results show that the Navier-Stokes solver is working well at moderate Reynolds numbers. However this algorithm does not verify the Volume of Fluid (PLIC) code, as a free surface is not present. One of the main tests for Volume of Fluid or free surface calculations is the so called dam-break problem which is discussed in the next section.

9.2 The dam-break problem

Initially a column of water with a free surface at the top is confined by a barrier to the right and solid wall both below and to the left. When the barrier is removed the water flows smoothly out. This is known as the dam-break problem and has been extensively studied, usually as a test for free surface and interfacial computational fluid dynamics codes. It is a good problem to test interfacial flow codes due to the simple initial configuration and simple boundary conditions. Figure 9.12 shows the set up: initially the fluid velocity is zero and the fluid remains stationary under atmospheric pressure. At $t = 0$ the barrier is released and the fluid flows out under the force of gravity.

This problem has been studied both analytically, experimentally and numerically. Analytical approaches can be found in [89] while Volume of Fluid simulations have been studied by [43], [59]. Here the dam-break problem is combined with impact onto a solid object and the subsequent motion. The problem is particularly relevant in the field of marine hydrodynamics, for example the run up of a wave onto the bow of a ship. Experimental studies can be found in the literature, for example [54].

We assume at first here that the air is negligible and that the water is inviscid. Using these approximations the free surface algorithm can be tested and compared to results previously obtained.

9.2.1 Set-up of the problem and results

Figure 9.12 shows the setup for the problem. Initially the stationary column of water which is bounded by the gate has dimensions a by h. When the gate is removed the fluid flows out smoothly under gravity and the free surface is tracked. Free surface plots are shown at several different times. Water is assumed to be inviscid and atmospheric pressure is taken to be zero. Free slip boundary conditions are applied on all of the walls. A dimensionless time and displacement are given by

$$\tau = t\sqrt{\frac{2g}{a}} \qquad \delta = \frac{x}{a}. \tag{9.2}$$

Here t is the time elapsed after the gate is taken away, $a = 1$ is the initial length of the water column, and g, the given acceleration due to gravity taken as -1.0 here.

The results shown in figure 9.14 are in good agreement with experiments [54]. The values for δ for the first three plots are given by 1.225, 2.05, and 2.75. Figure 9.13 shows a comparison between experimental results and those obtained in this work: a close agreement is found. (This figure shows more computational results than are presented in figure 9.14). The results here also agree with other computations with the VOF method [59] and boundary element method. Grid refinement showed that the results became closer to those obtained experimentally and by other VOF simulations. The bottom right of Figure 9.14 shows the free surface configuration after impact onto a vertical wall, to show that the code can deal with impacts successfully.

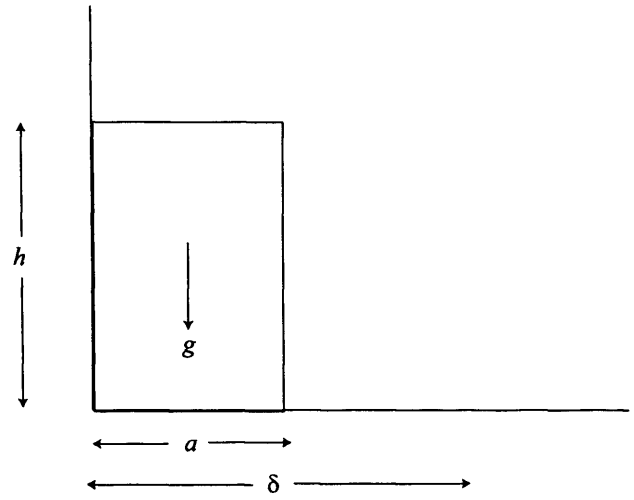

Figure 9.12: Initial configuration for the broken-dam problem. Hydrostatic pressure is initially set in the column of water with atmospheric pressure at the free surface. The height of the water column is initially h and the length of the column is a, while δ represents the eventual fluid displacement length.

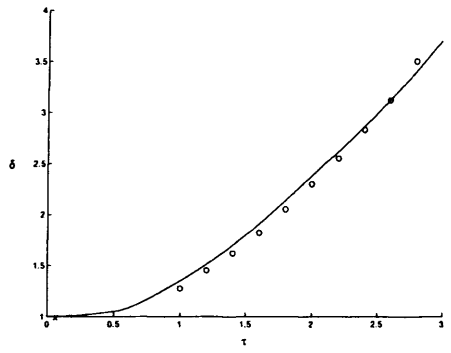

Figure 9.13: Horizontal displacement δ, for the broken-dam problem. Solid line- VOF computations, o- experiments by Morton and Moyse.

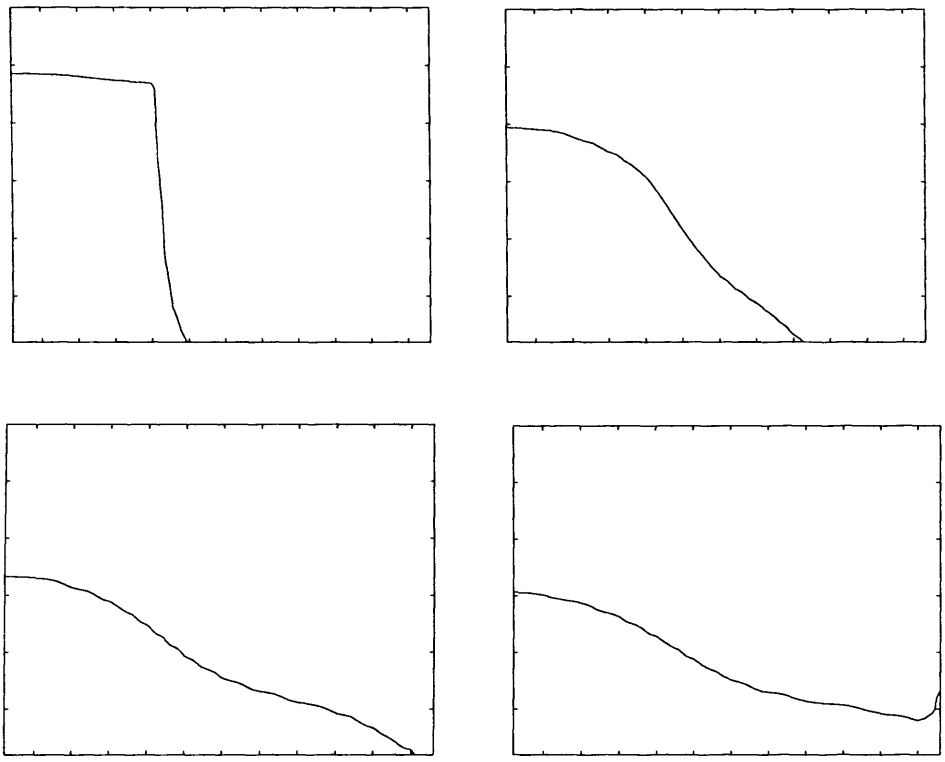

Figure 9.14: The broken-dam problem. Interface positions at non-dimensional times $\tau = 0.75$, $\tau = 1.75$, $\tau = 2.4$ and $\tau = 3$.

9.3 The fractured diaphragm problem

This problem is probably the simplest test case to set up for the two fluid solver. Similarly to the broken dam problem, a vertical barrier separates two fluids which are initially at rest. When the barrier is removed the fluid motion driven by the gravitational force is examined. Here we take both fluids to be incompressible and inviscid and free slip conditions are applied on all the walls. The top left of figure 9.15 shows the initial configuration ($t = 0$) of the fluids. The fluid on the left is of density 1 and the right hand side is of density 2. The figures show the interface position at five different times. These are all in good agreement with [99]. The heavier fluid 'collapses' towards the lighter fluid and a vortex is formed at the centre of the domain. After a time $t = 4.1$ the interface hits the top right hand corner of the domain and the lighter fluid is then totally above the heavier fluid. The interface then rides up the left hand wall and computations at later times show that the interface reaches the top corner of the domain again, as found also in [99].

9.4 The Rayleigh-Taylor instability

The well known Rayleigh-Taylor instability is another common test for numerical routines with an interface. The Rayleigh-Taylor instability here acts as a test for the two fluid solver, as outlined in section 8.3, and so this gives a good test for the two-fluid solver. Initially two fluids of different density are separated by a flat interface. A slight perturbation to the interface will result in an instability if a denser fluid is on top of a less dense fluid. Small perturbations to the interface will be amplified and the amplitude of the perturbation grows in time. This is an example of a fingering instability of an accelerated interface due to infinitesimal perturbations by a pressure gradient in the opposite direction to a density gradient [9]. The baroclinic torque $(\nabla\rho \times \nabla p)/\rho$

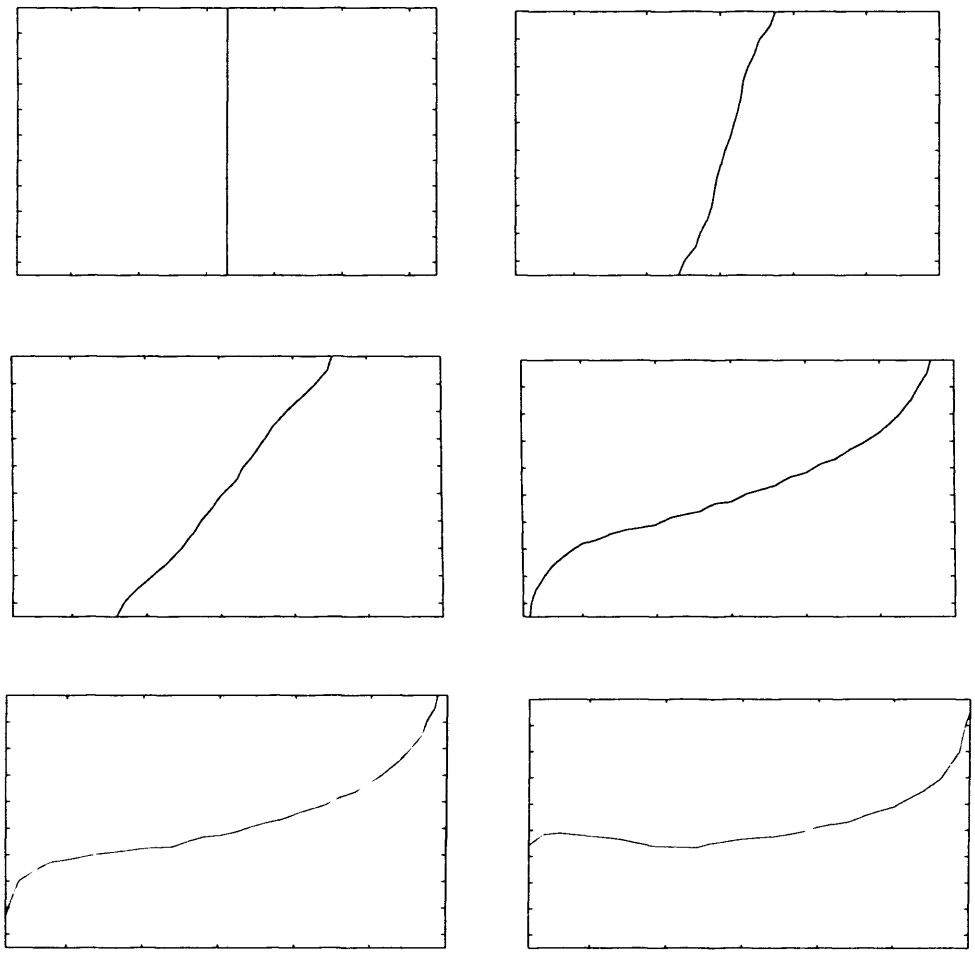

Figure 9.15: The evolution of the interface in the fractured diaphragm problem.

causes the fluids to mix. There are three main stages associated with this instability: an initial exponential growth stage, a constant growth stage and a free fall stage dominated by longer wavelengths, [9], [110]. A comprehensive review of the Rayleigh-Taylor instability for inviscid fluids is given by Tryggvason [97], where both analytical attempts and numerical results are shown. The numerical method of choice in this work is the AP method. The Volume of Fluid method has also been applied to the Rayleigh-Taylor instability [50]. The example of Rayleigh-Taylor instability proves a good test for the overall algorithm as errors in the colour function field, from solving the non-linear evolution equation for the kinematic condition, will affect the discrete value of the density appearing in the momentum equation. Numerous Volume of Fluid codes have been tested on the Rayleigh-Taylor instability, for example [66] and the PLIC method [50] .

First we consider two inviscid fluids of density ρ_1 and ρ_2 and the equations to be solved are the Euler-equations. Again the gravitational term is taken to be -1.0.

9.4.1 Problem set up

The choice of domain to study this instability is a box with width L and height H to test the numerical procedure for two different fluids. With no perturbation to the interface, i.e. a horizontal interface, the two fluids remain in their initial configurations. This is verified in the numerical routine. Next a slight perturbation to the interface $\tilde{f}$ is applied. This is given in other test cases performed as a cosine wave. Care is taken so that the perturbation is symmetric in the line $x = 1$, so that the flow solution should also be symmetric in this line. It should be noted here that no other symmetry conditions are used in this calculation. Initially the interface shape is given by

$$f = H/2 + a\sin(2x\pi/L), \tag{9.3}$$

where the second term represents the perturbation $\tilde{f}$ to the horizontal interface. Here a is the amplitude of the initial disturbance. The volume fractions are found in exactly the same way as described in chapter 4. Gravity is the only body force in this problem; this appears only in the y-momentum equation.

At first we consider two inviscid fluids of densities ρ_1 and ρ_2. Here the dimensions of the domain are taken as $H = 4$ and $L = 2$ to compare with Tryggvason's results [97]. The initial velocity field and pressure are both taken to be zero. It should be pointed out that although such pressure is clearly unrealistic due to the gravitational force acting in this situation, it is acceptable here as the solution at the next time-step is independent of the initial pressure.

The initial disturbance to the horizontal interface produces an acceleration of the heavier fluid into the lighter fluid. First, falling spikes of heavy fluid are seen penetrating into the lighter fluid, and bubbles of light fluid rising up into the heavier fluid. Figure 9.17 shows the evolution of the interface where the upper fluid is three times as dense as the lower fluid. As time increases, a 'mushroom cap' is formed and the flow becomes highly non-linear.

The computations are in agreement with results from [99] and Tryggvason's results [97] using the vortex in cell method. The results of this work capture the two downward travelling vortices very well. These effects are not resolved quite so well with the current method, however a highly refined grid probably would manage to capture the intricate details of the vortices. Figure 9.16 shows a comparison of interface shapes using different grids, and the highly refined grid does show the main effects of the flow. A very fine grid was not used in this section as its role is to act as a test for the numerical routine. The flow was also studied where the density of the heavier fluid $\rho_1 = 8$ and the lighter fluid $\rho_2 = 1$. The interface configurations at various times are shown in figure 9.18. Here the instability occurs much sooner, and tiny fragments of fluid detach from the main stem of the descending heavier fluid, just before the

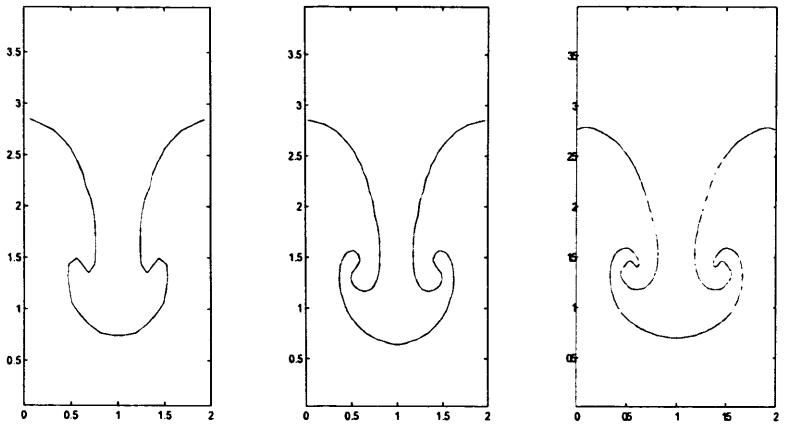

Figure 9.16: Comparison of different grids used for the Rayleigh-Taylor problem, with $\rho_1 = 3$ and $\rho_2 = 1$. Left to right 16 by 32, 32 by 64 and 64 by 128.

interface touches the bottom of the box. Computations were also undertaken at higher density ratios. However meaningful results were not obtained for density ratios greater than twenty. Section 8.3.3 deals with the reason for this failure and methods to try to correct this fault [75].

The interface shapes obtained are in agreement with those of Tryggvason and others although the configurations are found at different non-dimensional times. This is due to the fact that no exact details of the initial configuration of the interface are given by Trygvasson, only that the perturbation is of sinusoidal shape. Similar computations of the Rayleigh-Taylor instability can be found in [9] who gives a detailed account on stability analysis of both inviscid and viscous flow. He compares his results for the viscous case with those of [67]. This work concentrates on viscous fluids but the non dimensionalisation used is unclear. Other simulations using the Volume of Fluid method can be found in [75], and the Marker and Cell method can be found in [99].

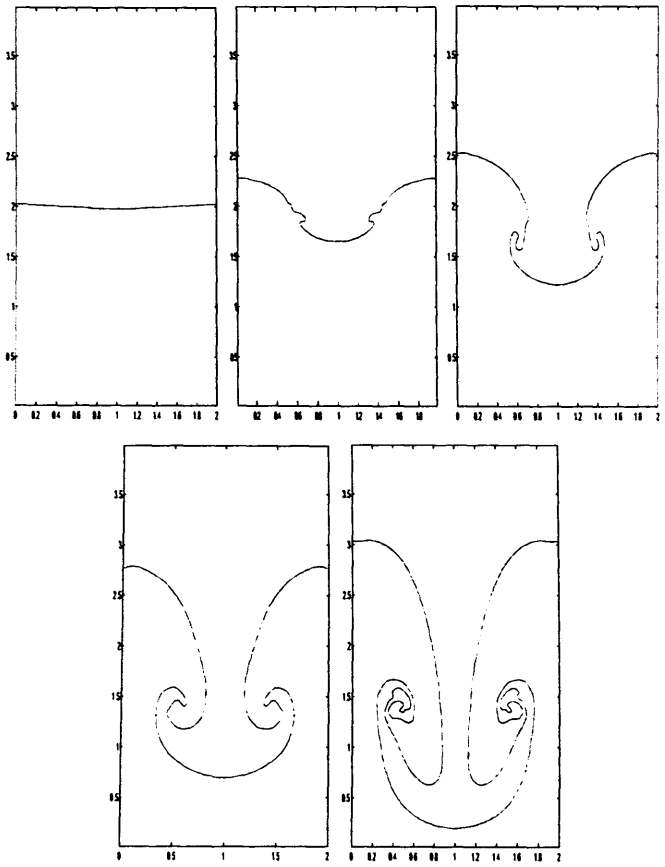

Figure 9.17: The Rayleigh-Taylor instability for inviscid, again with $\rho_1 = 3$ and $\rho_2 = 1$. From left to right, top to bottom $t = 0, 2, 3, 4$, and 5.

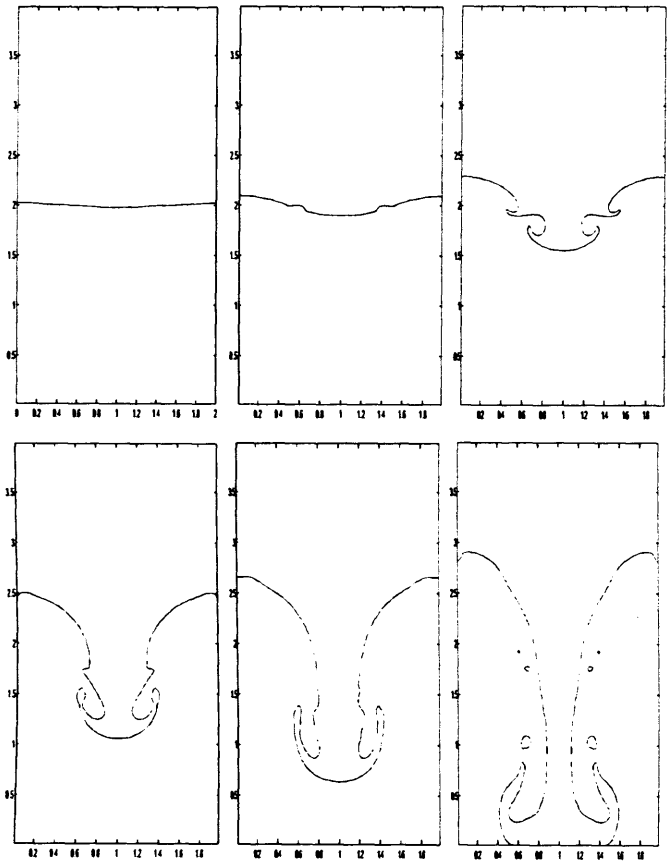

Figure 9.18: The Rayleigh-Taylor instability for higher density ratio. Here the upper fluid is of density 8 and the lower fluid of density 1. Interface positions at times $t = 0, 2, 3, 4, 5$ and 6.

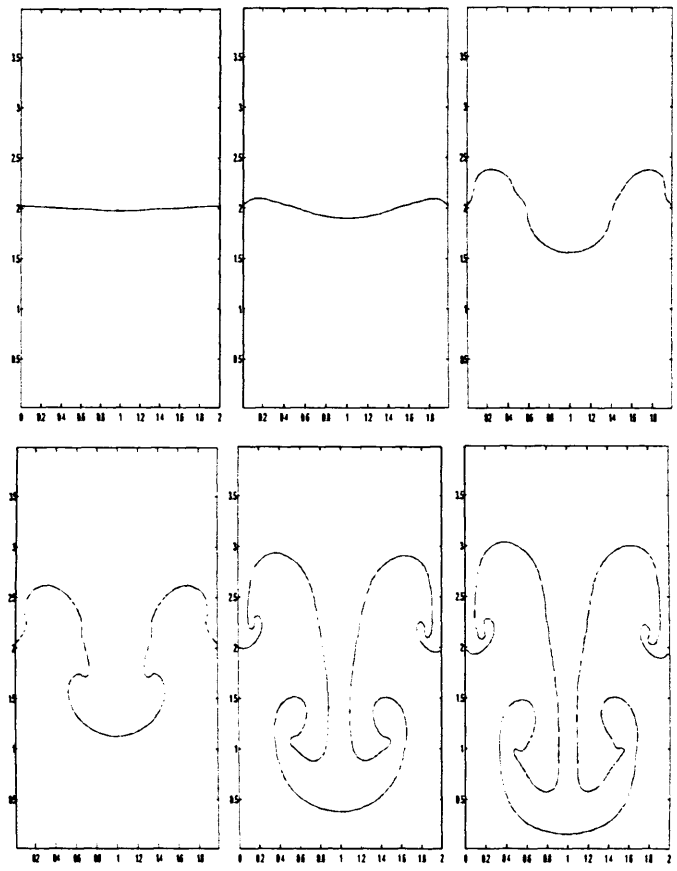

Figure 9.19: The Rayleigh-Taylor instability for viscous fluids. Here both fluids have viscosity $\mu = 0.01$. No slip conditions are applied on all the walls. Interface positions at times $t = 0, 2, 3, 4, 5$ and 6.

9.4.2 Viscous fluids

Figure 9.19 shows the Rayleigh-Taylor instability for two viscous fluids. Here the instability is slower to develop as expected, with viscous terms now present in the momentum equations. The no-slip condition also acts to retard the development of the spikes and bubbles. Simulations using the slip condition can be found as well as periodic boundary conditions [67], [99].

9.5 Comment

The numerical method has been described at length and has been shown to be working well. The application to embolization will be addressed in the following chapter.

Chapter 10

Application to the embolization procedure

The Volume of Fluid code has been proven to be able to deal with two fluids as demonstrated in the previous section. Now attention can be turned to the problem studied in this thesis: namely the embolization process. As the density of glue and blood are roughly the same, the numerical routine should be well suited to the flow of glue and blood. We first examine a simple model; here both the glue and the blood are taken to be inviscid. The artery where the glue is injected is assumed to be a channel of constant width and the effects of the blood on the flow of the glue are examined in the flow only in the mother. Flow to two or more daughters will be discussed in section 10.3.

10.1 Inviscid flow in a single mother

The first situation studied is the flow of glue and blood in a single mother channel. The non-dimensional width of the channel is taken to be 1. At $t = 0$ a droplet of radius 0.25 is positioned at the point (0.55,0.5), to preserve symmetry in the line $y = 1/2$. At the inflow boundary, $x = 0$ in this case, a

constant blood velocity $u = 0.5$ is imposed and $v = 0$. At the outflow $x = 4$, Neumann conditions are applied for each of the velocity components. A forcing term of 1.0 kg m/s^2 is applied and is included in the x-momentum equation to simulate the glue injection. In this case though the forcing term is applied over the whole domain, not just to the glue. When the forcing term was applied to the glue only, the method became unstable. In reality of course the forcing is only applied to the left hand edge of the glue, the part coming out of the catheter.

Figures 10.2 to 10.6 show results for the problem described above where the density of the glue is varied; the density of blood is set to unity in all the computations. Figure 10.2 shows the interface positions at different times when the density of the glue $\rho_1 = 2$. Here the glue spreads and indeed takes up most of the channel width by the time $t = 2.5$. However at $t = 3$, slight breakup is seen in the 'tail' of the droplet and at later times smaller droplets detach from the glue. Similar results are found when the density of the glue is increased and now the breakup happens at earlier times and further upstream. Results for $\rho_1 = 4$ and $\rho_1 = 10$ are shown in figures 10.3 and 10.4.

When $\rho_1 = \rho_2 = 1$, the droplet travels with the constant inflow velocity $u = 0.5$ and retains its circular shape throughout the domain. When the density of the glue is less than that of the blood, the situation is dramatically different. In this case the glue is trying to move through a denser fluid and the shape of the interface becomes concave at the front rather than the back, as was the case previously.

The cases where the density of the glue is set to be 0.5 and 0.25 are shown in figures 10.4 and 10.5. Again in these cases the shape of the interface for the two cases is quite similar. Indeed, as shown from the figures in the case where $\rho = 0.25$, the shape of the interface at time $t = 1.5$ is similar to that of the case where $\rho = 0.5$ at $t = 2$. This trend can also be seen at other times in the

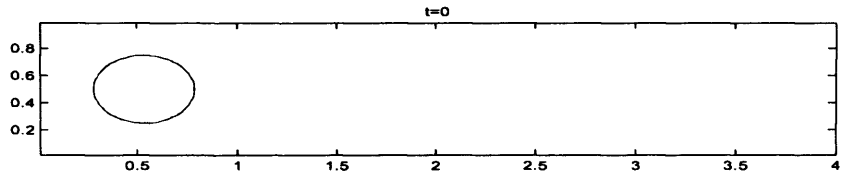

Figure 10.1: Initial configuration for the figures 10.2–10.6

two simulations. It can be seen for figure 10.6 that at time $t = 3$ the glue has spread to take up almost the whole channel width, even though slight breakup is seen on the downstream edge of the glue.

So it seems that in both cases- ρ being greater than or less than equal to one- the droplet spreads out over time. The lower the density of the glue, the faster the glue spreads over the feeding artery. However the lower the density of the glue, the less far the glue travels down the feeding artery.

It should be noted that although the computations above were for plug flow at the inlet, interface positions for other inlet velocities would yield the same interface positions but just shifted along the artery. This is a consequence of the Euler equations being invariant on the transformation $\bar{x} = x - ct$, $\bar{u} = u - c$, where c for instance could be the velocity at the inflow.

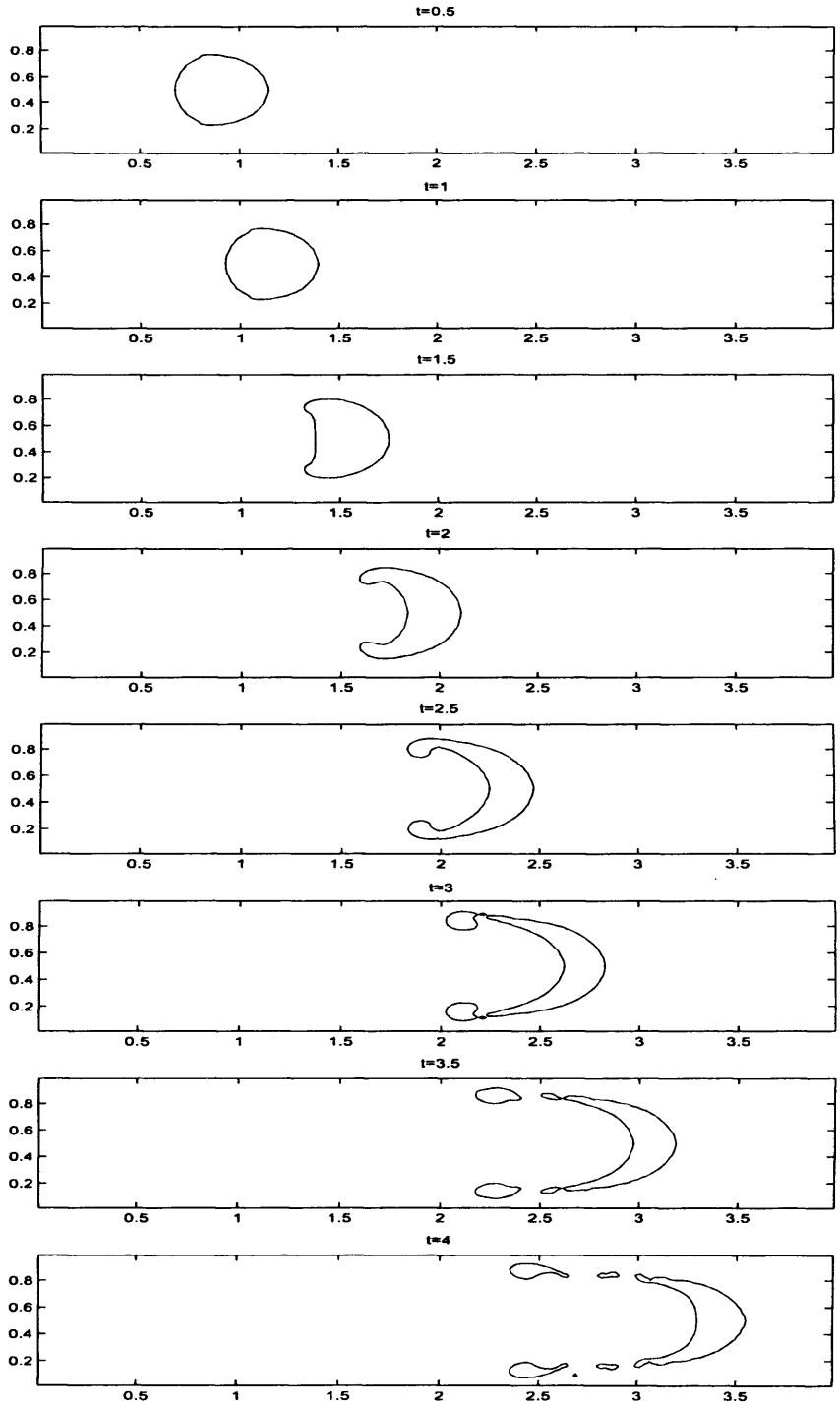

Figure 10.2: Interface positions for the case $\rho_1 = 2$, $\rho_2 = 1$

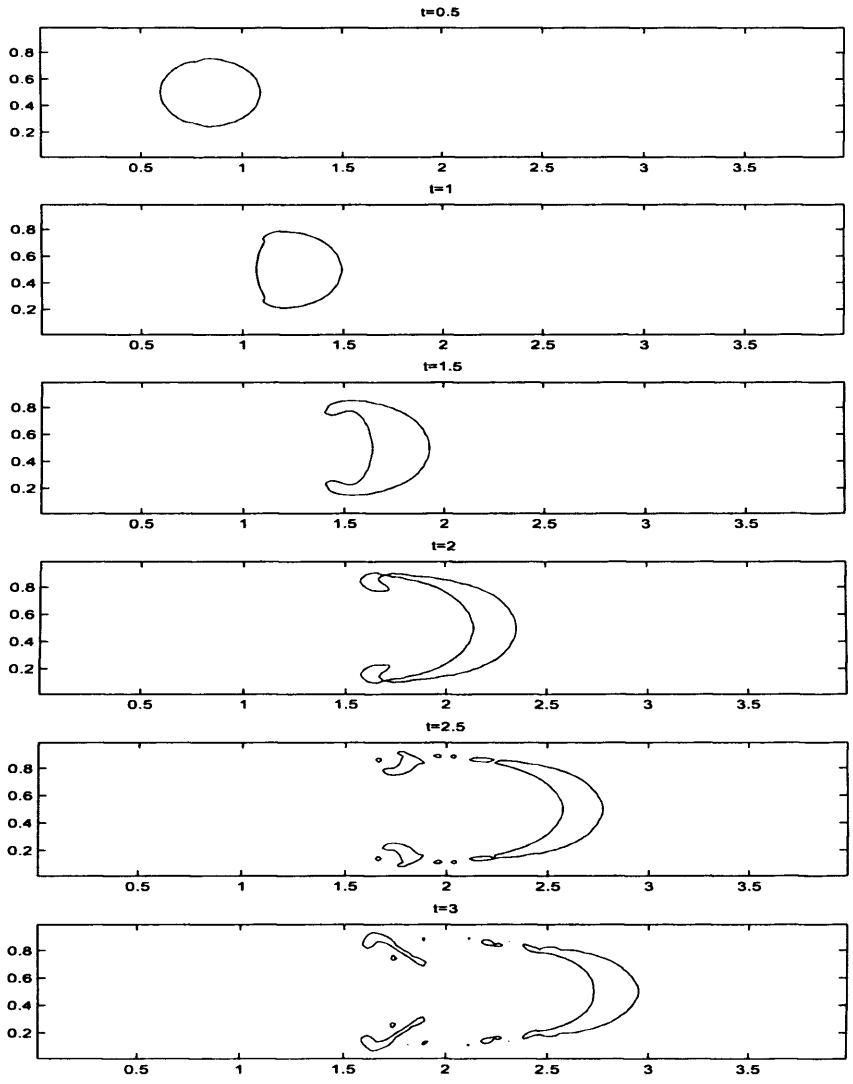

Figure 10.3: Interface positions for the case $\rho_1 = 4$, $\rho_2 = 1$

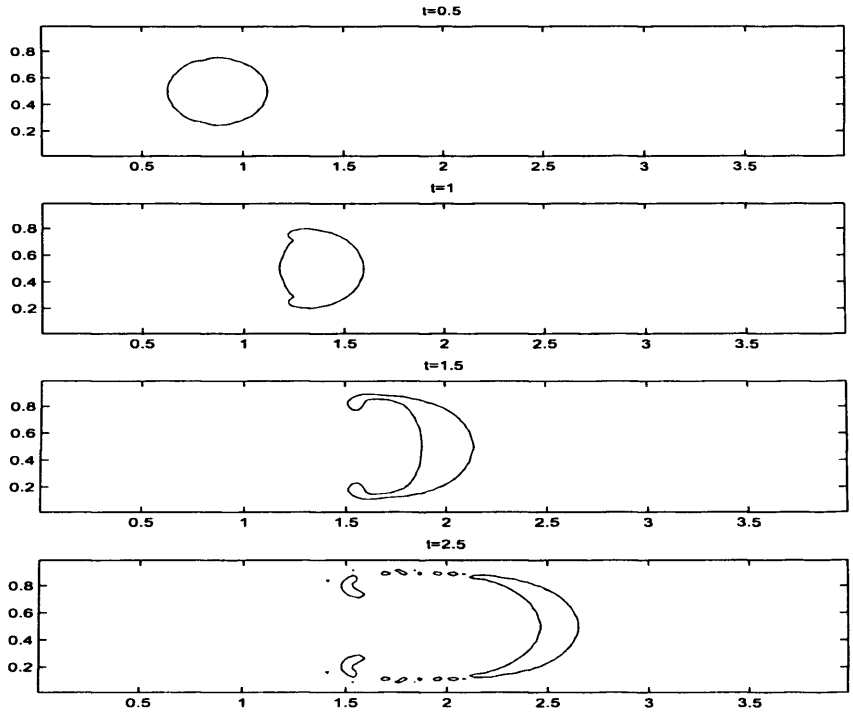

Figure 10.4: Interface positions for the case $\rho_1 = 10$, $\rho_2 = 1$

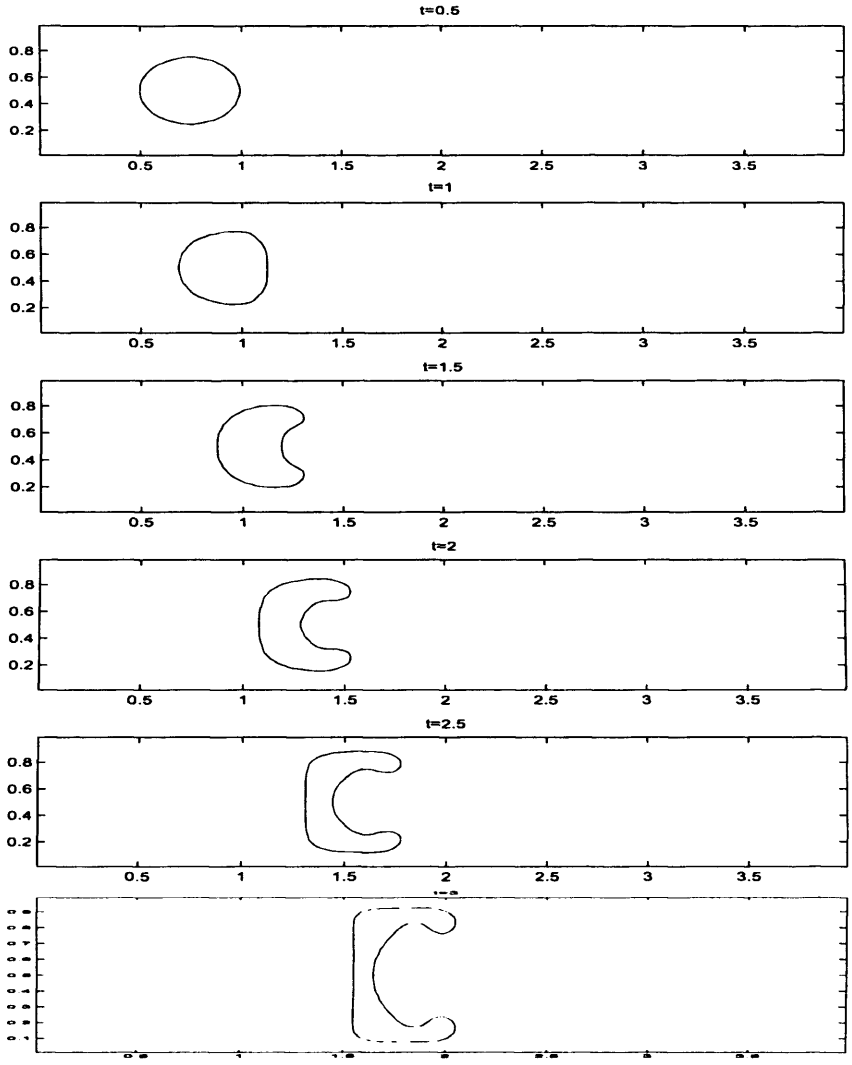

Figure 10.5: Interface positions for the case $\rho_1 = 0.5$, $\rho_2 = 1$

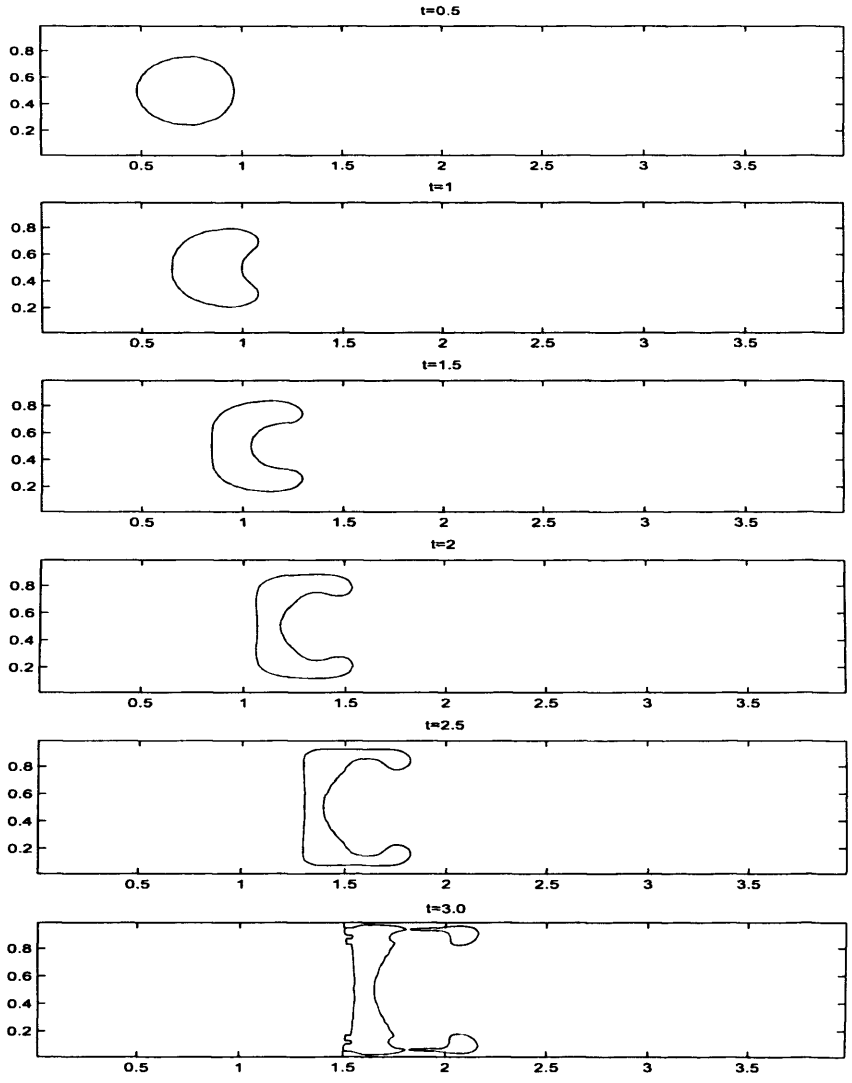

Figure 10.6: $\rho_1 = 1/4$, $\rho_2 = 1$

10.2 Constant injection of glue

In this section we analyse the motion where the glue is continuously injected as a constant stream. Both the glue and blood are again assumed to be inviscid here. The velocity of injection is assumed to be constant, so that comparisons can be made with the results obtained using the conformal mapping theory of chapter 3.

The initial configuration is shown in the top figure in 10.6. Here the width of the mother artery is again taken to be 1 and the width of the catheter taken to be 0.35 and so taking up approximately one third of the artery. The catheter tip is at $x = 0$ and so in the region we impose the constant inflow velocity of glue u_1 and in the blood we impose a constant inflow velocity u_2 in both the top and bottom regions. So the flow is assumed to be symmetric again in the line $y = 1/2$. Neumann conditions are again applied to the colour function at the inflow, which in this case corresponds to a constant injection of glue. The glue is injected as a column as shown in the top figure of 10.6, the width of the column is that of the catheter and the length of the column is 0.05.

When the densities of the two fluids were equal the interface stayed straight at all subsequent time steps, no matter which initial velocities at the inflow u_1 and u_2 were chosen. Indeed here the solution in the glue and the blood is just the initial velocity in each fluid and $v = 0$ and $p = 0$ throughout the domain. This is in contrast to the results obtained from the conformal mapping theory as found in chapter 3. There the velocity was assumed to be smooth, whereas in the Volume of Fluid simulations the discrete velocity changes at the interface.

10.2.1 Results

Again in all calculations in this section there is symmetry in the line $y = 1/2$. Results for different values of the glue velocity u_1 are shown in figures 10.7 to 10.12, where in all these simulations $u_2 = 1$. Figure 10.7 shows the interface positions at four different times for the case where $u_1 = 2$. Here the glue spreads out at front of the column, i.e. the downstream edge. At $t = 0.5$ though, the interface near the catheter is approximately straight, and so a unidirectional solution to the equations holds in this region. Indeed this characteristic can be seen in all the figures in section 10.2.

The cases where the inflow velocity of the glue is increased to 5 and 10 are shown in figures 10.8 and 10.9 respectively. The figures show that the greater the inflow velocity of the glue, the faster and further the glue spreads as expected. These results should also be compared to those obtained with the conformal mapping theory in chapter 3. The final plot in figure 10.8 shows that at $t = 0.55$ the glue has spread over most of the feeding artery. When u_2 is increased to 10 the glue spreads even further to take up the whole feeding artery at an earlier time.

The other situation studied is where the the inflow velocity of the glue is less than that of the blood. Only two cases are examined here for the cases $u_1 = 1/2$ and $u_1 = 1/4$. Here the glue travels in a uniform manner except at the downstream edge where a small tip develops as shown in figure 10.10. When u_1 is decreased still further to $u_1 = 1/4$ as shown in figure 10.11, the unidirectional solution is still seen near the catheter tip, however at the downstream edge of the glue an instability develops and a hole is formed in the middle of the column of glue. No more analysis on these cases was performed however, due to the limited application to the embolization process.

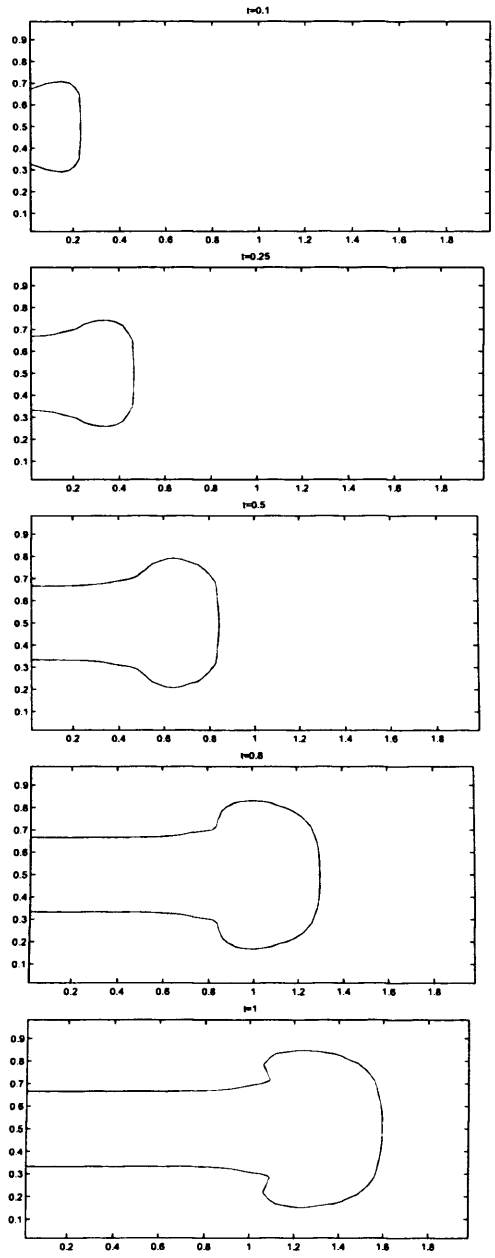

Figure 10.7: The case where the glue is injected as a constant stream. Here the initial velocities of the glue and blood are $u_1 = 2$ and $u_2 = 1$ respectively and $\rho = 1$.

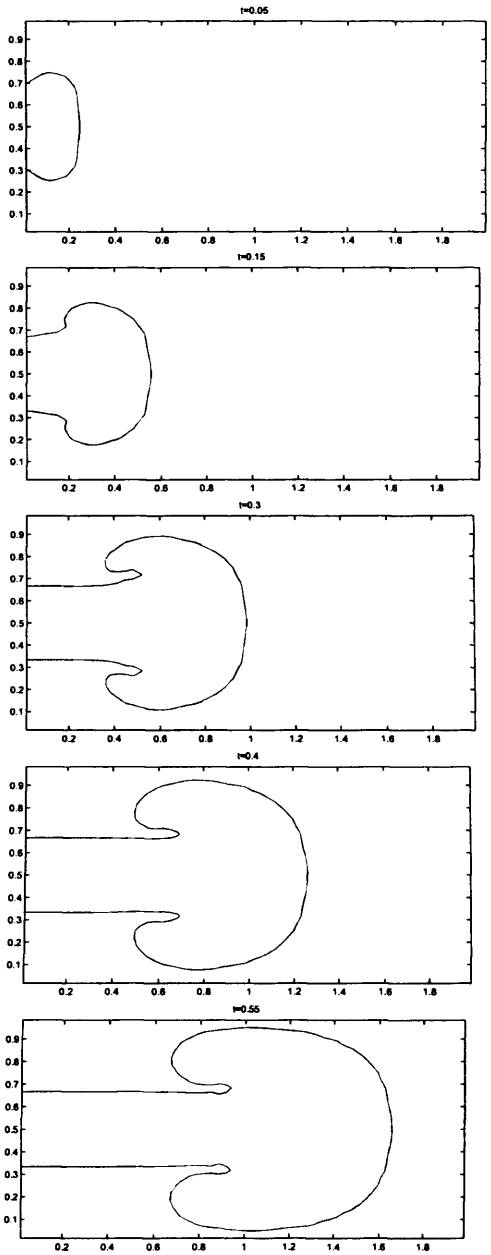

Figure 10.8: The case where the glue is injected as a constant stream. Here the initial velocities of the glue and blood are $u_1 = 5$ and $u_2 = 1$ respectively and $\rho = 1$.

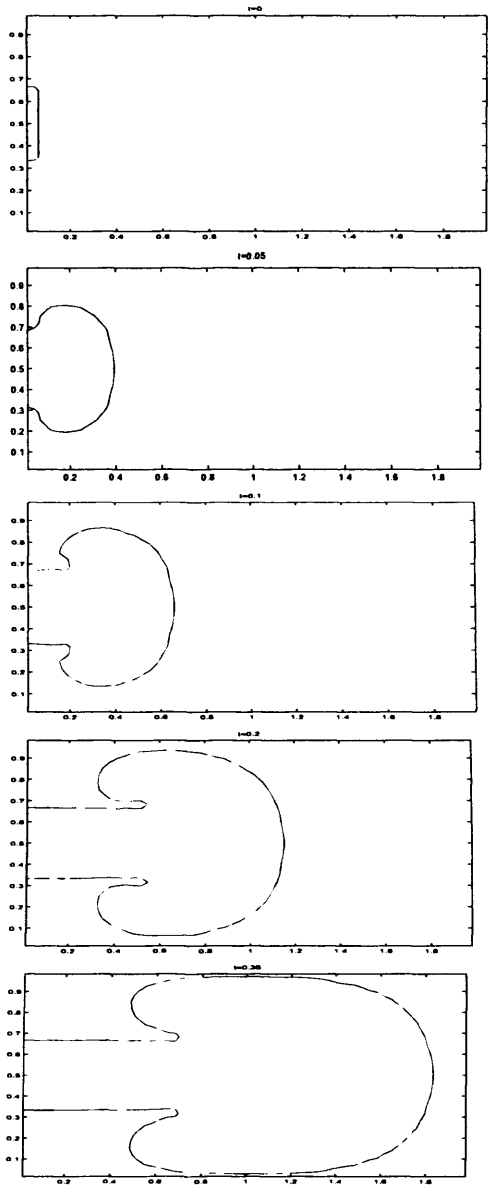

Figure 10.9: The case where the glue is injected as a constant stream. Here the initial velocities of the glue and blood are $u_1 = 10$ and $u_2 = 1$ respectively and $\rho = 1$.

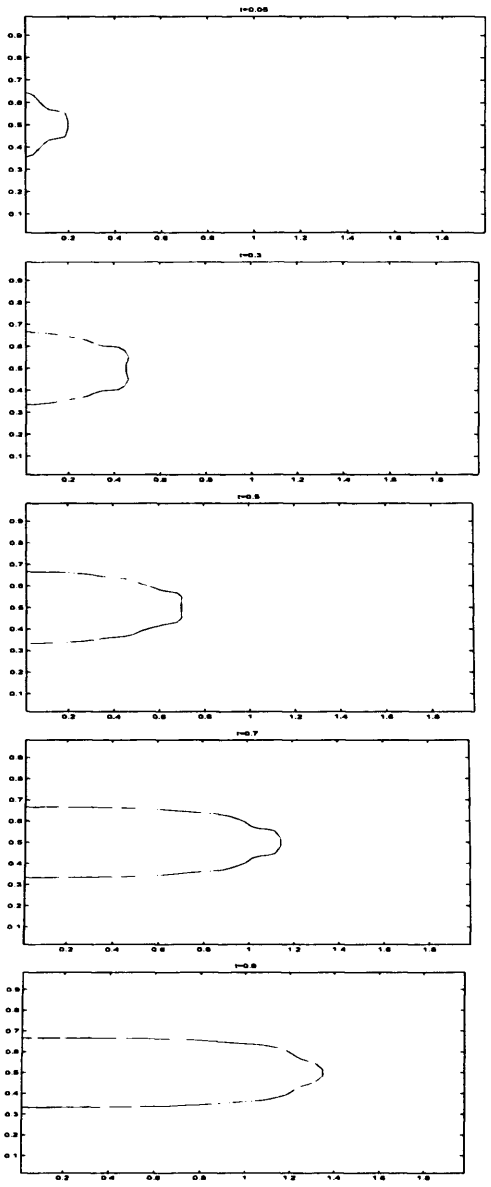

Figure 10.10: The case where the glue is injected as a constant stream. Here the initial velocities of the glue and blood are $u_1 = 1/2$ and $u_2 = 1$ respectively and $\rho = 1$.

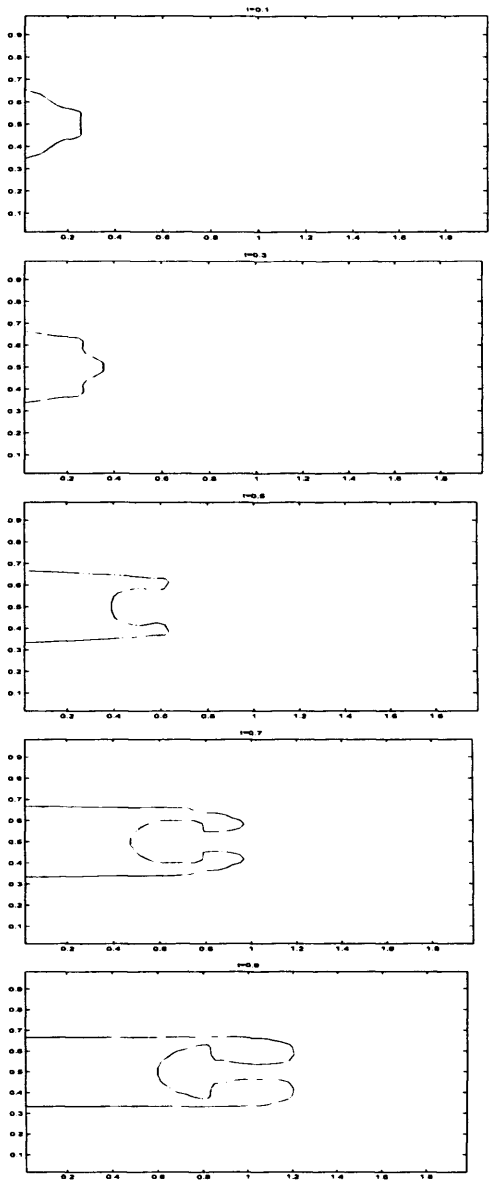

Figure 10.11: The case where the glue is injected as a constant stream. Here the initial velocities of the glue and blood are $u_1 = 1/4$ and $u_2 = 1$ respectively and $\rho = 1$.

10.3 The flow to two or more daughters

Previously the computations studied flow only in a single feeding artery. We now extend the numerical model to analyse the flow to two or more daughter vessels.

We first consider the case where the glue is injected as a droplet, close to the two daughters and in a symmetric position. Again the flow is taken to be inviscid. In all the figures the glue is injected at the point (0.55, 0.5) at $t = 0$ say. This plot is not shown in the figures but is the case for figures 10.12-10.18. Constant velocity of $u_2 = 1/2$ is again set at the inlet and Neumann boundary conditions are posed for the velocity components at the outflow in the daughters at the point $x = 2$.

10.3.1 Results

Figure 10.12 shows the interface position for different times where the density of the glue and the blood are the same. Again symmetry is preserved in the line $y = 1/2$. The front of the droplet changes shape dramatically before it reaches the bifurcation, but the upstream end of the droplet remains of roughly the same shape until the front of the droplet actually hits the bifurcation. This happens at t=2.5 although it should be noted that that there is a slight gap at the front of the bifurcation where no glue is present. The glue travels freely into the daughters and, as can be seen from the last plot in figure 10.12, takes up more than half of each of the daughters.

Similar interface positions are observed when the density of the glue is changed to the values of 2 and 1/2, which are shown in figures 10.13 and 10.14 respectively. When $\rho_1 = 1/2$ though, the upstream edge of the droplet changes shape as was observed in the single vessel calculations earlier in the chapter, so now there is droplet deformation at both the front and back, due to

the bifurcation and density ratio respectively. Indeed in this limit the droplet spreads more in a spatial sense and ends up blocking more of the daughter vessels in comparison with the case where $\rho_1 = 2$. It should be noted again that the times where the interface has been plotted are different for the different cases and, as was found earlier in this chapter the greater the density of glue, the quicker the glue travels.

Figure 10.15 shows a case where the glue is injected closer to the bifurcation and the length of the daughters is increased, so that they have length 1.18. Similar interface shapes are observed with the glue sticking to the walls of the daughters. However as can be seen in the last plot in the figure, there is detachment of glue at the start of the bifurcation and that at earlier times the glue actually moves backwards at this position. Figure 10.16 shows the case where the droplet is injected into the lower half of the feeding artery in an effort to block off the lower daughter. Now, the glue spreads in the daughter vessel to take up most of the vessel at time $t = 2.5$. However some glue has also traveled into the top daughter, which of course, is not desirable during the embolization process. Figures 10.17 and 10.18 show the case where there are now three and four daughters respectively. The first of these analyses flows in a symmetric configuration, with the aim of blocking off the largest daughter which is in the middle. The droplet travels straight into this vessel with no glue travelling to either of the other daughters. Finally in figure 10.18, the case of four daughters was analysed where one of the daughters was larger than the other three. In this case the droplet distorts prior to the branching and even though it is injected in the centre of the artery the droplet enters the largest artery and only a thin jet is seen in the daughter artery to the top. No glue enters either the top or bottom daughter at subsequent times.

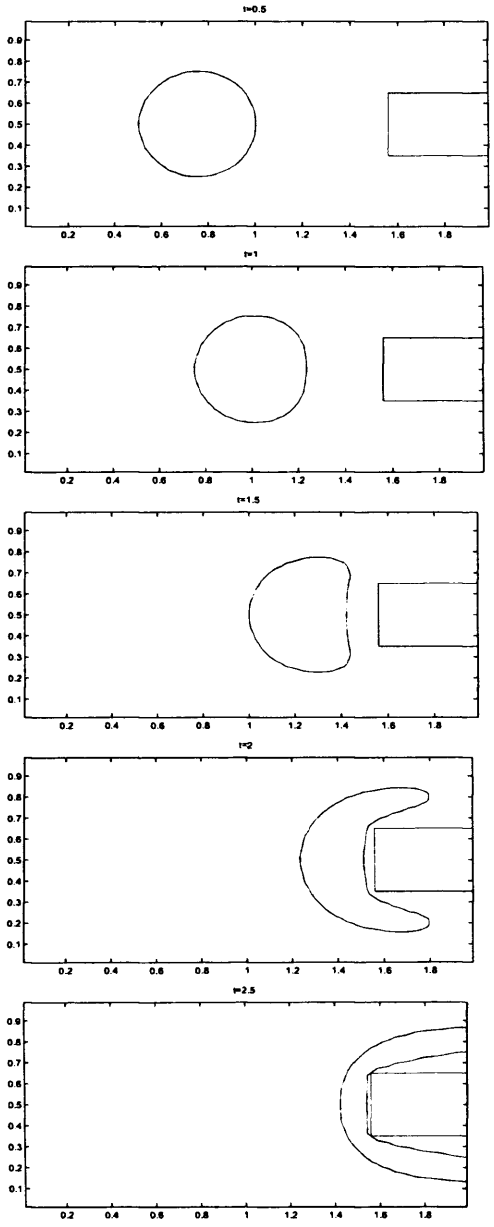

Figure 10.12: The case where the glue is injected to a bifurcation to two large daughters. Here the glue is injected as a droplet but no forcing is applied. The inflow velocity of the blood $u_1 = 0.5$ and the densities of the fluids are given by $\rho_2 = 1$, $\rho_1 = 1$. At times 0.5,1,1.5, 2

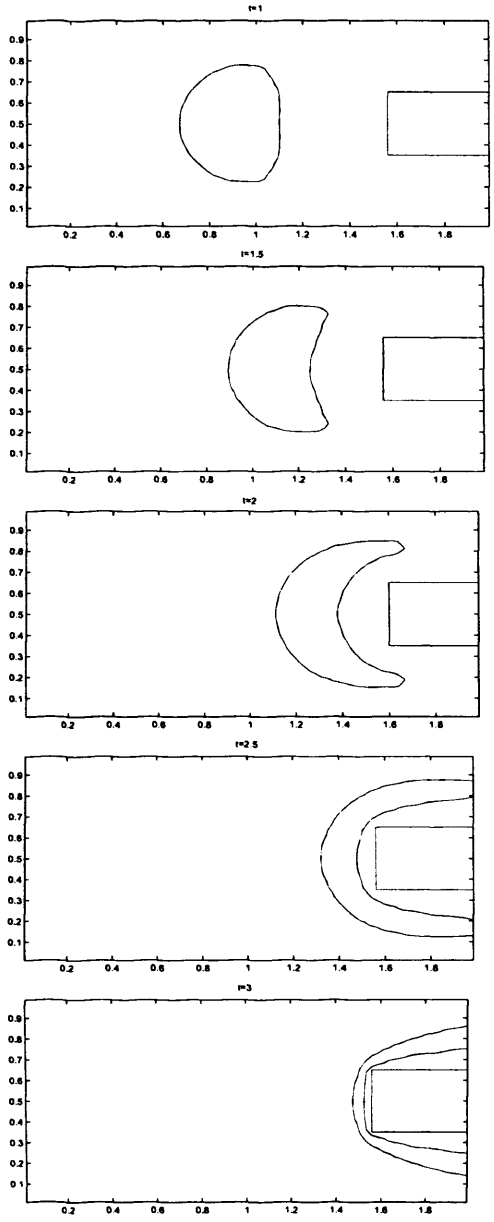

Figure 10.13: The case where the glue is injected to a bifurcation to two large daughters, the densities of the fluids are given by $\rho_2 = 1$, $\rho_1 = 1/2$.

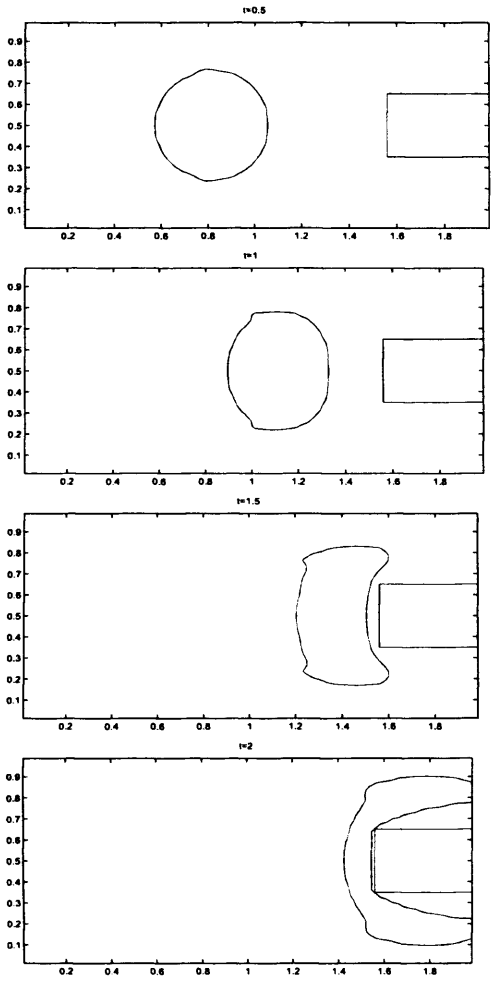

Figure 10.14: The case where the glue is injected to a bifurcation to two large daughters, $\rho_2 = 1$, $\rho_1 = 2$.

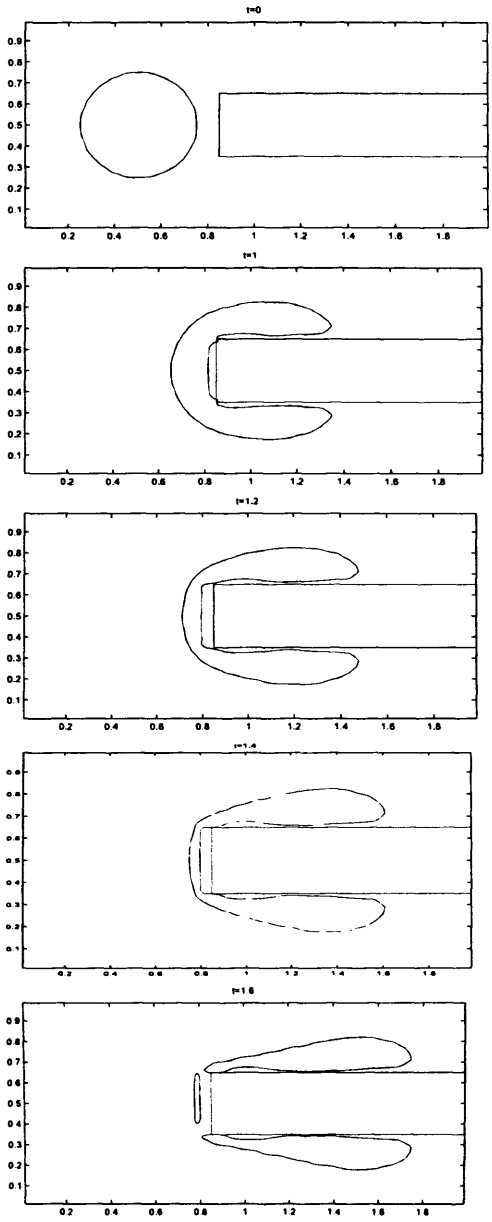

Figure 10.15: The case where the glue is injected close to a bifurcation to two large daughters, $\rho_2 = 1$, $\rho_1 = 1/2$.

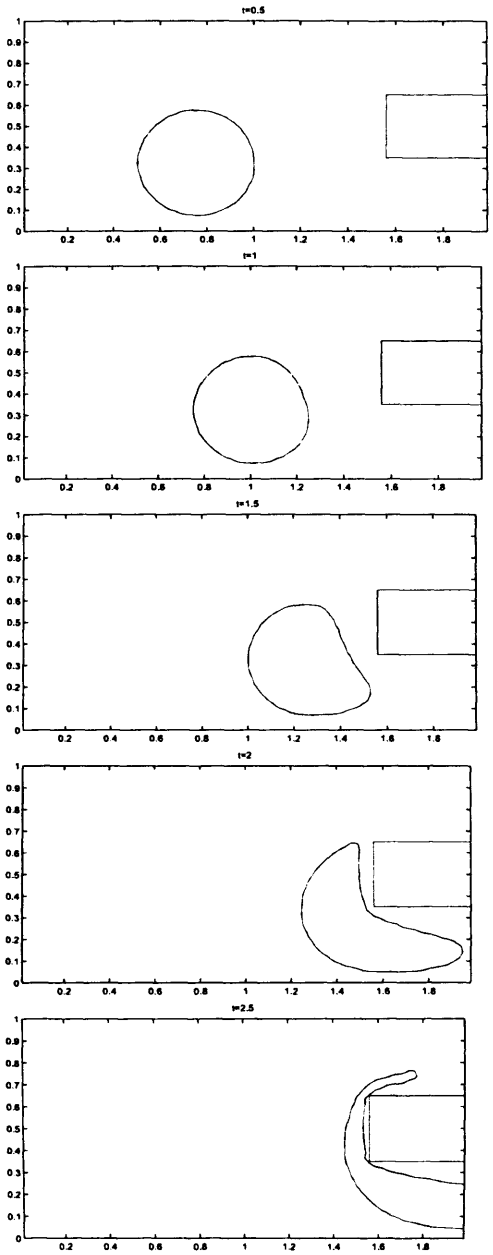

Figure 10.16: The case where the glue is injected to a bifurcation to two large daughters. The glue is injected near the lower wall with the aim of blocking flow in the lower daughter. Here $\rho_1 = \rho_2 = 1$.

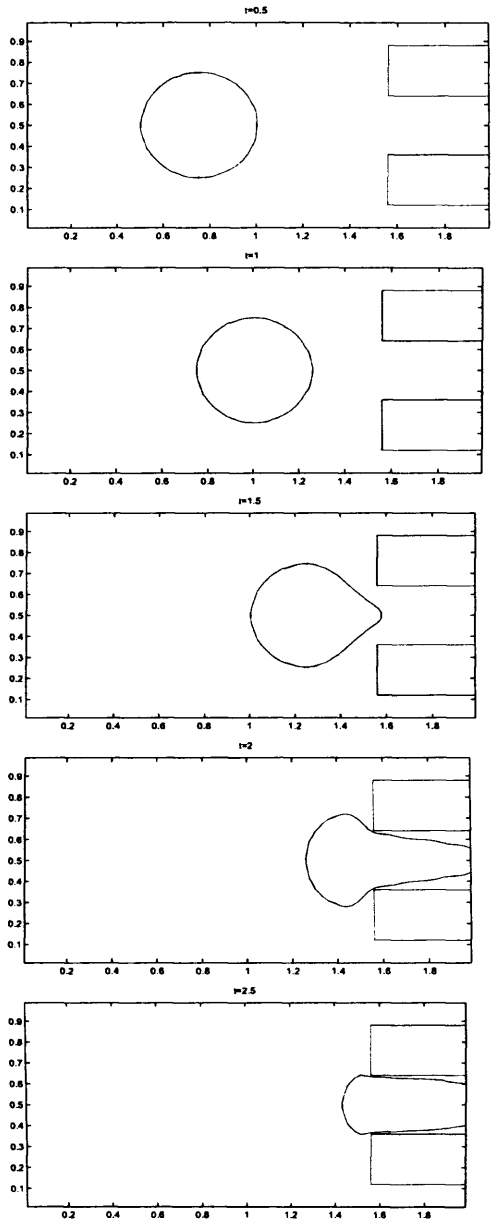

Figure 10.17: The case where the glue is injected symmetrically and three daughters are now present, one large daughter and two smaller daughters, with symmetry in the line $y = 1/2$. Again $\rho_1 = \rho_2 = 1$.

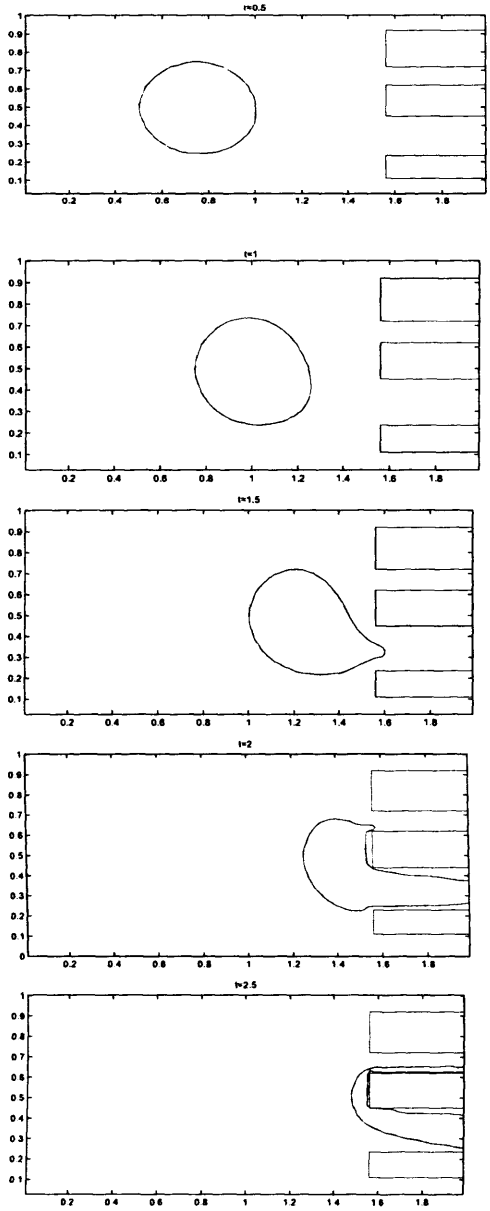

Figure 10.18: The case where four daughters are present. Here the glue is injected in the centre of the mother and travels predominantly through the largest daughter, with $\rho_1 = \rho_2 = 1$.

10.4 Viscous flow in a single mother vessel

Finally, the Volume of Fluid model is applied to the case where the two fluids are both taken to be viscous. The glue is again injected as a droplet in a single feeding artery. Now at the inlet the flow is taken as having a Poiseuille profile so as the channel width is non-dimensionalised to unity. We set the inflow velocity to

$$u_2(y) = y(1-y). \tag{10.1}$$

We non-dimensionalise quantities based on glue properties. The same non-dimensionalisation is used in each fluid,

$$\mathbf{x}^* = Lx, \qquad \mathbf{u}^* = U_\infty \mathbf{u}, \qquad t^* = tL/U_\infty, \qquad p^* = \rho_1 U_\infty p, \tag{10.2}$$

in the glue and blood in turn, where the starred variables are dimensional. Here L is the channel width, and U_∞ a representative velocity scale. Substitution into the dimensional Navier-Stokes equations (2.2) gives the equations

$$\frac{\partial \mathbf{u}_1}{\partial t} + (\mathbf{u}_1.\nabla)\mathbf{u}_1 = -\nabla p + \frac{1}{\mathrm{Re}}\nabla^2 \mathbf{u}_1, \tag{10.3}$$

$$\frac{\partial \mathbf{u}_2}{\partial t} + (\mathbf{u}_2.\nabla)\mathbf{u}_2 = -\left(\frac{\rho_1}{\rho_2}\right)\nabla p + \frac{1}{\mathrm{Re}}\left(\frac{\nu_2}{\nu_1}\right)\nabla^2 \mathbf{u}_2, \tag{10.4}$$

where the Reynolds number is given by $\mathrm{Re} = U_\infty L/\nu_1$.

Again to compare to the inviscid results the domain is taken to be of length 4. At the outflow again Neumann boundary conditions are used for both velocity components and the pressure is set to zero. In these simulations the values for the blood viscosity and density are each kept constant and are given respectively by 0.01 and 1.

10.4.1 Results

Figures 10.19 to 10.22 show the interface positions at different Reynolds numbers. Plots are shown for Re=1000, 400, 100, and 10. As can be seen from the

figures the higher the Reynolds number, the more distortion to the viscous glue droplet. Indeed an 'arrowhead' type of interface position is seen for Re=1000, 400 and 100. As can be seen from figures 10.19 and 10.20 the interface positions for Reynolds numbers of 400 and 1000 are similar. When the Reynolds number is lower, as would be the case for embolization, the glue travels slower and the upstream edge of the glue droplet is approximately flat. At later times however the arrowhead type of shape does develop.

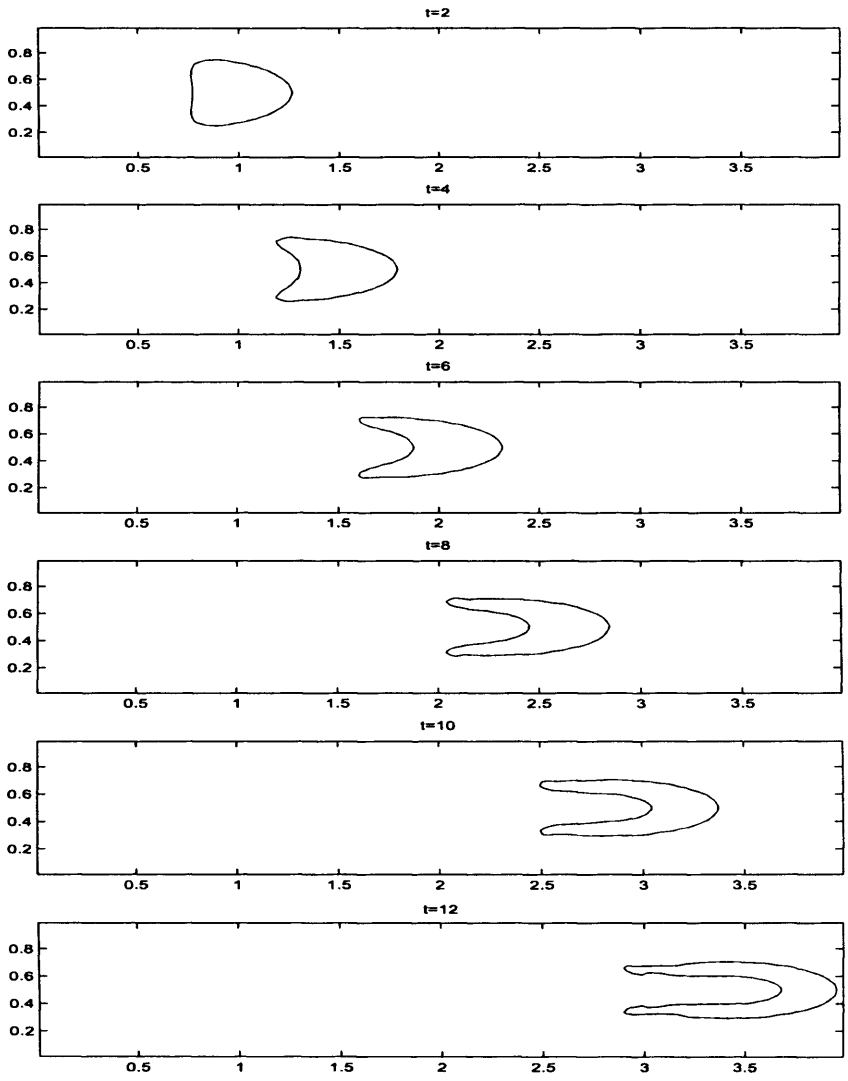

Figure 10.19: The case where Re=1000.

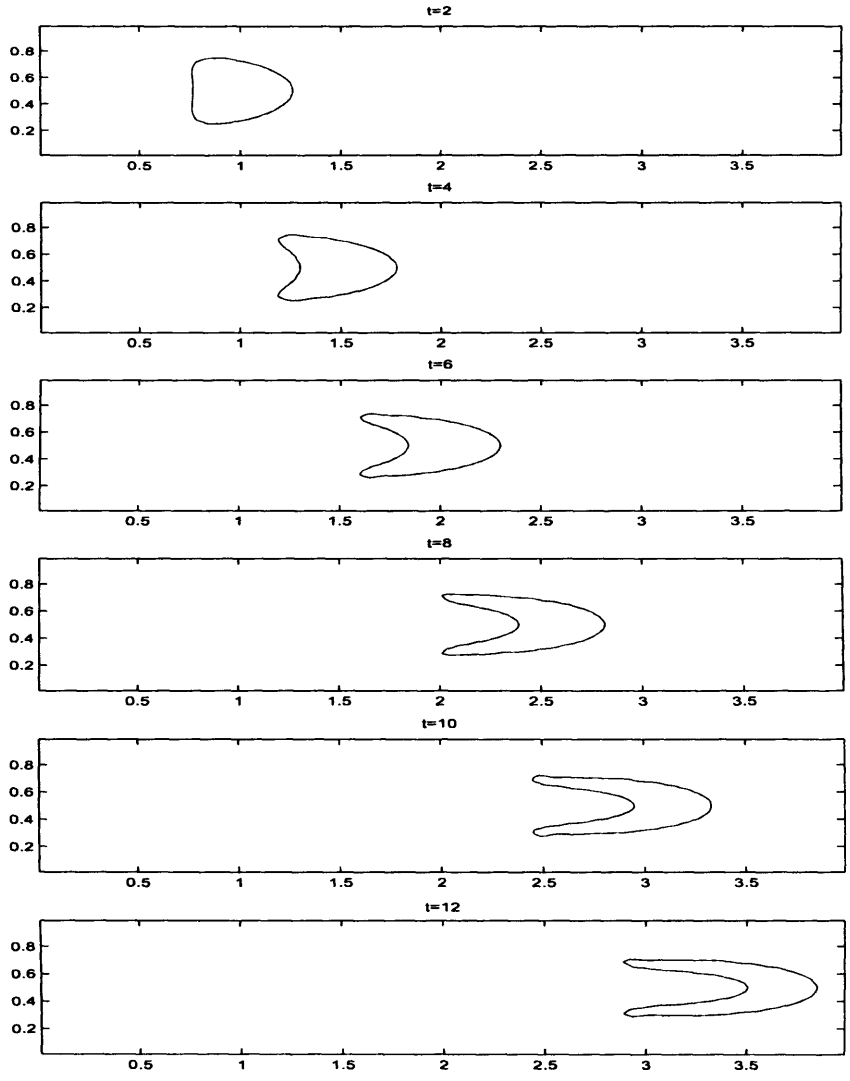

Figure 10.20: The case where Re=400.

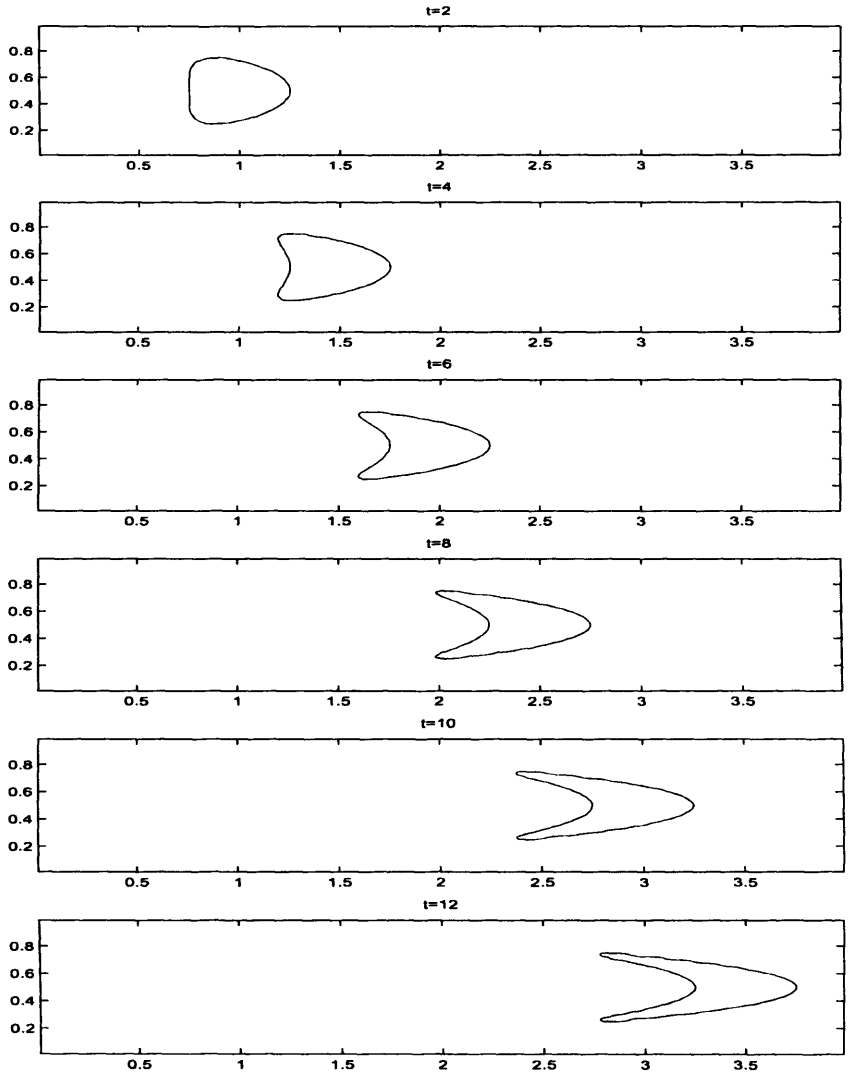

Figure 10.21: The case where Re=100.

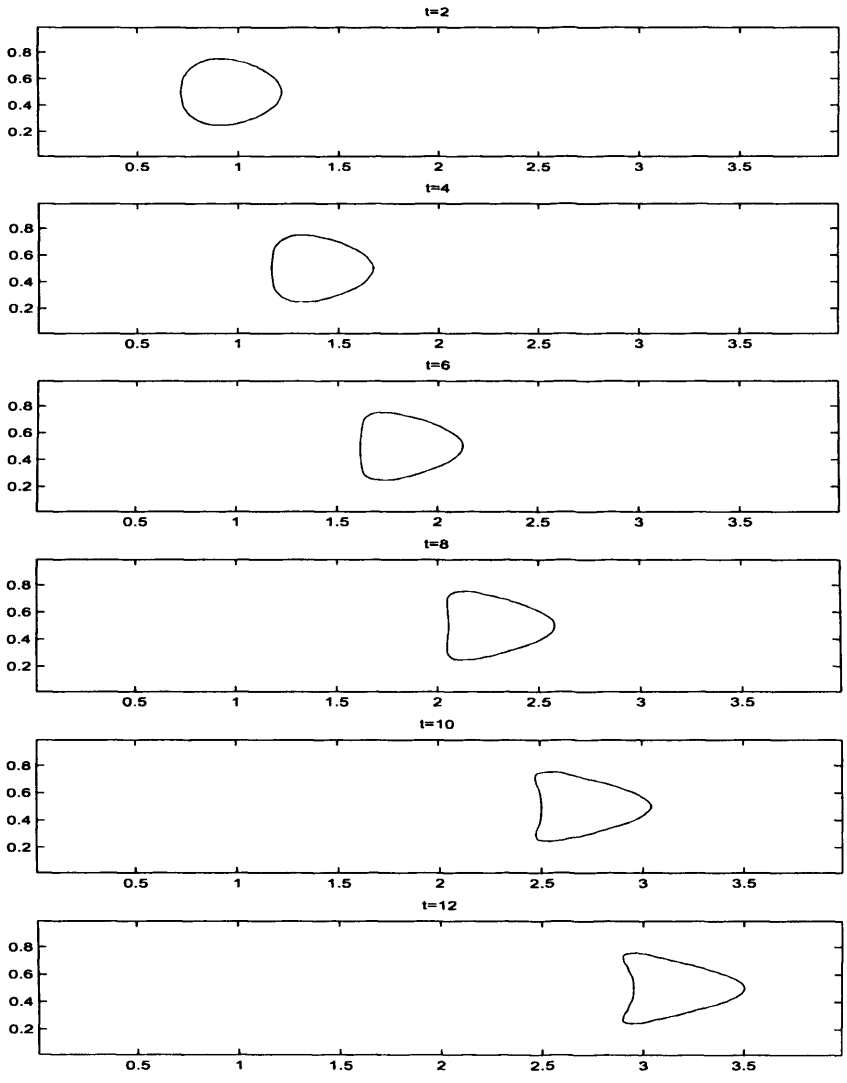

Figure 10.22: The case where Re=10.

Chapter 11

Conclusions and further work

11.1 Conclusions

The mathematical modelling in chapter 3 assumed that the flow of both the glue and blood was inviscid. First the densities of the two fluids were taken to be equal and the streamlines were found in the cases where the two fluids had different initial velocities, u_1 and u_2. The plots showed that the higher the initial velocity of the glue, the further the glue spread. Initial values of $u_1 = 10$ (glue) and $u_2 = 1$ (blood) showed that the glue spread quickly over space and soon the glue took up the whole feeding artery. Next the flow was considered when the densities of the two fluids, ρ_1 and ρ_2 in the glue and blood respectively, were not equal. This linearised analysis showed that there was a greater overall displacement of the streamlines when $\rho_1 > \rho_2$ with faster flow in the glue. Also the limits $\rho \to 0$ and $\rho \to \infty$ were considered and asymptotic expansions posed in this limit.

In chapter 4 viscous effects were introduced into the model and then the wall layer flows over a surface roughness and to two large daughters were calculated. The numerical results showed that as $\mu \to 0$, the interface f between the fluids rode up and over the wall shape with the shape of the roughness

and a constant distance f_0 away from it, where f_0 was the initial interface position far upstream of the roughness. In chapter 5 the problem was tackled using an asymptotic approach. Asymptotic expansions were posed for the small ratio viscosity limit for the fully non-linear equations. Again at leading order the solution agreed with the computations in the previous chapter. Also the linearised problem where the roughness height h was assumed small gave the same leading order solution. In each of these settings a relatively simple leading order solution was found in the glue, whereas the blood problem was more complicated and needed further numerical computation in both cases. Considering the flow to two large daughters, the interface position was found to obey the relation $f \sim x^{-1/2}$ far downstream for viscosity and density ratios of order one.

Chapter 6 continued the wall layer analysis to include a model of chemical effects occurring at the interface using a simple mass exchange condition $C_1\rho = C_2$. At first the parameters C_1 and C_2 were scaled as $|t|^{-1/2}$ and a similarity solution gave the unidirectional velocity profiles in this limit. It was found that when $\tilde{C}_2 = C_2|t|^{1/2}$ was large and $\rho > 2$, reversed flow occurred, whereas for small $\tilde{C}_2$ no reversed flow occurred irrespective of the value for ρ. More analysis for the chemical model parameters being order-one showed that the flow was always forward in this limit too.

At this point the emphasis changed somewhat and now the problem was considered from a purely numerical perspective. Chapters 7 and 8 gave a detailed description of the Volume of Fluid method as well as a brief outline of other commonly used methods for interfacial and multiphase flow dynamics. Chapter 9 showed the results when this method was applied to the problems of the dam-break, fractured diaphragm and Rayleigh-Taylor instability. These results were in good agreement with those in the literature.

Finally the method was applied to model the embolization process, with

results presented in chapter 10. First the problem of glue travel in a single artery was studied. The glue was injected as a droplet and the effect of varying the density of the glue was examined. It was found that when the density of the glue was greater than that of the blood the glue spread and small droplets detached from the glue. The detachment occurred at earlier times for larger values of ρ_1. When the density of the glue was greater than that of the blood the glue spread again but now little detachment was seen apart from at relatively late times. Indeed in this case the glue spread further and spread faster for smaller values of the glue density. Next simulations of constant glue injection showed that the larger the initial velocity of glue the faster the glue spread, where in this case the density of the two fluids was assumed equal.

Next the flow to two, three and four daughters was analysed with both symmetric configurations of daughter shapes and droplet positions considered. Finally the problem was made viscous, with the focus on flow of glue and blood in a single feeding artery. It was shown that the higher the viscosity of the glue the less deformation to the original droplet, whereas for lower values of glue viscosity the glue forms an 'arrowhead' type shape far downstream.

Although the model used in this work is relatively simple, some advice to the medical practitioners may be given. When the density of the glue and the blood are the same, it seems that injecting the glue close to the bifurcation is important if the artery to be embolised is smaller than neighbouring vessels. When the artery to be glued is larger it seems less important to inject close to the bifurcation, as the front of the droplet travels towards the largest daughter. Also it seems beneficial to use a glue with a density smaller than that of the blood. In this case the glue spreads well and minimal glue breakup is seen.

11.2 Further work

This work was in essence a first attempt to model extremely complicated phenomena. Perhaps the main next step would be to include the effects of solidification (glue setting) into the model. Other possibilities of extending the modelling are the inclusion of surface tension forces occurring at the interface, and extending the model to three dimensions. Also throughout both fluids were taken as Newtonian, so an extension to non-Newtonian fluids may be possible.

To develop the analysis in chapter three, the conformal mapping theory could in principle be used to study the flow to two or more daughters. The continuation of the non-equal density problem could be treated with the boundary element method.

There are many natural extensions to the analysis in chapters 4 and 5. To start with the slip velocity could be calculated for flows to three or more daughters, so that phenomena such as separation and upstream influence could be examined in such settings, to compare with the results obtained for the flow to two large daughters obtained in this work. To continue the flow to two large daughters, other vessel shapes could easily be incorporated into the model. The wall layer problem could be extended to three dimensions in a similar vein to [85], which details the equivalent analysis for the one fluid problem. In chapters 4 and 5 the x-length scale was strictly of order unity, but setting the viscous axial scale $x \sim \mathrm{Re}$ both for steady and unsteady flow, to make comparisons with the one fluid problem [87] could be performed. The wall layer problem could also be made unsteady in principle with the aim to resolve the non-linear properties of the equations for high frequency disturbances and the onset of Tollmein-Schlichting waves [84] in this multiphase setting.

There are numerous extensions to the analysis in chapter 6. Indeed the model could be extended to the core where the flow of glue only is inviscid and

the equations of motion analysed. Also chemical effects could be included in the model to the flow to two large daughters.

In order to continue the modelling of the flow to two large daughters, the analysis in [51] could potentially be developed. Adding the geometry of the daughters into this analysis effectively involves only the inclusion of the daughters' shape $f_3(x,t)$ into the governing equations of motion, as discussed on page 313 of this reference. Also the far field conditions in this analysis would need to be changed to the conditions at the vessel walls. Results from such analysis could be compared to both results from chapters 4 and 5 and Volume of Fluid results.

There are of course numerous improvements that could be made to the Volume of Fluid analysis of chapters 7-9. Perhaps the first main improvement to the model would be to include analysis of the flow to two or more daughters, where the walls of the daughters pass arbitrarily through the grid, rather than aligning with the grid as they have been assumed to do in this work. As stated in the text a Cartesian cut-cell method could be used similar to [43] to analyse flow into complicated geometric configurations of daughter vessels. Also to represent the pulsatile nature of the oncoming blood flow in the model, a time dependant inflow condition could easily be implemented in the numerical method.

Due to time constraints no results were obtained for viscous fluids to two or more daughters, but the numerical routine can deal with such problems. No attempt was made to model the solidification process occurring in the glue, but in principle solidification could be incorporated into the numerical model. Also three-dimensionality could be included in the model, with the advection scheme used here being applicable to three dimensional simulations [28]. To implement the three-dimensional solver for the Navier-Stokes equations, the successive over-relaxation technique would probably have to be replaced with

a more efficient solver, and indeed perhaps a multigrid method.

Appendix A

The stress tensor

The stress tensor is given by

$$\mathbf{T} = \mu[\nabla(\mathbf{u}) + \nabla(\mathbf{u})^T], \tag{A.1}$$

where $\mathbf{u} = (u, v)$. In component form and Cartesian coordinates this is given by

$$\mathbf{T} = \begin{bmatrix} 2\mu\frac{\partial u}{\partial x} & \mu\left(\frac{\partial u}{\partial y} + \frac{\partial v}{\partial x}\right) \\ \mu\left(\frac{\partial u}{\partial y} + \frac{\partial v}{\partial x}\right) & 2\mu\frac{\partial v}{\partial y} \end{bmatrix}. \tag{A.2}$$

Taking the divergence of the stress tensor gives

$$\nabla.\mathbf{T} = \begin{bmatrix} \mu(\frac{\partial^2 u}{\partial x^2} + \frac{\partial^2 u}{\partial y^2}) + 2\frac{\partial \mu}{\partial x}\frac{\partial u}{\partial x} + \frac{\partial \mu}{\partial y}(\frac{\partial u}{\partial y} + \frac{\partial v}{\partial x}) \\ \mu(\frac{\partial^2 v}{\partial x^2} + \frac{\partial^2 v}{\partial y^2}) + 2\frac{\partial \mu}{\partial y}\frac{\partial v}{\partial y} + \frac{\partial \mu}{\partial x}(\frac{\partial u}{\partial y} + \frac{\partial v}{\partial x}) \end{bmatrix}, \tag{A.3}$$

on using the continuity equation. Consider the first component of the vector, which we will denote L_x we write

$$\mathcal{L}_x = 2\frac{\partial}{\partial x}\left(\mu\frac{\partial u}{\partial x}\right) + \frac{\partial}{\partial y}\left(\mu\frac{\partial u}{\partial y}\right) + \frac{\partial}{\partial y}\left(\mu\frac{\partial v}{\partial x}\right), \tag{A.4}$$

and the y-component is given by

$$\mathcal{L}_y = 2\frac{\partial}{\partial y}\left(\mu\frac{\partial v}{\partial y}\right) + \frac{\partial}{\partial x}\left(\mu\frac{\partial v}{\partial x}\right) + \frac{\partial}{\partial x}\left(\mu\frac{\partial u}{\partial y}\right). \tag{A.5}$$

So the discrete expressions for these viscous terms for the calculation of $u_{i,j}$ and $v_{i,j}$ respectively now become

$$\mathcal{L}_x = 2\frac{\left(\mu_{i+1,j}(u_{i+3/2,j} - u_{i+1/2,j}) - \mu_{i,j}(u_{i+1/2,j} - u_{i-1/2,j})\right)}{\Delta x^2} + \frac{\left(\mu_{i+1/2,j+1/2}(u_{i+1/2,j+1} - u_{i+1/2,j}) - \mu_{i+1/2,j-1/2}(u_{i+1/2,j} - u_{i+1/2,j-1})\right)}{\Delta y^2} + \frac{\left(\mu_{i+1/2,j+1/2}v_{x,i+1/2,j+1/2} - \mu_{i+1/2,j-1/2}v_{x,i+1/2,j-1/2}\right)}{\Delta y}, \quad \text{(A.6)}$$

and

$$\mathcal{L}_y = 2\frac{\left(\mu_{i,j+1}(v_{i,j+3/2} - v_{i,j+1/2}) - \mu_{i,j}(v_{i,j+1/2} - v_{i,j-1/2})\right)}{\Delta x^2} + \frac{\left(\mu_{i+1,j+1/2}(v_{i+1,j+1/2} - v_{i,j+1/2}) - \mu_{i+1/2,j-1/2}(v_{i,j+1/2} - v_{i-1,j+1/2})\right)}{\Delta y^2} + \frac{\left(\mu_{i+1/2,j+1/2}u_{y,i+1/2,j+1/2} - \mu_{i-1/2,j+1/2}u_{y,i-1/2,j+1/2}\right)}{\Delta x}, \quad \text{(A.7)}$$

respectively. Here we define the viscosities at cell corners as

$$\mu_{i\pm1/2,j+1/2} = \frac{1}{4}(\mu_{i,j} + \mu_{i,j+1} + \mu_{i\pm1,j} + \mu_{i\pm1,j+1}), \quad \text{(A.8)}$$

$$\mu_{i\pm1/2,j-1/2} = \frac{1}{4}(\mu_{i,j} + \mu_{i,j-1} + \mu_{i\pm1,j} + \mu_{i\pm1,j-1}). \quad \text{(A.9)}$$

The velocity derivatives are

$$v_{x,i+1/2,j+1/2} = \frac{v_{i+1,j+1/2} - v_{i,j+1/2}}{\Delta x}, \quad \text{(A.10)}$$

$$v_{x,i+1/2,j-1/2} = \frac{v_{i+1,j-1/2} - v_{i,j-1/2}}{\Delta x}, \quad \text{(A.11)}$$

$$u_{y,i+1/2,j+1/2} = \frac{v_{i+1,j+1/2} - v_{i,j+1/2}}{\Delta y}, \quad \text{(A.12)}$$

$$u_{y,i-1/2,j+1/2} = \frac{v_{i,j+1/2} - v_{i-1,j+1/2}}{\Delta y}. \quad \text{(A.13)}$$

These expressions reduce to the expressions given in section 8.1.4 for the viscous stresses when the viscosity is constant.

Appendix B

The SIMPLE algorithm

First developed by Patankar and Spalding [62] the Semi-Implicit method for pressure linked equations (SIMPLE) algorithm became a popular method for numerical simulation of incompressible flows. Further details on the SIMPLE algorithm can be found in [40]. The main difference between the methodology for the SIMPLE algorithm and the projection method described in the text, is that in the SIMPLE method, the unknown pressure gradient term is left in the momentum equations and is adjusted iteratively until it is found.

Discretizations of the convective and viscous operators will be discussed here briefly as they are similar to those in the text or can be found in [4]. We start by writing the Navier-Stokes equations in conservative form, for example the x- and y-momentum equations are given respectively by

$$u_{i,j}^{(n+1)} = u_{i,j}^{(n)} + \Delta t A^{(n)} - \Delta t \left(\frac{p_{i+1,j}^{(n+1)} - p_{i,j}^{(n+1)}}{\Delta x} \right), \tag{B.1}$$

$$v_{i,j}^{(n+1)} = v_{i,j}^{(n)} + \Delta t B^{(n)} - \Delta t \left(\frac{p_{i,j+1}^{(n+1)} - p_{i,j}^{(n+1)}}{\Delta y} \right). \tag{B.2}$$

Here $A^{(n)}$ and $B^{(n)}$ are the contributions from the convective fluxes and viscous forces and at first are known explicitly from the previous time step and subsequently from the previous iteration. To start with we take a guess at the

pressure throughout the domain and denote this p^*. Using this guessed value we substitute into equation (B.1) and (B.2) for the other velocity component to find values for both velocity components which are denoted by u^*, v^*. For example the horizontal component u^* is given by

$$u^*_{i,j} = u^{(n)}_{i,j} + A^{(n)}\Delta t - \Delta t \left(\frac{p^{(*)}_{i+1,j} - p^{(*)}_{i,j}}{\Delta x} \right). \tag{B.3}$$

Because the pressure field and hence velocity field were guessed the velocity field will not in general satisfy the continuity equation. We now introduce the following formulae

$$u^{(n+1)} = u^* + \tilde{u}, \tag{B.4}$$

$$v^{(n+1)} = v^* + \tilde{v}, \tag{B.5}$$

$$p^{(n+1)} = p^* + \tilde{p}. \tag{B.6}$$

Here starred variables are the guessed values and variables with a tilde are the corrections to the guessed variables. Again considering the x-momentum equation, if we subtract equation (B.1) from equation (B.3) we find the correction to the velocity is given as

$$\tilde{u}_{i,j} = -\Delta t \left(\frac{\tilde{p}_{i+1,j} - \tilde{p}_{i,j}}{\Delta x} \right). \tag{B.7}$$

A similar expression holds for the y-momentum equation. Substituting this equation into these formulae into the equations for the velocity field at the next time step, we find

$$u^{(n+1)}_{i,j} = u^*_{i,j} - \Delta t \left(\frac{\tilde{p}_{i+1,j} - \tilde{p}_{i,j}}{\Delta x} \right), \tag{B.8}$$

$$v^{(n+1)}_{i,j} = v^*_{i,j} - \Delta t \left(\frac{\tilde{p}_{i,j+1} - \tilde{p}_{i,j}}{\Delta y} \right). \tag{B.9}$$

But the discrete continuity equation must be satisfied at the next time step so substitution into

$$\nabla . \mathbf{u}^{(n+1)} = 0, \tag{B.10}$$

gives the Poisson equation

$$\nabla^2 \tilde{p}\,\Delta t = \nabla.\mathbf{u}^*. \tag{B.11}$$

Again this equation can be solved by a successive relaxation (SOR) method, the Cholesky conjugate gradient method or other higher powered iterative method such as the GMRES routine due to Saad. Once the equation is solved for $\tilde{p}$ the pressure is updated as $p = p^* + \tilde{p}$. Next the correction to the velocity field is found and then a check is made on the continuity equation. If the equation is satisfied in all cells containing fluid then the routine is ready to pass to the next time step. If not, the pressure calculated becomes the initial guess at the start of the next iteration. Iteration is continued until continuity is satisfied in every full cell. Neumann-boundary conditions are imposed on the pressure correction

$$\nabla\tilde{p}.\mathbf{n} = 0. \tag{B.12}$$

Once the pressure has been calculated, the velocity is updated form equations (B.8) and (B.9). The pressure field and the velocity field are then substituted into equations (B.1) and (B.2) and the process is repeated until the continuity equation is satisfied throughout the domain.

Free surface conditions

There are only a few modifications to extending this algorithm to free surface flows. The velocities that are guessed are FF, SF or FS velocities. Other velocities are imposed later in the computational cycle. The Poisson equation is solved in all full cells, however in S-cells we must make sure that equation (B.10) is satisfied. However the Poisson equation is for $\tilde{p}$ so the conditions in the S-cells become

$$\tilde{p}_S = (1-\bar{h})p_F - p_S^*, \tag{B.13}$$

$$\tilde{p}_S = (1-\bar{h})p_F - p_S^* + 2\nu\frac{\partial \mathbf{u}^*}{\partial n}, \tag{B.14}$$

for the inviscid and viscous relations respectively. Here n is the normal direction to the interface and the viscosity ν is assumed to be constant. Again the interface is approximated as either horizontal or vertical from the known normal vector, giving the value for the normal velocity derivative appearing in the free surface condition. Once the new values for the velocities are found in the FS, SS and SF positions, the ES, SE and EE velocities are imposed in exactly the same way as in section 8.1.11. In this method though they need to be imposed at the end of each iteration.

Other comments

The SIMPLE algorithm involves solving a Poisson type equation at every iteration level, compared to the projection method described in the text where only one Poisson equation needs be solved for one time step. In effect the SIMPLE algorithm involves an outer and an inner iteration, the inner being the solution of a given Poisson equation with boundary conditions and the outer being continued until the continuity is satisfied in all cells. It was found that convergence is still achieved even when the Poisson equation was not satisfied at every inner iteration. Generally only 10 to 20 iterations were needed and the overall outer iterative procedure still converged, with the computation time greatly reduced. Other techniques to overcome this problem may be found for example in [71], where here the linear system is approximated where all off diagonal terms are neglected e.g $\tilde{p}_{i,j+1} = 0$, so the system can be solved directly

$$\tilde{p}_{i,j} = \frac{-\omega D_{i,j}(\Delta x)^2}{4\Delta t}, \tag{B.15}$$

where constant grid spacing is assumed in both coordinate directions. Although this is a major simplification it is justified as the Poisson equation is for the correction to the pressure, which may be very small in surrounding cells anyway. A similar methodology is adopted in [59] and other methods

pioneered at Los Alamos.

Overview of solver for free surface problems

1. Guess at $p^{(n+1)}$. First guess is $p^{(n)}$.
2. Find u^*, v^* from the momentum equations and the guessed pressure p^*.
3. Using these solve for $\tilde{p}$, with Neumann boundary conditions on $\tilde{p}$ at solid boundaries and free surface conditions (B.13) or (B.14) in S-cells.
4. Calculate p, u and v.
5. Set free surface conditions.
6. Check on continuity. If satisfied throughout the domain stop, if not go back to (1) with new guess $p^* = p$.

Bibliography

[1] S. Afkhami. A Volume of fluid based approach for accurate simulations of contact line-driven phenomena. *Unpublished.*

[2] S. Albensoeder and H. Kuhlmann. Non-linear three-dimensional flow in the lid-driven square cavity. *J. Fluid Mech.*, 569:465–480, 2006.

[3] A. Amsden and F. Harlow. The SMAC Method, A numerical method for calculating incompressible Fluid Flows. Los Alamos report LA-4370, 1970.

[4] J. D. Anderson Jr. Computational fluid dynamics, Mcgraw-Hill International Editions: Mechanical Engineering Series, 1995.

[5] H. Aref. Stirring by chaotic advection. *J. Fluid Mech.*, 143:1–21, 1984.

[6] E. Aulisa, S. Manservisi, R. Scardovelli, and S. Zaleski. A geometrical area-preserving Volume-of-Fluid method. *J. Comput. Phys.*, 192:355–364, 2003.

[7] G. K. Batchelor. Introduction to fluid dynamics, Cambridge mathematical library, Cambridge Univeristy press, 2000.

[8] G. K. Batchelor, H. K. Moffatt, and M. G. Worster. Perspectives in fluid dynamics, Cambridge University press; New edition (2002).

[9] F. Bierbrauer. Mathematical Modelling of Water-Droplet Impact on Hot Galvanised Steel Surfaces, PhD thesis, University of Wollongong, 2004.

[10] M. G. Blyth and A. J. Mestel. Steady flow in a dividing pipe. *J. Fluid Mech.*, 401:339–364, 1999.

[11] T. Boeck, J. Li, E. Lopez-Pags, P. Yecko, and S. Zaleski. Ligament formation in sheared liquid-gas layers. *Theoretical and Computational Fluid Dynamics*, 21(1):59–76, 2007.

[12] R. I. Bowles, S. C. R. Dennis, R. Purvis, and F. T. Smith. Multi-branching flows from one mother tube to many daughters or to a network. *Philos. Trans. R. Soc. Lond. Math. Phys. Eng. Sci.*, 363(1830):1045–1055, 2005.

[13] R. V. Brotherton Radcliffe. PhD thesis, University of London 1986.

[14] O. R. Burggraf. Analytical and numerical studies of the structure of steady separated flows. *J. Fluid Mech.*, (24):113–151, 1966.

[15] S. Chakravarty and P. K. Mandal. An analysis of pulsatile flow in a model aortic bifurcation. *Int. J, Engng Sci.*, 35(409-427):1418–1434, 1997.

[16] Q. Chen, G. Dai, and H. Liu. Volume of Fluid model for turbulence numerical simulation of stepped spillway overflow. *J.Hydr. Engrg.*, 128(7):683–688, 2002.

[17] A. J. Chorin. Numerical solution of the Navier-Stokes equations. *Math. Comp.*, 22:745–762, 1968.

[18] K. M. Cockroft, M. D. Hwang, and R. H. Rosenwasser. Endovascular treatment of cerebral arteriovenous malformations: Indications, techniques, outcome, and complications. *Neurosur. Clin. N. Am.*, 16:355–363, 2005.

[19] T. L. Cook, R. Demuth, and F. Harlow. PIC calculations of multiphase flow. *J. Comput. Phys.*, 41(2):51–67, 1981.

[20] P. Coveney and M. Mazzeo. Private communications.

[21] A. V. Coward, Y. Y. Renardy, M. Renardy, and J. R. Richards. Temporal evolution of periodic disturbances in two-layer Couette flow. *J. Comput. Phys.*, 132(2):346–361, 1997.

[22] H. Ding and D. Spelt. Inertial effects in droplet spreading: a comparison between diffuse interface and level-set simulations. *J. Fluid Mech.*, 576:287–296, 2007.

[23] L. Formaggia, D. Lamponi, and A. Quarteroni. One-dimensional models for blood flow in arteries. *J. Engrg. Math.*, 47(3-4):251–276, 2003. (Mathematical modelling of the cardiovascular system).

[24] E. Gao, Y. W. L., S. Pile-Speilman, H. Joshi, P. Duong, and Q. Ma. Cerebral arteriovenous malformation feeding artery aneurysms; a theoretical model of intravascular pressure changes after treatment. *Neurosurgery*, 41:1345–1358, 1997.

[25] K. N. Ghia and U. Ghia. Multigrid technique for the solution of incompressible Navier-Stokes equations, Computational methods in viscous flows,. *Recent Adv. Numer. Methods Fluids*, 3:101–135, 1984.

[26] M. Gounis, B. Lieber, A. Wakhloo, R. Siekmann, and L. Hopkins. Effects of glacial acetic acid and ethiodized oil concentration on embolization with N-Butyl 2-Cyanoacrylate: An inVivo Investigation. *Amer J. Nuero.*, 23:938–944, 2002.

[27] J. B. Grotberg and O. E. Jensen. Biofluid mechanics in flexible tubes. *Ann. rev. fluid mech.*, 36:121–147, 2004.

[28] D. Gueyffier, J. Li, A. Nadim, R. Scardovelli, and S. Zaleski. Volume of Fluid interface tracking with smoothed surface stress methods for three-dimensional flows. *J. Comput. Phys.*, 152(1):423–456, 1999.

[29] D. Guo. A second order accurate scheme for the Navier-Stokes equations: Application to the lid driven cavity problem. *App. Numer. Math.*, 35:307–322, 2000.

[30] G. J. Hademenos, T. F. Massoud, and F. Vinuela. A biomathematical model of intrecranial malformations based on electrical circuit network analysis. *Neurosurgery*, 38:1345–1358, 1996.

[31] F. Harlow and E. Welch. Numerical calculation of time-dependent viscous incompressible flow of fluids with free surface. *Phys. Fluids*, 8:2182–2189, 1965.

[32] C. Hirt, B. Nicholls, and N. Romero. SOLA- A Numerical solution algorithm for transient fluid flow. Los Alamos report LA-5852 1975.

[33] C. Hirt and J. Sicilian. A porosity technique for the definition of obstacles in rectangular cell meshes. *Proc. Fourth International Conf. Ship Hydro.*, National Academy of Science, Washington, DC., 1985.

[34] C. W. Hirt, A. A. Amsden, and J. L. Cook. An arbitrary Lagrangian-Eulerian computing method for all flow speeds [J. Comput. Phys. **14** (1974), no. 3, 227–253]. *J. Comput. Phys.*, 135(2):198–216, 1997. With an introduction by L. G. Margolin, Commemoration of the 30th anniversary {of J. Comput. Phys.}.

[35] C. W. Hirt and B. D. Nichols. Volume of Fluid (VOF) method for dynamics of free boundaries. *J. Comput. Phys.*, 39:201–225, 1981.

[36] J. U. Howington, C. W. Kerber, and L. Nelson Hopkins. Liquid embolic agents in the treatment of intacranial arteriovenous malformations. *Neurosur. Clin. N. Am.*, 16:355–363, 2005.

[37] K. Ishii, T. Nihei, and S. Adachi. Accurate numerical simulation of three-dimensional lid-driven cavity flows with different span lengths. In *Vortex dominated flows*, pages 87–98. World Sci. Publ., Hackensack, NJ, 2005.

[38] A. Ivankovic, A. Karac, E. Dendrinos, and K. Parker. Towards early diagnosis of atherosclerosis: the finite volume method for fluid-structure interaction. *Biorheology*, 3:401–407, 1995.

[39] D. Johnson, P. Raad, and S. Chen. Simulation of impacts of fluid free surfaces with solid boundaries. *Int. J. Numer. Meth. Fluids*, 19:153–176, 1994.

[40] R. Johnson. Handbook of fluid dynamics, CRC press; 1998.

[41] D. S. Kershaw. The incomplete Cholesky-conjugate gradient method for the iterative solution of systems of linear equations. *J. Computational Phys.*, 26(1):43–65, 1978.

[42] D. Khismatullin, Y. Renardy, and M. Renardy. Development and implementation of VOF-PROST for 3D viscoelastic liquidliquid simulations. *J. Non-Newtonian Fluid Mech.*, 140(1):120–131, 2006.

[43] K. F. T. Kleefsman. PhD thesis, University of Groningen 2005.

[44] D. Kothe, R. Mjoslness, and M. Torrey. RIPPLE: A computer program for incompressible flows with free surfaces. Los Alamos report Tech. Rep. LA-12007-MS, 1992.

[45] B. Lafaurie, C. Nardone, R. Scardovelli, S. Zaleski, and G. Zanetti. Modelling merging and fragmentation in multiphase flows with SURFER. *J. Comput. Phys.*, 113(1):134–147, 1994.

[46] L. Landau and E. M. Lifchitz. Fluid mechanics, Butterworth-Heinemann; 1987.

[47] M. T. Lawton. Spetzler Martin grade 3 arteriovenous malformations: surgical results and modification of grading scale. *Neurosurgery*, 52:740–748, 2003.

[48] R. J. Leveque. Finite volume methods for hyperbolic problems, Cambridge University Press (2002).

[49] R. J. Leveque. High-resolution conservative algorithms for advection in incompressible flow. *SIAM J. Numer. Anal.*, 33(2):627–665, 1996.

[50] J. Li. Calcul d'Interface Affine par Morceaux. *C.R. Acad. Sci. Paris*, 320:391–396, 1995.

[51] L. Li, D. P. Papadopolous, F. T. Smith, and G. X. Wu. Rapid plunging of a body partly submerged in water. *J. Engrg. Math.*, 42(3-4):303–319, 2002.

[52] M. J. Lighthill. Physiological fluid dynamics: a survey. *J. Fluid Mech.*, 52:475–497, 1972.

[53] A. Lussenhop and W. Spence. Artificial embolization of cerebral arteries: report of use in a case of arteriovenous malformation. *J. Amer. Medical. Assoc.*, 11:1153–1155, 1960.

[54] J. C. Martin and W. J. Moyce. An experimental study of the collapse of a liquid column on a rigid horizontal plane. *Phil. Trans. Roy. Soc. Lond*, 33:312–324, 1952.

[55] F. Matthews. Numerical methods using matlab, Prentice Hall; 4th edition 2004.

[56] J. M. McKibben. A Computational Fluid Dynamics Model for Transient Three-Dimensional Free Surface Flows, PhD thesis, The Institute of Paper Science and Technology, Atlanta, Georgia.

[57] L. Milne-Thomson. Theoretical hydrodynamics, Dover Publications inc.; New edition (1996).

[58] P. Nakaji and R. F. Spetzler. Indications for surgical treatment of arteriovenous malformations. *Neurosur. Clin. N. Am.*, 16:365–366, 2005.

[59] B. Nicholls, C. Hirt, and R. Hotchkiss. SOLA-VOF A solution algorithm for transient fluid flow with multiple free boundaries. Los Alamos report LA-8355, 1980.

[60] W. F. Noh and P. Woodward. SLIC (Simple Line Interface method, in: A.I. van de Vooren, P.J. Zandbergen (Eds.), Lecture Notes in Physics). 59(9):330–340, 1976.

[61] F. Numan, A. Omerolu, B. Kara, M. Cantademir, I. Adaletli, and F. Kantarc. Embolization of peripheral vascular malformations with ethylene vinyl alcohol copolymer (ONYX). *Journal of Vascular and Interventional Radiology*, 15:939–946, 2004.

[62] S. Patankar and D. Spalding. A calculation procedure for heat mass and momentum transfer in three dimensional parabolic flows. *Int. J. Heat Mass Transfer*, 15:1787, 1972.

[63] T. Pedley. The fluid mechanics of large blood vessels, Cambridge: Cambridge Univ. Press, 1980.

[64] C. S. Peskin and D. M. McQueen. A three-dimensional computational method for blood flow in the heart. I. Immersed elastic fibers in a viscous incompressible fluid. *J. Comput. Phys.*, 81(2):372–405, 1989.

[65] J. E. Pilliod, Jr. and E. G. Puckett. Second-order accurate Volume-of-Fluid algorithms for tracking material interfaces. *J. Comput. Phys.*, 199(2):465–502, 2004.

[66] S. Popinet. GERRIS: a tree-based adaptive solver for the incompressible Euler equations in complex geometries. *J. Comput. Phys.*, 190(2):572–600, 2003.

[67] E. G. Puckett, A. Almgren, S. Bell, D. Marcus, and W. Rider. A high order projection method for tracking fluid interfaces in variable density incompressible flows. *J. Comput. Phys.*, 130(1):269–282, 1997.

[68] R. Purvis and F. T. Smith. Droplet impact on water layers: post-impact analysis and computations. *Philos. Trans. R. Soc. Lond. Ser. A Math. Phys. Eng. Sci.*, 363(1830):1209–1221, 2005.

[69] M. Quero. PhD thesis, Cranfield University, 2006.

[70] Y. Renardy, S. Popinet, L. Duchemin, M. Renardy, M. Clarke, S. Zaleski, and C. Josserand. Impact of a viscous drop on a superhydrophobic surface and evolution to a pyramid. *J. Fluid. mech.*, 484:69–83, 2003.

[71] J. Richards. PhD thesis, University of Delaware, 1994.

[72] W. J. Rider and D. B. Kothe. Reconstructing volume tracking. *J. Comput. Phys.*, 141(2):112–152, 1998.

[73] L. Rosenhead(editor). Laminar boundary layers: An account of the development, structure and stability of laminar boundary layers in incompressible fluids, Clarendon Press, 1963.

[74] M. Rudman. Volume tracking methods for interfacial flow calculations. *Int. J. Numer. Meth. Fluids*, 24:671–691, 1997.

[75] M. Rudman. A volume tracking method for incompressible flows with large density gradients. *J. Comput. Phys.*, 28:357–378, 1998.

[76] M. Sahin. Lid driven cavity flows, PhD thesis, University of Lausanne, 2001.

[77] R. Scardovelli and S. Zaleski. Direct numerical simulation of free-surface and interfacial flow. *Annu. Rev. Fluid Mech.*, 31:567–603, 1999.

[78] R. Scardovelli and S. Zaleski. Interface reconstruction with least-square fit and split Eulerian-Lagrangian advection. *Int. J. Numer. Meth. Fluids*, 41(2):251–247, 2003.

[79] T. Seruga. Endovascular treatment of intercranial arteriovenous malformations. *Radiol. Oncology*, 36:201–208, 2002.

[80] J. A. Sethian. Level Set techniques for tracking interfaces. In *Curvature flows and related topics (Levico, 1994)*, volume 5 of *GAKUTO Internat. Ser. Math. Sci. Appl.*, pages 215–231. Gakkōtosho, Tokyo, 1995.

[81] J. A. Sethian and A. Vladimirsky. Ordered upwind methods for static Hamilton-Jacobi equations: theory and algorithms. *SIAM J. Numer. Anal.*, 41(1):325–363, 2003.

[82] F. T. Smith. Flow through symmetrically constricted tubes. *J. Inst.Maths Applics*, 21:145–156, 1978.

[83] F. T. Smith. On the high Reynolds number theory of laminar flows. *IMA J. Appl. Math.*, 28(3):207–281, 1982.

[84] F. T. Smith. Two-dimensional disturbance travel, growth and spreading in boundary layers. *J. Fluid Mech.*, 169:353–377, 1986.

[85] F. T. Smith and M. A. Jones. One-to-few and one-to-many branching tube flows. *J. Fluid Mech.*, 423:1–31, 2000.

[86] F. T. Smith and M. A. Jones. AVM modelling by multi-branching tube flow: large flow rates and dual solutions. *Math. Med. Biol.*, 20:183–204, 2003.

[87] F. T. Smith, N. C. Ovenden, P. T. Franke, and D. J. Doorly. What happens to pressure when a flow enters a side branch? *J. Fluid Mech.*, 479:231–258, 2003.

[88] S. Songdong Shao, C. Ji, D. I. Graham, R. E. Reeve, P. James, and A. J. Chadwick. Simulation of wave overtopping by an incompressible SPH model coastal engineering. *J. Comput. Phys.*, 53(9):723–735, 2006.

[89] P. K. Stansby, A. Chegini, and T. C. D. Barnes. The initial stages of dam-break flow. *J. Fluid Mech.*, 374:407–424, 1998.

[90] M. Sussman and E. Puckett. A coupled Level Set and Volume-of-Fluid method for computing 3D and axisymmetric incompressible two-phase flows. *J. Comput. Phys.*, 162(2):301–337, 2000.

[91] M. Tadjfar and F. T. Smith. Direct simulations and modelling of basic three-dimensional bifurcating tube flows. *J. Fluid Mech.*, 519:1–32, 2004.

[92] W. Taki, Y. Yonekawa, H. Iwata, A. Uno, K. Yamashita, and H. Amemiya. A new liquid material for embolization of arteriovenous malformations. *Amer J. Nuero.*, 11:163–168, 2002.

[93] X. Z. Tang and A. H. Boozer. A Lagrangian analysis of advection-diffusion equation for a three-dimensional chaotic flow. *Phys. Fluids*, 11(6):1418–1434, 1999.

[94] J. P. K. Tillett. On the laminar flow in a free jet of liquid at high Reynolds numbers. *J. Fluid Mech.*, 32:273–292, 1968.

[95] S. N. Timoshin and F. T. Smith. Singularities encountered in three dimensional boundary layers under an adverse or favourable pressure gradient. *Philos. Trans. R. Soc. Lond. Ser. A Math. Phys. Eng. Sci.*, 352(1698):45–87, 1995.

[96] M. Torrey, L. Cloutman, R. Mjolsness, and C. W. Hirt. NASA-VOF2D-A computer program for incompressible flows with free surfaces. Los Alamos Antional laboratory report LA-10612-MS.

[97] G. Tryggvason. Numerical solutions of the Rayleigh-Taylor instability. *J. Comput. Phys.*, 75:253–282, 1988.

[98] F. N. van de Vosse. Mathematical modelling of the cardiovascular system. *J. Engrg. Math.*, 47(3-4):175–183, 2003. Mathematical modelling of the cardiovascular system.

[99] J. Welch, F. Harlow, J. Shannon, and B. Daly. The MAC Method, a computing technique for solving viscous, incompressible fluid-flow problems involving free surfaces. Los Alamos report LA-3425, 1966.

[100] G. Wu. Two-dimensional liquid column and liquid droplet impact on a solid wedge. *Q. J. Mech. and app. math.*, in press, 2007.

[101] www.childrenshospital.org/az/Site1830/mainpageS1830P0.html.

[102] www.neuronet.pitt.edu/endovascular/treatments/avm.html.

[103] www.ninds.nih.govhealthandmedical/pubs/arteriovenous.html.

[104] www.strokecenter.org/pat/ich.htm.

[105] www.stroke.uscf.edu/pages/asnr Book3-AVM.html.

[106] S. Yamada. Arteriovenoous malformations in functional areas of the brain, Blackwell Futura 2002.

[107] K. Yokoi, F. Xiao, H. Liu, and K. Fukasaku. Finite element simulation of blood flow in a realistic model of a moving human right coronary artery, proceedings of the 10th annual conference of the CFD society of Canada. 202:317, 2005.

[108] K. Yokoi, F. Xiao, H. Liu, and K. Fukasaku. Three-dimensional numerical simulations of flows with complex geometries in a regular cartesian grid and its application to blood flow in cerebral artery with multiple aneurysms. *J. Comput. Phys.*, 202:1–19, 2005.

[109] D. Youngs. Time-dependent multi-material flow with large fluid distortion. *Numerical Methods for Fluid Dynamics*, 113(1):134–147, 1982.

[110] D. L. Youngs. Modelling turbulent mixing by Rayleigh-Taylor instability. *Phys. D*, 37(1-3):270–287, 1989. Advances in fluid turbulence (Los Alamos, NM, 1988).

[111] S. Zalesak. Fully multidimensional flux-corrected transport algorithms for fluids. *J. Comput. Phys.*, 335-362(2):335–354, 1979.